INFORMATION TO USERS

This manuscript has been reproduced from the microfilm master. UMI films the text directly from the original or copy submitted. Thus, some thesis and dissertation copies are in typewriter face, while others may be from any type of computer printer.

The quality of this reproduction is dependent upon the quality of the copy submitted. Broken or indistinct print, colored or poor quality illustrations and photographs, print bleedthrough, substandard margins, and improper alignment can adversely affect reproduction.

In the unlikely event that the author did not send UMI a complete manuscript and there are missing pages, these will be noted. Also, if unauthorized copyright material had to be removed, a note will indicate the deletion.

Oversize materials (e.g., maps, drawings, charts) are reproduced by sectioning the original, beginning at the upper left-hand corner and continuing from left to right in equal sections with small overlaps. Each original is also photographed in one exposure and is included in reduced form at the back of the book.

Photographs included in the original manuscript have been reproduced xerographically in this copy. Higher quality 6" x 9" black and white photographic prints are available for any photographs or illustrations appearing in this copy for an additional charge. Contact UMI directly to order.

Bell & Howell Information and Learning
300 North Zeeb Road, Ann Arbor, MI 48106-1346 USA
800-521-0600

(Revised 7/94)

PURDUE UNIVERSITY
GRADUATE SCHOOL
Thesis Acceptance

This is to certify that the thesis prepared

By Jim H. Qin

Entitled

NUMERICAL SIMULATIONS OF A TURBULENT AXIAL VORTEX

Complies with University regulations and meets the standards of the Graduate School for originality and quality

For the degree of Doctor of Philosophy

Signed by the final examining committee:

Gregory A. Blaisdell, chair

John Sullen

Steven Frankel

Marc H. Williams

Approved by: [signature] 12/8/98
Department Head Date

☐ is
This thesis ☒ is not to be regarded as confidential. Gregory A. Blaisdell
Major Professor

Format Approved by:

Gregory A. Blaisdell or _____
Chair, Final Examining Committee Thesis Format Adviser

NUMERICAL SIMULATIONS OF A TURBULENT AXIAL VORTEX

A Thesis
Submitted to the Faculty

of

Purdue University

by

Jim H. Qin

In Partial Fulfillment of the
Requirements for the Degree

of

Doctor of Philosophy

December 1998

谨献给我的母亲和妻子

ACKNOWLEDGMENTS

The opportunity to study at Purdue University has been an enjoyable experience and a privilege for which I am grateful. First, I would like to thank my advisor Professor Gregory Blaisdell for introducing me to two of the most challenging and interesting fields in Computational Fluid Dynamics: turbulence and parallel computation. His guidance, critique, encouragement, and advice are greatly appreciated. It has been a real honor and a privilege to work with him during my stay at Purdue University.

I would like to express my gratitude to Professor Marc Williams for the numerous discussions about this work and also for serving on my advisory committee. Likewise, I gratefully acknowledge Professors John Sullivan and Steven Frankel for their support and willingness to serve on my advisory committee.

I would like to acknowledge the financial support of the Purdue Research Foundation and the IBM/Purdue Shared University Research Program. This research would not have been possible without access to the computer resources of the Purdue University Computer Center, as well as the Pittsburgh Supercomputing Center.

The numerous discussions about this work with Dr. Karim Shariff, Dr. Philippe Spalart, and Professor Robert Moser were very enlightening and greatly appreciated.

In addition, I would like to thank all my friends and colleagues at Purdue University for their support and camaraderie. Some of them deserve special mention. The overall assistance of Dr. Evangelos Spyropoulos and Mr. Sridhar Kompella played a vital role during my stay at Purdue University. Also, my officemate, Mr. Chienchi Chao, put up with me for nearly three years.

I can not express enough love to my Mom for her constant love and unquestioning support during my extended stay in academia. I would like to thank my brothers for their continuing support and inspiration.

Last but not least, a big thank you to my wife, Sunny, for allowing me to pursue the goal of obtaining a Ph.D. degree while sacrificing much because of it. Her love and understanding through the duration of this work are greatly appreciated.

TABLE OF CONTENTS

Page

Page

LIST OF TABLES

LIST OF FIGURES

Figure Page

Figure Page

Appendix
Figure

NOMENCLATURE

Roman symbols

$\mathbf{A}$	Mass matrix, Section 4.3.4
$\mathbf{B}$	Viscous matrix, Section 4.3.4
g_l	B-spline polynomial, Section 4.3.2
C	Constant, Section 3.2.2
c_0^*	Dimensional speed of sound based on the initial mean temperature, Section 2.2
c_p^*	Specific heat at constant pressure, Section 2.2
C_{ij}	Convection tensor, Section 3.5
D_{ij}	Viscous diffusion tensor, Section 3.5
E	Aspect ratio of elliptic streamlines, Section 1.2.2
e	Internal energy per unit mass, Section 2.2
e_T	Total energy per unit mass, Section 2.2
$\mathcal{F}_n$	Fourier coefficient 2.4.1
$\mathbf{e_r}$, $\mathbf{e_\theta}$, $\mathbf{e_z}$	Unit vectors of cylindrical coordinate system, Section 4.3.1
$\mathbf{F}$	Nonlinear tensor, Section 4.3.5
f	Generic function, Section 2.3
f'	Derivative of f, Section 2.4.1
$\mathcal{K}$	Global turbulence kinetic energy, Section3.3.2
k	Turbulence kinetic energy, Section 3.3.1
k	Thermal conductivity, Section 2.2

k_n	Wavenumbers, Section 2.4.1
k_z	Wave number in the streamwise direction, Section 4.3.1
k_θ	Wave number in the azimuthal direction, Section 4.3.1
L_z	Length of the computational domain, Section 2.4.1
M_p	Initial tangential flow Mach number, Section 3.2.1
M_t	Initial maximum fluctuating Mach number, Section3.2.2
N_x	Grid points in the x-direction, Section 3.2.3
N_y	Grid points in the y-direction, Section 3.2.3
N_z	Grid points in the z-direction, Section 3.2.3 and 4.3.1
O_{ij}	Rotation tensor, Section 3.5
p	Pressure, Section 2.2
Pr	Prandtl number, Section 2.2
P_{ij}	Production tensor, Section 3.5
Pt_{ij}	Pressure transport tensor, Section 3.5
$\mathcal{Q}$	Global swirl number, Section 3.3.2
q	Swirl number, Section 3.3.2
q_0	Initial swirl number, Section 3.2.1
r	Radial coordinate, Section 3.2.1
r_0	Initial vortex core size, Section 3.2.1
$\hat{r}$	Dimensionless radial coordinate, Section 3.2.1
Re	Computational Reynolds number, Section 2.2 and 4.2
Re_Γ	Reynolds number based on circulation, Section 3.2.3
$S_{r\theta}$, S_{rz}	Shear rate, Section 3.3.5
T	Temperature, Section 2.2
	Time scale Section 3.3.2
T_{ij}	Turbulent transport tensor, Section 3.5
t	Time, Section 2.2
u	Velocity component in the x direction, Section 3.3.1
$\mathbf{u}$	Velocity vector, Section 4.2

$\mathbf{u}_l$	Vector expansion functions, Section 4.3.2
u_i	Velocity component in the i-th direction, Section 2.2
V_0	Initial wake velocity deficit, Section 3.2.1
V_r, V_θ, V_z	Components of mean velocity in r, θ, z direction, Section 3.3.3
$\mathbf{v}$	Numerical approximation to $\mathbf{u}$, Section 4.3.1
v	Velocity component in the y direction, Section 3.3.1
v_r, v_θ, v_z	Components of velocity in r, θ, z direction, Section 3.3.1
$\mathbf{w}_{l'}$	Vector weight function, Section 4.3.2
w	Velocity component of in the z direction, Section 3.3.1
x_i	Spatial coordinate, Section 2.2
x, y, z	Cartesian coordinates

Greek symbols

α	Streamwise wave number, Section 3.2.3
α', α'', α''	Constants in the time advance scheme, Section 2.4.4
α_{jml}	Expansion coefficients, Section 4.3.1
β', β'', β''	Constants in the time advance scheme, Section 2.4.4
Γ	Vortex circulation, Section 3.3.3
γ	Ratio of specific heats, Section 4.2
	Constant in the initial mean velocity profile, Section 3.2.1
Δt	Time step, Section 2.4.4
Δz	Grid Spacing in the streamwise direction, Section 2.4.1
ζ	Computational coordinate, Section 2.4.2
ϵ_{ij}	Dissipation tensor, Section 3.5
ϵ	Dissipation rate, Section 3.5
μ	Molecular viscosity, Section 2.2
ν	Kinematic viscosity, Section 2.2
ν_T, ν_{T1}, ν_{T2}	Eddy viscosity, Section 3.3.5

ρ	Density, Section 2.2

Other Symbols

$\overline{(\,)}$	Line or surface average 2.3
$(\,)^*$	Non-dimensional quantity, Sections 2.2 and 2.2
$(\,)^{\pm\pm}$	Indicates the class of expansion functions, Section 4.3.1
$'$	Reynolds fluctuating quantity.
$\hat{\Delta}$	Fourier transformed del operator.

Abbreviations

DNS	Direct numerical simulation
FFT	Fast Fourier transform.
LHS	Left hand side.
ODE	Ordinary differential equation.
RHS	Right hand side.
TKE	Turbulent kinetic energy.

ABSTRACT

ABSTRACT Qin, Jim Hongxin Ph.D., Purdue University, December 1998. Numerical Simulations of a Turbulent Axial Vortex. Major Professor: Gregory A. Blaisdell.

Although the vortex is present in most flows of engineering interest, the turbulent structure of the vortex is not well understood. Current prediction capabilities are especially weak for the vortex as well as other strongly rotating flows. The objective of this work is to aid the development of turbulence models for the vortex as well as strongly rotating flows in general by using direct numerical simulations of the vortex. The present study focuses on the turbulent axial vortex with and without an external strain field.

The numerical simulations of a turbulent axial vortex without strain, i.e. an isolated vortex, have been performed by using a pseudo spectral method for compressible flow. The results qualitatively match well with the experimental data.

The isolated vortex is stable unless the mean axial wake flow has sufficient magnitude. During the period of decay of disturbances, the mean tangential velocity profile exhibits anti-diffusion because a negative eddy viscosity develops near the center of the vortex. With the disturbance growth, the isolated vortex develops large-scale helical vortex structures , but they eventually disappear during the period of relaminarization.

The details of turbulent statistics have been examined. The turbulent structure is related to the in stability of the isolated vortex. The budgets for the Reynolds stresses reveal that the production term is the primary source term, but the pressure strain, pressure transport, and turbulent transport terms also make a large contribution to the budgets for the Reynolds stresses.

The numerical simulations of a turbulent axial vortex with strain, i.e. a strained vortex, have been performed using the B-spline method for incompressible flow. The results from the strained vortex show that, with the effect of an external strain field, the vortex is unstable for all time because of the presence of the Widnall instability. The turbulent structure within the vortex is altered by the presence of the external strain.

1. INTRODUCTION

1.1 Motivation

The vortex is one of the most fundamental structures in fluid mechanics, yet it is poorly understood. It contains structure that is almost purely potential in nature and structure in which viscosity plays a large role as shown in Figure 1.1 (Takahashi & McAlister 1987). The turbulent axial vortex is a complex turbulent flow, but it is simple enough to be studied in detail and generic enough to have a wide range of applications. The turbulent axial vortex is present in most flows of engineering interest. Turbulent axial vortices occur in the wakes of wings, propellers, control surfaces and other lifting surfaces, in turbomachinery, and in combustion systems.

One outstanding application is the wake-hazard problem. The trailing vortices shed from the wings of aircraft have been studied extensively and are important because of their slow rate of decay; the vortex shed from a large commercial transport aircraft can cause a small aircraft following miles behind to lose control. The vortices dramatically alter the flow over the trailing aircraft. Similarly, the vortex shed from a canard wing can alter the flow over a trailing main wing and the vortex shed from one rotor of helicopter can alter the flow over the trailing rotor. This last example, an interaction called blade slap, is largely responsible for the high noise production of helicopters.

In turbomachinery, turbulent vortices are found in very complex combinations on the turbine endwall and at the base of the turbine and compressor blades. They collect and sweep away the protective boundary layer allowing high rates of heat transfer between the hot stream and surface, damaging the underlying structure. Current design methods for turbine passages are mostly based on two-dimensional calculations which

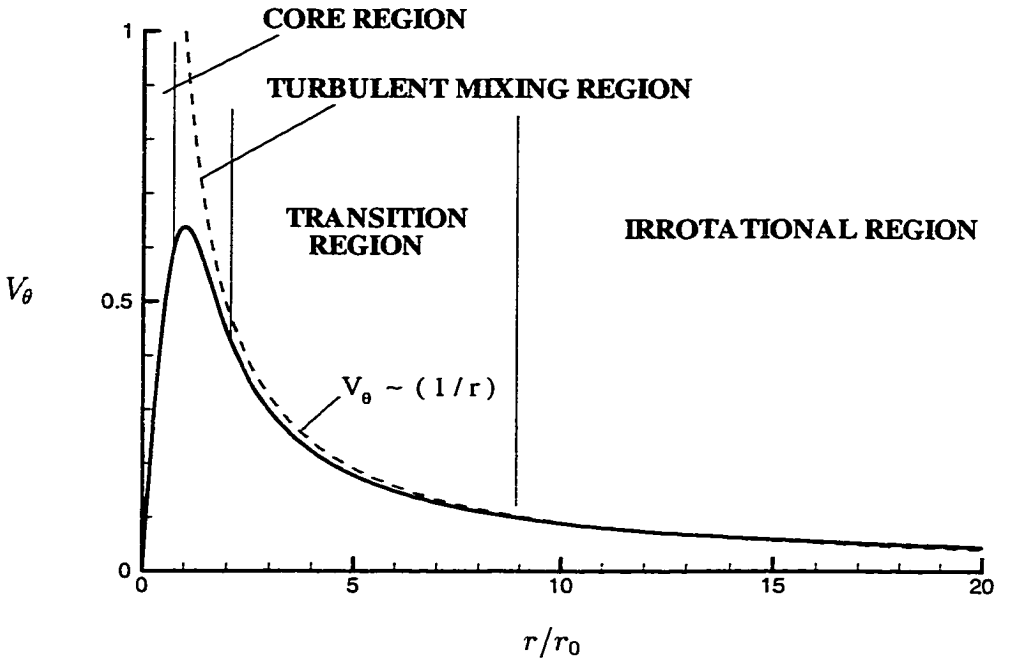

Figure 1.1 Structure of a typical axial vortex from Takahashi & McAlister (1987).

do not accurately predict these effects. Three-dimensional techniques are currently under development but require a detailed understanding of the vortex structure.

Turbulent axial vortices are also important in the area of underwater acoustics. They are the primary location for cavitation and, therefore, are a source of acoustic noise.

If vortices are so prevalent and so important, then why have they not been understood long ago; or, alternatively, why can we seemingly do just fine without really understanding them? The answer is simple. We could do better with better understanding, but we have become very clever in combining empirical correlations of their effects into our design methods. Workers have argued simple models using empirical corrections, but solid understanding of turbulent axial vortices offers two major benefits. First, with an improved understanding we can design flow systems which take advantage of the properties and structure of the turbulent axial vortex. Secondly,

improved understanding can be incorporated into analytical methods for engineering design.

Sometime in the future, engineering design methods will be based on solution of the full equation of motions without any turbulence models and the effects of vortices will be captured along with the solution for the entire flow field. Solution of the full equations without any turbulence models in complex passages at high Reynolds number will require immense computer resources. The purposes of this work is to aid the development of turbulence models for the vortex as well as strongly rotating flows in general by using direct numerical simulations of the vortex.

1.2 Literature Review

A large body of literature exists describing studies of axial vortices in their many forms. In order to review the literature effectively, the scope of this review will be limited to studies of the structure and development of axial vortices. The topics of these papers can be broken into three major categories: experimental measurement of vortices, theoretical analysis of vortices, and numerical simulation of axial vortices.

1.2.1 Experimental Measurement

There have been several experimental studies of a wingtip vortex in the roll up region or near field. Chigier & Corsiglia (1972) studied the trailing vortices off of a rectangular wing and a model of a Convair 990 in the NASA Ames 7 by 10 foot wind tunnel. They found that increasing the drag on the wing increases the magnitude of axial velocity defects in the core of the vortices, reduces the maximum tangential velocity, and increases the vortex core radius. Baker, Bofah & Saffman (1974) measured the mean and turbulent quantities in trailing vortices generated by two different platforms. They varied the free-stream velocity and angle of attack and made measurements in planes from five chord lengths to sixty chord lengths downstream of the wings. They point out that the vortex position is not fixed and that this wandering broadens the profiles and reduces the magnitude of gradients in the vicinity of the

vortex. The measurements of trailing vortices reveal a very high turbulence level in the core region of the vortex. Sampson (1977) made detailed measurements of the velocity, vorticity, and pressure distributions over a plane five chords downstream of a lifting wing. At that location he found a distinct vortex and a vortex sheet. The vortex sheet still contained from 10 to 30 percent of the vorticity depending on the generator angle of attack. He also found that the turbulent vortex model of Hoffmann & Joubert (1963) accurately described his results. Recently, Chow & Zilliac (1994) and Devenport, Rife, Liapis & Follin (1996) made turbulence measurements of a wingtip vortex. Experiments of Chow & Zilliac (1994) were carried out at less than one chord length downstream. They found that the peak turbulence levels in data planes measured over the wing were near the edge of the viscous core of the vortex and the turbulence decayed quickly with streamwise distance. They also pointed out that the Reynolds shear stresses (in Cartesian coordinates) were not aligned with the mean strain rate, indicating that an isotropic-eddy-viscosity based prediction method can not accurately model the turbulence in the vortex. Devenport et al. (1996) completed turbulence measurements of a wing-tip vortex from 5 to 30 chord lengths downstream. Their studies showed that outside the core the flow structure is dominated by the remainder of the wing wake which winds into an ever-increasing spiral and that turbulence stress levels vary along the wake spiral in response to the varying rates of strain imposed by the vortex. There is no large region of axisymmetric turbulence surrounding the core and little sign of turbulence generated by the rotational motion of the vortex.

While there have been very few reliable turbulence measurements in a tip vortex beyond the tip region, such measurements have been made on trailing vortices generated by split wings. Split-wing vortices appear less susceptible to wandering and are thus more easily measured (Devenport et al. 1996). Turbulence stress measurements have been made in split-wing vortices by Phillips & Graham (1984) and

Bandyopadhyay, Stead & Ash (1991), among others. Phillips & Graham (1984) presented detailed turbulence measurements for several types of manipulated line vortices. Their experiments were carried out at 45 or more chord lengths downstream of a double-branch generator. Their results are interesting in that the fluctuating velocity components in the core were high while Reynolds shear stresses generally tend to be low or zero near the center of the core. The Reynolds shear stresses peak at the point of maximum tangential velocity and then decay with increasing radial distance. At the same time, Philips and Graham's data show almost no discernable diffusion of the core (unless a strong axial jet or wake is superimposed). The study of Bandyopadhyay et al. (1991) also shows velocity fluctuations to be maximum in the vortex core. They concluded that for their range of test conditions, the Rossby number (axial velocity defect/maximum tangential velocity) was the controlling parameter for the turbulence structure, not the vortex Reynolds number (circulation/viscosity). They also concluded that the inner core is not a regional in solid-body rotation that does not interact with the outer vortex region, rather it is a relaminarizing region.

While these results are interesting, it should be borne in mind that tip and split-wing vortices can have a quite different turbulence structure. However, it is not surprising because spilt-wing vortices are formed by the merger of two vortices, the merging process producing a large region of roughly axisymmetric turbulence around the core that is absent from a tip vortex (Smith & Kummer 1985).

1.2.2 Theoretical Analysis of Vortices

Analyses of a tip vortex have been more successful in the far-field than in the near-field. Assumptions that are often made in simplifying the far-field analysis may not hold in the near-field. The main assumption that has been made in all previous analytic studies is that of axisymmetric flow. This approximation has had some success in predicting the far-field behavior of the tip vortex. In particular, similarity solutions have given estimates of the decay rate of a tip vortex far downstream of the

trailing edge of a wing. These types of analyses are most useful in analyzing the wake vortex encounter problem.

A few authors have analytically investigated the structure of laminar trailing vortices. The simplest model of an axial vortex is a Rankine vortex consisting of a core in solid body rotation surrounded by an irrotational field:

$$V_\theta = \frac{\Omega r_0^2}{r}, \qquad r \geq r_0 \tag{1.1}$$

$$V_\theta = \Omega r, \qquad r \leq r_0 \tag{1.2}$$

where Ω is the angular velocity of the solid body rotation and r_0 is the radius of the viscous core region, also defined here as the point of maximum tangential velocity. Another simple mode is Burnham's model(Reimer 1997)

$$V_\theta = \frac{\Gamma}{2\pi}\left[\frac{r}{r_0^2 + r^2}\right]. \tag{1.3}$$

Both models are simple approximations to the well known solution for the growth of a laminar 2D line vortex which can be found in Panton (1984). The velocity distribution of a laminar 2D line vortex is given as follows:

$$V_\theta = \frac{\Gamma}{2\pi r}\left[1 - \exp\left(-\frac{r^2}{4\nu t}\right)\right]. \tag{1.4}$$

However both models do not include an axial flow. Batchelor (1964) did an analysis on axial flow in a trailing vortex starting with the steady axisymmetric incompressible momentum equations. Using boundary-layer type approximations, he derived the axial velocity as follows:

$$V_z = U_\infty, \qquad r \geq r_0 \tag{1.5}$$

$$V_z = \left[U_\infty^2 + 2\Omega^2(r_0^2 - r^2)\right]^{\frac{1}{2}}, \qquad r \leq r_0 \tag{1.6}$$

Moore & Saffman (1972) sought to improve upon Batchelor's analysis and studied the influence of viscosity on the axial flow in a laminar trailing vortex. They generalized Batchelor's expression for arbitrary and internal structure.

All past analytical studies done on a turbulent tip vortex have assumed an isotropic eddy viscosity to represent the behavior of the turbulence. We shall see that this sort

of approximation fails badly, because for a vortex flow-field the shear stresses are not aligned with the mean strain rate. The analysis by Hoffmann & Joubert (1963) on a turbulent line vortex predicted a constant eddy viscosity and a logarithmic radial variation of circulation. Their circulation profile, $\Gamma(r)$, which is independent of viscosity is reported here:

(i) An "eye" of solid body rotation given by

$$\frac{\Gamma(r)}{\Gamma(r_0)} = 1.83\left(\frac{r}{r_0}\right)^2; \tag{1.7}$$

(ii) A transition between the solid body rotation and the logarithmic circulation;

(iii) A region in which circulation varies logarithmically with radius and is given by

$$\frac{\Gamma(r)}{\Gamma(r_0)} = 2.14\log_{10}\left(\frac{r}{r_0}\right) + 1. \tag{1.8}$$

Govindaraju & Saffman (1971) predicted an overshoot of circulation for a fully-rolled-up turbulent vortex under light loading conditions. Their model allows for $\Gamma(r_0)/\Gamma_\infty = 1.2$, whereas most investigators have found values ranging from 0.37 to 0.6. However, convincing experimental evidence of the existence of an overshoot of circulation is lacking.

Iversen (1976) and Uberoi (1979) studied the trailing vortex decay. Both of them pointed out that an isolated vortex decays very slowly by diffusion of vorticity. Uberoi explained the mechanism of decay of laminar and turbulent trailing vortices with increasing distance. For a turbulent vortex(Uberoi 1979), the change in the axial velocity difference between the core and the surrounding region causes radial convection and some associated axial convection of angular momentum. He also concluded that the axial velocity difference between the core and surrounding region is necessary for the sustenance of turbulence in the vortex core.

The bulk of the analytic work on axial vortices is in the area of stability analysis. Rayleigh (1916) was first to study the stability of planar shear flows with system rotation. He presented a necessary and sufficient condition for the stability of shearing

and rotating flows to axisymmetric disturbances without viscosity as follows:

$$\frac{d\Gamma^2}{dr} > 0, \tag{1.9}$$

where Γ is the circulation. Lessen, Singh & Paillet (1974) proposed the q-vortex model, which is a simplified version of the Batchelor vortex with the velocity field

$$V_\theta(r) = \frac{q}{r}\left(1 - e^{-r^2}\right) \quad \text{and} \quad V_z(r) = V_0 - e^{-r^2}\,. \tag{1.10}$$

The q-vortex is characterized by a swirl parameter q which is proportional to the ratio of the maximum tangential velocity to the axial velocity deficit or excess. Most of the studies on the stability of vortices in the past two decades used the q-vortex as a model. Lessen et al. (1974) and Lessen & Paillet (1974) presented inviscid and viscous calculations of the stability characteristics for the q vortex. They found that the axial vortex is most unstable to helical waves with negative azimuthal wavenumber (winding opposite to the rotation of the mean flow) and that increasing the swirl parameter q above 1.5 stabilizes all the modes regardless of their orientations. Leibovich & Stewartson (1983) used asymptotic methods to study the stability characteristics of q-vortex model. They presented a sufficient condition for the instability of an axial vortex as follows:

$$V_\theta \frac{d\Omega}{dr}\left[\frac{d\Omega}{dr}\frac{d\Gamma}{dr} + \left(\frac{dV_z}{dr}\right)\right] < 0, \tag{1.11}$$

where $\Omega = V_\theta/r$ is the angular velocity of the basic flow. They also found instabilities at $q = 1.58$. The corresponding growth rates were very small and indicated that the vortex shows strong instabilities with $q < \sqrt{2}$.

More recently, Khorrami (1991) obtained highly accurate results for a q-vortex that include the viscous effects also. He pointed out that there exist two unstable modes, azimuthal wavenumbers $m = 0$ and $m = 1$, for the trailing vortex and provided the first direct evidence that viscosity can have a destabilizing effect on swirling flow because the growth rates of the viscous modes are reported to be orders of magnitude smaller than those of the inviscid modes. Both of these viscous modes appear as fairly long-wave length instabilities with an axial wavelength that is of the same

order of magnitude as the vortex core radius. The experiments of Sarpkaya & Daly (1987) and Singh & Uberoi (1976) show results similar to the analysis of Khorrami. Duck & Khorrami (1991) extended this work focusing on these modes. Mayer & Powell (1992), using a spectral collocation and matrix eigenvalue method, mapped the entire unstable region in the swirl/axial-wavenumber space for various azimuthal wavenumbers.

The above instabilities are dependent on a sufficiently large axial velocity deficit, the presence of a circulation overshoot, or some combination following equation 1.11. As the axial flow decays downstream these instabilities can be diminished or eliminated. However, there are additional instability mechanisms which exist in airplane vortices.

A distinct behavior of trailing vortices is that each tip vortex induces a strain field on the other. The strain field can effect the stability of these vortices and thereby their turbulent structure downstream. The first quantitative analysis of the three-dimensional instability of trailing vortices in an ideal homogeneous fluid was given by Crow (1970). The results of his analysis are in good agreement with observations of the general features of long wave length aircraft wake instabilities and measurements of amplification rates. Strain also causes a small wave length instability, which was first studied in a vortex ring by Widnall & Sullivan (1973). Widnall, Bliss & Tsai (1974) extended this work focusing on a simple model for the vortex-ring instability. This instability indicated a vortex which is strained in the plane perpendicular to its axis is also unstable to small wave length disturbances. This instability mechanism could cause turbulence in a wake vortex to grow rather decay downstream.

An idealized homogeneous turbulent flow which is similar to the flow in the core of a strained vortex is the elliptic streamline flow. The elliptic streamline flow contains the effects of both rotation and strain. The elliptical flow can be described by

$$U_i = U_{i,j}x_j, \qquad U_{i,j} \equiv \begin{pmatrix} 0 & 0 & -\gamma-\epsilon \\ 0 & 0 & 0 \\ \gamma-\epsilon & 0 & 0 \end{pmatrix}. \tag{1.12}$$

The case $\epsilon = 0$ corresponds to pure rotation, while $0 < |\epsilon| < |\gamma|$ gives rotation dominated flows with geometrically similar elliptic streamlines with aspect ratio $E \equiv \sqrt{(\gamma+\epsilon)/(\gamma-\epsilon)}$. The linear stability of the elliptic streamline flow was studied in the context of rapid distortion theory (RDT) by Cambon *et al.* (1985, 1994). Bayly (1986), Peierrehumbert (1986), and Waleffe (1990) performed inviscid stability analyses. Bayly applied a Floquet-type stability analysis to show that the class of two-dimensional basic flows with closed elliptical streamlines can sustain certain planewave modes, owing to their periodic distortion. Bayly's study was prompted by the work of Peierrehumbert (1986), who found a short-wave instability in a numerical stability calculation for the Euler equations linearized about a locally elliptical flow. They found that for elliptical streamlines there exists a band of unstable modes in which the growth rate depends on the polar angle of the wavenumber vector. The band of unstable angles increases in width for increasing ellipticity of the streamlines. Also, the growth rate of the unstable models is independent of the magnitude of wavenumber vector. Therefore, arbitrarily small three-dimensional fluctuations can be created by an instability of a basic two-dimensional flow. The effects of viscosity were studied by Landman & Saffman (1987) and were included in the analysis of Cambon *et al.* (1985). The growth rate of the instabilities is modified by viscosity so that the grow rate is no longer independent of the magnitude of the wavenumber vector. They also found a high wavenumber cut-off of the instability. However, there is no low wavenumber cut-off, and arbitrarily large scales are unstable. This fact has important implications for doing numerical simulations of this flow, as pointed out by Blaisdell & Shariff (1994, 1996) . Waleffe (1990) also performed a weakly nonlinear stability analysis of the elliptic streamline flow.

The current study will include the effects of an applied strain field on the development of the turbulence within an axial vortex.

Another additional mechanism which can affect the stability of wake vortices is the generation of secondary vorticity in a stratified atmosphere can be generated through the baroclinic torque. The effects of stratification on wake vortices have

been considered by Spalart (1996); however, the current study does not consider stratification. Inclusion of this complication in turbulence simulation is left for future research.

1.2.3 Numerical simulation of axial vortices

Although there have been many computational studies of the roll-up of a vortex generated by a delta wing or of the process of vortex breakdown, few Navier-Stokes computational studies of the turbulent axial vortex exist.

Donaldson (1972) studied the decay of an isolated turbulent vortex in an infinite medium to evaluate his Reynolds stress transport turbulence model. Zheng & Ash (1993) evaluated algebraic, $k-\varepsilon$, and Reynolds stress models using an isolated vortex problem. The results showed that neither algebraic nor $k-\varepsilon$ models are capable of handling the curvature effects and turbulent-non-turbulent interfaces associated with vortex cores, but the Reynolds stress model results were in good agreement with the prediction of Donaldson (1972) and the related experimental results of Hoffmann & Joubert (1963). Zheng and Ash also predicted the turbulent wake vortex motion near the ground using a Reynolds stress model. Their prediction demonstrated that the turbulent kinetic energy has a maximum in the interface sheath between the core and the outer potential-vortex flow. Zeman (1995) used a full Reynolds stress model to study the far-field nature of turbulence in an isolated vortex. He did not include an axial flow and predicted a rapid decay of the initial turbulence in the vortex core. Also his contours of $\overline{v_r' v_\theta'}$ were qualitatively similar to those found in experiments(Chow 1994) and simulated in the present study.

Sreedhar and Ragab (1994, 1995a, 1995b) did a series of numerical simulations of a turbulent axial vortex using direct numerical simulation (DNS) and large eddy simulation (LES). Using LES, they (Sreedhar & Ragab 1994) first studied the effect of random disturbances on the stability of the Lamb-Oseen vortex and the Taylor vortex. The Taylor vortex has a region of decreasing circulation and is therefore unstable by the Rayleigh criterion; however, it is not representative of a realistic wing-tip vortex,

except possibly in the case of a stratified medium in which the generation of secondary vorticity may create a region of decreasing circulation. They found that the Taylor vortex went through a transition process while the Oseen vortex simply quenched the initial disturbances. These two simulations were for vortices with no axial velocity. Later, they investigated the effects of an axial velocity deficit on the structure of the q-vortex. They found that the axial velocity deficit is weakened faster than the tangential velocity. The combination of a weaker axial velocity deficit and swirling flow then quenches the turbulent motion and the core relaminarizes.

The study of an isolated vortex in the current work is similar to theirs. The main difference is the numerical method employed and the quality of the turbulent statistics. In contrast to the fourth order finite difference method with a finite domain used by Ragab & Sreedhar (1995*a*), a spectral method with an infinite domain is employed in the current work. Therefore, the image flows are moved infinitely far away. Also, the current results include more detailed turbulent statistics.

1.3 Objectives and Summary

The primary objectives of this work are to improve our understanding of how turbulence within the axial vortex behaves and how the turbulence affects the distribution of vorticity. Also, current turbulence models do not perform well for strongly rotating flows and the current study is able to provide necessary information to directly evaluate the turbulence closure models for such flows. The more specific objectives are the following:

- To determine whether axial vortices remain turbulent far down stream or the turbulence decays within a short distance.

- To characterize the turbulent structure of the vortex, whether the turbulence is concentrated in an annular region around a quasi-laminar core or whether the turbulent kinetic energy has a peak in the core.

- To complete an analysis of the Reynolds stress budgets and to understand the turbulent transport in the axial vortex.

- To understand how strain affects the turbulence development and the structure of the axial vortex.

The thesis is divided into two phases. First, a pseudo-spectral Fourier collocation method with a dual Cain's mapping is employed in a direct numerical simulation of a temporally developing isolated vortex. The methodology is briefly described in Chapter 2. The simulations of an isolated vortex and the results are described in Chapter 3. In the second phase, a B-spline spectral method is employed to consider the effects of strain on the vortex. The methodology is presented in Chapter 4. The numerical simulations of a strained vortex and the results are described in Chapter 5. Finally, the conclusions are summarized in chapter 6, together with recommendations for future work. Additional information regarding the transport equations for the Reynolds stress and the numerical method are given in the appendices. Appendix A gives the transport equation of Reynolds stress in cylindrical coordinates. Appendix B outlines the construction of B-splines and the properties of B-splines, and gives an introduction to the Galerkin method based on B-splines. Appendix C gives the definition of the mass, viscous and nonlinear term matrices in detail.

2. A PSEUDO-SPECTRAL METHOD WITH A DUAL CAIN'S MAPPING

2.1 Introduction

The direct numerical simulations (DNS) of an axial vortex without strain are implemented using the compressible DNS code of Blaisdell, Mansour & Reynolds (1991). This program was originally intended to simulate homogeneous turbulence. It uses a pseudo-spectral Fourier collocation method with a third-order Runge-Kutta time advancement scheme, and it has been ported to the Intel Paragon parallel computer. Modifications have been made for simulating an isolated vortex. A periodic array of vortices are imposed in the cross section to satisfy the periodic boundary conditions for the pseudo-spectral Fourier collocation method. In order to avoid the influence of the image flow, a dual Cain's mapping scheme is developed. The pseudo-spectral method is well documented in Blaisdell et al. (1991). In this chapter, the equations of motion governing compressible flow are presented in nondimensional form, and the definitions of averaging and the numerical method are briefly described.

2.2 Governing Equations

The staring point for the simulations of an axial vortex without strain is the compressible Navier-Stokes equations in Cartesian coordinates

$$\frac{\partial \rho}{\partial t} + \frac{\partial}{\partial x_i}(\rho u_i) = 0 \tag{2.1}$$

$$\frac{\partial}{\partial t}(\rho u_j) + \frac{\partial}{\partial x_i}(\rho u_j u_i) = -\frac{\partial}{\partial x_i}\left(p\delta_{ij} - \frac{\mu}{Re}\left(\frac{\partial u_i}{\partial x_j} + \frac{\partial u_j}{\partial x_i} - \frac{2}{3}\frac{\partial u_k}{\partial x_k}\delta_{ij}\right)\right) \tag{2.2}$$

$$\frac{\partial}{\partial t}(\rho e_T) + \frac{\partial}{\partial x_i}(\rho e_T u_i) = \frac{\partial}{\partial x_i}\left[\left(-p\delta_{ij} + \frac{\mu}{Re}\left(\frac{\partial u_i}{\partial x_j} + \frac{\partial u_j}{\partial x_i} - \frac{2}{3}\frac{\partial u_k}{\partial x_k}\delta_{ij}\right)\right)u_j + \frac{\mu}{(\gamma-1)RePr}\frac{\partial T}{\partial x_i}\right] \tag{2.3}$$

$$p = \rho T/\gamma \tag{2.4}$$

$$T = \gamma(\gamma-1)e \tag{2.5}$$

$$\rho e_T = \rho e + \frac{1}{2}\rho u_i u_i, \tag{2.6}$$

where ρ is the mass density; u_i, the velocity in the x_i direction; e_T, the total energy per unit mass; e, the internal energy per unit mass; p, the pressure; T, the temperature; and γ is the ratio of specific heats. Equations (2.1) to (2.6) have been nondimensionalized based on the following:

$$u_i = \frac{u_i^*}{c_0^*}, \quad t = \frac{t^* c_0^*}{L_0^*}, \quad x_i = \frac{x_i^*}{L_0^*}, \quad T = \frac{T^*}{T_0^*},$$
$$\rho = \frac{\rho^*}{\rho_0^*}, \quad p = \frac{p^*}{\rho_0^* c_0^{*2}}, \quad \mu = \frac{\mu^*}{\mu_0^*}, \tag{2.7}$$

where c_0^*, T_0^*, ρ_0^* and μ_0^* are the speed of sound, temperature, density and molecular viscosity, respectively, at the initial location of the maximum tangential velocity, and L_0^*, is the length scale which will be related to the computational box size. The computational Reynolds number and the Prandtl number in Equations (2.2) and (2.3) are defined as

$$Re = \frac{\rho_0^* c_0^* L_0^*}{\mu_0^*} \quad \text{and} \quad Pr = \frac{\mu^* c_p^*}{k^*}, \tag{2.8}$$

where k^* is the thermal conductivity, and c_p^* is the specific heat at constant pressure.

2.3 The Definitions of Averaging

In order to examine turbulence models, the turbulent fields are decomposed into mean and fluctuating components. For example, for an arbitrary variable f

$$f = \overline{f} + f'. \tag{2.9}$$

The definition of averaging which will be used in the rest of this work is described in this section.

In general, if a random variable is not statistically homogeneous in time or any space dimension, one has to use an ensemble average such as averaging over a large set of similar experiments:

$$\langle f(\mathbf{x},t)\rangle = \lim_{N\to\infty}\frac{1}{N}\sum_{n=1}^{N} f_n(\mathbf{x},t), \tag{2.10}$$

where angled brackets denote an assemble average.

If the field is statistically stationary, one can use a time average,

$$\overline{f}(\mathbf{x}) = \lim_{T\to\infty}\frac{1}{T}\int_0^T f(\mathbf{x},t)dt\,, \tag{2.11}$$

to replace the ensemble average. For a field which is statistically developing in time, the time average can not replace the ensemble average. But if the field is statistically homogeneous in all three spatial directions, one can use a spatial average,

$$\overline{f}(t) = \lim_{L\to\infty}\frac{1}{L^3}\int_0^L\int_0^L\int_0^L f(\mathbf{x},t)d\mathbf{x}\,, \tag{2.12}$$

to replace the ensemble average.

If the field is neither homogeneous in time nor in space, but is homogeneous on planes or along lines, an average on the planes or lines can be used to replace the ensemble average (Reynolds 1987). In the current work, the vortex is assumed to change slowly along its length, and so we assume the flow as homogeneous in the z direction (streamwise direction). Therefore, we preclude the case of vortex breakdown. In this case an average over the z direction,

$$\langle f(x,y,z,t)\rangle = \overline{f}(x,y,t) = \lim_{L_z\to\infty}\frac{1}{L_z}\int_0^{L_z} f(x,y,z,t)dz\,, \tag{2.13}$$

can be used to replace the ensemble average. Moreover, an axisymmetric flow is naturally homogeneous in the azimuthal direction, and the ensemble average is equivalent to an average over a θ - z cylindrical surface,

$$\langle f(r,\theta,z,t)\rangle = \overline{f}(r,t) = \lim_{L_z\to\infty}\frac{1}{2\pi L_z}\int_0^{L_z}\int_0^{2\pi} f(r,\theta,z,t)dzd\theta. \tag{2.14}$$

2.4 Numerical Method

A description of the numerical method is given in this section. The method chosen is a modified Fourier pseudo-spectral method with a compact storage third order Runge-Kutta time advancement scheme. Time advancement is performed in physical space rather than Fourier wave space for reasons of computational efficiency. The convective terms in the governing equations are modified to improve the accuracy and stability of the numerical method.

With the pseudo-spectral Fourier collocation method, periodic boundary conditions have to be applied in all three directions. The periodic boundary condition in the streamwise direction is obtained by an assumption of homogeneous flow. The periodic boundary conditions also can be satisfied in the cross section (x and y plane) by imposing an array of vortices around the domain as shown Figure 2.1. However, if the periodic boundary conditions are applied at finite boundaries of the cross section, the image flows will distort the original vortex circulation profile. As shown in the figure 2.2, the circulation profile of a Taylor vortex rather than the desired isolated vortex is generated with the influence of the image flows. A modification has been made to avoid the influence of the image flows. By mapping the finite computational domain to the infinite physical domain, the array of vortices is moved infinitely far away so that the influence of the image flows is automatically eliminated. A special mapping, Cain's mapping (Cain, Ferziger & Reynolds 1984), is used in this work. The reason for choosing Cain's mapping is that it has the advantage of retaining the efficiency of the FFT algorithm and, therefore, is ideally suited to the isolated vortex problem.

2.4.1 Spatial derivatives in the streamwise direction

Since the axial vortex flow is assumed to be homogeneous in the streamwise (z) direction, periodic boundary conditions are applied in the z direction. Therefore,

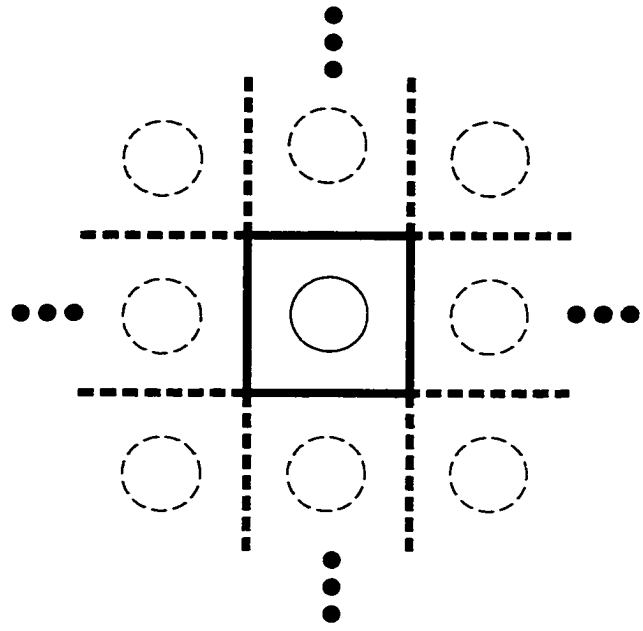

Figure 2.1 An array of vortices around the computational domain.

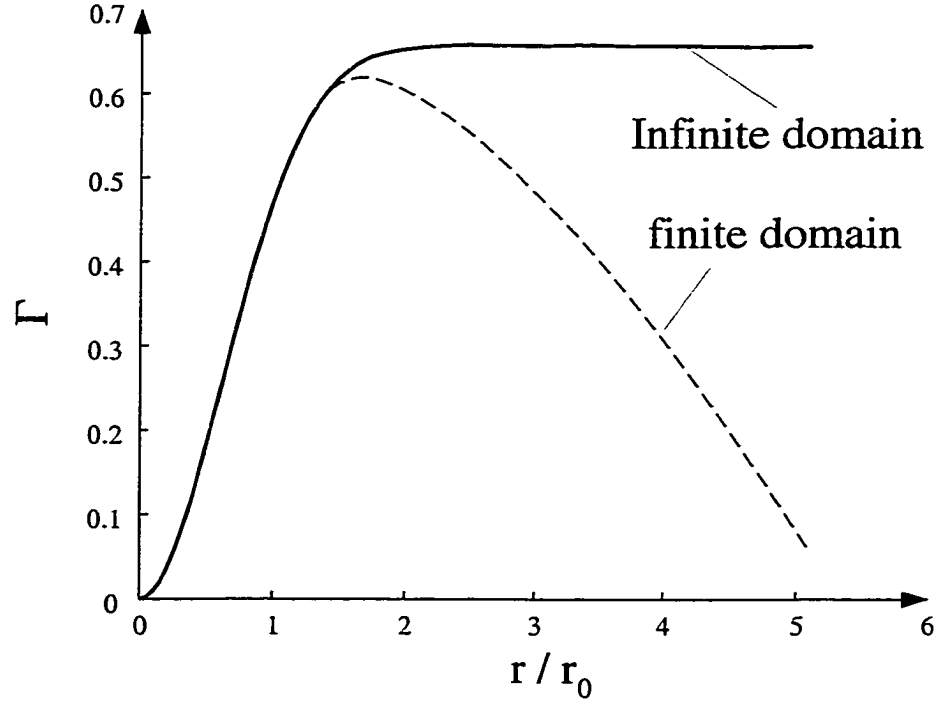

Figure 2.2 The circulation profile in a finite domain.

the partial derivatives in the z direction are evaluated spectrally using the standard Fourier scheme which is illustrated below.

Consider a function that is to be differentiated. The function is expressed as a discrete Fourier series, on a uniform grid in the domain $z \in [0, L_z]$,

$$f_j = f(z_j) = \sum_{n=-N_z/2+1}^{N_z/2} \mathcal{F}_n e^{ik_n z_j} \qquad j = 1, ..., N_z \ . \tag{2.15}$$

In the above, the nodal coordinate values and grid spacing are defined as

$$z_j = (j-1)\Delta z \ , \qquad \Delta z = L_z/N_z \ , \tag{2.16}$$

the wavenumbers are given by

$$k_n = \frac{2\pi n}{L_z} \ , \tag{2.17}$$

the number of grid points is N_z, and $i = \sqrt{-1}$. The Fourier coefficients,

$$\mathcal{F}_n = \frac{1}{N_z} \sum_{j=1}^{N_z} f_j e^{-ik_n z_j} \ , \tag{2.18}$$

are computed for efficiency using Fast Fourier Transform (FFT) routines.

From Equation (2.15), it is obvious that spatial derivatives can be obtained from

$$f'_j = f'(z_j) = \sum_{n=-N_z/2+1}^{N_z/2} ik_n \mathcal{F}_n e^{ik_n z_j} \ . \tag{2.19}$$

The Fourier coefficients of the derivative of $f(z)$ are given by

$$(\mathcal{F}')_n = ik_n \mathcal{F}_n \qquad . \tag{2.20}$$

Thus spatial derivatives in the streamwise direction can be easily evaluated by multiplying the Fourier coefficients of a function by ik_n.

2.4.2 Spatial derivates in the cross section

As mentioned at the beginning of this section, the influence of image flows introduced by the periodic boundary conditions has to be removed in the numerical method. By using the dual Cain's mapping, spatial derivatives in the x and y directions are evaluated in a finite computational domain using Cain's scheme instead

of the standard Fourier scheme. For simplicity, Cain's scheme is briefly illustrated below in one-dimension, since extension to two-dimensions is straightforward.

Suppose x is the physical coordinate and we introduce the computational coordinate ζ by means of the mapping

$$x = h(\zeta) = -a\cot(\frac{1}{2}\zeta)\,; \qquad 0 \le \zeta < 2\pi\,, \qquad -\infty \le x < \infty, \tag{2.21}$$

where a is an arbitrary constant which can be taken as a parameter for adjusting the grid density near the origin.

The derivatives in the two coordinate systems are related vis the chain rule:

$$\frac{df}{dx} = \frac{df}{d\zeta}\frac{d\zeta}{dx} = \frac{1}{h'}\frac{df}{d\zeta}\,, \tag{2.22}$$

where

$$\frac{1}{h'} = \frac{1}{a}\left[1 - \frac{e^{i\zeta} + e^{-i\zeta}}{2}\right]. \tag{2.23}$$

Using the mapping in Equation (2.23) and recalling Equation (2.22) and (2.19), we have

$$f'_j = f'(x_j) = \frac{1}{a}\sum_{n_\zeta=-N_\zeta/2+1}^{N_\zeta/2}\left[ik_{n_\zeta}\mathcal{F}_{n_\zeta} - \frac{ik_{n_\zeta-1}}{2}\mathcal{F}_{n_\zeta-1} - \frac{ik_{n_\zeta+1}}{2}\mathcal{F}_{n_\zeta+1}\right]e^{ik_{n_\zeta}x_j}, \tag{2.24}$$

where

$$k_{n_\zeta} = \frac{2\pi n_\zeta}{N_\zeta} \qquad \text{and} \qquad N_\zeta = N_x. \tag{2.25}$$

The Fourier coefficients of the derivative of $f(x)$ are given by

$$(\mathcal{F}')_{n_\zeta} = \frac{1}{a}\left[ik_{n_\zeta}\mathcal{F}_{n_\zeta} - \frac{ik_{n_\zeta-1}}{2}\mathcal{F}_{n_\zeta-1} - \frac{ik_{n_\zeta+1}}{2}\mathcal{F}_{n_\zeta+1}\right]. \tag{2.26}$$

Thus spatial derivatives can be easily evaluated by the Fourier coefficients of a function.

2.4.3 Modified convective term

Since the numerical method is a pseudo-spectral method, the nonlinear terms are evaluated in physical space. In general, the nonlinear terms can be either evaluated in wave space from convolution sums or formed directly in physical space. However, one

usually chooses to evaluate the nonlinear terms in physical space, because convolution sums are too expensive to be taken in numerical calculations. On other hand, the nonlinear terms for compressible flow, which involve divisions and exponentiation, can not be calculated exactly in wave space. Aliasing errors generated during the calculation of the convective terms have to be removed. The most popular dealiasing method is the "3/2" rule (Orszag 1971) which requires having the flow field in wave space. However, in the current method, the flow fields are never fully transformed into wave space (more detail is given in section 2.4.4) so that dealiasing is impossible in practice. In the current work, aliasing errors are controlled by making modifications to the convective terms. The convective terms in Equations.(2.2) and (2.3) are modified to the skew-symmetric form,

$$\frac{\partial}{\partial x_j}(fu_j) \longrightarrow \frac{1}{2}\frac{\partial}{\partial x_j}(fu_j) + \frac{1}{2}u_j\frac{\partial f}{\partial x_j} + \frac{1}{2}f\frac{\partial u_j}{\partial x_j} \quad . \tag{2.27}$$

in the simulations. This modification reduces the effect of aliasing errors (Blaisdell, Spyropoulos & Qin 1996, Zang 1991).

2.4.4 Time advance

There are two key issues regarding the time advancement scheme. The first issue is where time advancement is performed. In other words, should time advancement be done in physical space or wave space. Since the FFTs are the most expensive calculation in the current work, the decision for this issue is heavily dependent on the number of FFTs required. If the time advancement is done in wave space, the evaluation of each nonlinear term requires one extra backward FFT beside transforming the dependent variables to physical space, since the nonlinear terms evaluated in physical space. If the time advancement is implemented in physical space, the calculation of each derivative requires one extra forward FFT beside transforming the dependent variables to wave space. The number of derivatives that need to be calculated are fewer than the number of nonlinear terms in the governing equation, therefore, it is easy to choose advancement in physical space.

The second issue is which numerical time advancement scheme should be chosen. The basic requirements are high accuracy, stability and low memory requirements. One may not consider memory requirements now as seriously as before in other numerical simulations, but it still is a key factor in DNS, since DNS requires a huge memory. For example, even though the Reynolds number in the current simulations is three orders of magnitude lower than for practical cases, it still required about 1.5 GB of memory space which only can be done on supercomputers. A special third-order Runge-Kutta scheme developed by Wray (1986) is used. It only requires two memory locations per dependent variable including storage for the time derivative. Blaisdell et al. (1991) gave a detailed description about the accuracy and stability analysis for this method.

The formulation of this method is outlined in Table 2.4.4, for the ordinary differential equation

$$\frac{du}{dt} = f(u,t)\,. \tag{2.28}$$

The constants in Table 2.4.4 are

$$\begin{aligned} \alpha_1 &= \frac{2}{3}\,, \quad \alpha_2 = \frac{5}{12}\,, \quad \alpha_3 = \frac{3}{5}\,, \\ \beta_1 &= \frac{1}{4}\,, \quad \beta_2 = \frac{3}{20}\,, \quad \beta_3 = \frac{3}{5}\,. \end{aligned} \tag{2.29}$$

Table 2.1 Wray's compact third-order Runge-Kutta scheme.

Time	Location A (Variable or Derivative)	Location B (Variable)
t_n	u_n	u_n
t_n	$f(u_n, t_n)$	u_n
	$u'_1 = u_n + \alpha_1 \Delta t f(u_n, t_n)$	$u'_2 = u_n + \beta_1 \Delta t f(u_n, t_n)$
$t' = t^n + \alpha_1 \Delta t$	$f(u'_1, t')$	u'_2
	$u''_1 = u'_2 + \alpha_2 \Delta t f(u'_1, t')$	$u''_2 = u'_1 + \beta_2 \Delta t f(u'_1, t')$
$t'' = t_n + (\alpha_2 + \beta_1)\Delta t$	$f(u''_1, t'')$	u''_2
	$u'''_1 = u''_2 + \alpha_3 \Delta t f(u''_1, t'')$	$u'''_2 = u'''_1$
$t_{n+1} = t_n + \Delta t$	$u_{n+1} = u'''_1$	$u_{n+1} = u'''_2$

3. ISOLATED AXIAL VORTEX

3.1 Introduction

The numerical simulations of an isolated axial vortex (without strain) are implemented using the method described Chapter 2. In order to study the effects of initial conditions, several cases with different initial turbulent kinetic energy distributions are examined. An ensemble of simulations are completed to improve the quality of statistical quantities. Based on the ensemble of simulations, various statistical quantities of importance in turbulence modeling, like the mean velocity and turbulent stresses, are presented in this chapter. In addition, a detailed analysis of the Reynolds stress budgets based on the ensemble of simulations is also completed.

3.2 Initial Conditions

3.2.1 Mean velocity profiles

Since the linear stability characteristics of the q-vortex as a model of aircraft trailing vortices are well documented, the q-vortex is also used as a model in this study. The tangential velocity of the q-vortex is given by

$$\frac{V_\theta}{V_0} = \frac{q_0}{\hat{r}}(1 - e^{-\hat{r}^2}) \tag{3.1}$$

and the axial component of the velocity is given by

$$\frac{V_z}{V_0} = (1 - e^{-\hat{r}^2})\,. \tag{3.2}$$

Since the velocities are nondimensionalized by the speed of sound, the initial axial velocity deficit V_0 is related to the initial mean tangential flow Mach number M_p at $r = r_0$

$$V_0 = \frac{M_p \gamma}{q_0(1 - e^{-\gamma^2})}\,, \tag{3.3}$$

where $\hat{r} = \gamma r/r_0$ is the dimensionless coordinate, $\gamma = 1.12090642$ is the root of $1 + 2\gamma^2 = e^{\gamma^2}$. The initial swirl number q_0 is the relative strength of the tangential

component to the axial velocity deficit. It is noted by Lessen et al. (1974) that the temporal stability characteristics of the q-vortex are unaffected by the addition or subtraction of a constant V_0 to the axial velocity profile or by the inversion of the wake-like profile to a jet-like profile. Simulations presented in this study are for the wake profile given by Equation (3.2). The parameter q_0 is chosen to be 1 so that the flow is initially unstable. Figure 3.1 shows the profiles of initial mean velocities.

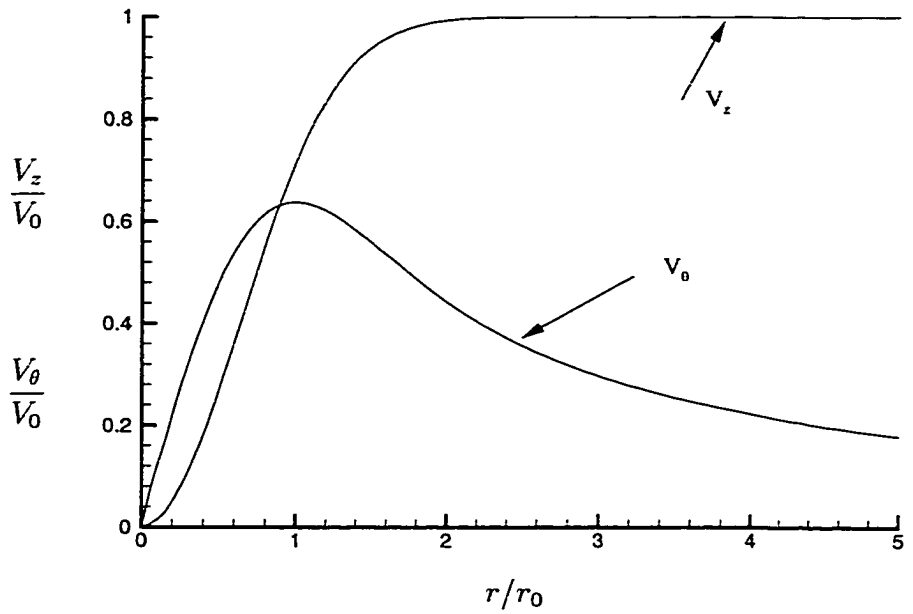

Figure 3.1 The initial mean velocity profiles.

3.2.2 Initial fluctuating velocity components.

The initial flow fields are generated by modifying an isotropic flow field. This is specified as random fields by assigning random phases to the Fourier coefficients of the dependent variables which are defined by a spectrum of desired form (see Blaisdell et al. (1991) for details). A three-dimensional inverse transform is performed to obtain the variables in physical space. The fluctuating velocity field is then multiplied by a specified function to obtain the desired profile of the initial turbulent kinetic energy as shown in Figure 3.2.

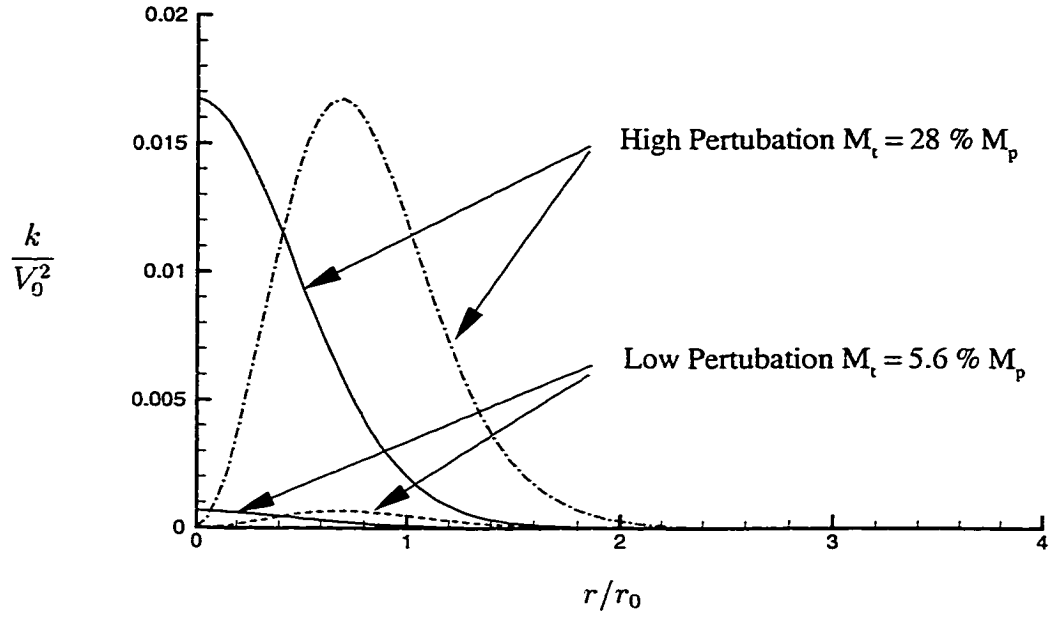

Figure 3.2 Profiles of the initial turbulence kinetic energy.

The Reynolds normal stresses, taken from Donaldson (1972), are given by

$$\overline{v_r'^2} = \frac{Ch(\hat{r})\left(1 - e^{-\gamma^2\hat{r}^2}\right)}{\gamma^2\hat{r}^2}, \tag{3.4}$$

$$\overline{v_\theta'^2} = Ch(\hat{r})e^{-\gamma^2\hat{r}^2}, \tag{3.5}$$

and

$$\overline{v_z'^2} = \frac{1}{2}\left[\overline{v_r'^2} + \overline{v_\theta'^2}\right] \quad , \tag{3.6}$$

where $C = (2/9)M_t^2 e^{2\gamma^2}$, M_t is the initial maximum fluctuating Mach number, and $h(\hat{r})$ is a function of the dimensionless coordinate $\hat{r}$ and must be specified. Donaldson (1972) assumed $h(\hat{r})$ was in the form

$$h(\hat{r}) = e^{-\gamma^2\hat{r}^2}, \tag{3.7}$$

which causes the initial maximum kinetic energy to occur along the vortex axis as shown in Figure 3.2 (solid line). Zheng & Ash (1993) modified Equation (3.7) and chose a slightly different form :

$$h(\hat{r}) = \hat{r}^2 e^{-\gamma^2\hat{r}^2}, \tag{3.8}$$

which causes the initial maximum kinetic energy to occur near $r/r_0 = 0.7$ (see Figure 3.2). In order to investigate the effects of initial conditions, the two different functions (3.7) and (3.8) are used to generate two different profiles of the initial turbulent kinetic energy in this work.

3.2.3 Summary of cases

In this work, a total of nine simulations are completed. One case is to examine the wake in the axial direction on the vortex. Five cases are conducted to examine the effect of initial conditions and the resolution of the numerical simulations. An additional three cases based on the baseline case are designed to complete an ensemble of simulations for providing high qualitative statistical quantities.

The initial peak mean tangential flow Mach number M_p is chosen to be 0.15 for all cases so that compressibility effects are negligible. The assumption is verified by the simulations which show less than 3% variation in the mean density. For all simulations of the isolated vortex, the Reynolds number

$$Re_\Gamma = \frac{\Gamma_\infty}{\nu} \ , \tag{3.9}$$

is chosen to be 16500 so that the simulations are numerically well resolved. This is verified by considering several issues. First, the grid size is less than five times of the minimum Kolmogorov length scale for all simulations. Secondly, the one-dimensional spectra in Section 3.4 fall off at high wavenumber without a significant pile-up of energy. In addition, the grid resolution study (comparing Case A and B) verifies the numerical resolution is adequate (see Section 3.3.2).

The length of the computational domain in the streamwise direction is a multiple of the streamwise wave length of the most unstable mode from linear stability theory,

$$L_z = m\frac{2\pi}{\alpha} \tag{3.10}$$

where m is the multiplier and the streamwise wave number α is 0.6 for all cases.

Table 3.1 lists the summary of the cases. Case A is the baseline case that has a low level of initial turbulence which peaks on the center. The grid for Case A has $128 \times 128 \times 256$ points. The computational domain is twice as long as the streamwise wave length (m=2).

The purpose of Case B is to check the numerical resolution of Case A in the cross section. Therefore, the grid for Case B is doubled to 256×256 in the cross section.

Table 3.1 Case parameters for the isolated axial vortex.

Case	Re	M_p	M_t	m	N_x	N_y	N_z	$h(\hat{r})$
A	16500	0.15	0.009	2	128	128	256	Eq. (3.7)
A_1	16500	0.15	0.009	2	128	128	256	Eq. (3.7)
A_2	16500	0.15	0.009	2	128	128	256	Eq. (3.7)
A_3	16500	0.15	0.009	2	128	128	256	Eq. (3.7)
B	16500	0.15	0.009	1	256	256	128	Eq. (3.7)
C	16500	0.15	0.043	2	128	128	256	Eq. (3.7)
D	16500	0.15	0.043	2	128	128	256	Eq. (3.8)
E	16500	0.15	0.009	2	128	128	256	Eq. (3.8)
F	16500	0.15	0.009	2	128	128	256	Eq. (3.7)

However, due to the limitation of the available computer resources, the grid points are reduced to 128 in the streamwise direction and the length of the computational domain is shortened to one half of Case A.

The purpose of Case C is to study the effect of the initial turbulence level. The level of initial turbulence of Case C is chosen to be five times as large as that of Case A.

The purpose of Cases D and E is to study the effects of the initial perturbation distributions. In contrast to cases A and C respectively, Cases D and E have the same parameters except for the initial turbulence distribution, which peaks at $r/r_0 = 0.7$ instead of on the centerline.

The purpose of Case F is to examine the effect of the axial wake. Case F which is the Oseen vortex has the same parameters as Case A except without the axial wake.

Cases A_1, A_2, and A_3 are designed to complete an ensemble of simulations based on the baseline Case A for improving the quality of statistical quantities. They have the exact same initial parameters as Case A, but the initial random phases for the fluctuating flow are different by setting different random seed numbers for each case.

3.3 Turbulence Statistics

The investigation of turbulent statistical quantities for the isolated vortex is described in this section. Because of the axisymmetric nature of the axial vortex, we would like to investigate the statistical quantities in terms of cylindrical coordinates. As mentioned in Section 2.3, the ensemble average is equivalent to an average over a $\theta - z$ cylindrical surface for an axisymmetric flow. The definition of averaging for statistical quantities in this section is given by Equation (2.14).

3.3.1 Transformation equation

Since the direct numerical simulations are completed in Cartesian coordinates, all statistical quantities first have to be transformed into cylindrical coordinates. The transformation equations for each quantity are given by

$$V_r = \overline{u}\cos\theta + \overline{v}\sin\theta, \tag{3.11}$$

$$V_\theta = -\overline{u}\sin\theta + \overline{v}\cos\theta, \tag{3.12}$$

$$V_z = \overline{w}, \tag{3.13}$$

$$\overline{v_r'^2} = \cos^2\theta\overline{u'^2} + 2\cos\theta\sin\theta\overline{u'v'} + \sin^2\theta\overline{v'^2}, \tag{3.14}$$

$$\overline{v_\theta'^2} = \sin^2\theta\overline{u'^2} - 2\cos\theta\sin\theta\overline{u'v'} + \cos^2\theta\overline{v'^2} \tag{3.15}$$

$$\overline{v_z'^2} = \overline{w'^2} \tag{3.16}$$

$$\overline{v_r'v_\theta'} = (\cos^2\theta - \sin^2\theta)\overline{u'v'} - \cos\theta\sin\theta(\overline{u'^2} - \overline{v'^2}) \tag{3.17}$$

$$\overline{v_r'v_z'} = \cos\theta\overline{u'w'} + \sin\theta\overline{v'w'}, \tag{3.18}$$

$$\overline{v_\theta'v_z'} = \cos\theta\overline{v'w'} - \sin\theta\overline{u'w'}, \tag{3.19}$$

$$k = \frac{1}{2}\left(\overline{v_r'^2} + \overline{v_\theta'^2} + \overline{v_z'^2}\right) = \frac{1}{2}\left(\overline{u'^2} + \overline{v'^2} + \overline{w'^2}\right), \tag{3.20}$$

where θ is the angle measured counterclockwise from the x axis; r, the radial coordinate; u, v, and w, the components of velocity in the x, y, and z directions respectively; v_r, v_θ, and v_z, the components of velocity in the r, θ, and$z$ directions; $\overline{v_r'^2}$, $\overline{v_\theta'^2}$, $\overline{v_z'^2}$, $\overline{v_r'v_\theta'}$, $\overline{v_r'v_z'}$, and $\overline{v_\theta'v_z'}$, the components of Reynolds stresses in cylindrical coordinates; $\overline{u'^2}$, $\overline{v'^2}$, $\overline{w'^2}$, $\overline{u'v'}$, $\overline{u'w'}$, and $\overline{v'w'}$, the components of Reynolds stresses in Cartesian coordinates, and k is the turbulent kinetic energy (hereafter TKE). It should be pointed out that without axisymmetry, the definition of averaging for quantities in Cartesian coordinates is given by Equation (2.13).

3.3.2 Global turbulent kinetic energy

One can get a global sense of the stability of the flow by considering the global TKE. The definition of the global TKE is given by

$$\mathcal{K} = \frac{1}{\pi R^2 L_z} \int_0^R \int_0^{2\pi} \int_0^{L_z} k r dr d\theta dz \,, \tag{3.21}$$

where $R = 5r_0$ and L_z is the length of computational domain in the streamwise direction.

The evolution of the global TKE for cases A and F is compared in Figure 3.3. Time is scaled with the initial mean flow time scale given by

$$T = \frac{2\pi r_0}{V_\theta(r)\Big|_{r=r_0}} \,, \tag{3.22}$$

where r_0 is the initial location of $(V_\theta)_{max}$. Case F, the Oseen vortex, as expected by linear stability theory, shows decay of the global TKE because without the wake flow in the axial direction, the monotonically increasing initial circulation makes the vortex centrifugally neutrally stable. On the other hand, the global TKE in case A shows a rapid growth after a short transition time. The transition period is due to

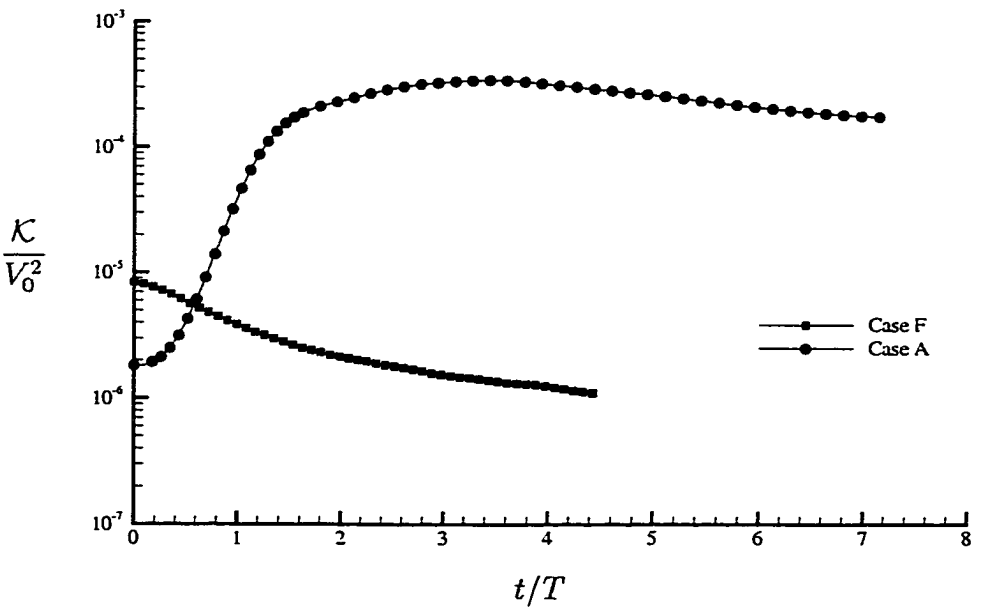

Figure 3.3 Evolution of the global TKE for Case A And Case F.

the unphysical nature of the initial random disturbance and the reorganization of the vortex flow field. Once the vortex adjusts itself, various modes start to grow (more details in Section 5.2.2) since the initial mean flow is unstable ($q_0 = 1$). As expected by linear stability theory, the global TKE shows an exponential growth rate after a short time. Then, the global TKE keeps growing until it is near saturation, but the growth rate decrease gradually in the time. Eventually the TKE decays as the mean flow stabilizes. Since case F, the Oseen vortex, simply shows a decay of the global TKE, this work will mainly focus on the isolated vortex with an axial wake.

The evolution of the TKE for five cases A, B, C, D, and E is shown in Figure 3.4. For Case A , B, and E, since the imposed initial disturbance is weak, the disturbances need to be amplified enough so that they start to interact nonlinearly with themselves and with the mean flow. A similar behavior of the global TKE has been obtained by Sreedhar and Ragab (1994, 1995a, 1995b). The interesting feature is that the five cases match during the growing stage, if Cases C, D and E are shifted in time by t_0 as shown in Figure 3.5. To see the exponential growth of the global TKE at early times, the evolution of the global TKE is also plotted on semilog axes in Figure 3.6. Especially, Cases A and B are almost identical when $t < 2T$. This indicates that Case A has a reasonable numerical resolution in the cross section. Also, it should

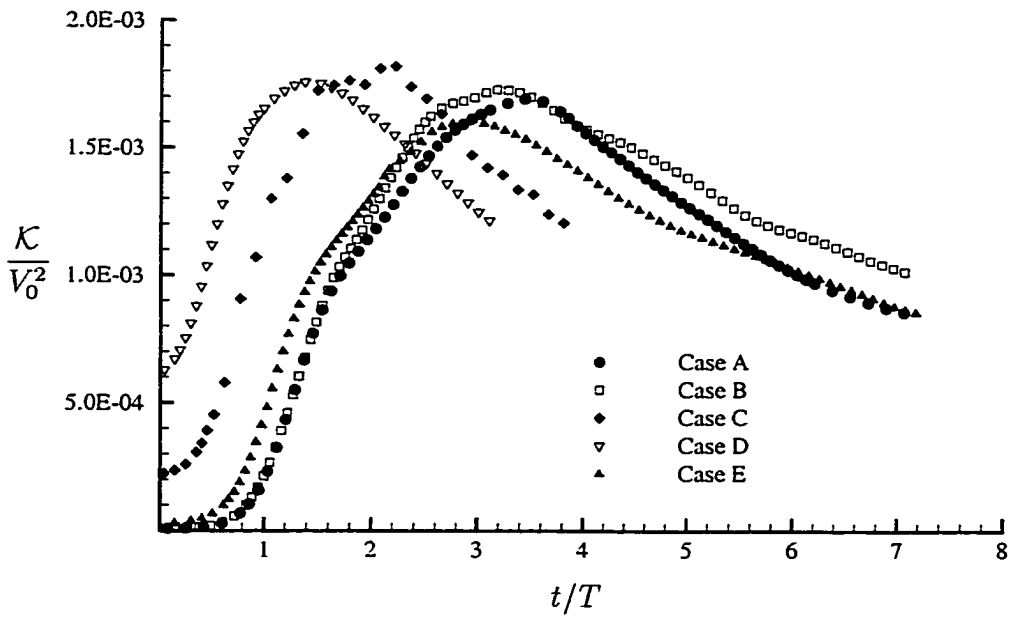

Figure 3.4 Evolution of the global TKE $\mathcal{K}$ for five cases.

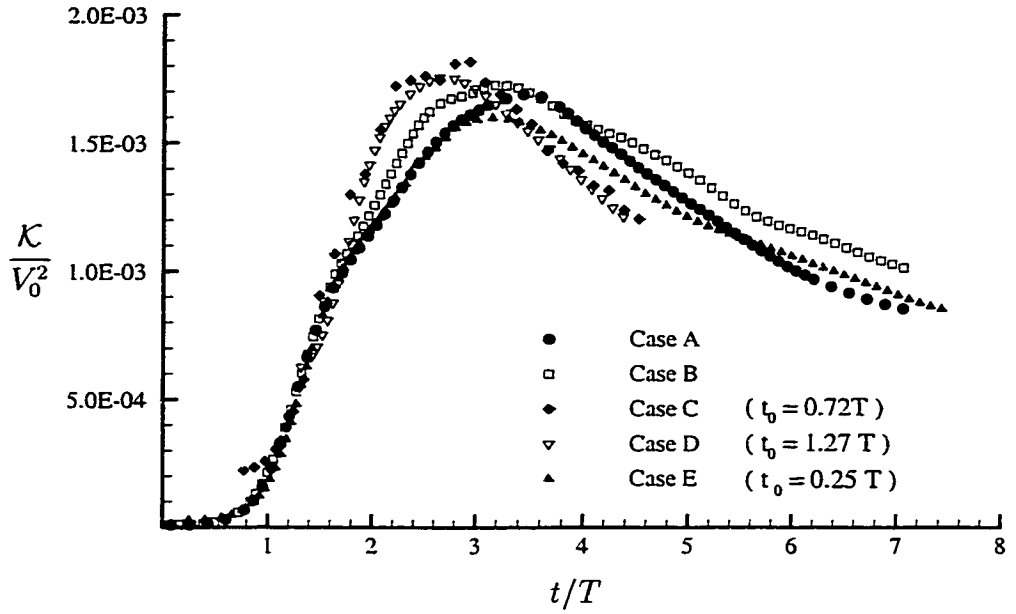

Figure 3.5 Evolution of the global TKE $\mathcal{K}$ shifted by time t_0.

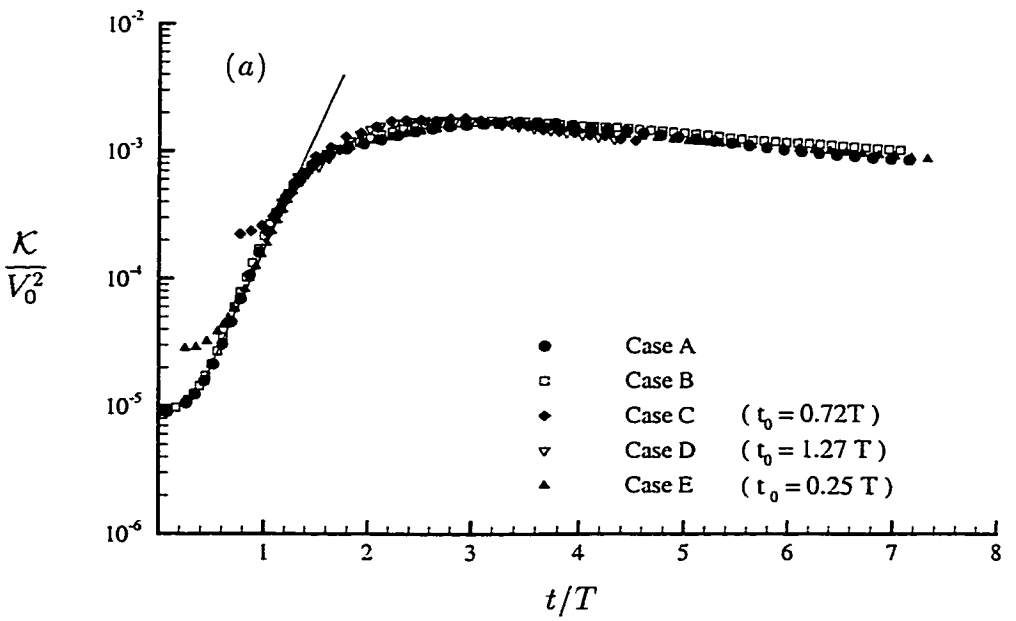

Figure 3.6 The evolution of the global TKE shifted by time t_0.

be noted that there are some difference after the TKE is near saturation, but the general behavior is the same. The difference may be caused by a low statistical sample in computing the TKE. Therefore, the development of the turbulent kinetic energy seems to be independent of the imposed initial disturbances. Actually it is controlled by the mean flow.

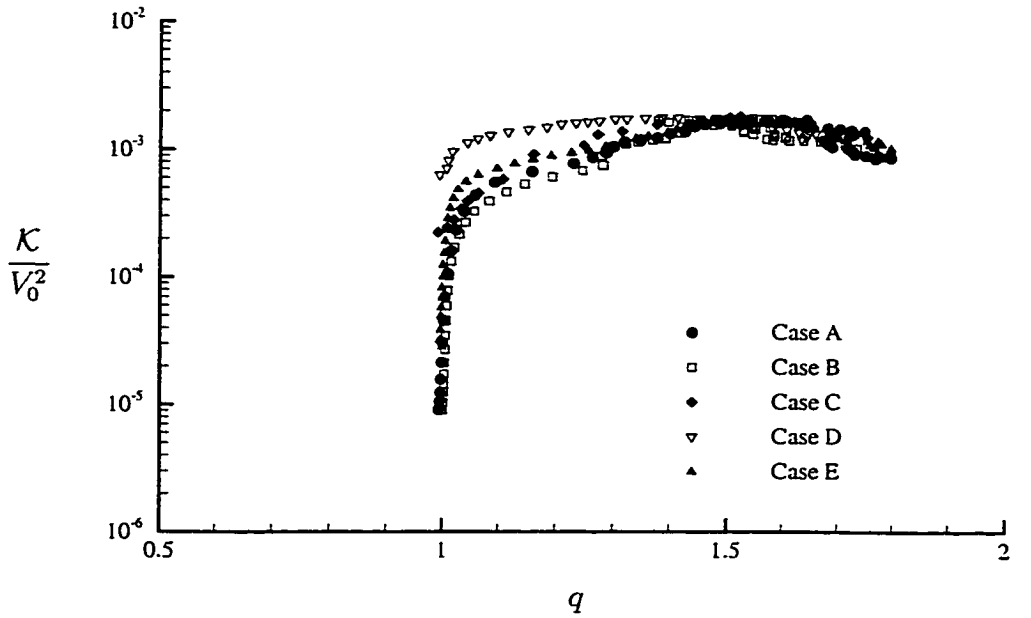

Figure 3.7 Global TKE $\mathcal{K}$ as function of swirl number q.

Figure 3.7 shows the relationship between the global turbulent kinetic energy and the swirl number, which is defined as

$$q = \frac{(V_\theta)_{\max}}{V_z(r)\big|_{r=\infty} - V_z(r)\big|_{r=0}} . \tag{3.23}$$

All five cases almost collapse on one curve. It is clear that the swirl number almost does not change until $(\mathcal{K}/V_0^2) > 2 \times 10^{-4}$, because the disturbance is too weak to interact with the mean flow. Also it is seen that the global TKE begins to decay for q greater than 1.5. It is noted that a small sample size in evaluating the velocity deficit causes the jagged behavior of the swirl number.

A global swirl number $\mathcal{Q}$ is defined as

$$\mathcal{Q} = \frac{\int_0^R V_\theta dr}{\int_0^R [V_z(\infty) - V_z(r)]\, dr}. \tag{3.24}$$

where, $R = 5.0r_0$. Figure 3.8 shows that the relationship between the global TKE and $\mathcal{Q}$ is similar to that seen in Figure 3.7 but that the jagged behavior almost disappears. This indicates that there is a low statistical sample difficulty in computing the desired statistics.

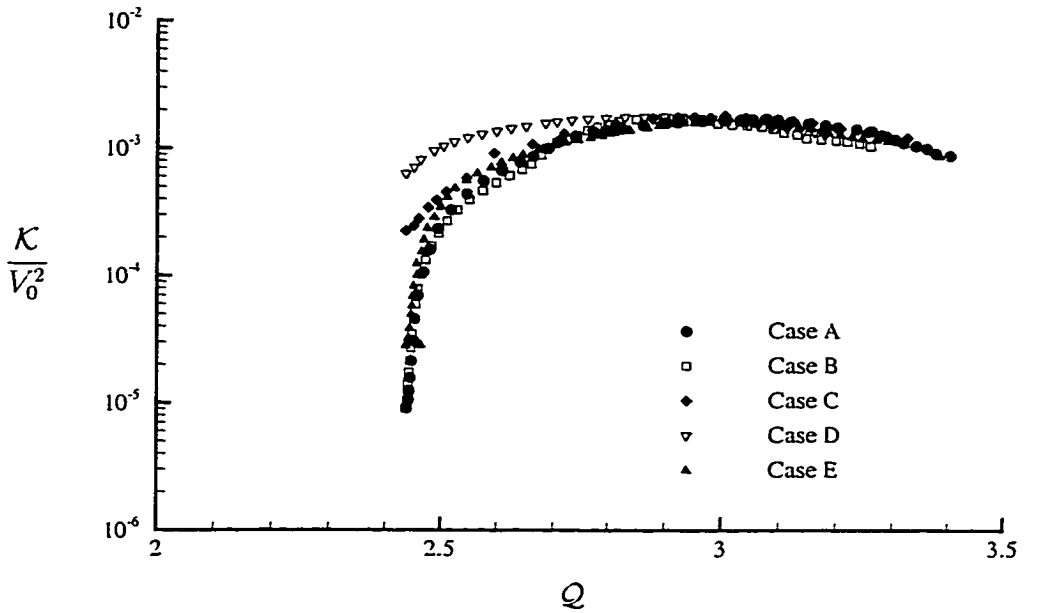

Figure 3.8 Global TKE $\mathcal{K}$ as function of global swirl number $\mathcal{Q}$.

Figure 3.9 shows the global TKE for cases A, A_1, A_2 and A_3. It is shown again that there are some difference after the global TKE is near saturation even though the simulations are started from the same initial conditions, except for the seed in the random number generator. Thus, it is clear that the differences result from the small statistical sample size. The global TKE based on the ensemble of simulations is shown in Figure 3.10, where the error bar indicates one standard deviation. The maximum relative error is about 9%. Figures 3.11 and 3.12 shows the relationship between the global TKE and swirl numbers for the ensemble of simulations. The jagged behavior

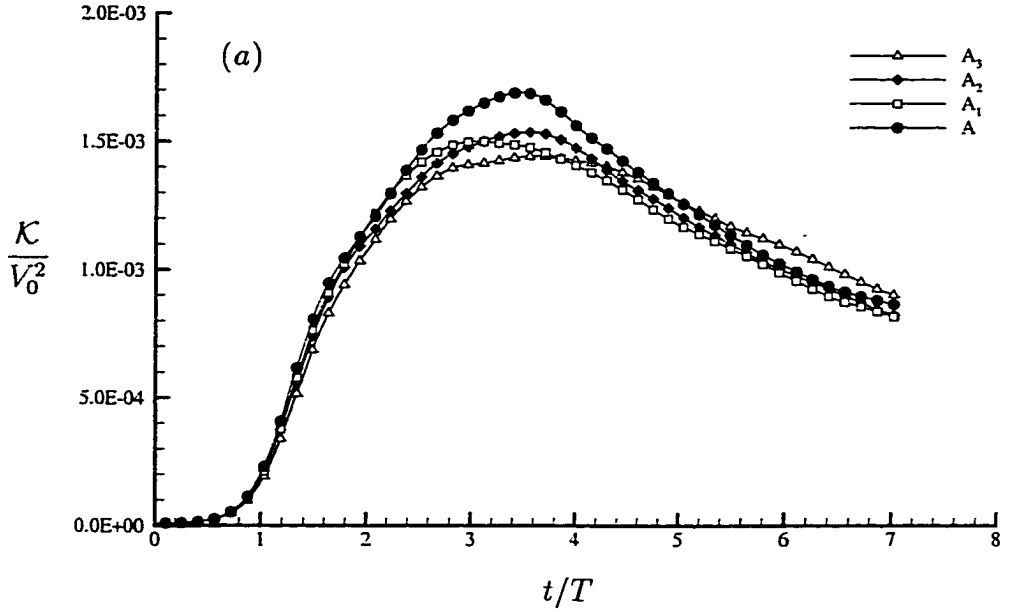

Figure 3.9 Time history of the global TKE $\mathcal{K}$ for the ensemble simulations.

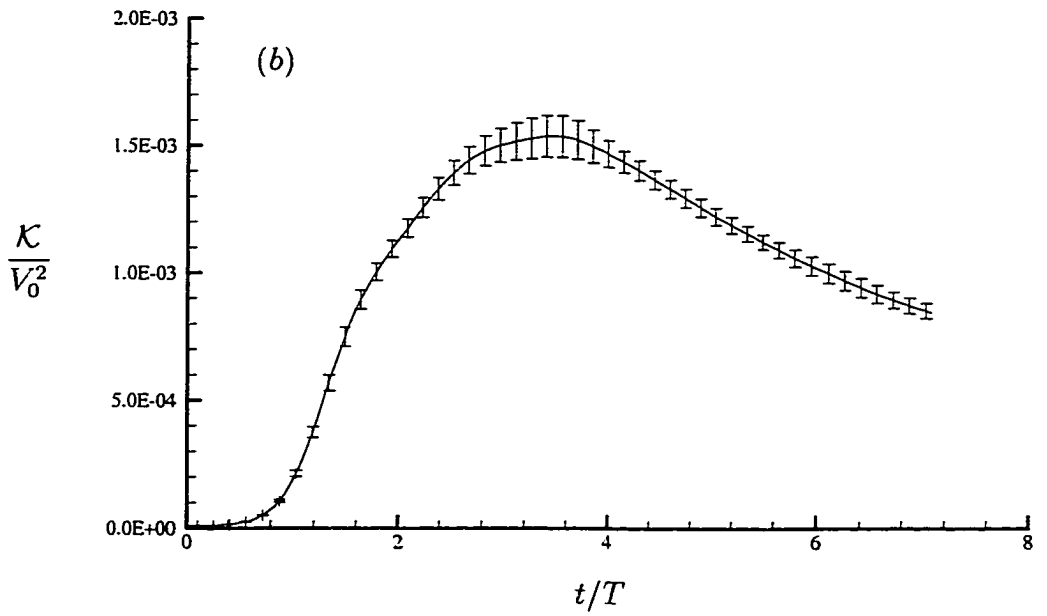

Figure 3.10 Mean and standard deviation of $\mathcal{K}$ for the ensemble simulations.

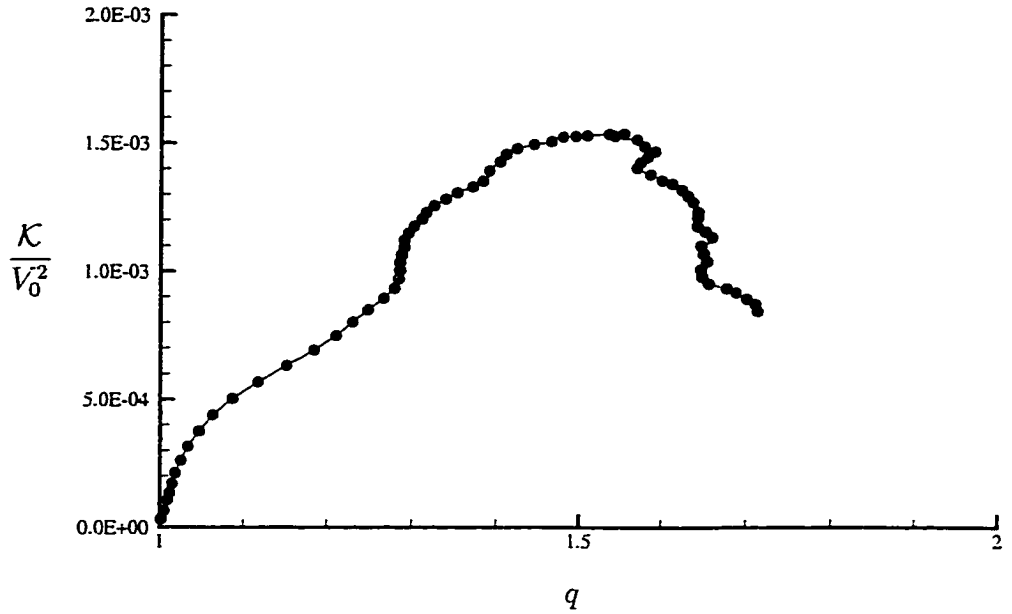

Figure 3.11 Global TKE $\mathcal{K}$ as function of swirl number q for the ensemble of simulations.

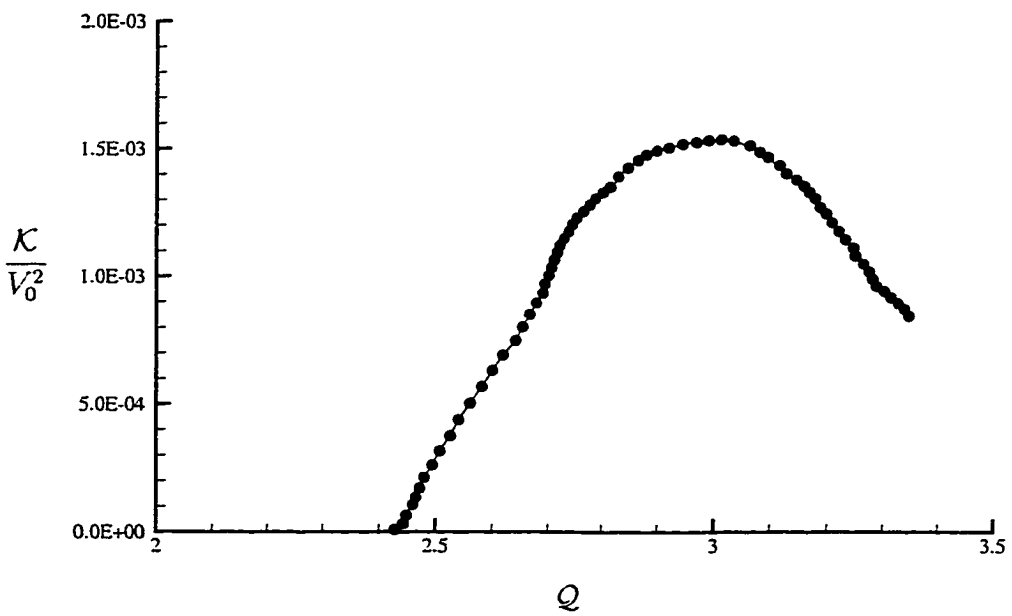

Figure 3.12 Global TKE $\mathcal{K}$ as function of global swirl number $\mathcal{Q}$.

in Figures 3.7 and 3.8 disappears. Note that $\mathcal{K}/V_0^2$ is plotted on a linear axis rather than a logarithmic axis. It is clear that the global TKE begins to decay at $q \approx 1.5$ and $\mathcal{Q} \approx 3.0$. This agrees well with linear stability theory results (Leibovich & Stewartson 1983, Lessen et al. 1974).

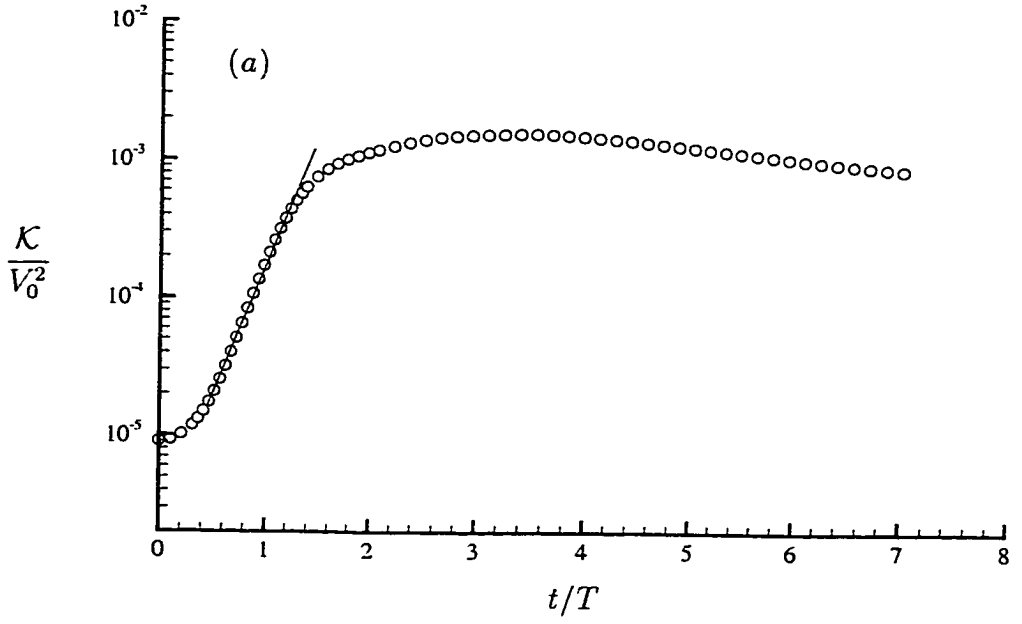

Figure 3.13 The evolution of the global TKE $\mathcal{K}$ for the ensemble simulations.

To clearly examine growth rate of the global TKE, the evolution of the global TKE based on the ensemble of simulations (Figure 3.10) is replotted on semilog axes as shown in Figure 3.13. The development of the isolated vortex can be roughly divided into five periods by the behavior of global TKE (Figure 3.13). The first period, from $0.0T$ to $0.5T$, is the transition period which shows a very small growth rate because the vortex need adjust itself from the unphysical nature of initial perturbations. The second period, from $0.5T$ to $1.4T$, is a linear unstable period when the global TKE has an exponent growth rate. The third period, from $1.4T$ to $2.6T$, can be called the growing period. During this period, the growth rate of the global TKE gradually decreases with the decay of the axial velocity deficit (more in Section 3.3.3). From $2.6T$ to $3.8T$, the fourth period when the TKE appears to saturate, can be called the saturating period. After $3.8T$, the fifth period can be called the relaminarizing period. The decay of the axial velocity deficit results in the centrifugally stabilizing motion of the vortex core taking over the destabilizing effect of the axial velocity.

The global TKE shows a slow decay. The vortex returns eventually toward a laminar state.

Since the simulation results are mostly independent of the type of initial disturbance, subsequent discussions will focus mainly on the ensemble of simulations.

3.3.3 Mean quantities

The mean flow quantities presented in the following section are obtained by taking the average in the axial direction(see Section2.3). The radial profiles result from a bin-averaging procedure in the θ direction after averaging in the z direction. All results presented in this section are based on the ensemble of simulations from cases A, A_1, A_2, and A_3.

The history of the mean velocity profiles are shown in Figures 3.14 and 3.15. The magnitude of the wake decays in time due to both viscous and turbulent diffusion as one would expect. As mentioned in Section 3.3.2, in the transition period, the disturbance is too weak to interact with mean flow so that the wake shows a very slow decay. The mean tangential velocity also shows the vortex diffusing for the first three periods. However, an interesting feature of the development of tangential velocity is that the peak in the tangential velocity moves inward rather than continuing to diffuse outward at the last two periods when the vortex is stabilized. During this time the tangential velocity near the center of the vortex is seen to increase rather than decrease. This indicates that the vortex core is undergoing negative diffusion.

Consistent with Figure 3.15, the mean axial vorticity as shown in Figure 3.16 decreases and then increases in the core. As shown later in Section 3.3.5 this anti-diffusion is associated with a negative eddy viscosity. One usually thinks of turbulent flows as being diffusive; however, here we see a case where at later times the turbulence does work on the mean flow field causing the vortex to wind tighter. This may in part help explain the persistence of aircraft wake vortices, although there are certainly many physical processes occurring in aircraft wakes that are not include here.

The evolution of the circulation profiles are presented in Figure 3.17. The turbulent vortex develops a visible overshoot of about 3% of Γ_∞ in circulation at later times. As shown later in Section 3.3.4, corresponding to this overshoot, the peak of the Reynolds stress $\overline{v_r' v_\theta'}$ moves to the location of the overshoot rather than staying at the edge of vortex core as the other shear stresses $\overline{v_r' v_z'}$ and $\overline{v_\theta' v_z'}$.

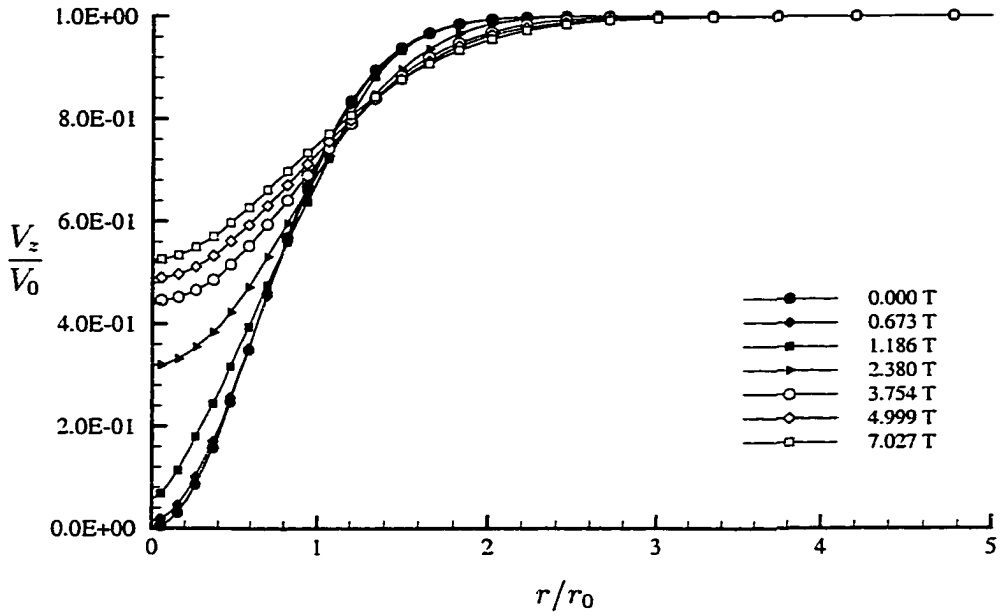

Figure 3.14 Evolution of the mean axial velocity V_z profiles for Case A.

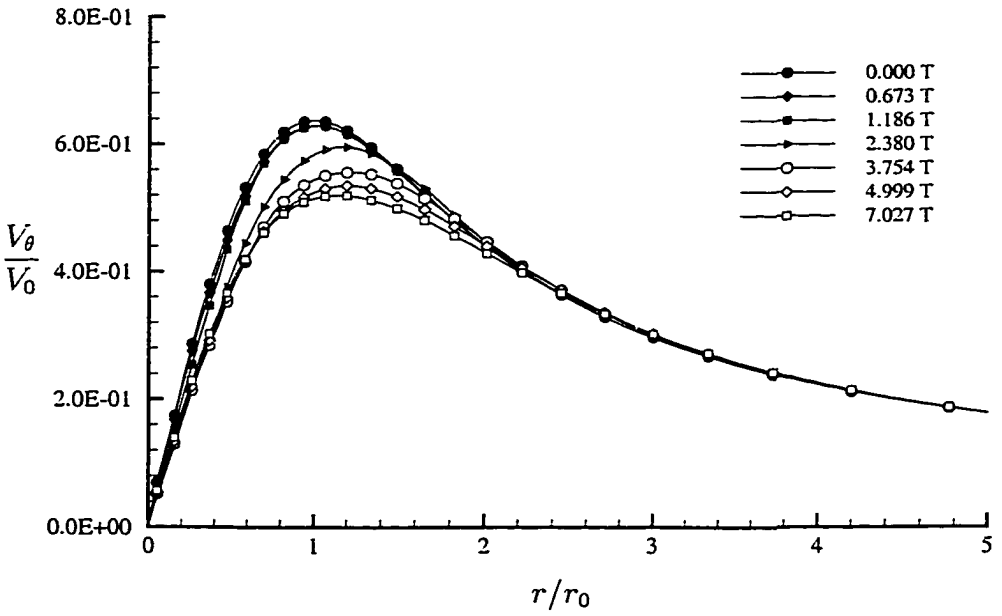

Figure 3.15 Evolution of the mean tangential velocity V_θ profiles.

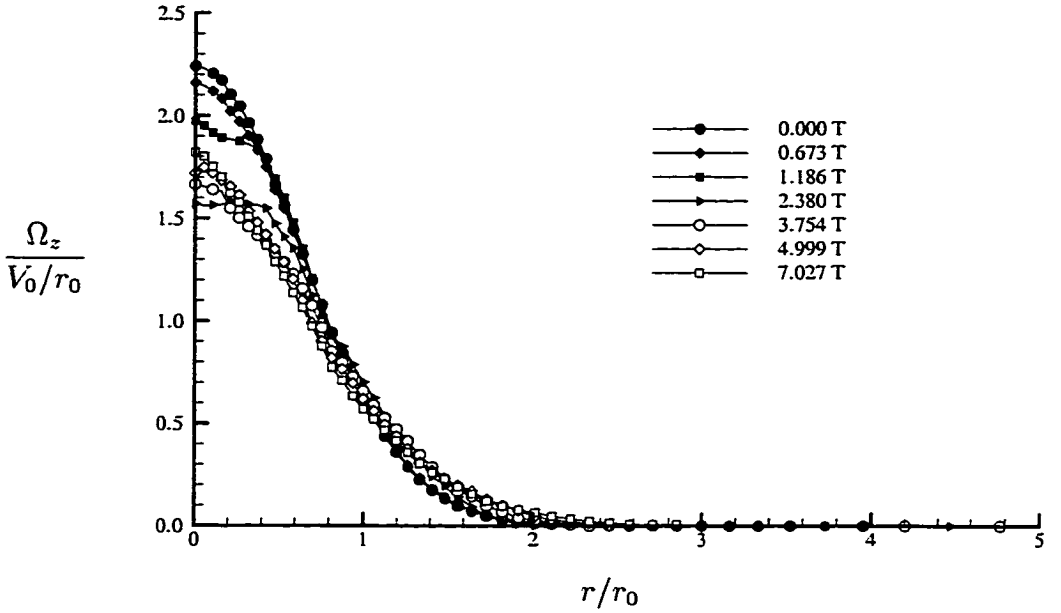

Figure 3.16 Evolution of the mean axial vorticity Ω_z profiles.

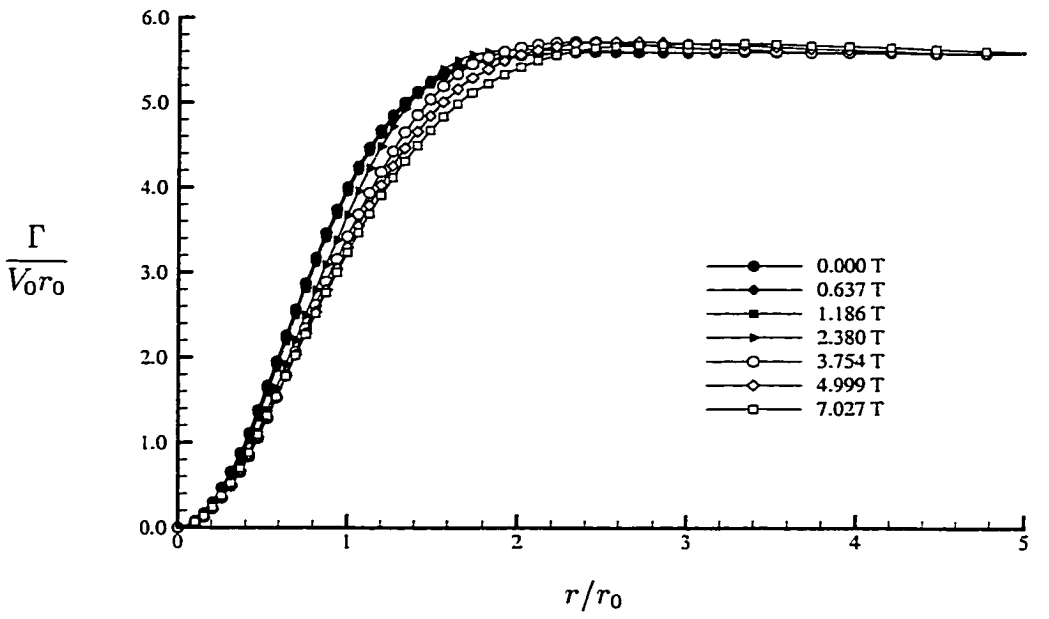

Figure 3.17 Evolution of the circulation Γ profiles.

The evolution of angular momentum per unit length defined as

$$\mathcal{I}(r) = 2\pi \int_0^r r^2 V_\theta dr \tag{3.25}$$

is shown in Figure 3.18. The angular momentum grows quadraticly for large r.

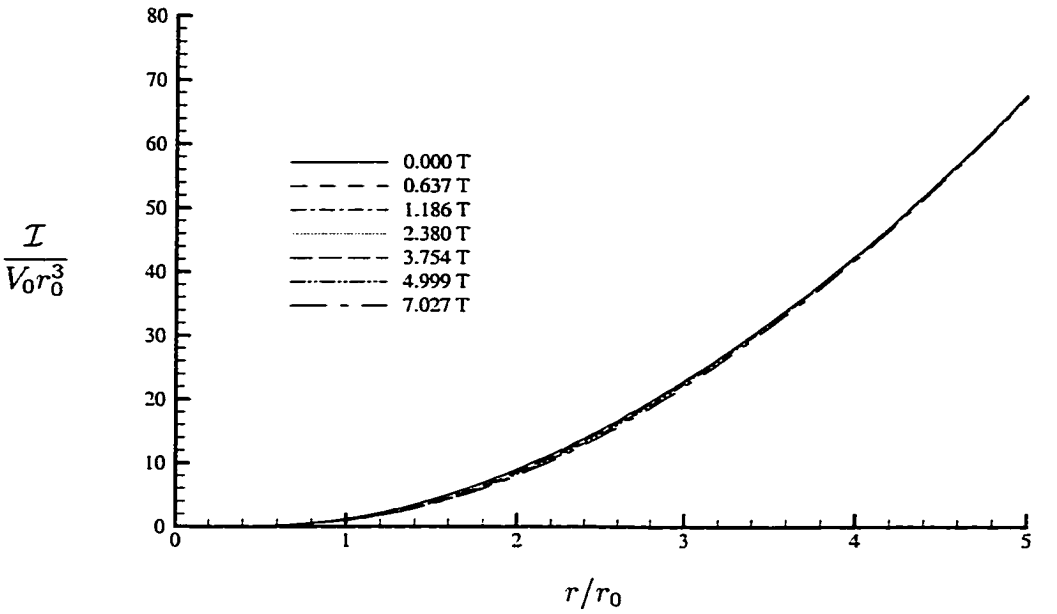

Figure 3.18 Evolution of the angular momentum.

From the mean momentum equation

$$\frac{\partial V_\theta}{\partial t} = -\frac{1}{r^2}\frac{\partial}{\partial r}\left(r^2\overline{v_r' v_\theta'}\right) + \frac{\nu}{r^2}\frac{\partial}{\partial r}\left[r^3\frac{\partial}{\partial r}\left(\frac{V_\theta}{r}\right)\right], \tag{3.26}$$

Multiplying by r^2 and integrating Equation (3.26), we obtain

$$\frac{\partial \mathcal{I}}{\partial t} = -r^2\overline{v_r' v_\theta'}\Big|_r + \nu r^3\frac{\partial}{\partial r}\left(\frac{V_\theta}{r}\right)\Big|_r. \tag{3.27}$$

Since for large r, the viscous torque,

$$\nu r^3\frac{\partial}{\partial r}\left(\frac{V_\theta}{r}\right)\Big|_r \approx \nu r^3\frac{\partial}{\partial r}\left(\frac{\Gamma_\infty}{2\pi r^2}\right) = -\frac{\Gamma_\infty^2}{4\pi Re_\Gamma},$$

is negligible for a large Reynolds number Re_Γ, if $\overline{v_r' v_\theta'} \longrightarrow 0$ for large r, then

$$\frac{d\mathcal{I}}{dt} = 0,$$

and the angular momentum at large r is conserved. In order to check the conservation of angular momentum, the difference between the angular momentum of a potential vortex and the isolated vortex,

$$d\mathcal{I} = 2\pi \int_0^r r^2 \left(\frac{\Gamma_\infty}{2\pi r}\right) dr - 2\pi \int_0^r r^2 V_\theta dr \,, \tag{3.28}$$

is calculated and shown in Figure 3.19. The difference approaches a constant that changes slowly in time. The change in value at large r is a small percentage of the value of the angular momentum and may be attributed to the Reynolds stress $\overline{v_r' v_\theta'}$ is not being zero which will be given at the next section.

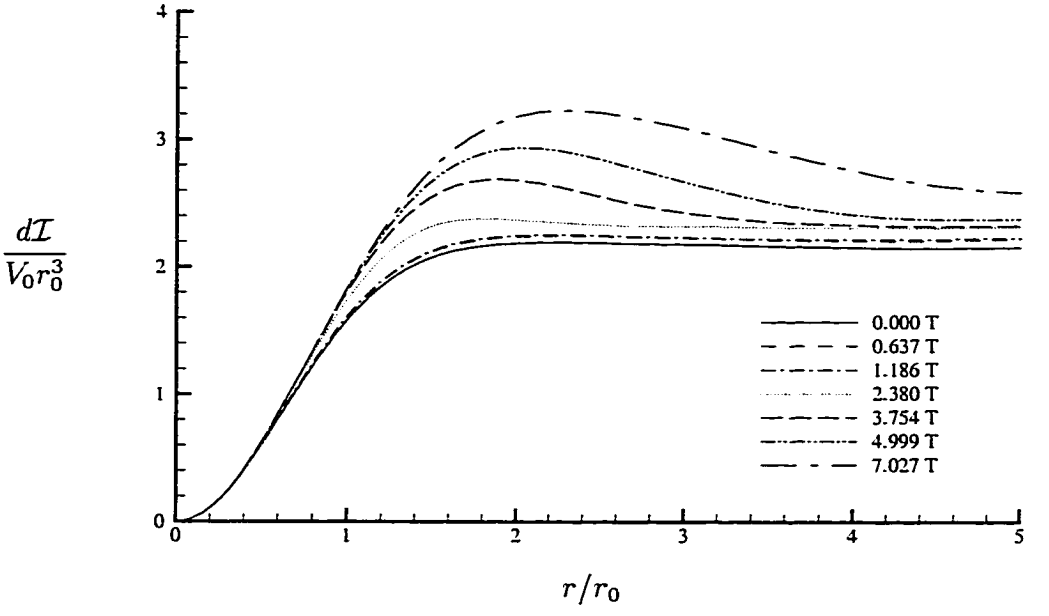

Figure 3.19 Evolution of the angular momentum difference between a potential vortex and isolated vortex.

Figure 3.20 shows the time variation of the peak tangential velocity. Note that Figure 3.20 is plotted on logarithm axes rather than linear axes, but it is difficult to tell for the small ranges. Phillips (1981) found two modes for the decay of peak tangential velocity for the trailing vortex using a similarity solution. One is that $V_\theta(r)_{max}$ decays like $t^{-\frac{1}{2}n}$ in the near field of a trailing vortex; and the other is that $V_\theta(r)_{max}$ decays like $t^{\frac{1}{2}(n-2)}$ in the downstream region of trailing vortex; $0 < n < 1$, for elliptic wing loading $n \approx \frac{1}{2}$. In this work, there are three modes for the decay of peak tangential velocity. At the early time, $V_\theta(r)_{max}$ decays like $t^{-0.23}$ which is very

close the Phillips' first mode $t^{-0.25}$ for elliptic wing. When the vortex is stabilized, $V_\theta(r)_{max}$ decays like $t^{-0.73}$ which is close to the Phillips' downstream mode $t^{-0.75}$. In the linearly unstable period, the peak tangential velocity $(V_\theta)_{max}$ decays as $t^{-2.48}$ which was not discovered by Phillips (1981) since the similarity solution does not exist during this period of the vortex development.

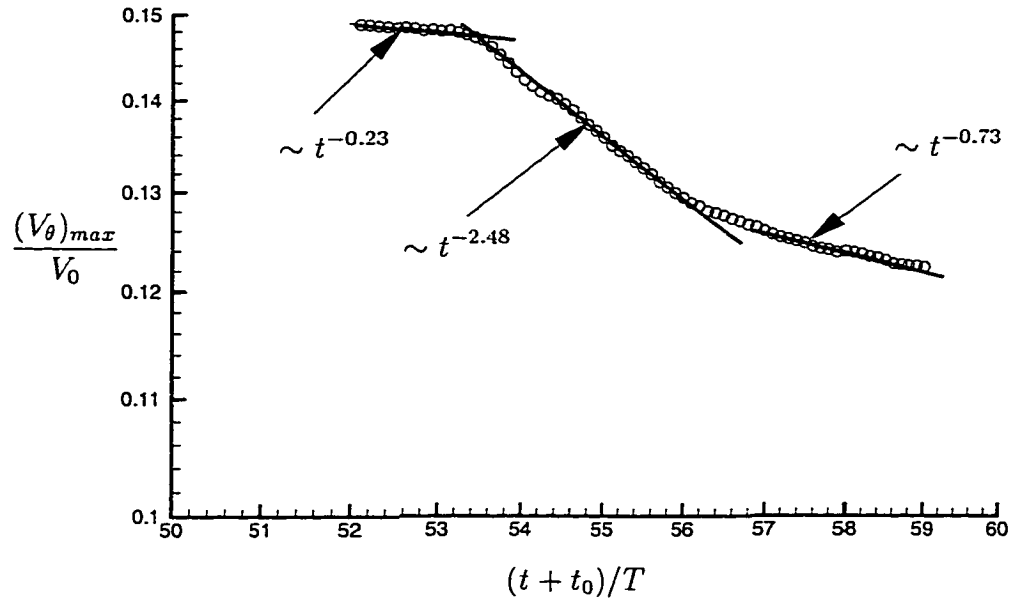

Figure 3.20 Evolution of the peak of the mean tangential velocity.

3.3.4 Turbulent kinetic energy and Reynolds stress

The TKE and Reynolds stress profiles are studied in this section. Also, all results presented in this section are based on the ensemble of simulations from case A, A_1, A_2, and A_3.

The profiles of the TKE are shown in Figure 3.21. The initial amplitude is small. During the transition period, the TKE grows slowly and a peak appears in an annular region inside of the vortex core. Once the vortex adjusts itself from the unphysical nature of the initial random disturbances and the disturbances are amplified enough, the TKE grows significantly, since the disturbances start to interact with the mean flow, while the peak of TKE moves towards the edge of the vortex core. At later times the flow is stabilized and the TKE decays. When this happens the peak of TKE moves

to the center of the vortex. Chow & Zilliac (1994) observed similar behavior for TKE in their experiment in the near field of a wingtip vortex. They found that the peak TKE is original located near the edge of the core of the vortex. However, a short distance downstream, the peak TKE moves to a location at $r \approx 0.3r_0$. Finally, the peak decrease downstream of trailing edge. However, they did not see the peak move to the centerline because their measurement was taken in the near field of a wingtip vortex.

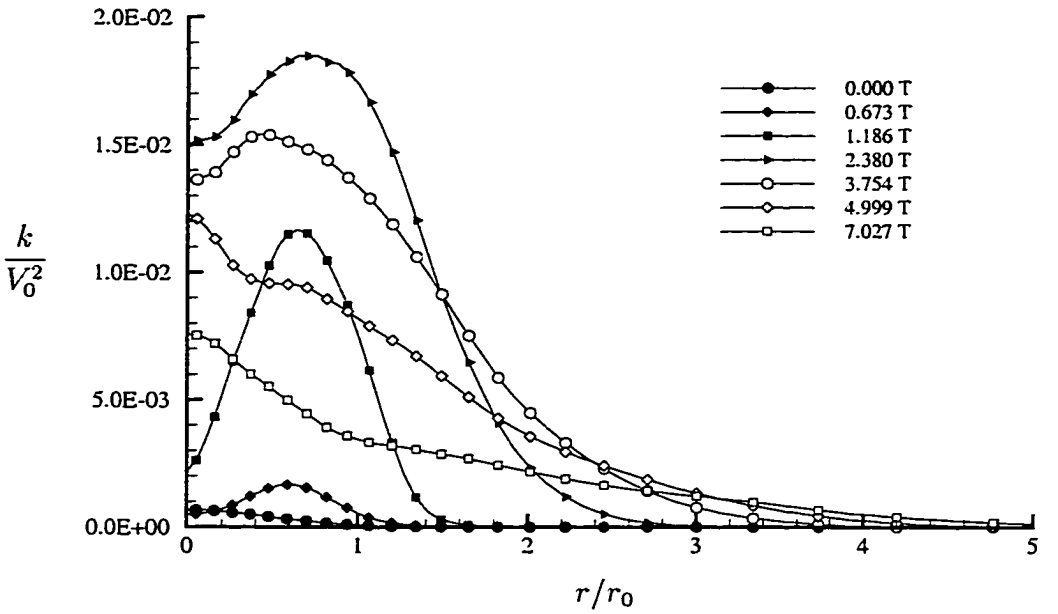

Figure 3.21 Evolution of the TKE k profiles.

Figures 3.22 to 3.24 show the profiles of the three normal Reynolds stresses. Features similar to those seen in the development of the TKE are also found in all three normal stresses. Phillips & Graham (1984) observed that the peak of the normal Reynolds stresses is located at the center of the vortex core at their far downstream measurement station. The normal Reynolds stress profiles at later times in this work qualitatively match the results of Phillips experiment very well. It is also noted that at early times the radial normal stress $\overline{v_r'^2}$ is larger than the tangential normal stress $\overline{v_\theta'^2}$. As shown later in Section 3.5, the different sign of the production term for the $\overline{v_r'^2}$ and $\overline{v_\theta'^2}$ transport equations is the key to explaining the anisotropy in the normal stress levels.

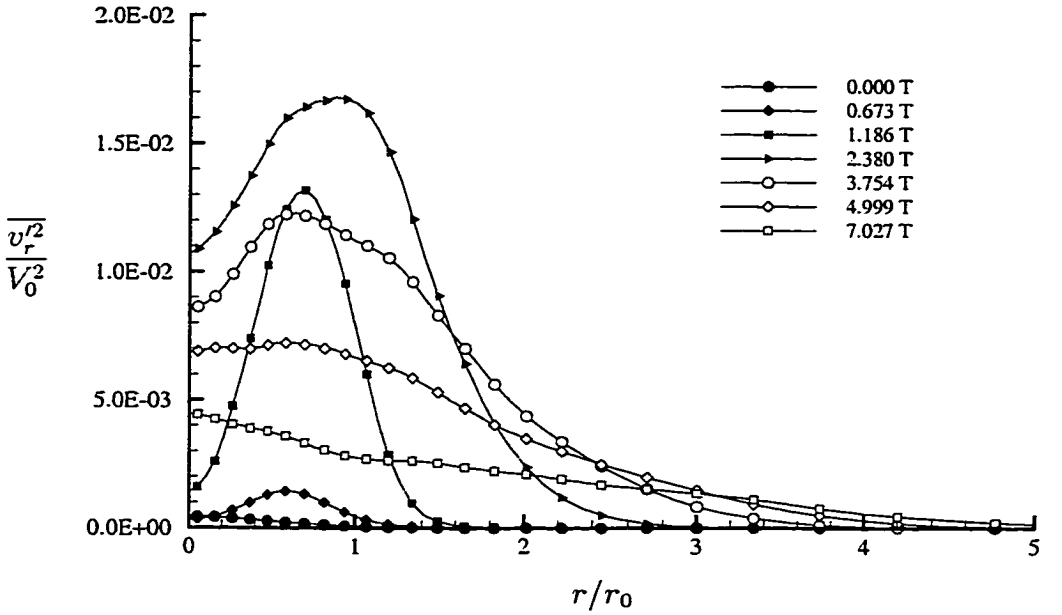

Figure 3.22 Evolution of the Reynolds stress $\overline{v_r'^2}$ profiles.

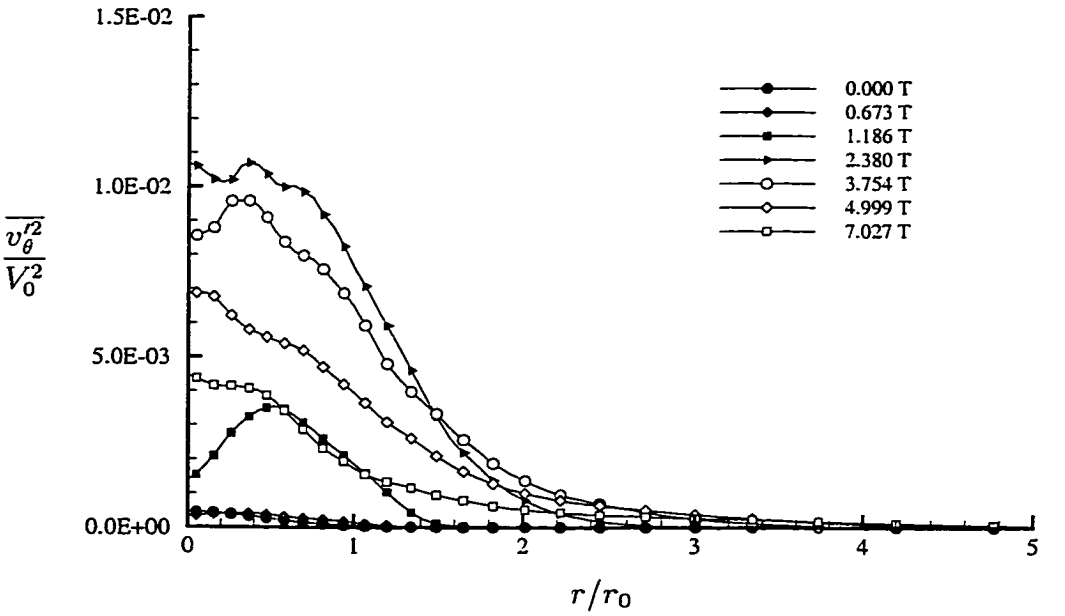

Figure 3.23 Evolution of the Reynolds stress $\overline{v_\theta'^2}$ profiles.

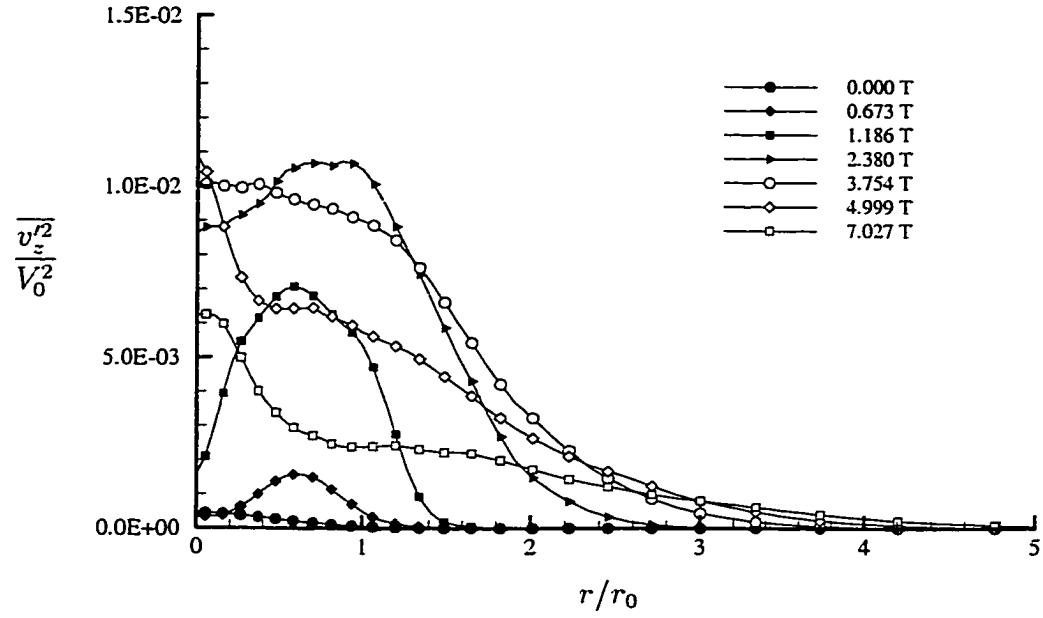

Figure 3.24 Evolution of the Reynolds stress $\overline{v_z'^2}$ profiles.

The evolution of shear stress $\overline{v_r'v_\theta'}$ is shown in Figure 3.25. The peak in $\overline{v_r'v_\theta'}$ also occurs in an annular region near the edge of the core at early times, but it continues to move outward as the flow is stabilized rather than moving to the center of the vortex, which is what happens for the normal stresses. The peak of $\overline{v_r'v_\theta'}$ at later times is located at $r \approx 2r_0$ which matches with Phillips' results. As mentioned in Section 3.3.3 the location of the peak coincides with the overshoot in circulation. The important feature as shown in this picture is that the stress $\overline{v_r'v_\theta'}$ shows a different sign near the center of the vortex at later times. This is the key explaining the negative eddy viscosity that causes the anti-diffusion for the mean tangential velocity. Phillips & Graham (1984) also observed a negative $\overline{v_r'v_\theta'}$ in the region near the core of the vortex. Figures 3.26 and 3.27 present the profiles of shear stresses $\overline{v_r'v_z'}$ and $\overline{v_\theta'v_z'}$. The stresses $\overline{v_r'v_z'}$ and $\overline{v_\theta'v_z'}$ show features similar to each other except for the different sign. In contrast to $\overline{v_r'v_\theta'}$, the peaks of $\overline{v_r'v_z'}$ and $\overline{v_\theta'v_z'}$ stay near the edge of the vortex. Also, both stresses develop a different sign near the center of the vortex at later times, resulting in a negative eddy viscosity as shown in the next section.

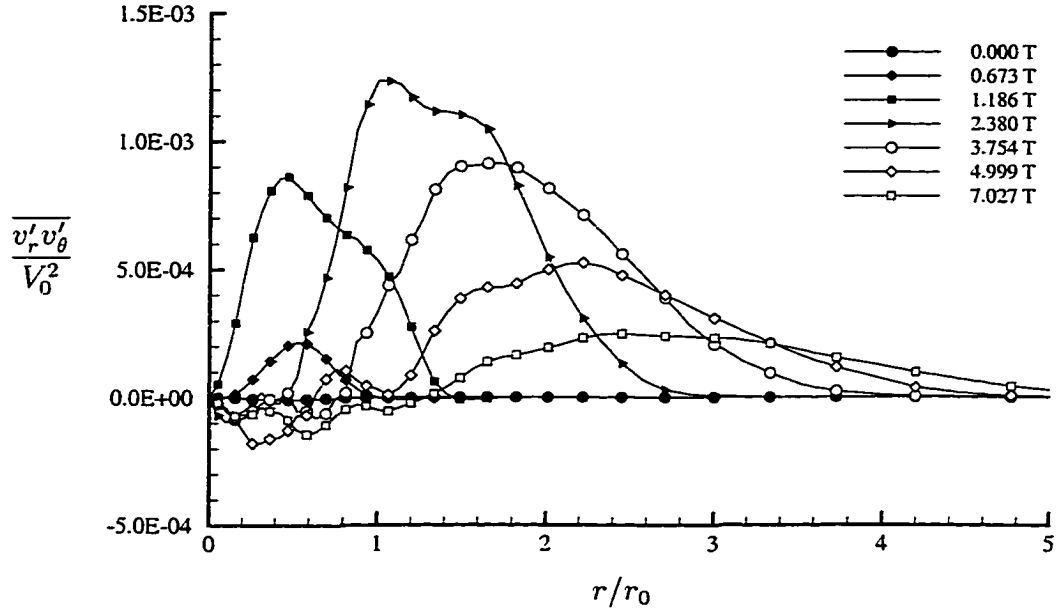

Figure 3.25 Evolution of Reynolds stress $\overline{v_r' v_\theta'}$ profiles.

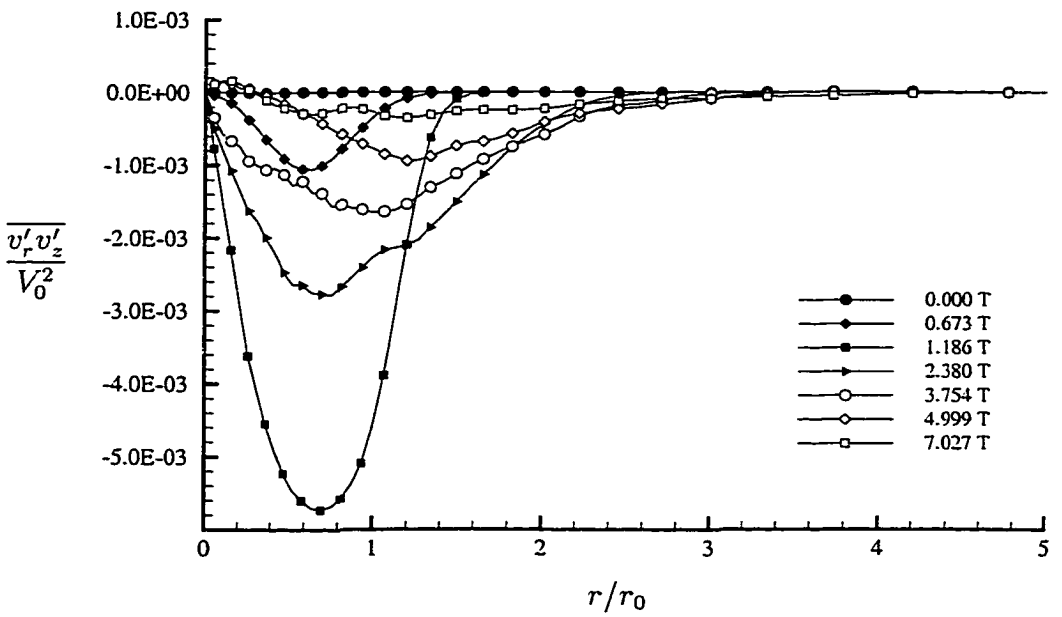

Figure 3.26 Evolution of the Reynolds stress $v_r' v_z'$ profiles.

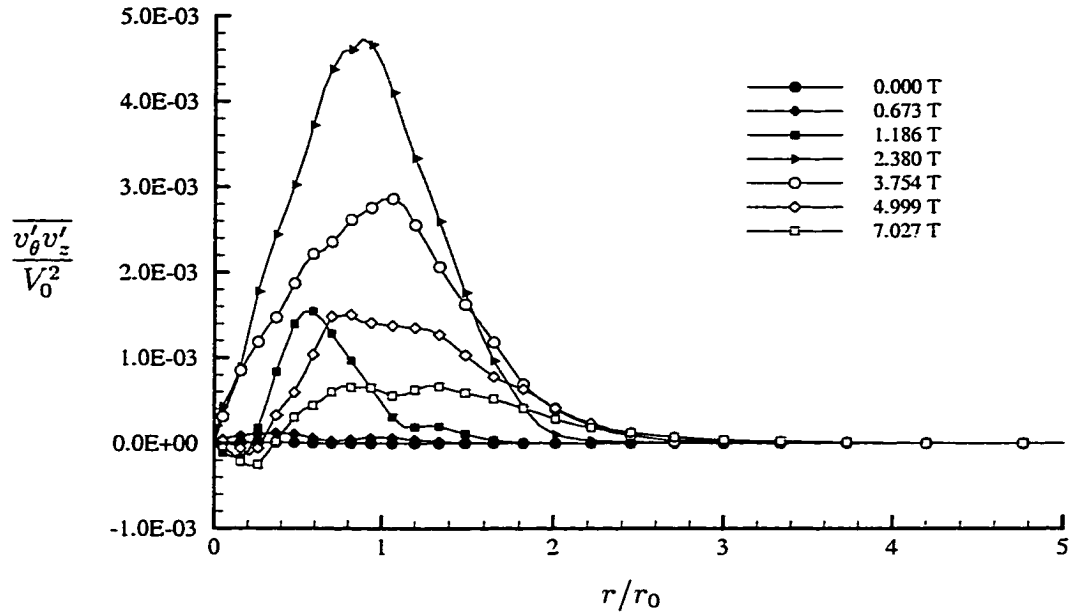

Figure 3.27 Evolution of Reynolds stress $\overline{v'_\theta v'_z}$ profiles.

3.3.5 Eddy viscosity

The production of TKE can be simplified as

$$\mathcal{P} = -\overline{v'_r v'_\theta} S_{r\theta} - \overline{v'_r v'_z} S_{rz} \,, \tag{3.29}$$

where, with axisymmetry,

$$S_{r\theta} = r\frac{\partial}{\partial r}\left(\frac{V_\theta}{r}\right) \qquad \text{and} \qquad S_{rz} = \frac{\partial V_z}{\partial r}. \tag{3.30}$$

From the Boussinesq approximation the Reynolds stresses can be modeled as

$$-\overline{v'_r v'_\theta} = \nu_T S_{r\theta} \quad \text{and} \quad -\overline{v'_r v'_z} = \nu_T S_{rz} \,, \tag{3.31}$$

where ν_T is the eddy viscosity. Substituting Equation (3.31) into equation (3.29), one can define the eddy viscosity as

$$\nu_T = -\frac{\overline{v'_r v'_\theta} S_{r\theta} + \overline{v'_r v'_z} S_{rz}}{2(S_{r\theta}^2 + S_{rz}^2)} \tag{3.32}$$

Figure 3.28 shows that the ratio of ν_T/ν is large except at the initial time. It indicates that turbulent transport of momentum is much more important than molecular

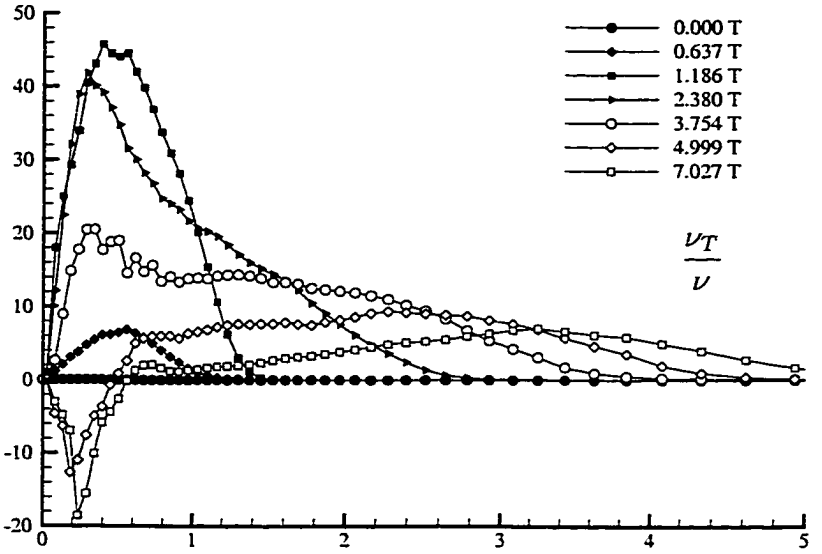

Figure 3.28 Evolution of the eddy ν_T/ν profiles.

transport. The interesting feature is that for later time, when the vortex becomes stable, a negative eddy viscosity develops in the vortex core since the sign of the shear stresses $\overline{v_r' v_\theta'}$ and $\overline{v_r' v_z'}$ in the vortex core is changed. It is believed that this negative eddy viscosity is responsible for the anti-diffusion of the tangential velocity seen in Figure 3.15.

In order to investigate the contribution of each of the shear stress, the eddy viscosity is then split into two parts

$$\nu_T = \nu_{T1} + \nu_{T2}\,, \tag{3.33}$$

where

$$\nu_{T1} = -\frac{\overline{v_r' v_\theta'} S_{r\theta}}{2(S_{r\theta}^2 + S_{rz}^2)} \quad \text{and} \quad \nu_{T2} = -\frac{\overline{v_r' v_z'} S_{r\theta}}{2(S_{r\theta}^2 + S_{rz}^2)}. \tag{3.34}$$

The two parts give the contribution to ν_T from each of the Reynolds stresses. From Figures 3.29 and 3.30, it is noted that both ν_{T1} and ν_{T2} show negative values in the vortex core at later time and that ν_{T2} is a dominant factor in the total eddy viscosity. Also, it is noted that ν_{T1} extends to large r/r_0 at later time while ν_{T2} is localized to $r/r_0 < 2$, similar to the behavior of the shear stresses $\overline{v_r' v_\theta'}$ and $\overline{v_r' v_z'}$ respectively.

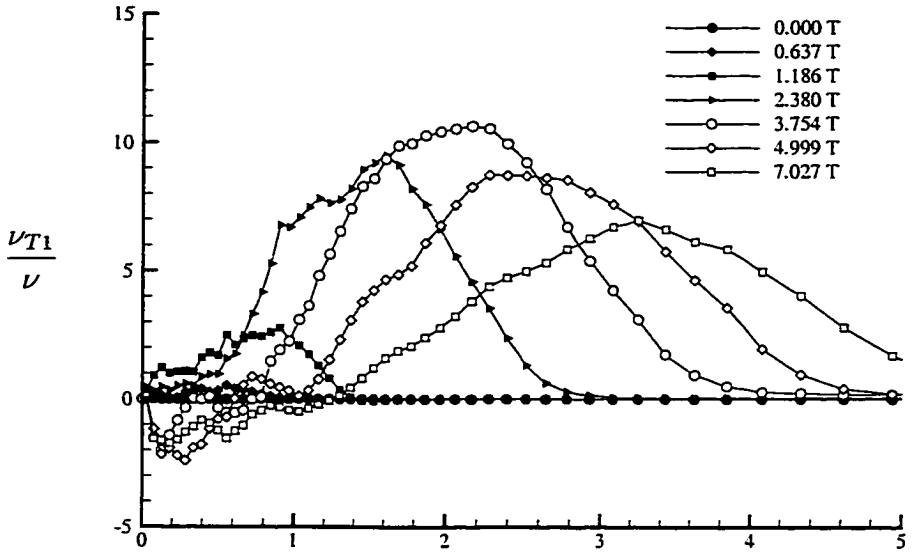

Figure 3.29 Evolution of the eddy ν_{T1}/ν profiles.

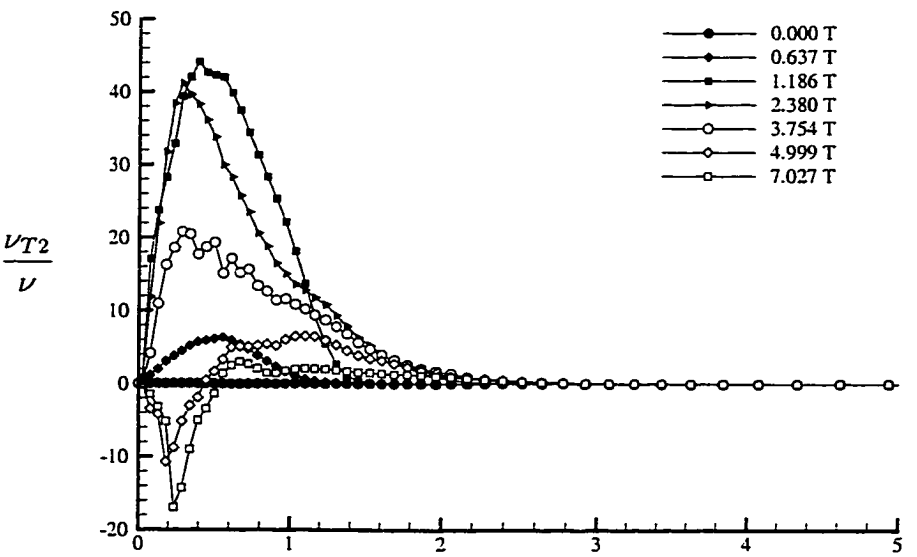

Figure 3.30 Evolution of the eddy ν_{T2}/ν profiles.

3.4 One-Dimensional Energy Spectra

The one-dimensional spectrum, $E_z(r, k_z)$, is defined by

$$E_z(r, k_z) = \frac{1}{2\pi} \int_0^{2\pi} \widehat{u_i'}(x, y, k_z) \widehat{u_i'}(x, y, k_z) d\theta \,, \tag{3.35}$$

where, $x = r\cos(\theta)$, $y = r\sin(\theta)$, and $\widehat{u_i'}(x, y, k_z)$ is the Fourier coefficients of the fluctuating velocity. As shown in Figures 3.31 to 3.36, the turbulence has developed to be broad band. The spectra fall off at high wavenumber without a significant pile-up of energy, which indicates that the flow field is well resolved. The scatter in the spectra show the effect of a small statistical sample size. Once the isolated vortex adjusts itself from the initial isotropic flow field, the spectra show a region where $E_z(k_z)$ varies approximately as k_z^{-c}. However, the exponent c is not constant, but varies with time of t.

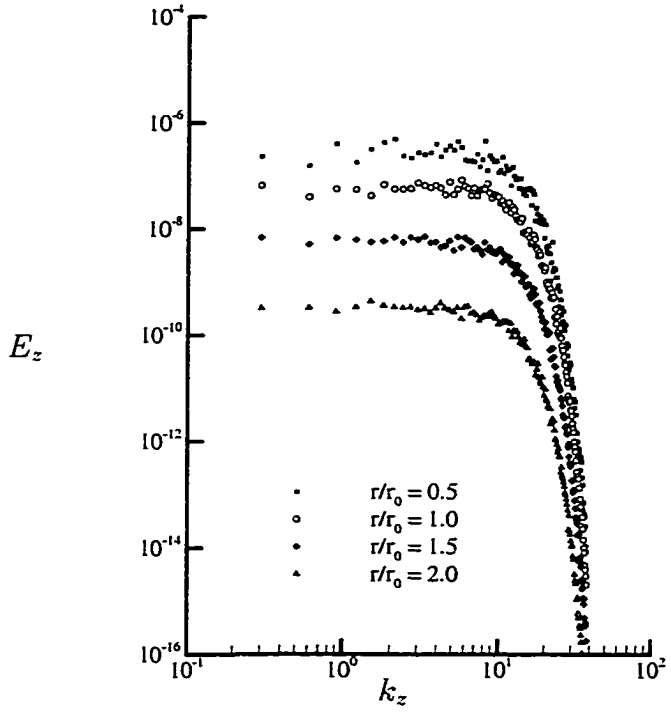

Figure 3.31 One-dimensional spectra E_z at time $t = 0.00T$.

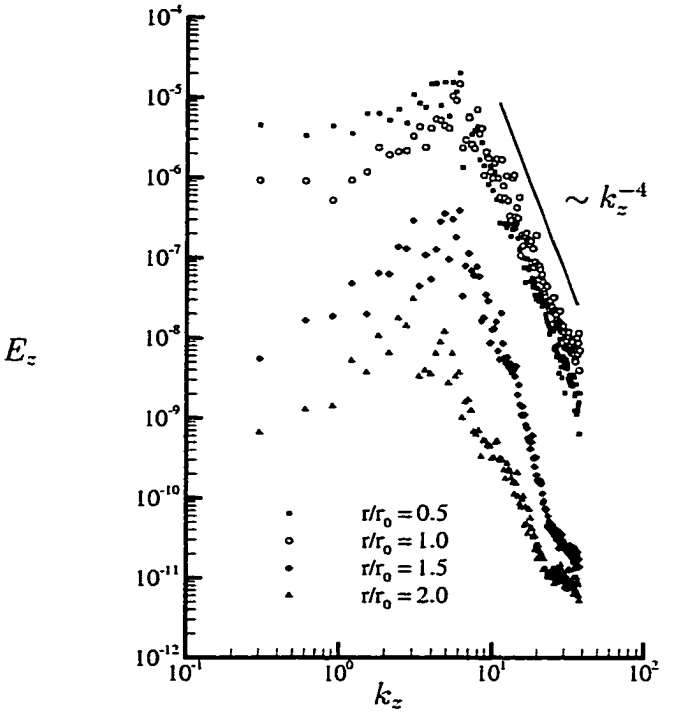

Figure 3.32 One-dimensional spectra E_z at time $t = 1.05T$.

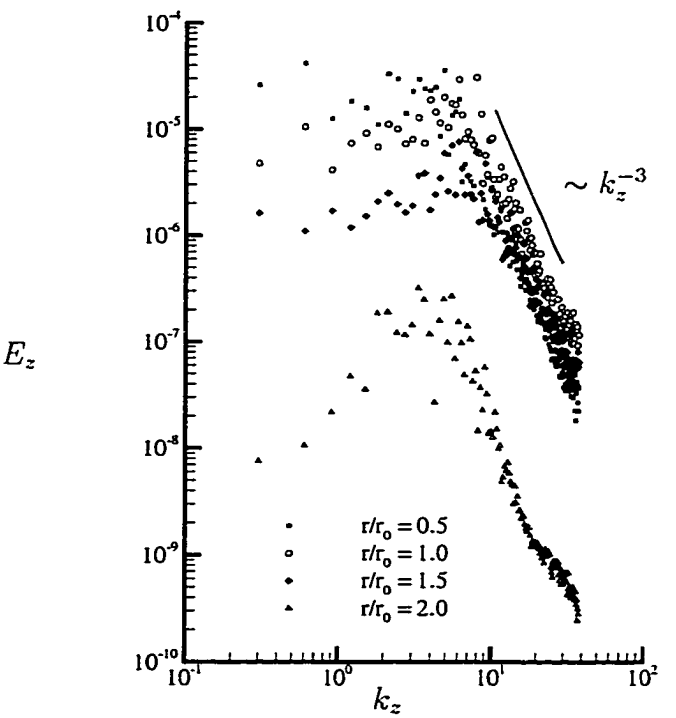

Figure 3.33 One-dimensional spectra E_z at time $t = 1.62T$.

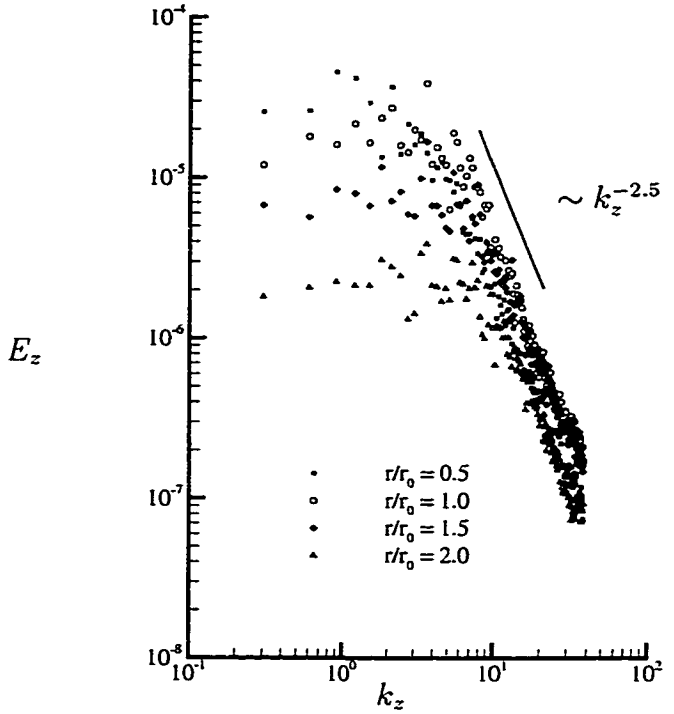

Figure 3.34 One-dimensional spectra E_z at time $t = 2.78T$.

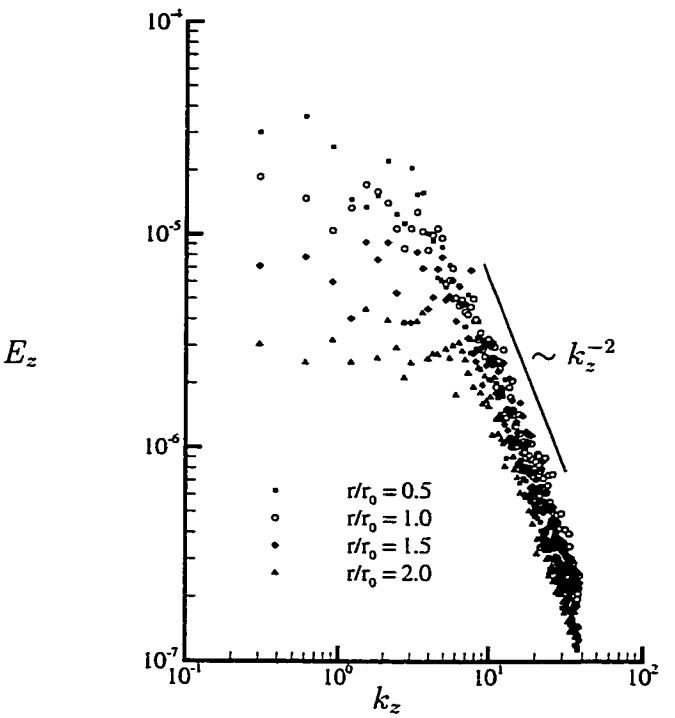

Figure 3.35 One-dimensional spectra E_z at time $t = 3.97T$.

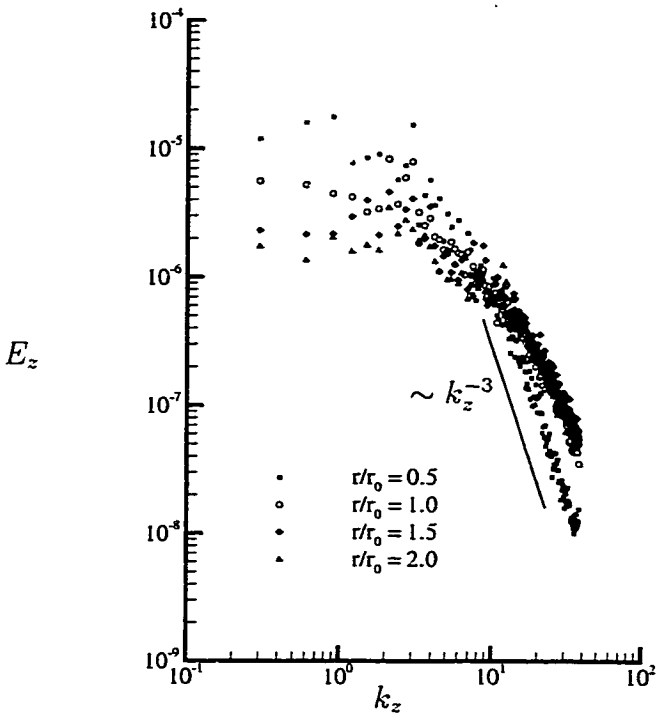

Figure 3.36 One-dimensional spectra E_z at time $t = 6.46T$.

3.5 Budgets of the Turbulent Transport Equations

The objective of this section is to present the budget analyses for the Reynolds stresses and the TKE. Because high quality turbulence measurements are difficult to take due to the issue of vortex meandering, it is impossible to make a direct comparison of the turbulence closure models with experimental data. However, the budget analysis provides necessary information to directly evaluate turbulence closure models. Thus, the budget analysis will provide valuable guidelines for studying turbulence modeling of the vortex or other rotating flows. In addition, the budget analysis will also be very helpful to increase our understanding of turbulence in the vortex. A detailed analysis of the Reynolds stress and the TKE budgets, corresponding to the five instances in time given in Section 3.3.2, is presented in this section.

The transport equations for the Reynolds stresses in tensor form are given by

$$\frac{\partial}{\partial t}\left(\overline{v_i' v_j'}\right) = C_{ij} + P_{ij} + O_{ij} + \Pi_{ij} + T_{tij} + P_{tij} + D_{ij} - \epsilon_{ij} \,, \qquad (3.36)$$

where the terms on the right hand side of Eq. 3.36 are given by

$$C_{ij} = -U_k(\overline{u_i'u_j'})_{,k} \quad \text{Convection,}$$

$$P_{ij} = -\frac{1}{2}\left(\overline{u_i'u_k'}(U_{k,j}+U_{j,k}) + \overline{u_j'u_k'}(U_{k,i}+U_{i,k})\right) \quad \text{Production ,}$$

$$O_{ij} = \frac{1}{2}\left(\overline{u_i'u_k'}(U_{k,j}-U_{j,k}) + \overline{u_j'u_k'}(U_{k,i}-U_{i,k})\right) \quad \text{Rotation,}$$

$$\Pi_{ij} = \overline{p'(u_{i,j}'+u_{j,i}')}/\rho \quad \text{Pressure strain,}$$

$$T_{tij} = -(\overline{u_i'u_j'u_k'})_{,k} \quad \text{Turbulent transport,}$$

$$P_{tij} = -(\overline{p'u_j'}\delta_{ik} + \overline{p'u_i'}\delta_{jk})_{,k} \quad \text{Pressure transport,}$$

$$D_{ij} = \nu(\overline{u_i'u_j'})_{,kk} \quad \text{Viscous diffusion,}$$

$$\epsilon_{ij} = 2\nu\overline{u_{i,k}'u_{j,k}'} \quad \text{Dissipation,}$$

and U_k is the mean velocity. The transport equation for each individual Reynolds stress in cylindrical coordinates is presented in Appendix A.

3.5.1 Budgets of TKE

Figures 3.37 to 3.41 gives the budgets of TKE at different periods in time. Since the flow is axisymmetric with low Mach number, the rotation term, convective term, and pressure strain term are nearly zero. value.

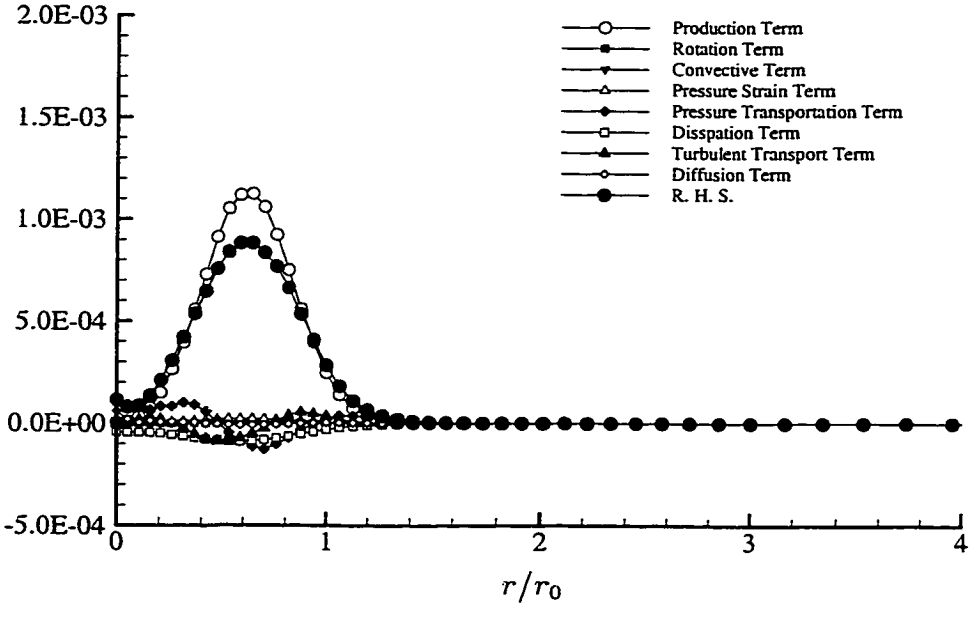

Figure 3.37 Budget for the transport equation of TKE at $t = 0.637T$.

During the transition period, as shown in Figure 3.37, the budget for the TKE is dominated by the production term. The right hand side term (hereafter RHS) has a peak near the edge of the vortex core ($r = 0.6r_0$) resulting in the peak in TKE occurring in an annular region at the corresponding location. The other terms show very small contributions. After the flow develops for a while, the disturbance is large enough to interact with the mean flow.

As shown in Figure 3.38, the production is still a dominant term, but the magnitude of the rest of the terms shows significant growth. The pressure transport term and turbulent transport term show a very complicated behavior, but the interesting feature is that they have different signs and almost cancel each other except near the center of vortex core ($r < 0.4r_0$). The dissipation term is also developed and shows a slight peak corresponding the location of the peak of the production term. The RHS shows a nearly constant value in the vortex core region and suddenly drops to zero at the edge of vortex core.

Figure 3.39 shows the budget of the TKE during the growing period. Even though the production term has the largest contribution to RHS, the peak of the production has shown a decay and moved towards the edge of vortex core. However, the dissipation term still keeps growing. Although the pressure transport term and turbulent transport term still have different signs, the turbulent transport term shows a large peak at the region near vortex center, which results in the TKE at the center of the vortex having a large growth rate as shown in Figure 3.21.

Figure 3.40 shows the budget of TKE at $3.74T$ when the global TKE has a peak value. Negative production appears in the center of the vortex due to the Reynolds stresses having a different sign in the center of the vortex, as mentioned in Section 3.3.4. Except in the center of the vortex, the RHS has a negative value resulting in a decay of TKE. However, the peak of the turbulent transport term in the region near the vortex center causes the growth rate of the TKE in the region near the vortex center to be much larger than in the location of the peak of the TKE as shown in Figure 3.21. In other words, the peak of the TKE is flattened. The dissipation term has a nearly constant value in the region of vortex core.

During the period of TKE decaying as shown in Figure 3.41, with the flow stabilizes, the magnitude of all the terms shows a decay. The production term is the same order of magnitude as the dissipation term except inside the vortex core, where the production term shows a negative value. The RHS outside the vortex core is mainly

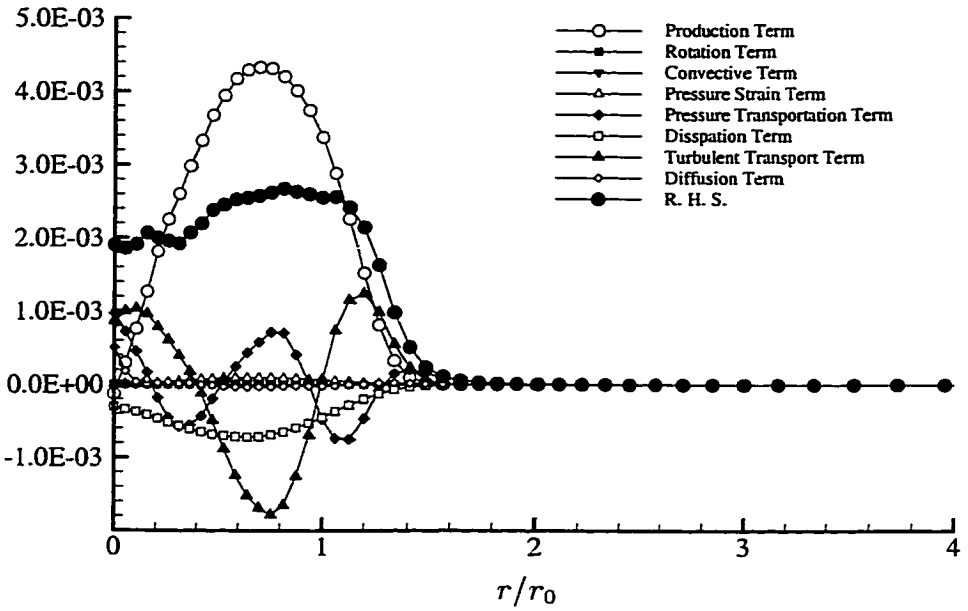

Figure 3.38 Budget for the transport equation of TKE at $t = 1.186T$.

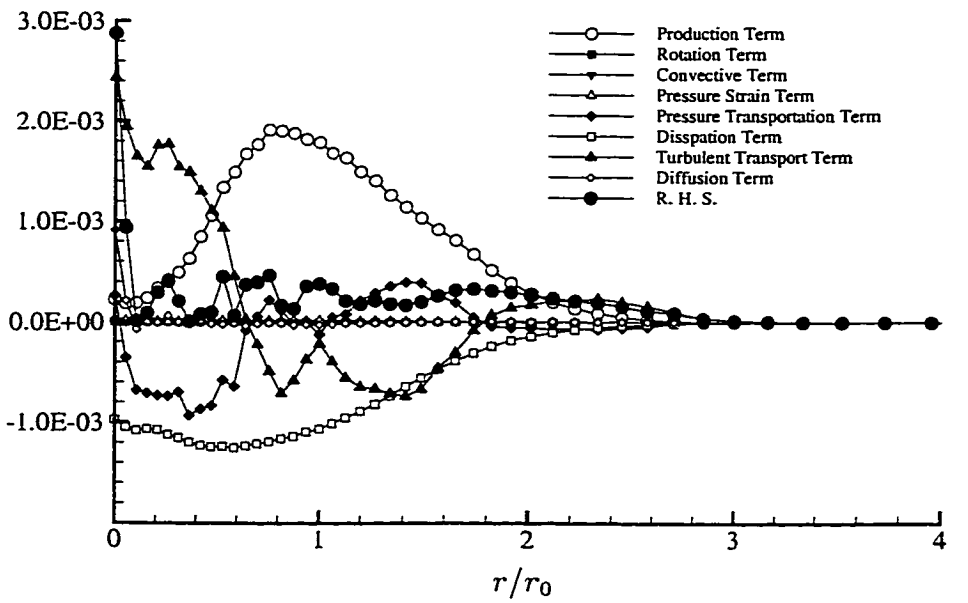

Figure 3.39 Budget for the transport equation of TKE at $t = 2.380T$.

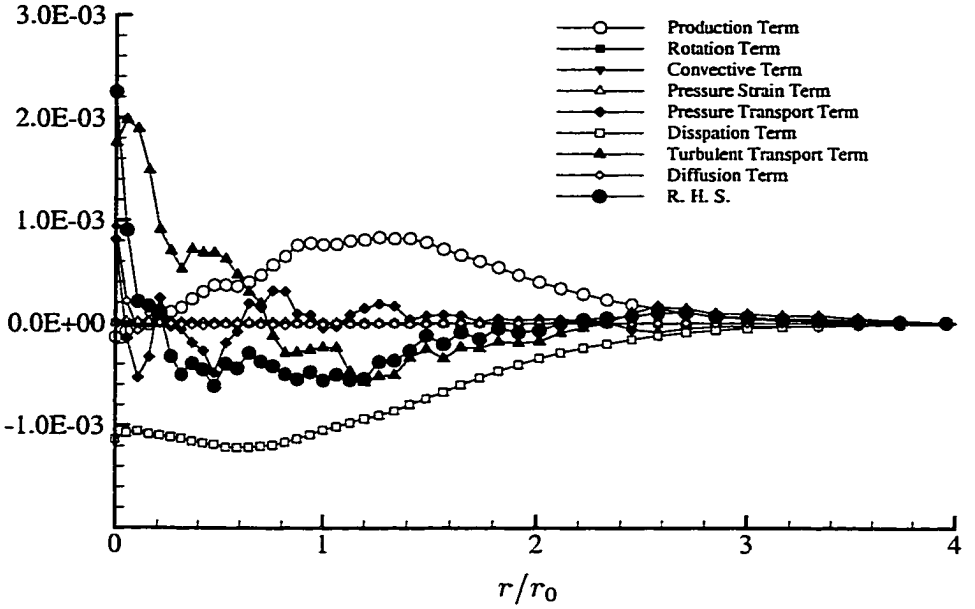

Figure 3.40 Budget of the transport equation of TKE at $t = 3.754T$.

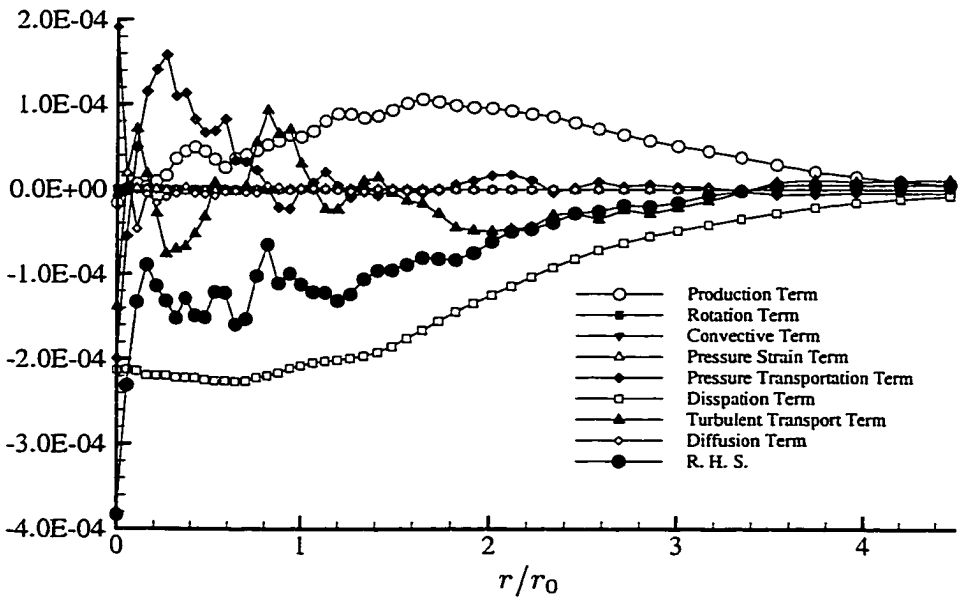

Figure 3.41 Budget for the transport equation of TKE at $t = 7.027T$.

contributed from the turbulent transport term. It is noted that the viscous diffusion is negligible during the entire period of the isolated vortex development.

Figure 3.42 shows a ratio of the production term to the dissipation term for Case A. It is noted that the production term is dominant at the early time, $t = 1.11T$; then at $t = 2.02T$ the production term is of the same order of the magnitude as the dissipation term but the production term is still larger than the dissipation term except near the center of the vortex ($r < 0.4r_0$); finally at the later time, the production term is nearly equal to the dissipation term except inside the vortex core where the production term shows a negative

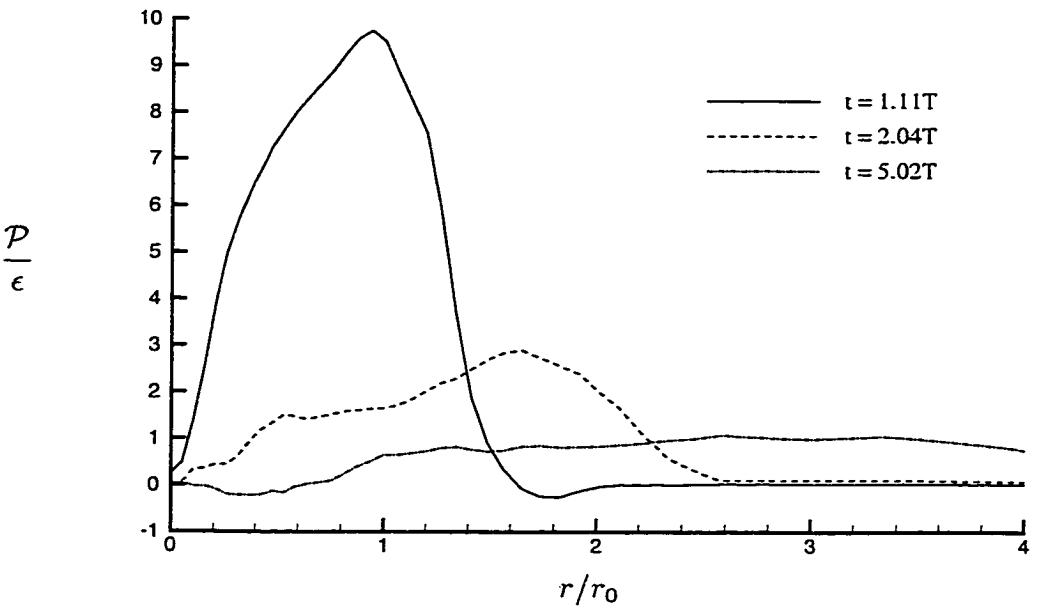

Figure 3.42 The ratio of the production term to the dissipation term.

3.5.2 Budgets of $\overline{v_r'^2}$

The budget of stress component $\overline{v_r'^2}$ is shown in Figures 3.43 to 3.47. For the isolated vortex with axisymmetry and low Mach number, the rotation term is nearly zero and the convective term is identical to the production term. During the starting period as shown in Figure 3.43, the production term, turbulent transport term, pressure transport term, and dissipation term have the same behaviors as in the budget of TKE shown in Figure 3.37, but the production term is not the dominant term. The pressure strain term makes the largest contribution to RHS. The pressure strain

term is trace free and exchanges energy among the velocity components. The positive pressure strain term means to taking the energy from other component. As shown in later, the energy going into $\overline{v_r'^2}$ comes from $\overline{v_z'^2}$. RHS also peaks at $r = 0.6r_0$ which result in the peak in $\overline{v_r'^2}$ occurring in the corresponding location.

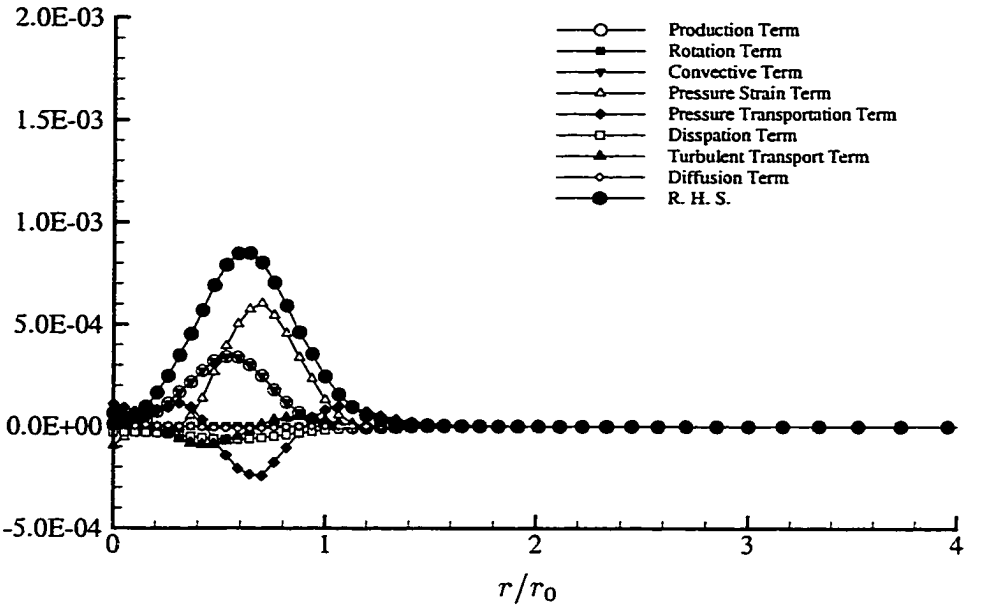

Figure 3.43 Budget for the transport equation of $\overline{v_r'^2}$ at $t = 0.637T$.

For the budget of $\overline{v_r'^2}$ during the linearly unstable period as shown in the Figure 3.44, the magnitude of all of the terms show a significant increase. The pressure transport term and turbulent transport term show similar features as in the TKE budget which is that the two term have different signs and almost cancel each other. The peak in the production term as well as the convective term is weakened since the production term is growing faster in the region close to the edge of vortex than in the region near the vortex center. An interesting feature is shown in the pressure strain term. The peak of pressure strain moves towards the edge of the vortex core while there are two negative regions appearing at $r = 0.2r_0$ and $r = 1.4r_0$. The negative pressure strain in the region near the vortex center causes the growth rate of $\overline{v_r'^2}$ in the region near the vortex center to be much slower than in the location of the peak.

Figure 3.45 shows the budget of $\overline{v_r'^2}$ during the growing period. Negative production appears in the center of the vortex and the peak of the production moves towards the edge of the vortex. The regions of negative pressure strain are enlarged and the peak

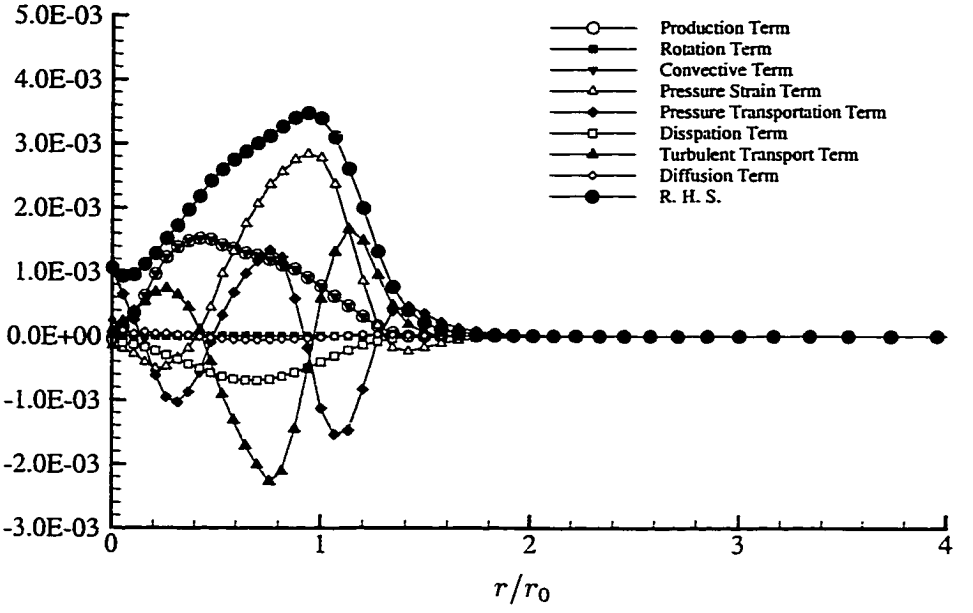

Figure 3.44 Budget for the transport equation of $\overline{v_r'^2}$ at $t = 1.186T$.

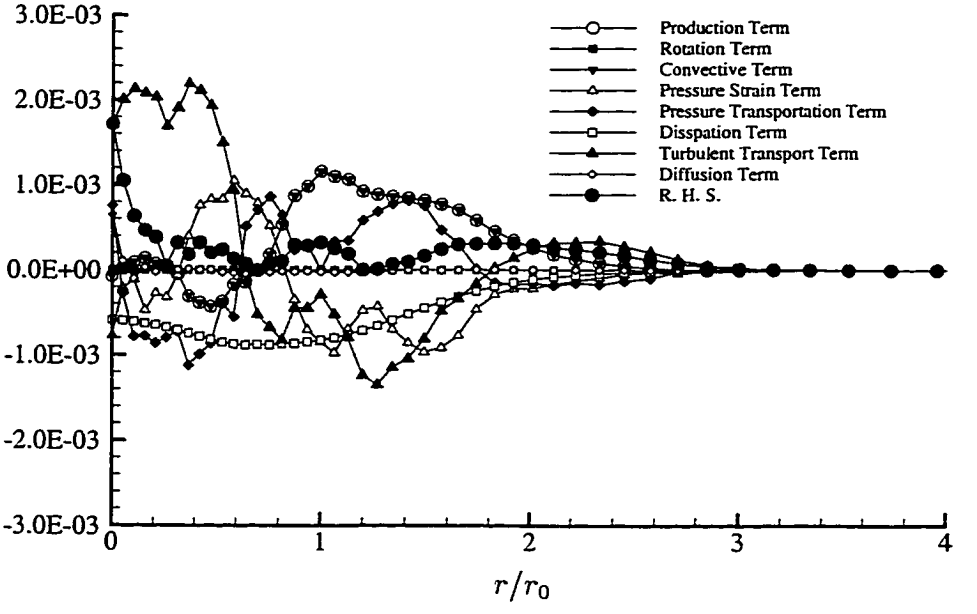

Figure 3.45 Budget for the transport equation of $\overline{v_r'^2}$ at $t = 2.380T$.

of pressure strain is weakened. The turbulent transport term shows a different sign compared with the pressure transport term, but the turbulent transport term has a large positive value which results in the RHS term having a peak at the center of the vortex. Therefore, it is the turbulent transport term that causes $\overline{v_r'^2}$ to have a much larger growth in the region near vortex center than in the location of the peak.

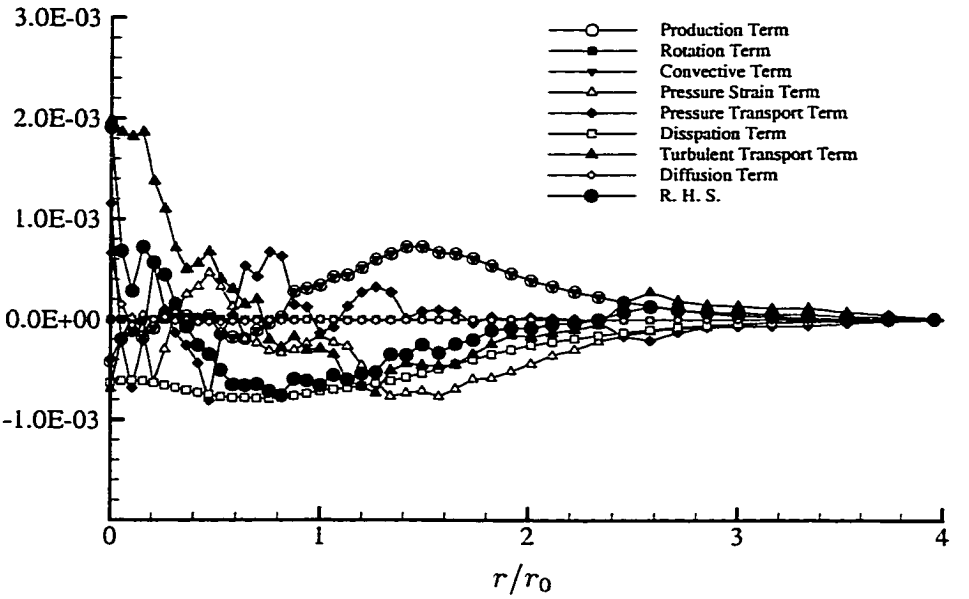

Figure 3.46 Budget for the transport equation of $\overline{v_r'^2}$ at $t = 3.754T$.

During the saturating period shown in the Figure 3.46, the magnitude of all of the terms show decay. The dissipation shows a constant value inside the vortex core. The production decays to the same order of magnitude as the dissipation. The pressure strain term becomes negative at most of regions. We will see later, the energy is transfered to $\overline{v_z'^2}$. The pressure term equalizes the normal Reynolds stresses and makes the turbulence to be more nearly isotropic (Bradshaw 1988). The RHS term shows a negative value except in the region of the vortex center. Therefore $\overline{v_r'^2}$ starts to decay.

As shown in Figure 3.47, comparing with the previous time during the saturating period, the budget of $\overline{v_r'^2}$ during relaminarizing period only shows some quantitative changes rather than any qualitative change. Again, it is noted that the viscous diffusion is negligible during the entire period of the isolated vortex development.

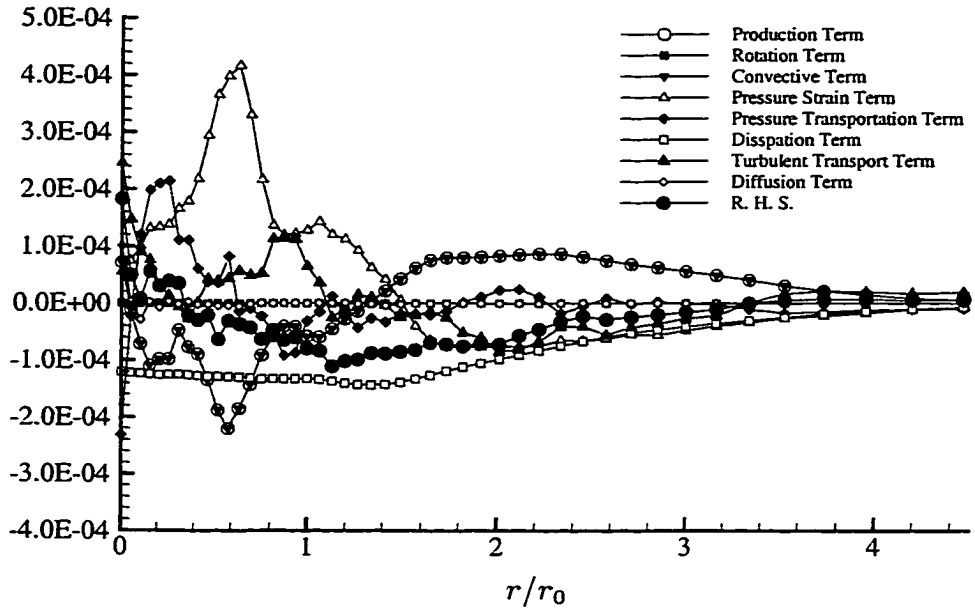

Figure 3.47 Budget for the transport equation of $\overline{v_r'^2}$ at $t = 7.027T$.

3.5.3 Budgets of $\overline{v_\theta'^2}$

Figures 3.48 to 3.52 present the budgets of $\overline{v_\theta'^2}$ during the different periods. For the budget of the azimuthal component $\overline{v_\theta'^2}$ at the transition period, as shown in Figure 3.48, the pressure strain term is the primary source of production. As shown in Section 3.3.4, at early time, since $\overline{v_\theta'^2}$ has the lowest level of energy, the pressure strain term takes energy from $\overline{v_z'^2}$ and tends to equalize normal Reynolds stresses. In contrast to the budget of $\overline{v_r'^2}$, the production term and convective term are negative, resulting in the magnitude of $\overline{v_\theta'^2}$ having a much lower growth rate than that of $\overline{v_r'^2}$ during the starting period, as mentioned in Section 3.3.4. Comparing to the other terms, the pressure transport term and turbulent transport term have a much smaller magnitude.

During the linearly unstable period, as shown in Figure 3.49, the magnitude of all of the terms increases significantly. Similar to the budget of $\overline{v_r'^2}$, the pressure transport term and turbulent transport term cancel each other in most of the vortex core. The dissipation term is much smaller than the production term. The significant growth of pressure strain is the driving force to cause $\overline{v_\theta'^2}$ to grow quickly.

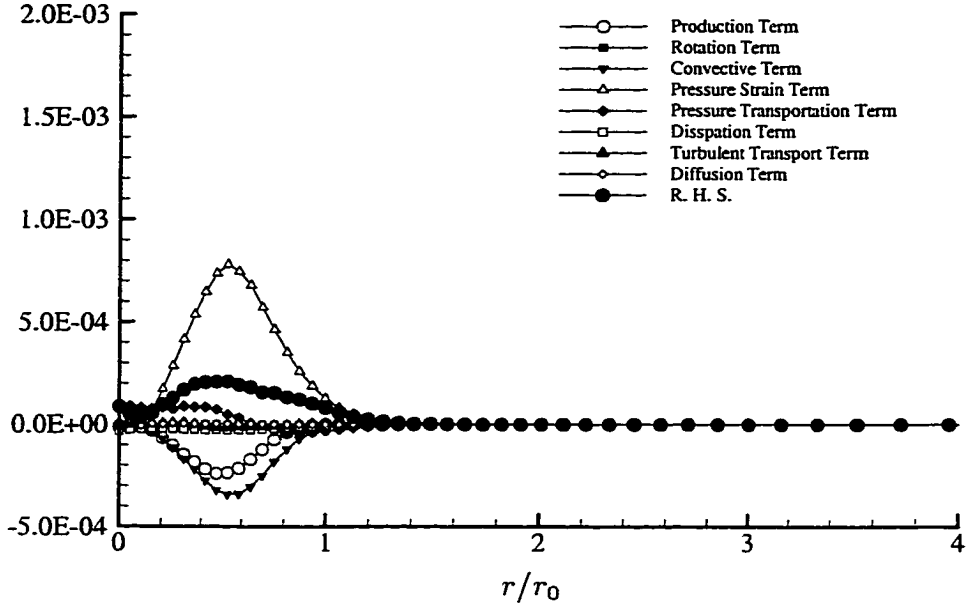

Figure 3.48 Budget for the transport equation of $\overline{v_\theta'^2}$ at $t = 0.637T$.

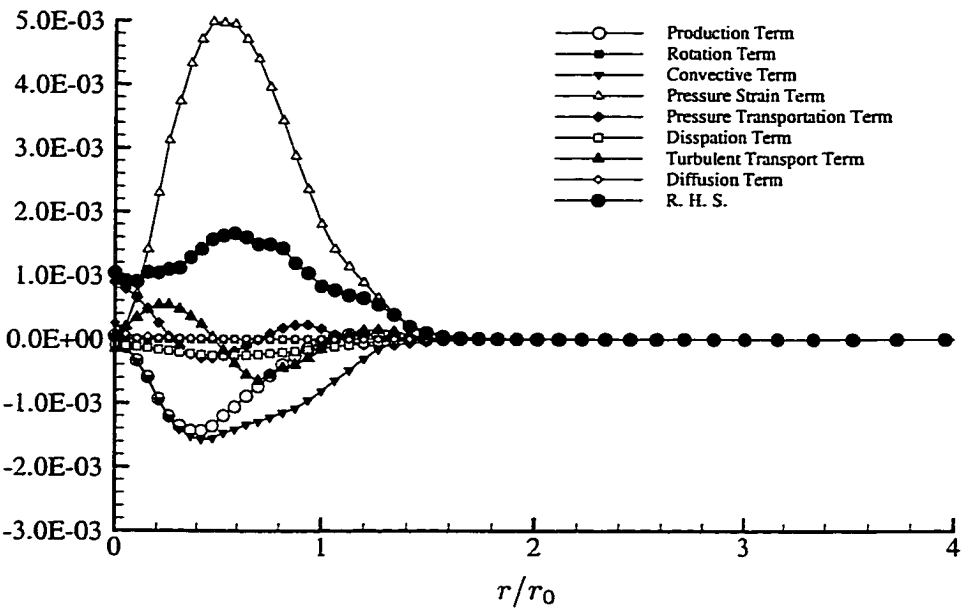

Figure 3.49 Budget for the transport equation of $\overline{v_\theta'^2}$ at $t = 1.138T$.

Figure 3.50 shows the budget of $\overline{v_\theta'^2}$ during the growing period. A negative pressure strain appears in the region near the vortex center, but not in the outer region as with $\overline{v_r'^2}$ (see Figure 3.45). Both the pressure strain term and production term show decay, but the pressure transport term, turbulent transport term, and dissipation term keep growing. The magnitude of the convective term remains almost unchanged, but a positive peak in the convective term appears in the location at $r = 0.5r_0$. The production term not only displays a positive peak at the same location where convective term has a positive peak, but also the production term develops a positive value outside the vortex core. Similar to the feature in the budget of $\overline{v_r'^2}$, the turbulent transport term forms a positive peak near the center of the vortex, which causes the peak of $\overline{v_\theta'^2}$ to moves towards the vortex center. RHS remains a positive value at most locations but its magnitude is small.

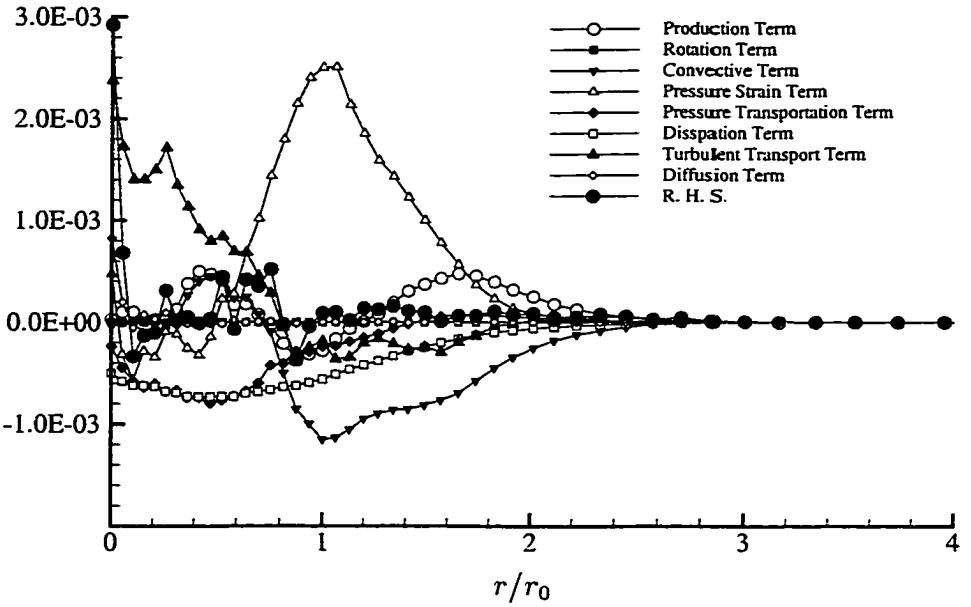

Figure 3.50 Budget for the transport equation of $\overline{v_\theta'^2}$ at $t = 2.380T$.

During the saturating period shown in Figure 3.51, the magnitude of all of the terms decays and the pressure strain drops quickly. The production term and the convective term are close to zero inside the vortex and almost cancel each other outside of vortex. As in the budget of $\overline{v_r'^2}$, the dissipation term shows a constant value inside the vortex. Overall, RHS has a negative value corresponding the decay

of $\overline{v_\theta'^2}$ except in the region near the vortex center where the turbulent transport term maintains a positive peak.

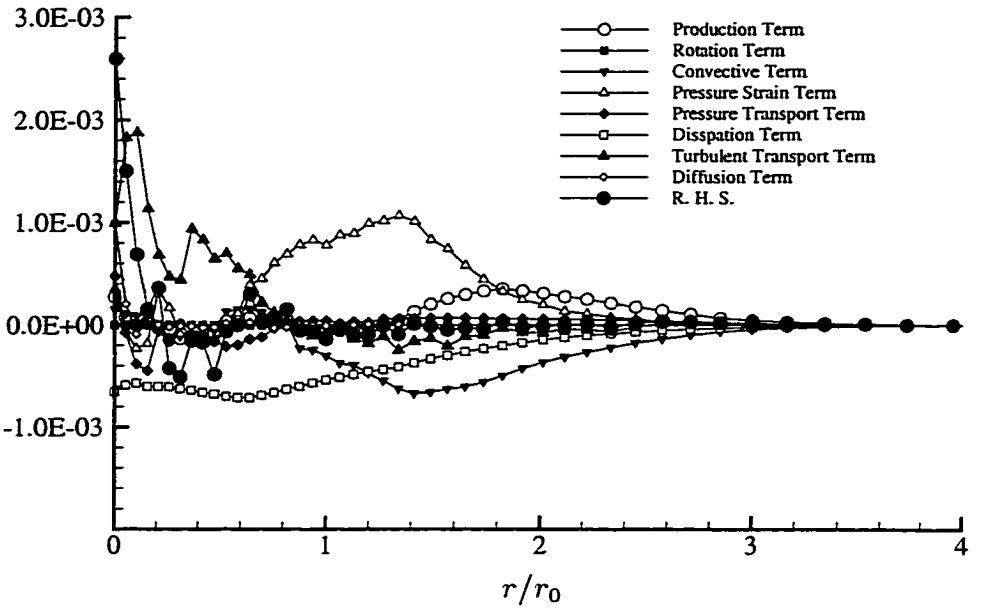

Figure 3.51 Budget for the transport equation of $\overline{v_\theta'^2}$ at $t = 3.754T$.

During the relaminarizing period shown in Figure 3.52, like the features in the budget of $\overline{v_r'^2}$, the budget of $\overline{v_\theta'^2}$ only show some quantitative changes rather than any qualitative change. Corresponding to a slow decay of $\overline{v_\theta'^2}$, RHS has a small negative value.

3.5.4 Budgets of $\overline{v_z'^2}$

The budgets of $\overline{v_z'^2}$ during different periods are shown in Figures 3.53 to 3.57. With the axisymmetry of an isolated vortex and by neglecting the compressible effect with a low Mach number, the rotation term, convective term, and pressure transport term are zero. The viscous diffusion term also is negligible as shown later. Figure 3.53 shows the budget of $\overline{v_z'^2}$ during the transition period. Production and pressure strain are the two dominant terms. In contrast to the budget of $\overline{v_r'^2}$ and $\overline{v_\theta'^2}$, the pressure strain term is negative. As mentioned before, this indicates that energy is transfered from $\overline{v_z'^2}$ to the other components. RHS has a peak at $r = 0.6r_0$ which results in the peak of $\overline{v_z'^2}$ moving from the center of the vortex to the corresponding location.

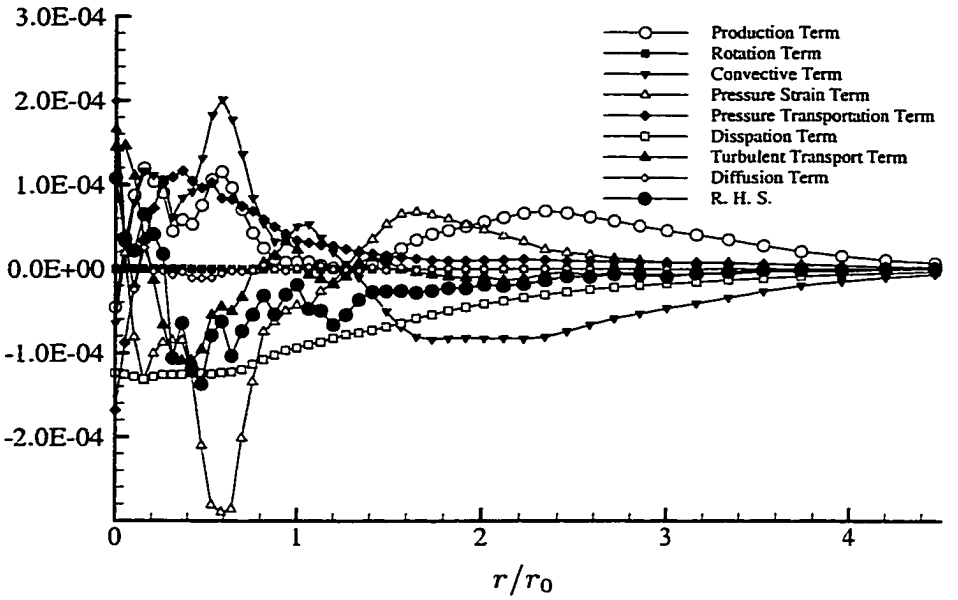

Figure 3.52 Budget for the transport equation of $\overline{v_\theta'^2}$ at $t = 7.027T$.

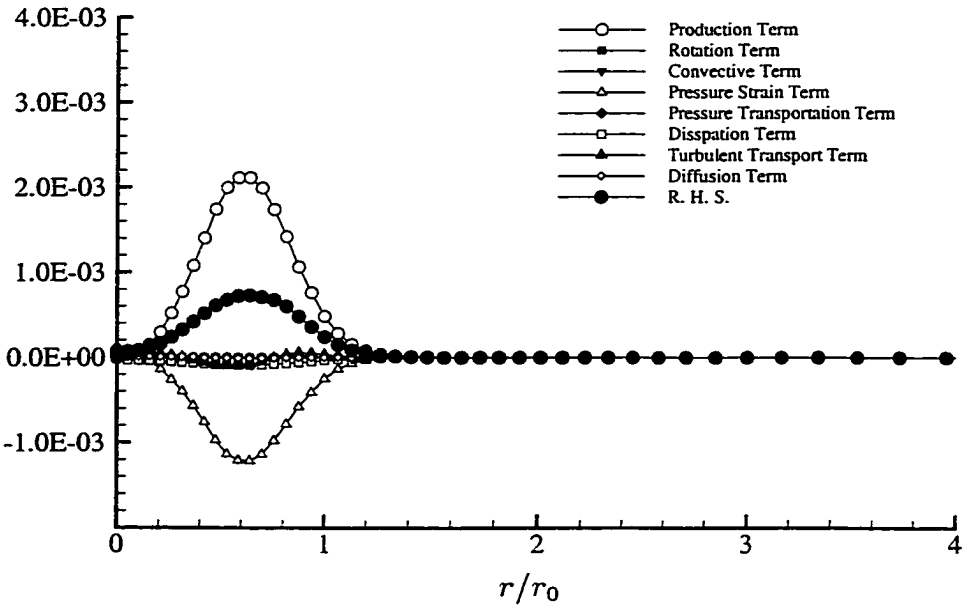

Figure 3.53 Budget for the transport equation of $\overline{v_z'^2}$ at $t = 0.637T$.

During the linearly unstable period shown in Figure 3.54, the turbulent transport term has two peaks at the locations of the vortex center and the vortex edge and has a negligible value throughout the rest of the vortex core. The dissipation term maintains a small value. An interesting feature is that the profiles of pressure strain and production have the same shape except opposite sign and diffident magnitudes. Therefore, RHS has a constant value except at the center and the edge of the vortex where the contribution from the turbulent transport term is significant.

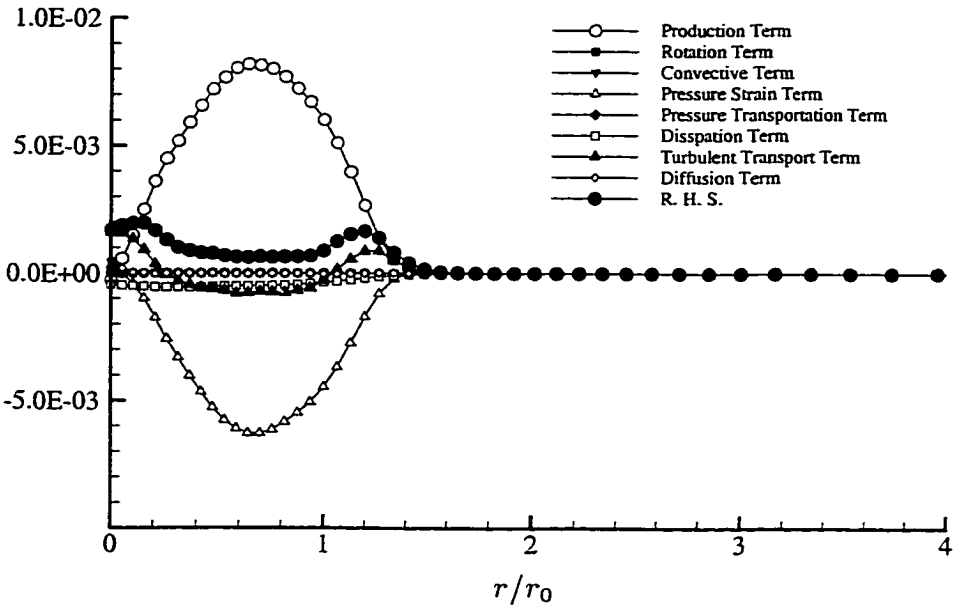

Figure 3.54 Budget for the transport equation of $\overline{v_z'^2}$ at $t = 1.138T$.

During the growing period as shown in Figure 3.55, the magnitude of the pressure strain term and production term shows decay. As shown in the budget of $\overline{v_r'^2}$ of Figure 3.45, the pressure strain displays two small peaks but with positive values at the locations of $r = 0.2r_0$ and $r = 1.6r_0$. The dissipation term keeps growing to a notable value. RHS remains positive value over most of the vortex core which corresponds to the continue growth of $\overline{v_z'^2}$ during the growing period.

For the budget of $\overline{v_z'^2}$ at the saturating period as shown in Figure 3.56, the production and pressure strain keeps decaying while the dissipation term remains almost unchanged. RHS has a negative value inside the vortex core which corresponds to the decay of $\overline{v_z'^2}$.

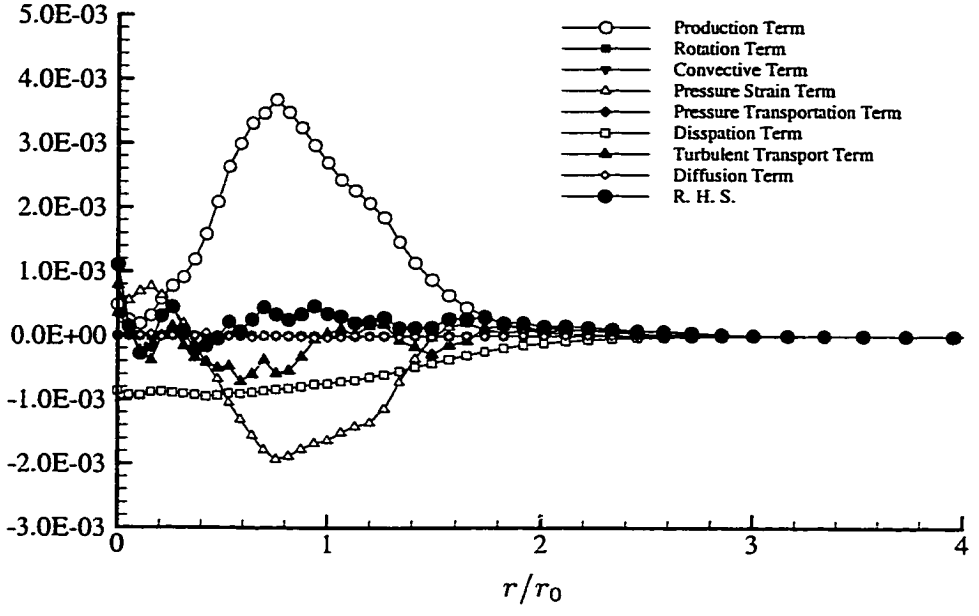

Figure 3.55 Budget for the transport equation of $\overline{v_z'^2}$ at $t = 2.380T$.

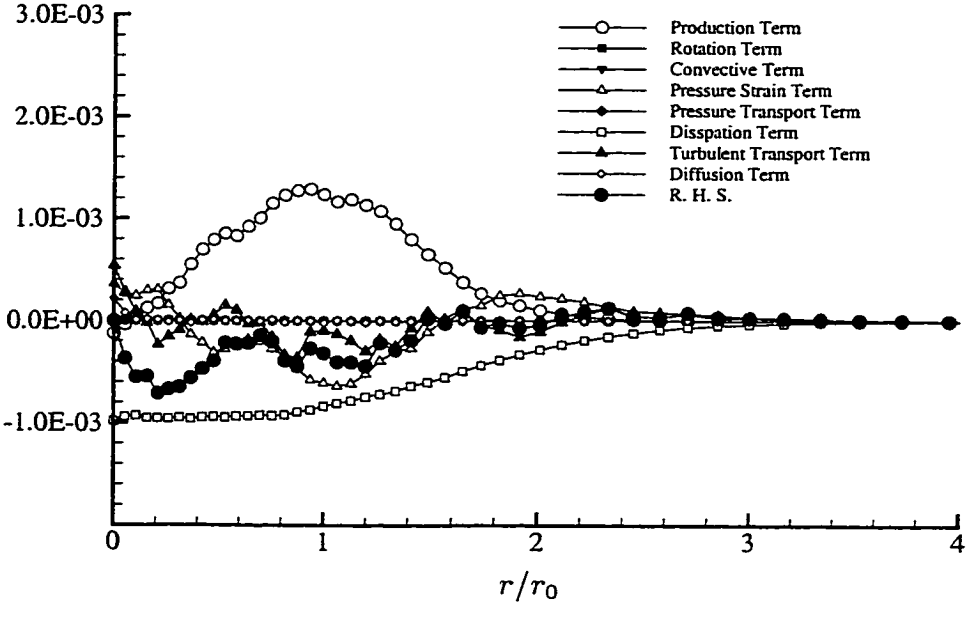

Figure 3.56 Budget for the transport equation of $\overline{v_z'^2}$ at $t = 3.754T$.

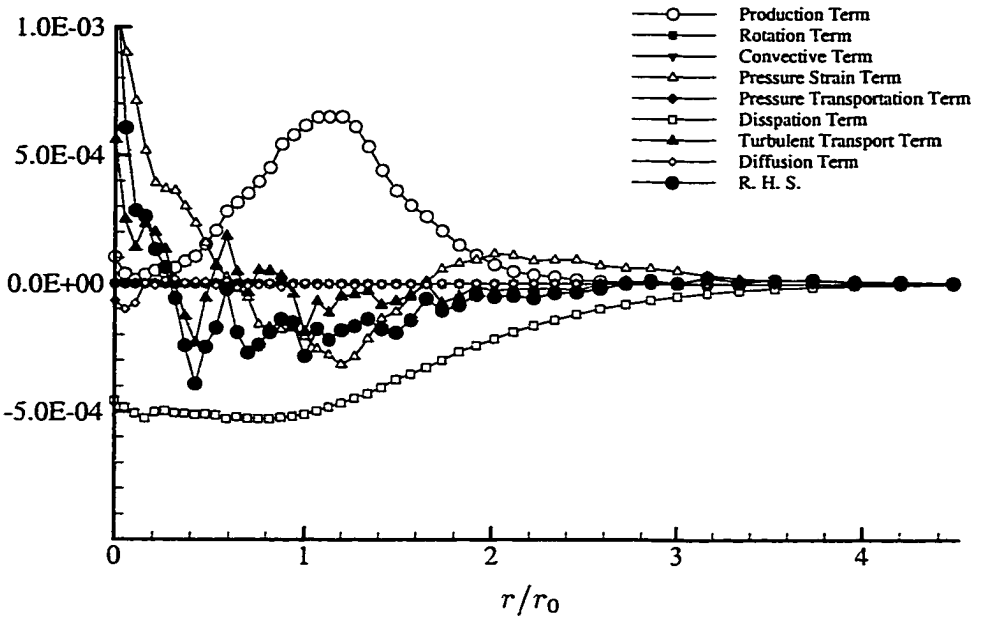

Figure 3.57 Budget for the transport equation of $\overline{v_z'^2}$ at $t = 7.027T$.

Figure 3.57 shows the budget of $\overline{v_z'^2}$ during the relaminarizing period. The magnitude of all of the terms decay at this time, but pressure strain and turbulent transport peak at the vortex center resulting in RHS having a positive peak at the vortex center. The positive pressure strain term takes energy from the component $\overline{v_r'^2}$. This is why at $t = 7.027T$, Reynolds stress component $\overline{v_z'^2}$ display growth rather than decay at the location of the vortex center.

3.5.5 Budgets of $\overline{v_r'v_\theta'}$

The budgets of the Reynolds stress $\overline{v_r'v_\theta'}$ during the different periods are shown in Figures 3.58 to 3.62. During the transition period shown in Figure 3.58, the production term is positive but not a dominant term. The convective term and rotation term have a negative peak at the location $r = 0.6r_0$ and the pressure strain has a positive peak at the same location. On other hand, the pressure transport term has a negative value in the regions near the center and the edge of vortex core and a positive value occurring in an annular region at $r = r_0$. Overall, RHS has a slight peak at $r = 0.6r_0$, but a small positive value which results in $\overline{v_r'v_\theta'}$ having a smaller magnitude than $\overline{v_r'v_z'}$.

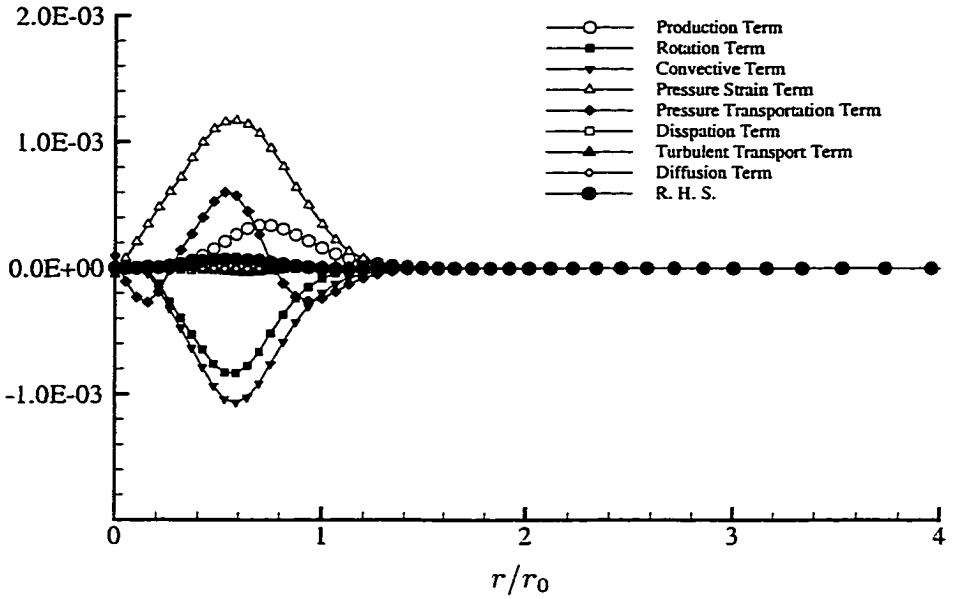

Figure 3.58 Budget for the transport equation of $\overline{v_r' v_\theta'}$ at $t = 0.638T$.

Figure 3.59 shows the budget of $\overline{v_r' v_\theta'}$ during the linearly unstable period. Like the other component, the magnitude of all of the terms shows a significant growth. The peaks of production, pressure strain, convective, and rotation terms slowly move towards the edge of the vortex core. The negative pressure transport near the region of the center of the vortex core disappears. Also, the turbulent transport term grows to a notable value. Overall, RHS has a negative value inside the vortex core and changes to a positive value outside the vortex core. Therefore, the Reynolds stress component $\overline{v_r' v_\theta'}$ in Figure 3.25 decays inside the vortex core and grows outside the vortex core from the linearly unstable period to growing period.

During the growing period shown in Figure 3.60, the pressure strain, convective term, and rotation term drop dramatically. The magnitude of the production term remains almost unchanged, but its peak moves to the region near the edge of the vortex core. The production term and pressure strain term also have a negative region near the center of the vortex core. The negative peak of RHS moves to the region near the edge of the vortex core and the positive peak moves to the location at $r = 2.0r_0$.

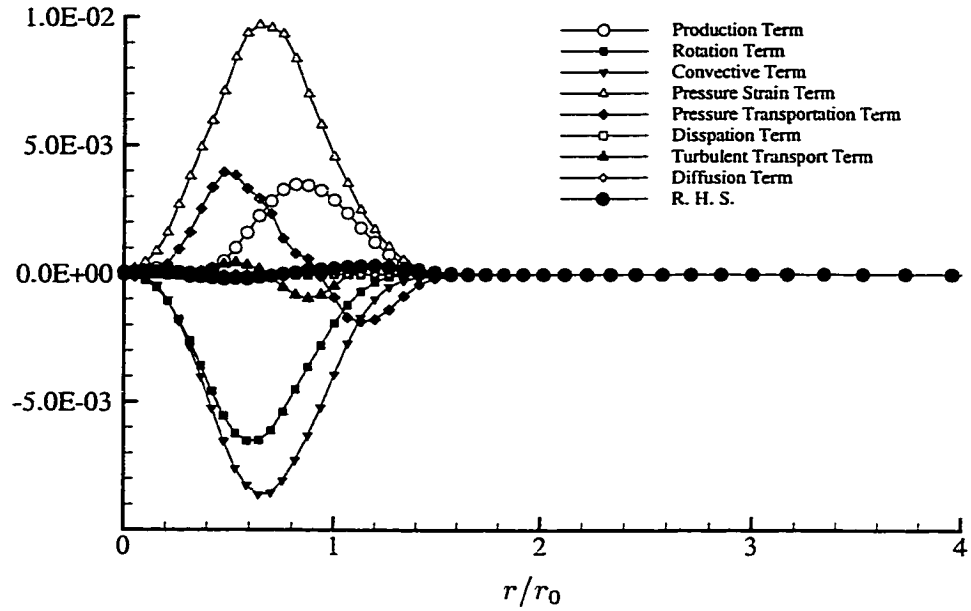

Figure 3.59 Budget for the transport equation of $\overline{v_r' v_\theta'}$ at $t = 1.138T$.

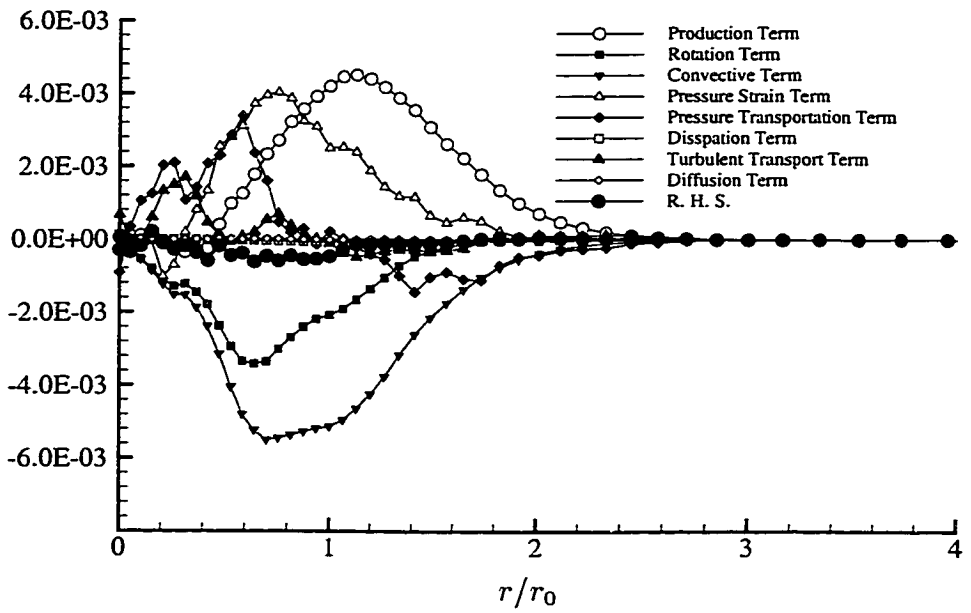

Figure 3.60 Budget for the transport equation of $\overline{v_r' v_\theta'}$ at $t = 2.380T$.

Figure 3.61 shows the budget of $\overline{v_r' v_\theta'}$ during the saturating period. Like the budget of other components, the magnitude of all of the terms decays. The pressure strain and pressure transport term show an oscillating behavior and they have the opposite signs.

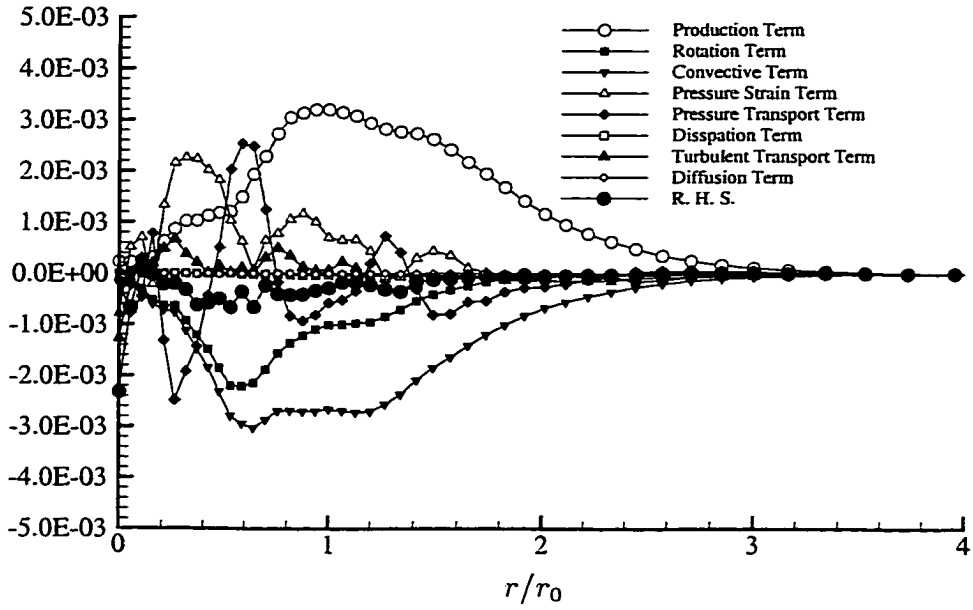

Figure 3.61 Budget for the transport equation of $\overline{v_r' v_\theta'}$ at $t = 3.754T$.

For the budget of $\overline{v_r' v_\theta'}$ during the relaminarizing period shown in Figure 3.62, the peak of the production term moves back inside the vortex core. Unlike the budget of other periods, both the production term and convective term decay very slowly outside the vortex core. The pressure strain term and pressure transport term maintain the opposite peaks respectively inside the vortex core, but they quickly die outside of the vortex core. The slow decay of the production term causes the peak of the Reynolds stress component $\overline{v_r' v_\theta'}$ to move towards the outside rather than showing a simple decay as the other components. In contrast to the budgets of the normal Reynolds stress components, the contribution of the turbulent transport term to RHS is minor. In addition, like the budget of $\overline{v_r' v_z'}$, the dissipation term and the viscous term is negligible during the entire period of the vortex development.

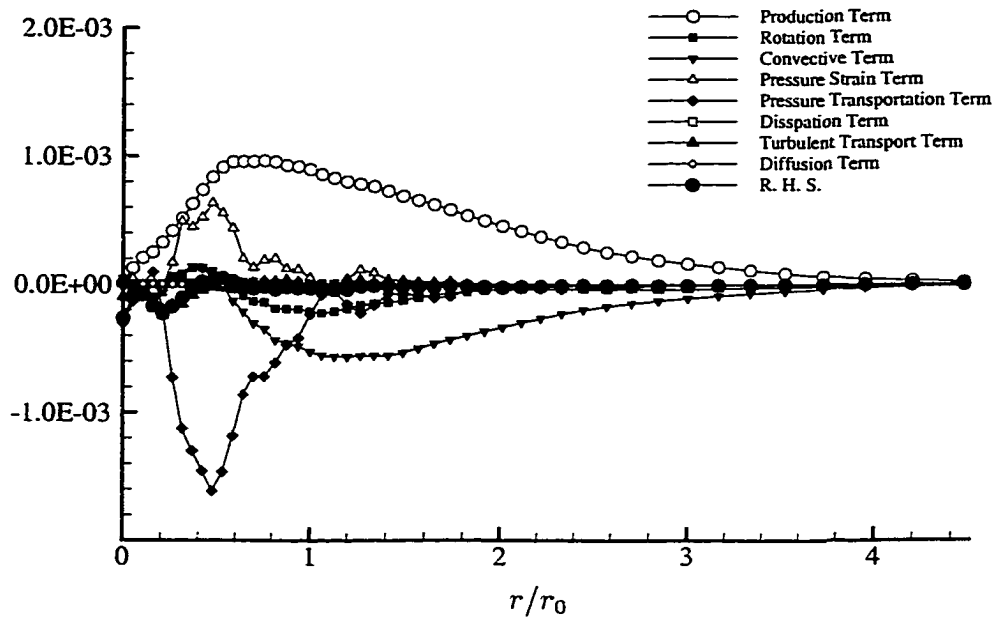

Figure 3.62 Budget for the transport equation of $\overline{v_r' v_\theta'}$ at $t = 7.027T$.

3.5.6 Budgets of $\overline{v_r' v_z'}$

The budgets of shear stress component $\overline{v_r' v_z'}$ are shown in Figures 3.63 to 3.67. During the transition period shown in Figure 3.63, the production term is the dominant term. The pressure strain term and pressure transport term show a complicated behavior. The pressure strain shows an alternating sign from the center region of the vortex to the region near the edge of the vortex core, so does the pressure transport term but with opposite sign. The rotation term and convective term make minor contribution to RHS. The dissipation term is negligible at this point.

Figure 3.64 shows the budget of $\overline{v_r' v_z'}$ during the linearly unstable period. The magnitude of all of the terms except the dissipation term and the viscous diffusion term increases significantly. The region with negative pressure strain disappears, but the pressure transport term remains the feature unchanged. The rotation term, convective term, and turbulent transport term show a notable growth. RHS is nearly a constant due to the behavior of the pressure transport term.

During the growing period shown in Figure 3.65, the production, rotation, and convective terms remain slowly growing, but the magnitude of the pressure strain and pressure transport terms show a slow decay. The interesting feature is that both the

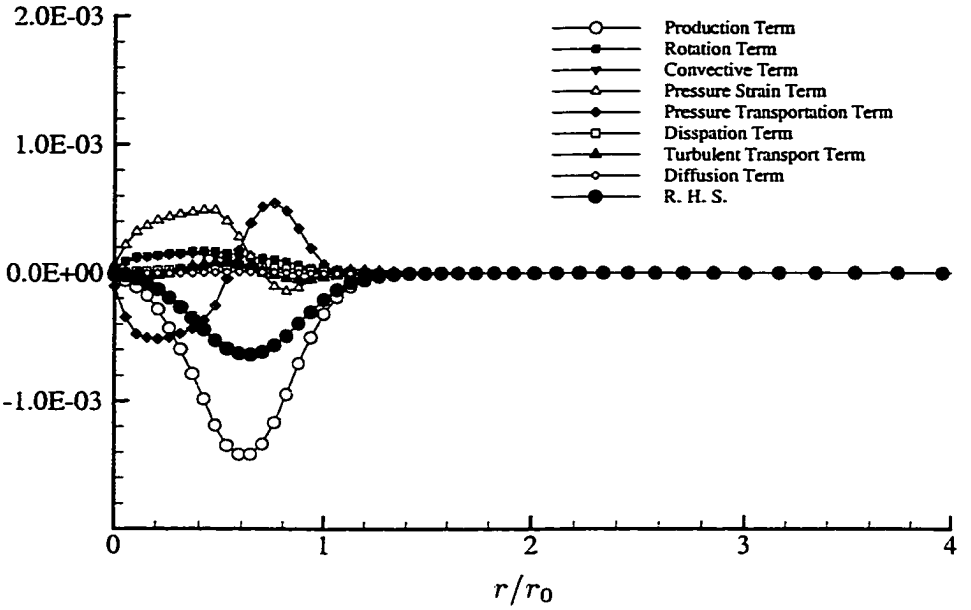

Figure 3.63 Budget for the transport equation of $\overline{v_r' v_z'}$ at $t = 0.637T$.

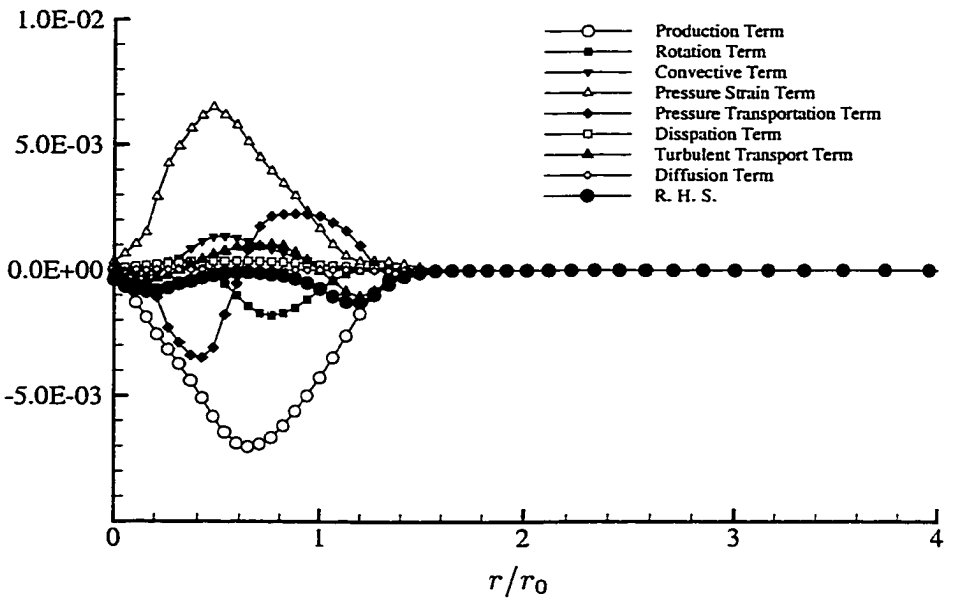

Figure 3.64 Budget for the transport equation of $\overline{v_r' v_z'}$ at $t = 1.138T$.

pressure strain and pressure transport terms form a peak near $r = 0.5r_0$, but with opposite sign. In addition, unlike the phenomena in the budget of all the normal Reynolds stresses, the contributions of the turbulent transport and dissipation terms are negligible. Overall, RHS has a positive value inside the vortex core and changes to a negative value outside the vortex core. Therefore, the Reynolds stress $\overline{v_r' v_z'}$ during the growing period, as shown in Figure 3.26, shows decay inside the vortex core and a grow outside the vortex core.

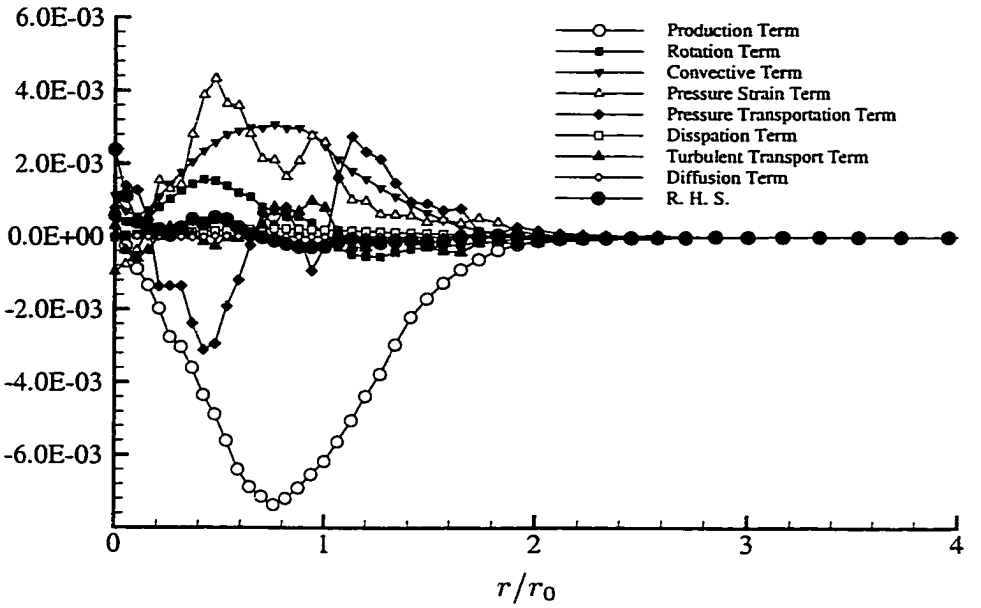

Figure 3.65 Budget for the transport equation of $\overline{v_r' v_z'}$ at $t = 3.754T$.

When the flow reaches the saturating period, the magnitude of all of the terms except the turbulent transport term decays as shown in Figure 3.66. Unlike the budgets of all the normal Reynolds stresses, the production term remains the dominant term over most of the region. The peaks of pressure strain and pressure transport move towards the vortex center, but the peaks cancel each other. However, the turbulent transport term forms a small peak near the vortex center ($r = 0.2r_0$), which makes RHS have a positive peak at the corresponding location. It is this fact that causes the Reynolds stress component $\overline{v_r' v_z'}$ to change sign near the vortex center at the later time shown in Figure 3.26.

During the relaminarizing period, the magnitude of all of the terms shows a significant decay as shown in Figure 3.67. It is surprising that the pressure strain and

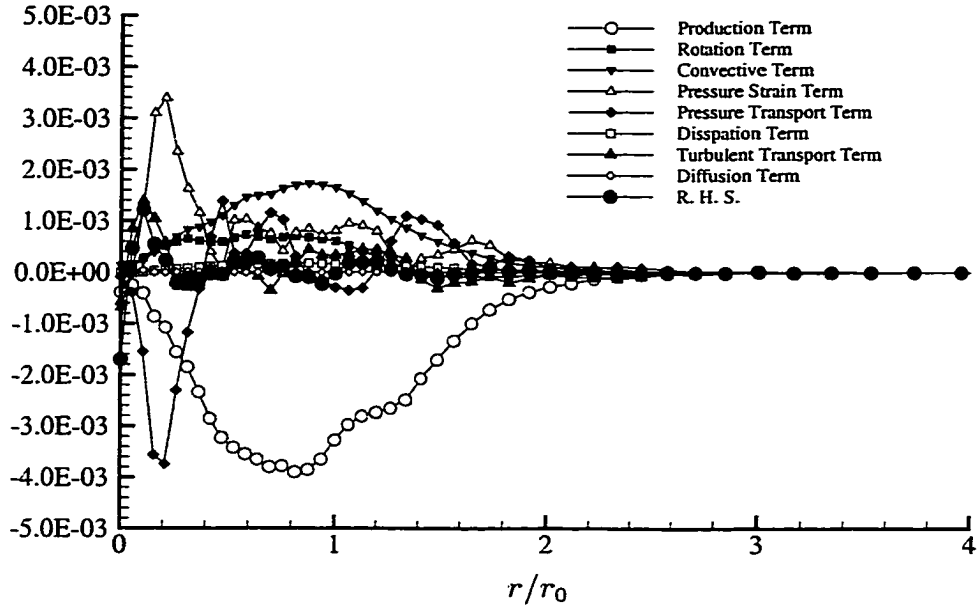

Figure 3.66 Budget for the transport equation of $\overline{v_r' v_z'}$ at $t = 4.999T$.

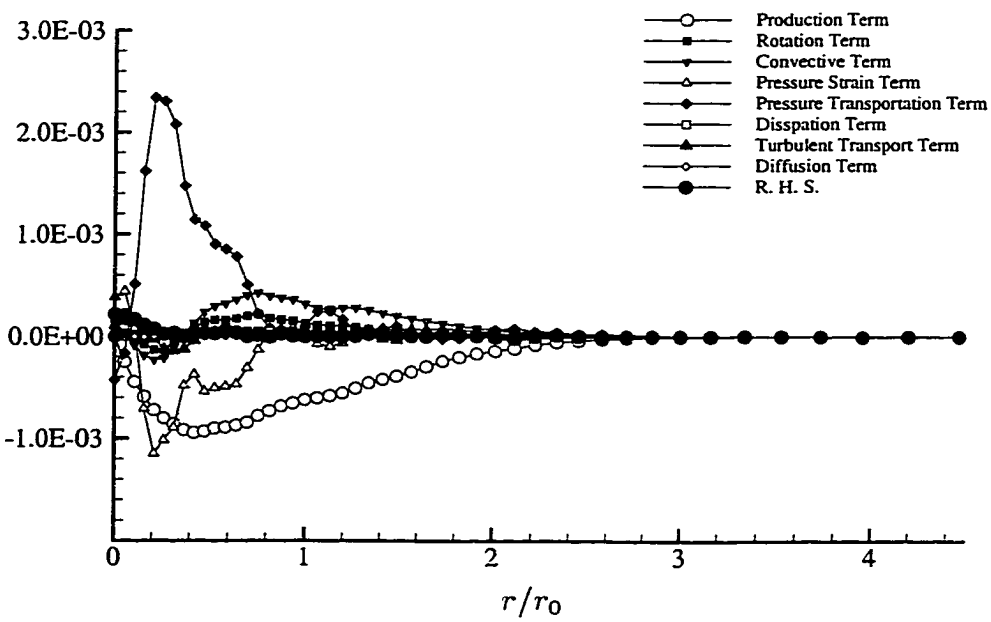

Figure 3.67 Budget for the transport equation of $\overline{v_r' v_z'}$ at $t = 7.027T$.

pressure transport terms maintain a peak at the same location, but the signs have changed to relative what they were previous. In addition, they quickly die out outside the vortex core. It is also notable that the viscous term is not the only negligible term as was the case with the budget of all the normal Reynolds stresses, but also the dissipation term is negligible during the entire development period.

3.5.7 Budgets of $\overline{v'_\theta v'_z}$

Figures 3.68 to 3.72 show the budgets of $\overline{v'_\theta v'_z}$ during the different periods. With the axisymmetry of the isolated vortex and neglecting the effect of compressibility at low Mach number, the pressure transport term is identically zero. As with the other Reynolds shere stress components, $\overline{v'_r v'_\theta}$ and $\overline{v'_\theta v'_z}$, the pressure strain term plays an important role in the budget of $\overline{v'_\theta v'_z}$, but it appears with opposite sign. During the transition period shown in Figure 3.68, the production term also has a negative value. The convective term and the rotation term make major contributions to RHS. RHS shows a peak at $r = 0.5r_0$ which results in $\overline{v'_\theta v'_z}$ developing a peak at the location at early times.

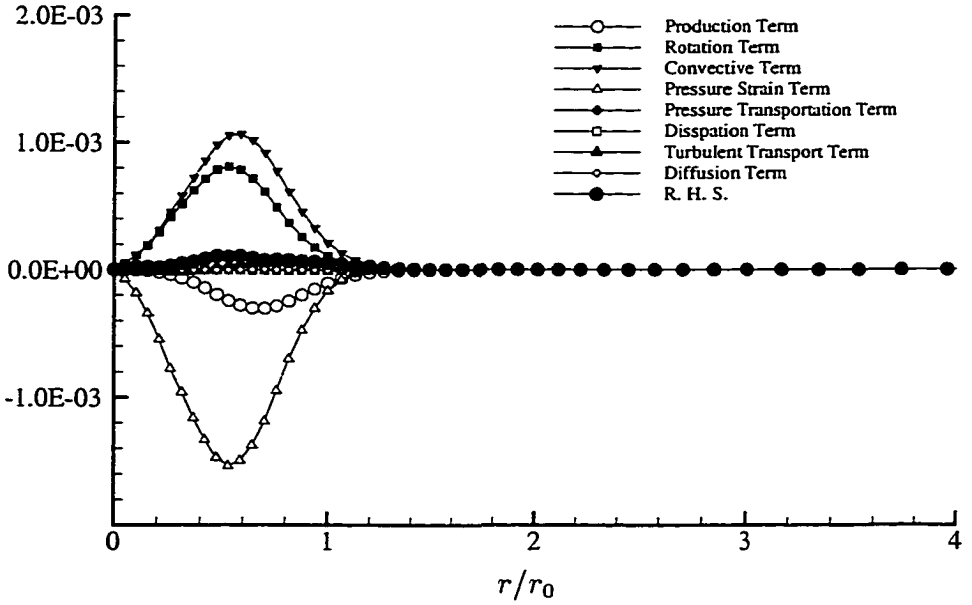

Figure 3.68 Budget for the transport equation of $\overline{v'_\theta v'_z}$ at $t = 0.637T$.

Like the budgets of the other components during the linearly unstable period shown in Figure 3.69, the magnitude of all of the terms shows a significant growth, especially the turbulent transport term which grows to a notable level. The surprising feature is that RHS is negative in the region near the center of vortex core which results in the Reynolds stress $\overline{v'_\theta v'_z}$ having a different sign at the corresponding location during this period.

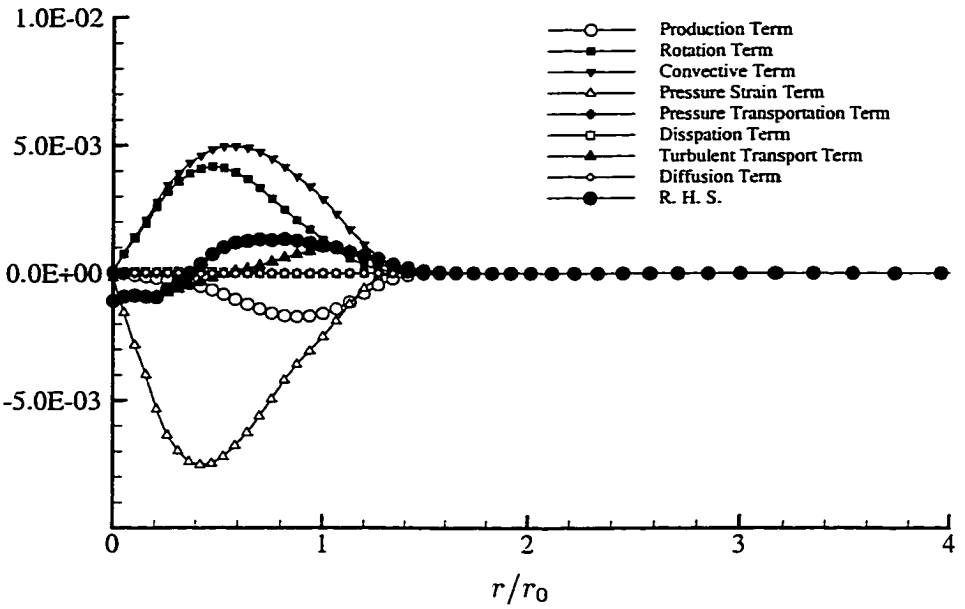

Figure 3.69 Budget for the transport equation of $\overline{v'_\theta v'_z}$ at $t = 1.186T$.

During the growing period shown in Figure 3.70, the pressure strain term, convective term, and rotation term show a decay, but the production term and turbulent transport term remains at the same level. The interesting feature is that at this time the source terms, the convective term and rotation term, are balanced by the pressure strain term and the production term. RHS is very close to the turbulent transport term. The decay of $\overline{v'_\theta v'_z}$ in the region near center at $t = 2.38T$ is consistent with the negative RHS occurring in the same region.

During the saturating period shown in 3.71, the magnitudes of all the terms show a decay, the peaks of the convective term and rotation term almost disappear. Production has a positive region near the vortex center. The balance among the pressure

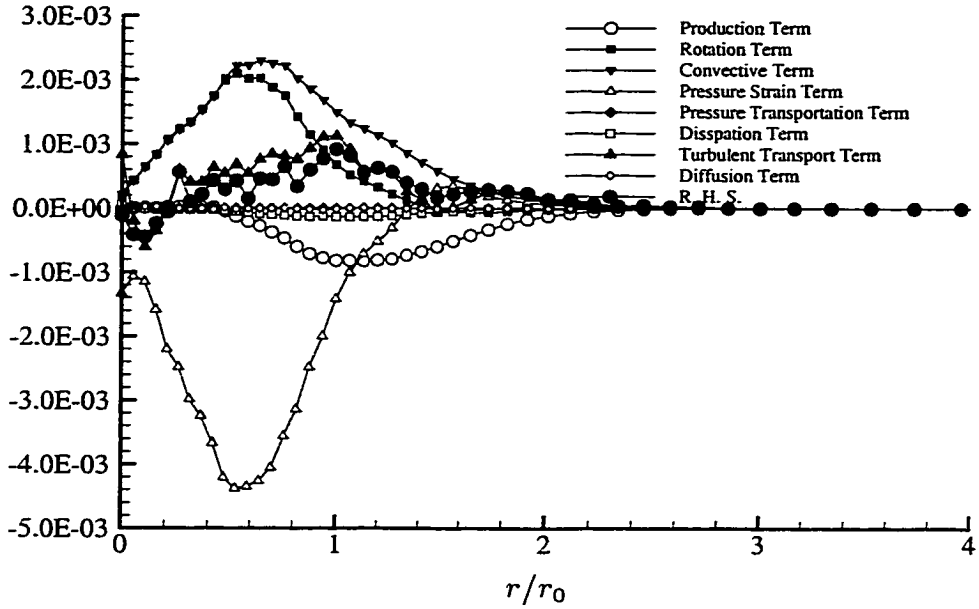

Figure 3.70 Budget for the transport equation of $\overline{v'_\theta v'_z}$ at $t = 2.380T$.

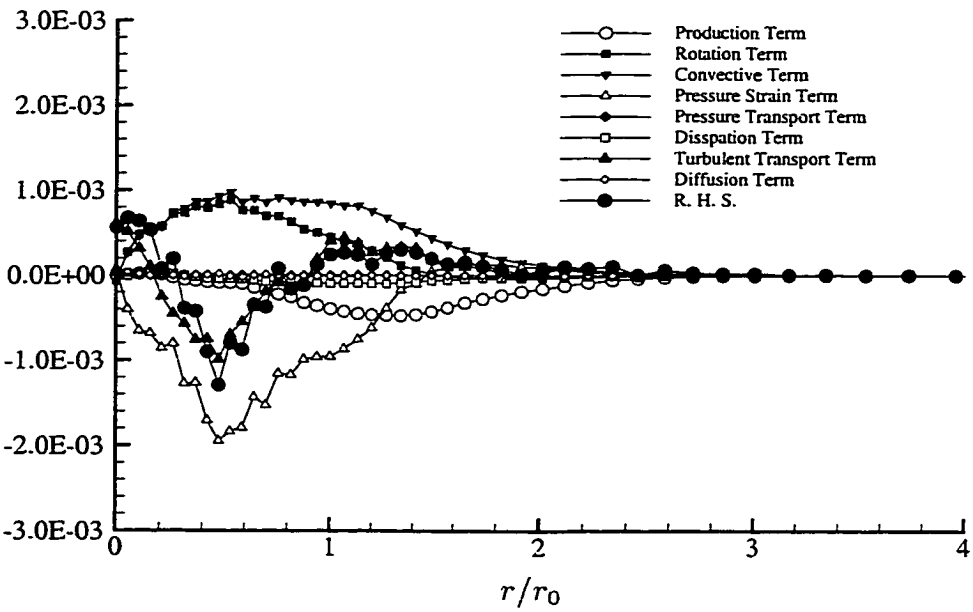

Figure 3.71 Budget for the transport equation of $\overline{v'_\theta v'_z}$ at $t = 3.754T$.

term, the production term, convective term and rotation term remains. The turbulent transport term changes to be negative so that the magnitude of $\overline{v'_\theta v'_z}$ starts to decay from the growing period to the saturating period.

As shown in Figure 3.72, the budget of $\overline{v'_r v'_\theta}$ only shows some quantitative changes rather than any qualitative change. Corresponding to a slow decay of $\overline{v'_\theta v'_z}$, RHS has a small negative value.

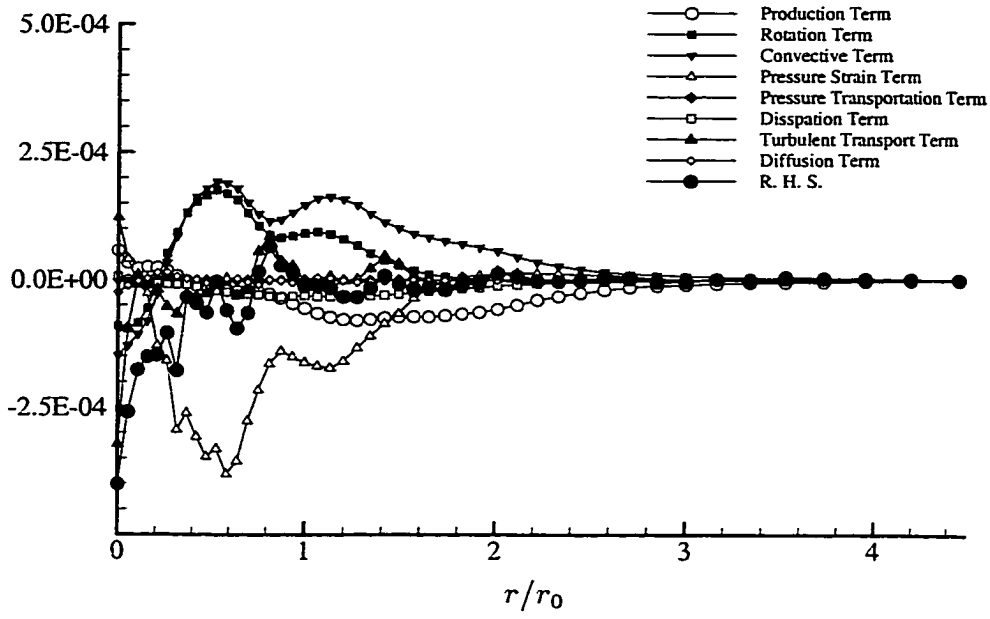

Figure 3.72 Budget for the transport equation of $\overline{v'_\theta v'_z}$ at $t = 7.027T$.

3.6 Large-scale structures

From Eqs (3.1) and (3.2), we note that, in the absence of any disturbance, the isovorticity surfaces are concentric cylindrical shells, and the maximum vorticity occurs at $r = 0$. Figure 3.73 shows the isovorticity surface and vorticity contours in an x-y cross plane at t = 1.05T. The mean axial flow is from the lower left corner to the upper right corner of the figure. Looking downstream, one would see counter-clockwise swirling helical vortices, similar to the instability waves from linear stability analysis. Vortex sheets appear to be branching out of the core. In the 2-D contour plot, we observe that most of the disturbances are concentrated outside the core in the form of spiral filaments of high vorticity. Also seen are high-order azimuthal modes.

This large scale structure is quenched when the flow is stabilized with the decay of the axial velocity deficit as shown in Figure 3.74. In the 2-D contour plot of Figure 3.74, we observe that the core tends to regain its laminar structure. The relaminarizing tendency of the q-vortex has been observed experimentally by Bandyopadhyay et al. (1991) and numerically by Ragab & Sreedhar (1994).

An isosurface of Reynolds stress $\overline{v_r' v_z'}$ is shown in Figure 3.75. The isosurface of Reynolds stress consists of two patterns. One is with $v_r' > 0$ and the other is with $v_r' < 0$. An interesting feature is the isovorticity surface, as shown in Figure 3.76, is just in the middle of the two patterns. So outside fluid with low turbulent kinetic energy is swept inward by helical vortices ($v_r' < 0$) and inner fluid is ejected outward($v_r' < 0$). In Figure 3.77, again the isosurface of vorticity is sandwiched by the isosurface of the production of TKE. Therefore, the helical vortex structures are responsible for the generation of the Reynolds stress.

3.7 Summary of the Isolated Vortex

Direct numerical simulations of an isolated turbulent axial vortex have been performed including an ensemble of simulations for improving the quality of turbulent statistical quantities. The q vortex with a wake-type axial velocity profile is used as a model for an isolated axial vortex . The monotonically increasing initial circulation makes the vortex centrifugally neutrally stable. The presence of the axial velocity deficit causes the instability of an isolated axial vortex. The results show that a linearly unstable axial vortex amplifies the perturbations, resulting in the formation of large-scale helical vortex structures, as seen in the previous simulation of Ragab & Sreedhar (1994). Flow visualization shows that these vortical structures are responsible for the generation of the Reynolds stresses. The decay of the axial velocity deficit results in the centrifugally stabilizing motion of the vortex core taking over the destabilizing effect of the axial velocity. The vortex returns eventually toward a laminar state, but with a weakened axial velocity deficit.

The development of the isolated vortex can be divided into five periods by the behavior of the global TKE. After a short transition period, the global TKE grows exponentially. The growth rate decreases gradually during the growing period with the decay of the axial velocity deficit. Then, it tends to a saturated state when the swirl number q falls the range of $1.45 \sim 1.55$ which agrees well with linear stability

Figure 3.73 Isovorticity surface ($\Omega_{magn}/(V_0/r_0) = 1.0$) and vorticity contours in middle cross plane for Case A at t = 1.05T.

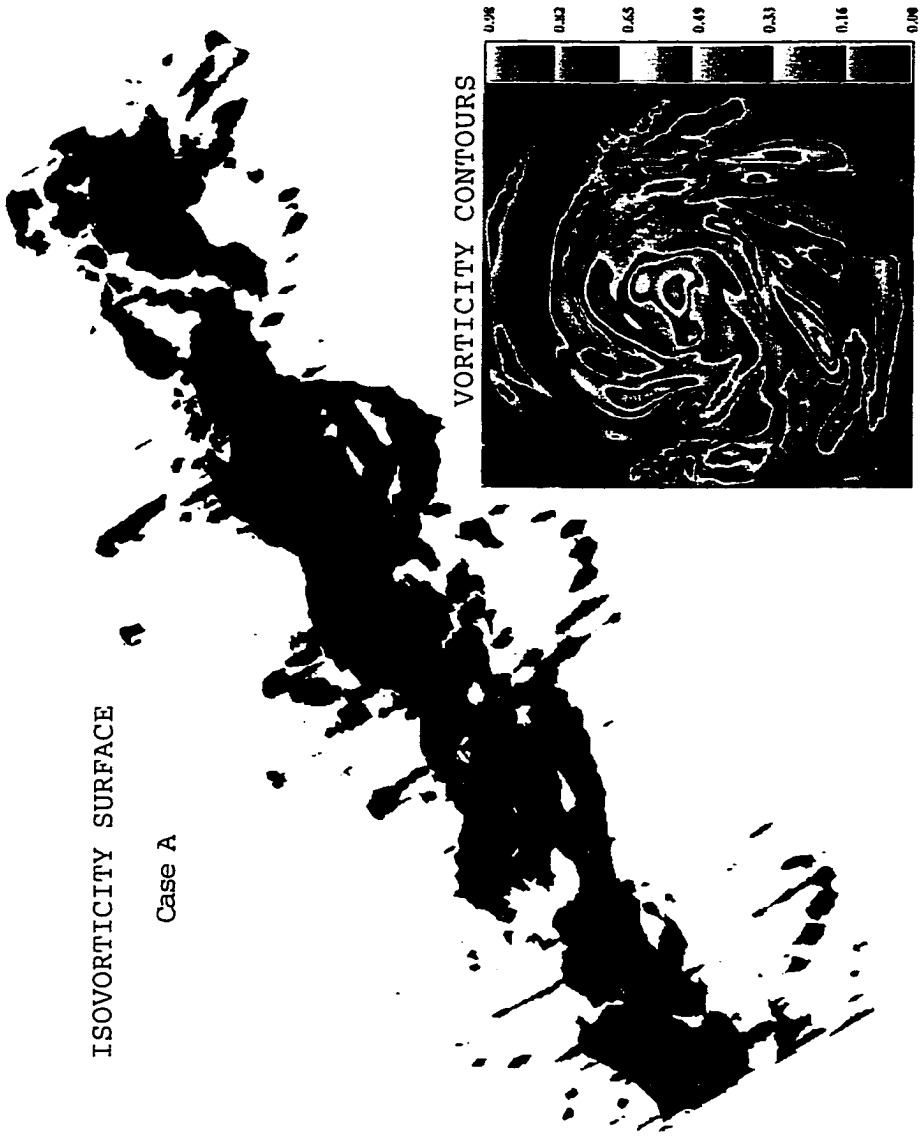

Figure 3.74 Isovorticity surface ($\Omega_{magn}/(V_0/r_0) = 0.6$) and vorticity contours in middle cross plane for Case A at t = 6.95T.

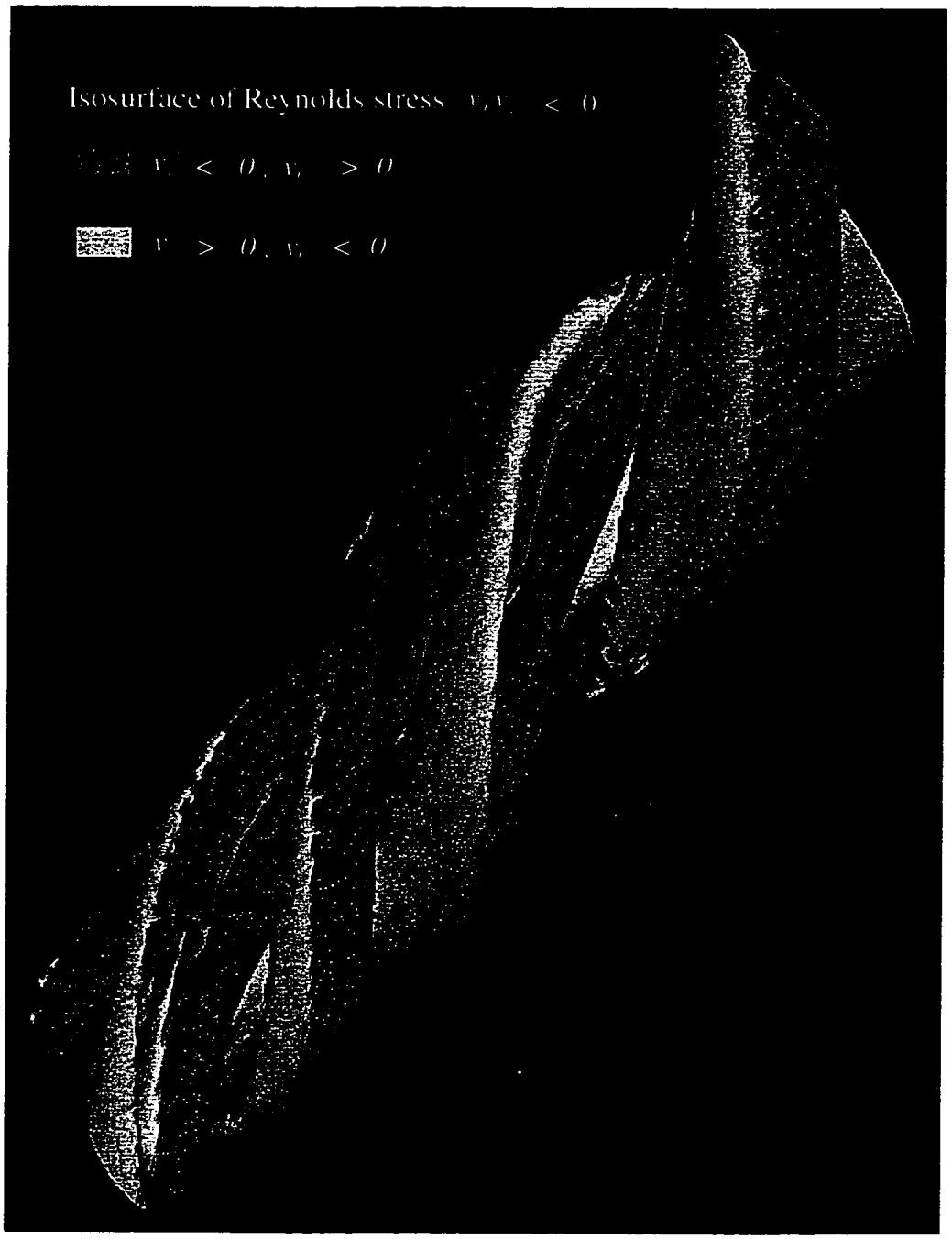

Figure 3.75 Isosurface of Reynolds stress for Case A ($v_r'v_z'/V_0^2 = -2.0 \times 10^{-3}$).

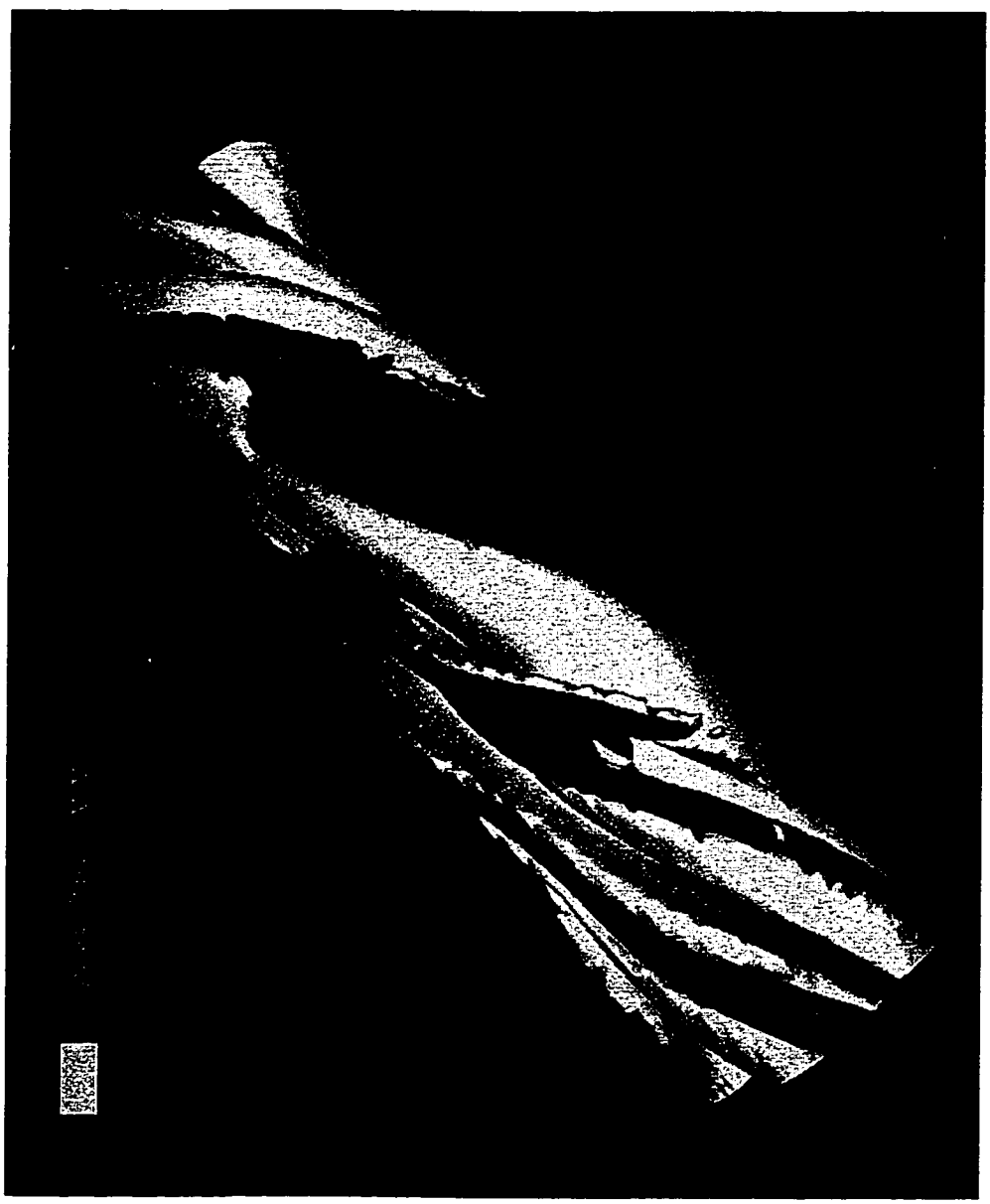

Figure 3.76 Isosurfaces of vorticity and Reynolds stress for Case A.

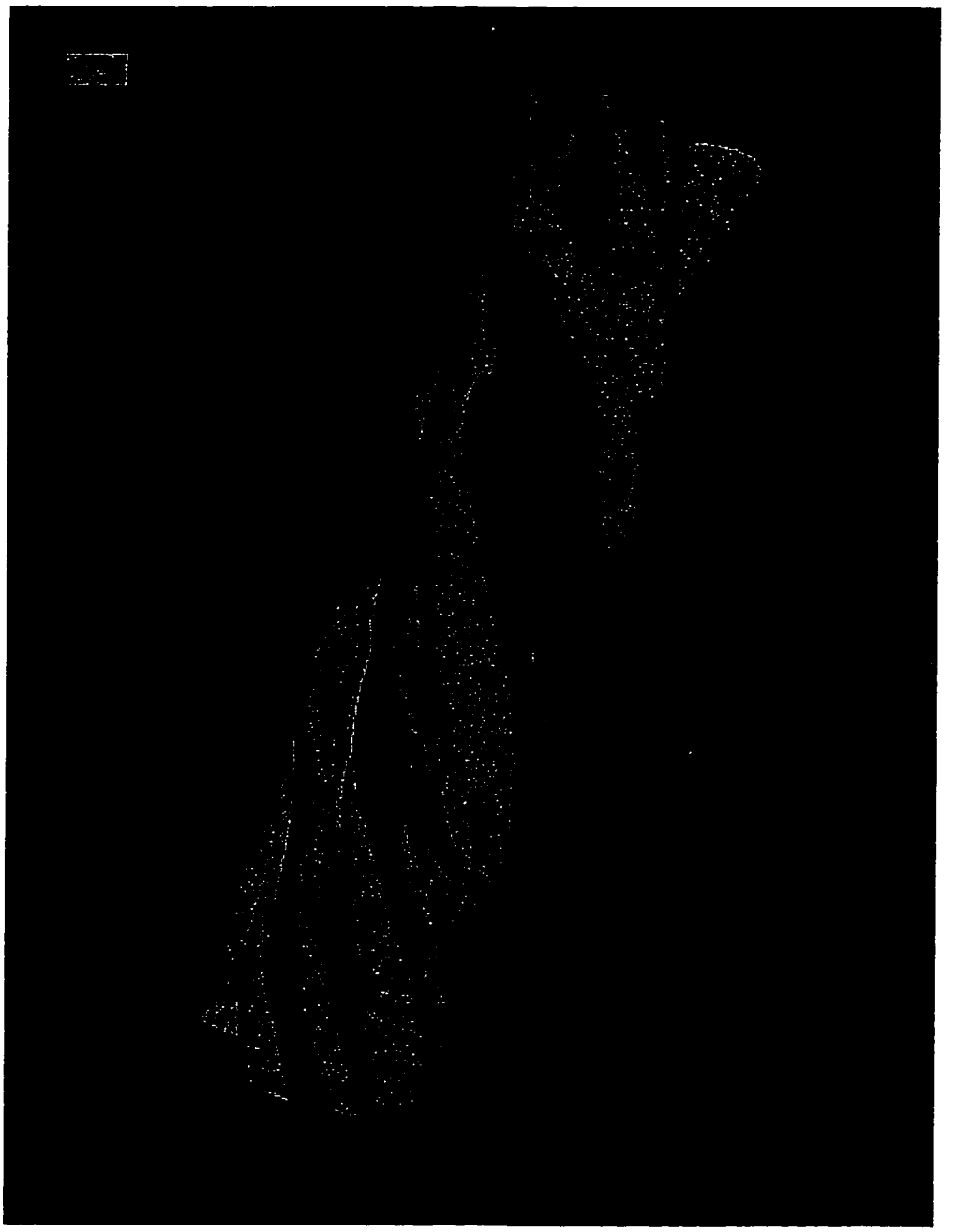

Figure 3.77 Isosurfaces of vorticity and production of TKE for Case *A*.

theory (Leibovich & Stewartson 1983, Lessen et al. 1974). Eventually, a period of slow decay prevails and the vortex tends to regains its laminar structure.

During the period of amplification and decay of disturbances, the mean axial velocity profile shows a decrease in the velocity deficit. However, the mean tangential velocity profile exhibits anti-diffusion in the region in the vortex core. This is associated with a negative eddy viscosity coefficient that develops near the center of the vortex. Also, the circulation profile shows a slight overshoot during the period of decay.

During the unstable periods, the normal Reynolds stresses develop a peak in an annular region, which moves to the edge of the vortex core, but then eventually moves back to the center of the vortex core when the vortex stabilizing motion becomes dominant. These behaviors also have been observed in experiments by Phillips & Graham (1984) and Chow & Zilliac (1994). The production from $\overline{v_r' v_\theta'}$ causes the anisotropy of the normal stresses, $\overline{v_r'^2} > \overline{v_\theta'^2}$. However, when the vortex reaches the relaminarizing period, shear stress components show quite different behaviors. The peaks do not move back to the center of the vortex core. Instead, the peaks of $\overline{v_r' v_z'}$ and $\overline{v_\theta' v_z'}$ stay near the edge of the vortex and the peak in $\overline{v_r' v_\theta'}$ moves to the location of circulation overshoot which also has been observed by Phillips & Graham (1984). With the decay of $\overline{v_r' v_\theta'}$, the normal stresses tends to be isotropic.

From the analysis of the Reynolds stress budgets, it is clear that not only the production term plays an important role in the complicated behavior of the Reynolds stresses, but also the pressure strain term, the pressure transport term, and the turbulent transport term make a large contribution to the profiles of Reynolds stress. The interesting feature is that although the pressure transport term and turbulence transport term in the normal Reynolds stress components show an oscillating behavior, they always have opposite sign. Particularly, those two terms in the TKE equation almost cancel each other. This is valuable information for studying turbulence modeling of the vortex or other rotating flows because it is almost impossible to model those two term individually. The pressure strain term is the key factor that makes the peaks of the Reynolds stress components occurring in an annual region near the edge of the vortex during the unstable periods and cause them to move back to the center of the vortex core when the vortex is stabilized.

4. A B - SPLINE SPECTRAL METHOD

4.1 Introduction

As mentioned in Chapter 3, the direct numerical simulations (DNS) of an isolated vortex are implemented using a pseudo-spectral Fourier collocation method. The computer code was originally developed for compressible homogeneous turbulence. Even though the dual Cain's mapping scheme eliminates the influence of image flows, so that the simulations of an isolated vortex can be completed, for the vortex problem there are still several disadvantages of the code. For most of the simulations using 128 grid points in the x and y directions (see Table 3.1), only 30% of the points lie within the turbulent region that is within three core radii of the vortex center, as was shown in Chapter 3. Thus, the majority of the grid points are wasted. Also, the infinite physical domain is not suited to the strained vortex problem since there are stagnation points occurring in the computational domain and the compressible formulation does not allow a steady strain field to be imposed. Therefore, a numerical method that allows for the simulation of a finite physical domain is desirable.

A new numerical method which is used to solve the incompressible Navier-Stokes equations in cylindrical coordinates has been developed by Loulou (1996). A Fourier spectral method is used in the homogeneous streamwise and azimuthal directions, while in the radial direction a new method based on B-splines is employed. This method is much better suited to simulating an axial vortex with strain because a vortex in an infinite flow can be simulated in a finite domain size.

The original sequential code was run on a Cray C90 and was used to simulate turbulent flow in a pipe. Appropriate boundary conditions have been developed for simulating the vortex problem. Also, in order to run the code on parallel computers that provide larger memory and higher speed, the original B-spline code has been parallelized in this work. The MPI message passing library was used so that the program is portable to any parallel machine. The new parallel B-spline code will be a powerful tool for simulating other turbulent flows such as a jet or a wake. The work

to develop the parallel B-spline code was completed on an IBM SP2 at the Purdue University Computer Center.

The B-spline method has been well documented in Loulou (1996). A brief description of the methodology is described below.

4.2 Governing Equations

The incompressible Navier-Stokes equations can be written as

$$\frac{\partial \mathbf{u}}{\partial t} - \mathbf{u} \times \omega = - \nabla P + \frac{1}{Re} \triangle \mathbf{u} \tag{4.1}$$

$$\nabla \cdot \mathbf{u} = 0 \ , \tag{4.2}$$

where $\mathbf{u}$ is the velocity vector and ω is the vorticity. The modified pressure P is given by

$$P = \frac{p}{\rho} + \frac{1}{2}\mathbf{u} \cdot \mathbf{u} \, , \tag{4.3}$$

where p is the pressure and ρ is the density. All quantities have been normalized using the radius of the domain R as the length scale, and the initial axial velocity deficit

$$V_0 = V_z(r)|_{r=\infty} - V_z(r)\Big|_{r=0} \, , \tag{4.4}$$

as the velocity scale, where $V_z(r)$ is mean axial velocity. So, the Reynolds number in Equation (4.1) is given by

$$Re = \frac{V_0 R}{\nu} \, , \tag{4.5}$$

where R is the radius of the computational domain as shown in Figure 4.1.

4.3 Numerical Method

4.3.1 Weak form

Let $\mathbf{v}$ be our numerical approximation to $\mathbf{u}$. With the continuity constraint, there are only two independent components of the velocity vector so that $\mathbf{v}$ can be represented in terms of two distinct classes of divergence free vectors. In this work, since the streamwise direction is assumed to be homogeneous and the azimuthal direction is naturally periodic, the representation of $\mathbf{v}$ is given by

$$\mathbf{v}(r,\theta,z,t) = \sum_j \sum_m \sum_l \left[\alpha^+_{jml}(t) \mathbf{q}^+_l(r,\theta,z;k_\theta,k_z) + \alpha^-_{jml}(t) \mathbf{q}^-_l(r,\theta,z;k_\theta,k_z) \right] \ , \tag{4.6}$$

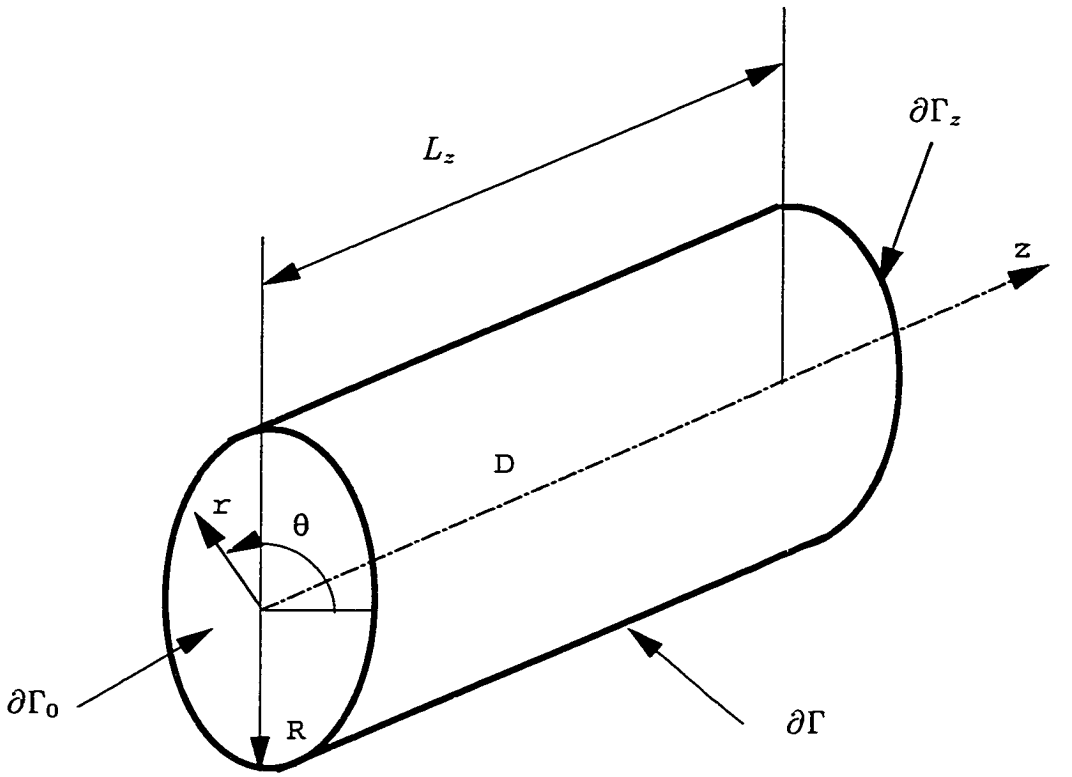

Figure 4.1 The coordinate systems and the computational domain.

where $\alpha^{\pm}$ are the expansion coefficients, the streamwise wavenumber k_z and the azimuthal wavenumber k_θ are defined as

$$k_z = \frac{2\pi m}{L_z}, \quad -N_z/2 \leq m \leq N_z/2 - 1\,, \tag{4.7}$$

and

$$k_\theta = j\,, \quad -N_\theta/2 \leq k_\theta \leq N_\theta/2 - 1\,. \tag{4.8}$$

The method of divergence-free expansions was developed by Leonard & Wray (1982). The expansion vectors $\mathbf{q}^{\pm}(r, \theta, z; k_\theta, k_z)$ belong to the function space $\mathcal{V}$ defined as

$$\mathcal{V} = \{\mathbf{q} : \mathbf{q} = (\mathbf{H}^1(D))^3, \nabla \cdot \mathbf{q} = 0\}\,, \tag{4.9}$$

where D is an open set in $\mathcal{R}^3$ with boundary $\partial\Gamma$, and $(\mathbf{H}^1(D))^3$ is the Hilbert space (Loulou 1996).

Furthermore, let two distinct classes of vector weight functions $\xi^{\pm}(r, , \theta, z; k_\theta, k_z)$ belong to the space $\mathcal{W}$ defined as

$$\mathcal{W} = \{\xi \,:\, \xi = (\mathbf{H}^1(D))^3,\ \nabla \cdot \xi = 0,\ \xi = 0 \text{ on } \partial\Gamma\}\,, \tag{4.10}$$

where $\partial\Gamma$ represents the surface $r = R$ as shown in Figure 4.1.

Substituting $\mathbf{v}$ for $\mathbf{u}$ in Equation (4.1) and following the standard weighted residual technique, we can obtain a weak form of the Navier-Stokes Equations,

$$\left(\xi^{\pm}, \frac{\partial v}{\partial t}\right) + \left(\xi^{\pm}, \nabla P\right) = \left(\xi^{\pm}, (\mathbf{v} \times \omega)\right) + \frac{1}{Re}\left(\xi^{\pm}, (\nabla \cdot \nabla \mathbf{v})\right) , \tag{4.11}$$

where $\omega = \nabla \times \mathbf{v}$ and the inner product is defined as

$$(\mathbf{a}, \mathbf{b}) = \int_D \mathbf{a} \cdot \mathbf{b}\, dV \ . \tag{4.12}$$

The pressure term can be eliminated from Equation (4.11) by a further simplification. First, the pressure term can be rewritten as

$$\int_D \xi^{\pm} \cdot \nabla P\, dV = \int_D \nabla \cdot (P\xi^{\pm})\, dV - \int_D P \nabla \cdot \xi^{\pm}\, dV \ . \tag{4.13}$$

Then, applying the divergence theorem and using the property of the weight functions, $\nabla \cdot \xi^{\pm} = 0$ on ∂D, we have

$$\int_D P \nabla \cdot \xi^{\pm} dV = \int_{\partial\Gamma} P\xi \cdot \mathbf{n}\, dA \ , \tag{4.14}$$

where $\mathbf{n}$ is the unit normal vector. From the assumption of homogeneous flow in the streamwise direction at the beginning of this section, any surface integral on $\partial\Gamma_0 \cup \partial\Gamma_{L_z}$ vanishes with the periodicity of all variables in the streamwise direction. Therefore, only the integral on $\partial\Gamma$ remains

$$\int_D \xi^{\pm} \cdot \nabla P dV = \int_{\partial\Gamma} P\xi \cdot \mathbf{e}_r dA \ . \tag{4.15}$$

Since weight vectors $\xi^{\pm}$ are homogeneous, $\xi^{\pm} = \Gamma$ on ∂D, we can eliminate the pressure term from the weak formulation in Equation (4.11) to obtain

$$\left(\xi^{\pm}, \frac{\partial \mathbf{v}}{\partial t}\right) = \left(\xi^{\pm}, (\mathbf{v} \times \omega)\right) + \frac{1}{Re}\left(\xi^{\pm}, (\nabla \cdot \nabla \mathbf{v})\right) \ . \tag{4.16}$$

This form has the advantage of automatically satisfying the continuity Equation (4.2) and eliminating the pressure term.

4.3.2 Expansion and weight functions

The expansion and weight functions are chosen as follows :

$$\mathbf{q}_l^{\pm}(r, \theta, z; k_\theta, k_z) = \mathbf{u}_l^{\pm}(r, k_\theta, k_z) e^{i(k_\theta \theta + k_z z)} \tag{4.17}$$

Table 4.1 Summary of expansion vectors and weight vectors.

	$k_0 = 0$	$k_0 > 0$
$k_z = 0$	$\mathbf{u}_l^+ = \begin{pmatrix} 0 \\ g_l(r) \\ 0 \end{pmatrix}$, $\mathbf{u}_l^- = \begin{pmatrix} 0 \\ 0 \\ \frac{g_l(r)}{r} \end{pmatrix}$	$\mathbf{u}_l^+ = \begin{pmatrix} -ik_0 g_l(r) \\ (r g_l(r))' \\ 0 \end{pmatrix}$, $\mathbf{u}_l^- = \begin{pmatrix} 0 \\ 0 \\ g_l'(r) + \frac{(1-k_0)}{r} g_l(r) \end{pmatrix}$
	$\mathbf{w}_k^+ = \begin{pmatrix} 0 \\ g_k(r) \\ 0 \end{pmatrix}$, $\mathbf{w}_k^- = \begin{pmatrix} 0 \\ 0 \\ \frac{g_k(r)}{r} \end{pmatrix}$	$\mathbf{w}_k^+ = \begin{pmatrix} ik_0 g_k(r) \\ (r g_k(r))' \\ 0 \end{pmatrix}$, $\mathbf{w}_k^- = \begin{pmatrix} 0 \\ 0 \\ g_k'(r) + \frac{(1-k_0)}{r} g_k(r) \end{pmatrix}$
$k_z \neq 0$	$\mathbf{u}_l^+ = \begin{pmatrix} 0 \\ k_z g_l(r) \\ 0 \end{pmatrix}$, $\mathbf{u}_l^- = \begin{pmatrix} -ik_z g_l(r) \\ k_z g_l(r) \\ g_l'(r) + \frac{g_l(r)}{r} \end{pmatrix}$	$\mathbf{u}_l^+ = k_z \begin{pmatrix} -ik_0 g_l(r) \\ (r g_l(r))' \\ 0 \end{pmatrix}$, $\mathbf{u}_l^- = \begin{pmatrix} -ik_z g_l(r) \\ k_z g_l(r) \\ g_l'(r) + \frac{(1-k_0)}{r} g_l(r) \end{pmatrix}$
	$\mathbf{w}_k^+ = \begin{pmatrix} 0 \\ g_k(r) \\ 0 \end{pmatrix}$, $\mathbf{w}_k^- = \begin{pmatrix} ik_z g_k(r) \\ k_z g_k(r) \\ \frac{g_k(r)}{r} \end{pmatrix}$	$\mathbf{w}_k^+ = k_z \begin{pmatrix} ik_0 g_k(r) \\ (r g_k(r))' \\ 0 \end{pmatrix}$, $\mathbf{w}_k^- = \begin{pmatrix} ik_z g_k(r) \\ k_z g_k(r) \\ g_k'(r) + \frac{(1-k_0)}{r} g_k(r) \end{pmatrix}$

and

$$\xi_k^{\pm}(r,\theta,z;k_\theta,k_z) = \mathbf{w}_k^{\pm}(r,k_\theta,k_z)e^{-i(k_\theta\theta+k_z z)} \tag{4.18}$$

where $\mathbf{u}_l^{\pm}$ are the basis expansion vectors and $\mathbf{w}_k^{\pm}$ are the basis weight vectors.

Within the divergence-free restriction, the choice of the basis expansion vectors $\mathbf{u}_l^{\pm}$ is arbitrary, but in this work there is a certain constraint. The basis expansion vectors must have the proper regularity (Loulou 1996) at the origin so that any quantity evaluated at the origin be bounded and smooth. The problem of how to construct the $\mathbf{u}_l^{\pm}$ has been well documented by Loulou (1996) and Moser, Moin & Leonard (1983) and is not repeated here. The definitions of the basis expansion vectors are listed in Table 4.3.1, where $g_l(r)$ is the B-spline function as described by de Boor (1978) and $g_l'(r)$ is the derivative of $g_l(r)$. Detailed information on the construction of B-splines and their properties is given in Appendix B.

The set of basis weight vectors $\mathbf{w}_k^{\pm}$ is chosen to be the complex conjugate of the set of expansion vectors $\mathbf{u}_l^{\pm}$ as shown in Table 4.3.1, except that in order to satisfy an additional restriction on the weight functions, $\xi_k = 0$ on ∂D. Those vectors having support on the boundaries are eliminated from the set (also see section 4.4).

4.3.3 Velocity and vorticity representation

Substituting Equation (4.17) and the basis vectors in Table 4.3.1 into Equation (4.6) and using the summation convection for repeated indices ($a_l b_l = \sum_{l=1}^{N_r} a_l b_l$), the velocity and vorticity components can be represented as

$$v_r(r,\theta,z,t) = K_l g_l(r) \tag{4.19}$$

$$v_\theta(r,\theta,z,t) = J_l g_l'(r) + I_l g_l(r) \tag{4.20}$$

$$v_z(r,\theta,z,t) = -G_l g_l'(r) - F_l \frac{g_l(r)}{r} \tag{4.21}$$

$$\omega_r(r,\theta,z,t) = A_l g_l(r) + B_l r g_l'(r) + C_l \frac{g_l(r)}{r^2} + D_l \frac{g_l'(r)}{r} \tag{4.22}$$

$$\omega_\theta(r,\theta,z,t) = E_l g_l(r) + F_l \left(\frac{g_l'(r)}{r} - \frac{g_l(r)}{r^2} \right) + G_l g_l''(r) \tag{4.23}$$

$$\omega_z(r,\theta,z,t) = H_l \frac{g_l(r)}{r} + (I_l + 2J_l) g_l'(r) + J_l r g_l''(r) \tag{4.24}$$

where v_r, v_θ and v_z are the velocity components, ω_r, ω_θ and ω_z are the vorticity components, and the coefficients A_l to K_l are defined as

$$A_l(r,\theta,z,t) = \sum_{k_\theta}\sum_{k_z} -ik_z{}^2(\alpha_l^+ + \alpha_l^-)e^{i(k_\theta\theta+k_z z)} \tag{4.25}$$

$$B_l(r,\theta,z,t) = \begin{cases} \sum_{k_\theta}\sum_{k_z} -ik_z{}^2\alpha_l^+ e^{i(k_\theta\theta+k_z z)} & , \quad k_\theta \neq 0 \\ 0 & , \quad k_\theta = 0 \end{cases} \tag{4.26}$$

$$C_l(r,\theta,z,t) = \sum_{k_\theta}\sum_{k_z} -ik_\theta(k_\theta-1)\alpha_l^- e^{i(k_\theta\theta+k_z z)} \tag{4.27}$$

$$D_l(r,\theta,z,t) = \sum_{k_\theta}\sum_{k_z} ik_\theta\alpha_l^- e^{i(k_\theta\theta+k_z z)} \tag{4.28}$$

$$E_l(r,\theta,z,t) = \sum_{k_\theta}\sum_{k_z} k_z{}^2(k_\theta\alpha_l^+ + \alpha_l^-)e^{i(k_\theta\theta+k_z z)} \tag{4.29}$$

$$F_l(r,\theta,z,t) = \sum_{k_\theta}\sum_{k_z}(k_\theta-1)\alpha_l^- e^{i(k_\theta\theta+k_z z)} \tag{4.30}$$

$$G_l(r,\theta,z,t) = \begin{cases} \sum_{k_\theta}\sum_{k_z} -\alpha_l^- e^{i(k_\theta\theta+k_z z)} & , \quad k_\theta \neq 0 \text{ or } k_z \neq 0 \\ 0 & , \quad k_\theta = k_z = 0 \end{cases} \tag{4.31}$$

$$H_l(r,\theta,z,t) = \begin{cases} \sum_{k_\theta}\sum_{k_z} k_z(1-k_\theta)((1+k_\theta)\alpha_l^+ + \alpha_l^-)e^{i(k_\theta\theta+k_z z)} & , k_z \neq 0 \\ \sum_{k_\theta}\sum_{k_z}(1-k_\theta{}^2)\alpha_l^+ e^{i(k_\theta\theta+k_z z)} & , k_z = 0 \end{cases} \tag{4.32}$$

$$I_l(r,\theta,z,t) = \begin{cases} \sum_{k_\theta}\sum_{k_z} k_z(\alpha_l^+ + \alpha_l^-)e^{i(k_\theta\theta+k_z z)} & , k_z \neq 0 \\ \alpha_l^+ e^{i(k_\theta\theta+k_z z)} & , k_z = 0 \end{cases} \tag{4.33}$$

$$J_l(r,\theta,z,t) = \begin{cases} \sum_{k_\theta}\sum_{k_z} k_z\alpha_l^+ e^{i(k_\theta\theta+k_z z)} & , k_z \neq 0 \text{ and } k_\theta \neq 0 \\ \sum_{k_\theta}\sum_{k_z} \alpha_l^+ e^{i(k_\theta\theta+k_z z)} & , k_z = 0 \text{ and } k_\theta \neq 0 \\ 0 & , k_\theta = 0 \end{cases} \tag{4.34}$$

$$K_l(r,\theta,z,t) = \begin{cases} \sum_{k_\theta}\sum_{k_z} -k_z(k_\theta\alpha_l^+ + \alpha_l^-)e^{i(k_\theta\theta+k_z z)} & , k_z \neq 0 \text{ and } k_\theta \neq 0 \\ \sum_{k_\theta}\sum_{k_z} -ik_\theta\alpha_l^+ & , k_z = 0 \text{ and } k_\theta \neq 0 \\ 0 & , k_z = k_\theta = 0 \end{cases} \tag{4.35}$$

4.3.4 System equations

Substituting Equations (4.6), (4.17), and (4.18) into Equation (4.16) and evaluating the integrals, the following system of ordinary differential Equations can be obtained for each Fourier mode (k_z , k_θ):

$$\begin{pmatrix} \mathbf{A}^{++} & \mathbf{A}^{-+} \\ \mathbf{A}^{+-} & \mathbf{A}^{--} \end{pmatrix} \begin{pmatrix} \dot{\alpha^+} \\ \dot{\alpha^-} \end{pmatrix} = \begin{pmatrix} \mathbf{B}^{++} & \mathbf{B}^{-+} \\ \mathbf{B}^{+-} & \mathbf{B}^{--} \end{pmatrix} \begin{pmatrix} \alpha^+ \\ \alpha^- \end{pmatrix} + \begin{pmatrix} \mathbf{F}^+ \\ \mathbf{F}^- \end{pmatrix} \tag{4.36}$$

where $\dot{\alpha}^{\pm}$ is the time derivative of $\alpha^{\pm}$,

$$\mathbf{A}^{++} = \int_0^R \mathbf{w}_k^+ \cdot \mathbf{u}_l^+ r\, dr \qquad \mathbf{A}^{+-} = \int_0^R \mathbf{w}_k^- \cdot \mathbf{u}_l^+ r\, dr \tag{4.37}$$

$$\mathbf{A}^{-+} = \int_0^R \mathbf{w}_k^+ \cdot \mathbf{u}_l^- r\, dr \qquad \mathbf{A}^{--} = \int_0^R \mathbf{w}_k^- \cdot \mathbf{u}_l^- r\, dr \tag{4.38}$$

are the mass matrices,

$$\mathbf{B}^{++} = \int_0^R \mathbf{w}_k^+ \cdot (\widehat{\nabla} \cdot \widehat{\nabla}\mathbf{u}_l^+) r\, dr \qquad \mathbf{B}^{+-} = \int_0^R \mathbf{w}_k^- \cdot (\widehat{\nabla} \cdot \widehat{\nabla}\mathbf{u}_l^+) r\, dr \tag{4.39}$$

$$\mathbf{B}^{-+} = \int_0^R \mathbf{w}_k^+ \cdot (\widehat{\nabla} \cdot \widehat{\nabla}\mathbf{u}_l^-) r\, dr \qquad \mathbf{B}^{--} = \int_0^R \mathbf{w}_k^- \cdot (\widehat{\nabla} \cdot \widehat{\nabla}\mathbf{u}_l^-) r\, dr \tag{4.40}$$

are the viscous matrices, and

$$\mathbf{F}^{\pm} = \frac{1}{2\pi L_z} \int_0^{L_z} \int_0^{2\pi} \int_0^R \mathbf{w}_k^{\pm} \cdot (\mathbf{v} \times \omega) e^{-i(k_\theta \theta + k_z z)} r\, dr\, d\theta\, dz. \tag{4.41}$$

are the nonlinear terms. The volume integrals for the mass matrices and the viscous matrices in Equation (4.16) are reduced to single integrals in r by the orthogonality property

$$\int_0^{2\pi} e^{-ik\theta} e^{il\theta} d\theta = 2\pi\delta_{kl}\,. \tag{4.42}$$

In the mass and viscous matrices, the row index corresponds to the weight vectors $\mathbf{w}_k^{\pm}$, and the column index corresponds to the expansion vector $\mathbf{u}_l^{\pm}$. The complete expression for mass and viscous matrices and components of the nonlinear terms are given in Appendix C.

4.3.5 Nonlinear terms

Since the integral

$$\frac{1}{2\pi L_z} \int_0^{2\pi} \int_0^{L_z} \mathbf{w}_k^{\pm} \cdot (\mathbf{v} \times \omega) e^{-i(k_\theta \theta + k_z z)}\, d\theta\, dz \tag{4.43}$$

in the right hand side of Equation (4.41) is the definition of the inverse Fourier transform for the product $\mathbf{w}_k^{\pm} \cdot (\mathbf{v} \times \omega)$, the nonlinear term can be computed by the pseudo spectral method to avoid the high computational cost associated with evaluation of convolution sums in Fourier space. Thus, the B-spline coefficients A_l to K_l in the velocity and vorticity expansions are transformed from Fourier wave space to physical space using the "3/2 rule" (Orszag 1971) for de-aliasing reasons. The production $\mathbf{w}_k^{\pm} \cdot (\mathbf{v} \times \omega)$ is evaluated in physical space and the nonlinear term is finally obtained by the inverse Fourier transform. By using FFTs, the pseudo spectral

method only needs $O(N\log_2 N)$ operations rather than $O(N^2)$ operations required for a full spectral approach. The complete expressions and the details on how to evaluate the nonlinear term are given in Appendix C.

4.3.6 Time advancement

The system of ordinary differential Equations (4.36) can be solved for the B-spline expansion coefficients $\alpha^{\pm}$ with a standard time-stepping algorithm. In this work, the time advancement is performed by using a mixed explicit-implicit method of Spalart, Moser & Rogers (1991). The linear viscous term is time-marched implicitly using a Crank-Nicholson scheme and the nonlinear terms are computed explicitly using a third order Runge-Kutta scheme.

For the system of equations

$$\frac{\partial \mathbf{f}}{\partial t} = L(\mathbf{f}) + N(\mathbf{f}) \,, \tag{4.44}$$

where $L(\mathbf{f})$ is the linear viscous term and $N(\mathbf{f})$ is the nonlinear convective term, the formulation of the scheme to advance from $\mathbf{f}_n$, at time t, to $\mathbf{f}_{n+1}$, at time $t + \Delta t$, is given by

$$\mathbf{f}' = \mathbf{f}_n + \Delta t[L(\alpha_1 \mathbf{f}_n + \beta_1 \mathbf{f}') + \gamma_1 N(\mathbf{f}_n)] \tag{4.45}$$

$$\mathbf{f}'' = \mathbf{f}'_n + \Delta t[L(\alpha_2 \mathbf{f}' + \beta_2 \mathbf{f}'') + \gamma_2 N(\mathbf{f}') + \zeta_1 N(\mathbf{f}_n)] \tag{4.46}$$

$$\mathbf{f}_{n+1} = \mathbf{f}''_n + \Delta t[L(\alpha_3 \mathbf{f}'' + \beta_3 \mathbf{f}_{n+1}) + \gamma_3 N(\mathbf{f}'') + \zeta_1 N(\mathbf{f}')] \tag{4.47}$$

where

$$\alpha_1 = \frac{29}{96} \,, \quad \alpha_2 = -\frac{3}{40} \,, \quad \alpha_3 = \frac{1}{6} \,, \tag{4.48}$$

$$\beta_1 = \frac{37}{160} \,, \quad \beta_2 = \frac{5}{24} \,, \quad \beta_3 = \frac{1}{6} \,, \tag{4.49}$$

$$\gamma_1 = \frac{8}{15} \,, \quad \gamma_2 = \frac{5}{12} \,, \quad \gamma_3 = \frac{3}{4} \,, \tag{4.50}$$

$$\zeta_1 = \frac{17}{60} \,, \quad \zeta_2 = \frac{5}{12} \,. \tag{4.51}$$

Applying this method to Equation (4.36) and rearranging the formulations, we can obtain

$$\widetilde{\mathbf{A}}_1 \alpha' = \tilde{\mathbf{B}}_1 \alpha_n + \Delta t \gamma_1 \mathbf{F}(\alpha_n) \tag{4.52}$$

$$\widetilde{\mathbf{A}}_2 \alpha'' = \tilde{\mathbf{B}}_1 \alpha' + \Delta t \left[\gamma_2 \mathbf{F}(\alpha') + \zeta_1 \mathbf{F}(\alpha_n)\right] \tag{4.53}$$

$$\widetilde{\mathbf{A}}_3 \alpha_{n+1} = \tilde{\mathbf{B}}_1 \alpha'' + \Delta t \left[\gamma_3 \mathbf{F}(\alpha') + \zeta_2 \mathbf{F}(\alpha')\right] \tag{4.54}$$

$$\tag{4.55}$$

where the vectors of the nonlinear terms $\mathbf{F}$ and α are defined as

$$\mathbf{F} = \begin{pmatrix} \mathbf{F}^{+} \\ \mathbf{F}^{-} \end{pmatrix}, \quad \alpha = \begin{pmatrix} \alpha^{+} \\ \alpha^{-} \end{pmatrix}, \tag{4.56}$$

$\widetilde{\mathbf{A}}_i$ and $\widetilde{\mathbf{B}}_i$ are, respectively, the effective mass and viscous matrices defined as

$$\widetilde{\mathbf{A}}_i = \begin{pmatrix} \mathbf{A}^{++} & \mathbf{A}^{-+} \\ \mathbf{A}^{+-} & \mathbf{A}^{--} \end{pmatrix} - \beta_i \Delta t \begin{pmatrix} \mathbf{B}^{++} & \mathbf{B}^{-+} \\ \mathbf{B}^{+-} & \mathbf{B}^{--} \end{pmatrix}, \tag{4.57}$$

and

$$\widetilde{\mathbf{B}}_i = \begin{pmatrix} \mathbf{A}^{++} & \mathbf{A}^{-+} \\ \mathbf{A}^{+-} & \mathbf{A}^{--} \end{pmatrix} - \alpha_i \Delta t \begin{pmatrix} \mathbf{B}^{++} & \mathbf{B}^{-+} \\ \mathbf{B}^{+-} & \mathbf{B}^{--} \end{pmatrix}. \tag{4.58}$$

Although the scheme requires three storage locations, it can be made to need only two storage locations. The outline of the algorithm is given in Table 4.2.

Table 4.2 The algorithm using two storage location for the SMR method.

Time	Location 1	Location 2
t_n	$\alpha^1 = \alpha_n$	$\alpha^2 = \alpha_n$
t_n	$\alpha^1 = \mathbf{F}(\alpha^1)$	$\alpha^2 = \widetilde{\mathbf{B}}_i \alpha^2$
	$\alpha^1 = \alpha^2 + \gamma_1 \Delta t \alpha^1$	$\alpha^2 = (\alpha^2 - \alpha^1)/(\gamma_1 \Delta t)$
	$\alpha^1 = \alpha' = \widetilde{\mathbf{A}}_1^{-1} \alpha^1$	$\alpha^2 = \widetilde{\mathbf{B}}_i \alpha^1 + \zeta_1 \Delta t \alpha^2$
t_n	$\alpha^1 = \alpha^2 + \gamma_2 \Delta t \mathbf{F}(\alpha^1)$	$\alpha^2 = (\alpha^2 - \alpha^1)/(\gamma_1 \Delta t)$
	$\alpha^1 = \alpha'' = \widetilde{\mathbf{A}}_2^{-1} \alpha^1$	$\alpha^2 = \widetilde{\mathbf{B}}_3 \alpha^1 + \zeta_2 \Delta t \alpha^2$
t_n	$\alpha^1 = \alpha^2 + \gamma_3 \Delta t \mathbf{F}(\alpha^1)$	$\alpha^2 = \alpha^2$
	$\alpha^1 = \alpha''' = \widetilde{\mathbf{A}}_3^{-1} \alpha^1$	$\alpha^2 = \alpha^1$
$t_{n+1} = t_n + \Delta t$	$\alpha_{n+1} = \alpha'''$	$\alpha_{n+1} = \alpha'''$

The $\widetilde{\mathbf{A}}_i^{-1}$ in Table 4.2 indicates that a linear system is solved. There is a separate linear system to be solved for each set of wave numbers (k_θ, kz) which facilitates the parallel implementation of the algorithm.

4.4 Boundary Conditions

As mentioned in section 4.3.2, the basis weight vectors in Table 4.3.1 which do not satisfy the additional restriction on the weight function, $\xi(R) = 0$, have to be eliminated from the set of basis weight vectors. Thus, the equations related to those basis weight vectors are lost from the system of Equations (4.36) and we have to develop boundary conditions to make up for those equations. Based on potential flow boundary conditions, appropriate boundary conditions for the vortex problem have been developed in this work. The details for each Fourier mode are described in this section.

For modes $k_\theta = 0$ and $k_z = 0$, there are two basis weight vectors $\mathbf{w}^+_{Nr}$ and $\mathbf{w}^-_{Nr}$ with non-zero value at the boundary $\partial\Gamma$. Two equations related to $\mathbf{w}^+_{Nr}$ and $\mathbf{w}^-_{Nr}$ have to be eliminated from the system of Equations (4.36), but we can replace them by using potential flow boundary conditions,

$$\sum_{l=1}^{N_r} \alpha_l^+(R,0,0) g_l(R) = \widehat{V_\theta}^p(R,0,0)\,, \tag{4.59}$$

$$\sum_{l=1}^{N_r} \alpha_l^-(R,0,0) \frac{g_l(R)}{R} = \widehat{V_z}^p(R,0,0), \tag{4.60}$$

where $\widehat{V_\theta}^p(R,0,0)$ and $\widehat{V_z}^p(R,0,0)$ are the velocity components of the potential flow in Fourier wave space at mode $k_\theta = 0$ and $k_z = 0$.

For modes $k_\theta \neq 0$ and $k_z = 0$, there are four basis weight vectors $\mathbf{w}^+_{Nr-1}$, $\mathbf{w}^+_{Nr}$, $\mathbf{w}^-_{Nr-1}$, and $\mathbf{w}^-_{Nr}$ having non-zero components at the boundary. After eliminating those four equations from the system of equations, we can make up three equations from potential flow boundary conditions,

$$\sum_{l=1}^{N_r} -ik_\theta \alpha_l^+(R,k_\theta,0) g_l(R) = \widehat{V_r}^p(R,k_\theta,0) \tag{4.61}$$

$$\sum_{l=1}^{N_\theta} \alpha_l^+(R,k_\theta,0)(g_l(R) + R g_l'(R)) = \widehat{V_\theta}^p(R,k_\theta,0) \tag{4.62}$$

$$\sum_{l=1}^{N_z} \alpha_l^-(R,k_\theta,0) \left(g_l'(R) + \frac{1-k_\theta}{R} g_l(r) \right) = \widehat{V_z}^p(R,k_\theta,0)\,. \tag{4.63}$$

The last constrain will come from a new weight vector which satisfies the restriction, $\xi(r) = 0$. A new basis weight vector can be formed from a linear combination of the eliminated basis vectors

$$\mathbf{w}'_{new}(r) = c_1\mathbf{w}^+_{Nr-1}(r) + c_2\mathbf{w}^+_{Nr}(r) + c_3\mathbf{w}^-_{Nr-1}(r) + c_4\mathbf{w}^-_{Nr}(r)\,. \tag{4.64}$$

If unconstrained, we could form four linearly independent weight vectors by choosing four sets of coefficients (c_1, c_2, c_3, c_4) arbitrarily. However we have the constraint $\mathbf{w}'_{new}(R) = 0$ so that we are allowed to assign only one value arbitrarily. By choosing $c_3 = 1$ and applying the constraint, we can obtain the set of coefficients

$$(0, 0, 1, \frac{g'_{Nr-1}(R)}{g'_{Nr}(R) + \frac{1-k_\theta}{R}g_{Nr}})\,, \tag{4.65}$$

and the new basis weight vector,

$$\mathbf{w}'_{new}(r) = \mathbf{w}^-_{Nr-1}(r) - \frac{g'_{Nr-1}(R)}{g'_{Nr}(R) + \frac{1-k_\theta}{R}g_{Nr}}\mathbf{w}^-_{Nr}(r). \tag{4.66}$$

Thus, the last equation is implemented from the linear combination of the four eliminated equations by using the set of coefficients in Equation (4.65).

For modes $k_\theta = 0$ and $k_z \neq 0$, there are three basis weight vectors $\mathbf{w}^+_{Nr}$,$\mathbf{w}^-_{Nr-1}$, and $\mathbf{w}^-_{Nr}$ having non-zero components at the boundary. We can make up three equations from potential flow boundary conditions,

$$\sum_{l=1}^{N_r} -ik_z\alpha^-_l(R, 0, k_z)g_l(R) = \widehat{V_r}^p(R, 0, k_z) \tag{4.67}$$

$$\sum_{l=1}^{N_\theta} k_z g_l(R)(\alpha^+_l(R, 0, k_z) + \alpha^-_l(R, 0, k_z)) = \widehat{V_\theta}^p(R, 0, k_z) \tag{4.68}$$

$$\sum_{l=1}^{N_z} \alpha^-_l(R, 0, k_z)\left(g'_l(R) + \frac{1-k_\theta}{R}g_l(r)\right) = \widehat{V_z}^p(R, 0, k_z)\,, \tag{4.69}$$

where $\widehat{V_r}^p(R, 0, k_z)$, $\widehat{V_\theta}^p(R, 0, k_z)$, and $\widehat{V_z}^p(R, 0, k_z)$ are the velocity components of the potential flow in Fourier wave space at modes $k_\theta = 0$ and $k_z \neq 0$. Therefore, no linear combination of basis weight vectors is needed for these modes.

For mode $k_\theta \neq 0$ and $k_z \neq 0$, there are four basis weight vectors $\mathbf{w}^+_{Nr-1}$,$\mathbf{w}^+_{Nr}$,$\mathbf{w}^-_{Nr-1}$, and $\mathbf{w}^-_{Nr}$ having non-zero components at the boundary. Like the modes $k_\theta \neq 0$ and $k_z = 0$, we can make up three equations from potential flow boundary conditions,

$$\sum_{l=1}^{N_r} -ik_z g_l(R)(k_\theta \alpha_l^+(R,k_\theta,k_z) + \alpha_l^-(R,k_\theta,k_z)) = \widehat{V_r}^p(R,k_\theta,k_z) \tag{4.70}$$

$$\sum_{l=1}^{N_\theta} \alpha_l^+(R,k_\theta,k_z)(g_l(R) + Rg_l'(R)) + \alpha_l^-(R,kt,k_z)g_l(R) = \widehat{V_\theta}^p(R,k_\theta,k_z) \tag{4.71}$$

$$\sum_{l=1}^{N_z} \alpha_l^-(R,k_\theta,k_z)\left(g_l'(R) + \frac{1-k_\theta}{R}g_l(r)\right) = \widehat{V_z}^p(R,k_\theta,k_z)\,. \tag{4.72}$$

We have to use a linear combination of basis weight vectors to obtain the last equation. Following the same approach at modes $k_\theta \neq 0$ and $k_z = 0$, we can obtain the set of coefficients

$$(1, \frac{Rg'_{Nr}(R)}{Rg'_{Nr}(R)+1-k_\theta}, -k_\theta, \frac{-k_\theta Rg'_{Nr}(R)}{Rg'_{Nr}(R)+1-k_\theta})\,, \tag{4.73}$$

and the new basis weight vector,

$$\begin{aligned}\mathbf{w}''_{new}(r) = \;& \mathbf{w}^+_{Nr-1}(r) + \frac{Rg'_{Nr}(R)}{Rg'_{Nr}(R)+1-k_\theta}\mathbf{w}^+_{Nr}(r) - \\ & k_\theta \mathbf{w}^-_{Nr-1}(r) + \frac{-k_\theta Rg'_{Nr}(R)}{Rg'_{Nr}(R)+1-k_\theta}\mathbf{w}^-_{Nr}(r).\end{aligned} \tag{4.74}$$

Thus, the last equation is implemented from linear combination of the four eliminated equations by using the set of coefficients (4.73).

5. TURBULENT AXIAL VORTEX WITH STRAIN

5.1 Introduction

As shown in Chapter 3, an isolated axial vortex with a wake-like mean axial flow is stable unless the mean axial wake flow has sufficient magnitude. A similar behavior has been already observed by Bandyopadhyay et al. (1991) and Chow (1994), and simulated by Zeman (1995) and Ragab & Sreedhar (1994). However, a distinct behavior of trailing vortices is that each tip vortex induces a strain field on the other. This external strain causes an instability as described in Section 1.2.2. This instability may cause the trailing vortices to remain turbulent instead of relaminarizing. Results of the linear stability analysis indicate that the pair of trailing vortices are unstable to short wave length disturbances (Widnall et al. 1974) in addition to long wave length modes of the Crow instability (Crow 1970). Therefore, the turbulent structure within the vortex may be altered by the presence of external strain.

In this chapter, the new numerical method described in the previous chapter and the parallelization of the computer code is first validated by repeating the simulation of an isolated vortex (Case A in Chapter 3). The numerical simulation of a turbulent axial vortex with strain is then completed. Various statistical quantities are presented in this chapter.

5.2 Isolated vortex simulation

The simulation of Case A in Chapter 3 is repeated by using the B-spline method in order to validate the code. Comparisons between the two methods are presented in this section.

5.2.1 Initial conditions

The simulation of an isolated vortex is started with mean velocity profiles, for the mode ($k_\theta = 0$ and $k_z = 0$),

$$\frac{V_\theta}{V_0} = \frac{q_0}{\hat{r}}(1 - e^{-\hat{r}^2}), \quad \text{and} \quad \frac{V_z}{V_0} = (1 - e^{-\hat{r}^2}), \tag{5.1}$$

where V_0 is the initial axial velocity deficit and $\hat{r}$ is the dimensionless coordinate as defined in Equation (3.1). The rest of the modes are given by random perturbations with a specified power spectrum. It should be noticed that the velocity profiles given in Equation (5.1) have to be converted to expansion coefficients by using the method given in Appendix B.3, since the time advancement is developed in Fourier wave space. The grid size $N_r = 96$ and $N_\theta = 96$ is used in the cross section to have the same resolution as in Case A in Chapter 3 and $N_z = 192$ is chosen in the streamwise direction.

5.2.2 Results

The comparison of global TKE between the pseudo spectral method in Chapter 2 (hereafter spectral method) and the B-spline method in Chapter 4 (hereafter B-spline method) is shown in Figure 5.1. The B-spline method needs a longer transition time than the spectral method to adjust the flow from the unphysical nature of the initial random disturbances. As in the other cases shown in Figure 3.4, the global TKE of the two methods matches well during the linearly unstable period if time is shifted backward by $t_0 = 1.155T$ for the B-spline method. The difference appears again after the linearly unstable period because of a low sample size in the streamwise direction. Given the differences in the initial disturbances, the two methods show good agreement. The mean axial velocity profiles are shown in Figure 5.2. The numbers in the parentheses are the time shifted by $t_0 = 1.155T$ for comparison with Case A. Comparing with Figure 3.14, the wake shows a very slow decay during the transition period. Then the decay rate of the axial deficit increases significantly

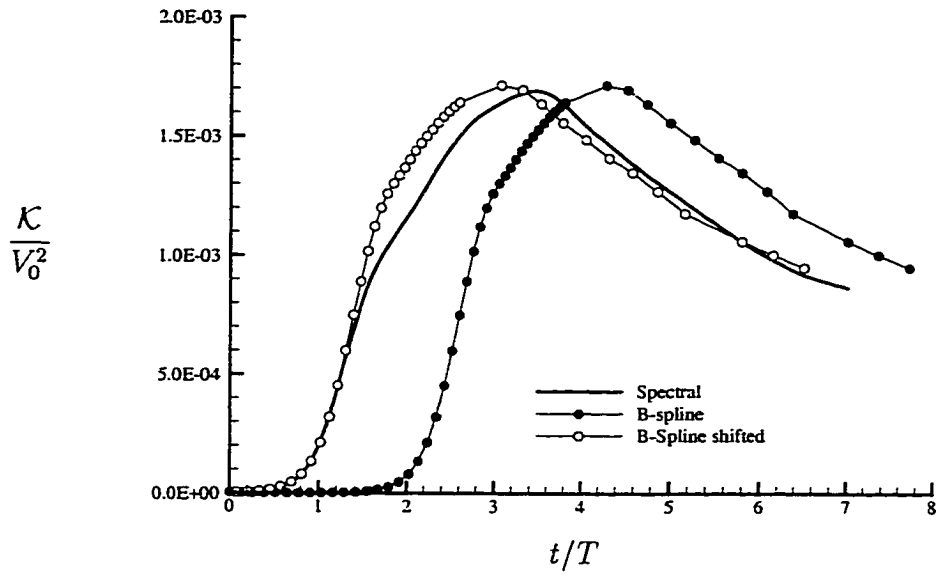

Figure 5.1 The evolution of the global TKE.

until the vortex approaches the saturating period. Finally the decay rate of the wake decreases gradually when the vortex is stabilized.

Figure 5.3 shows the mean tangential velocity profiles. The results qualitatively match well with those in Figure 3.15. The peak in the tangential velocity shows a decay during the vortex unstable periods and moves inward at later periods. The anti-diffusion phenomena at the region near vortex core also occurs at the later periods. The profiles of TKE shown in Figure 5.4 are similar to those in Figure 3.21. The TKE has a peak in an annular region inside the vortex core during the unstable periods of the vortex. Eventually, the peak moves to the center of the vortex core and shows a decay. Overall, the results of the B-spline method qualitatively match well with those from the spectral method.

The evolution of the TKE in different azimuthal modes shown in Figure 5.5 displays three phases: transition, linear instability and decay. As mentioned in Section 3.3.2, once the vortex adjusts itself from the unphysical nature of the initial perturbations, various modes start to grow. The modes $k_\theta = 2$ to $k_\theta = 5$ show an exponential growth rate early, at $t = 1.0T$, but the mode $k_\theta = 1$ does not grow exponentially

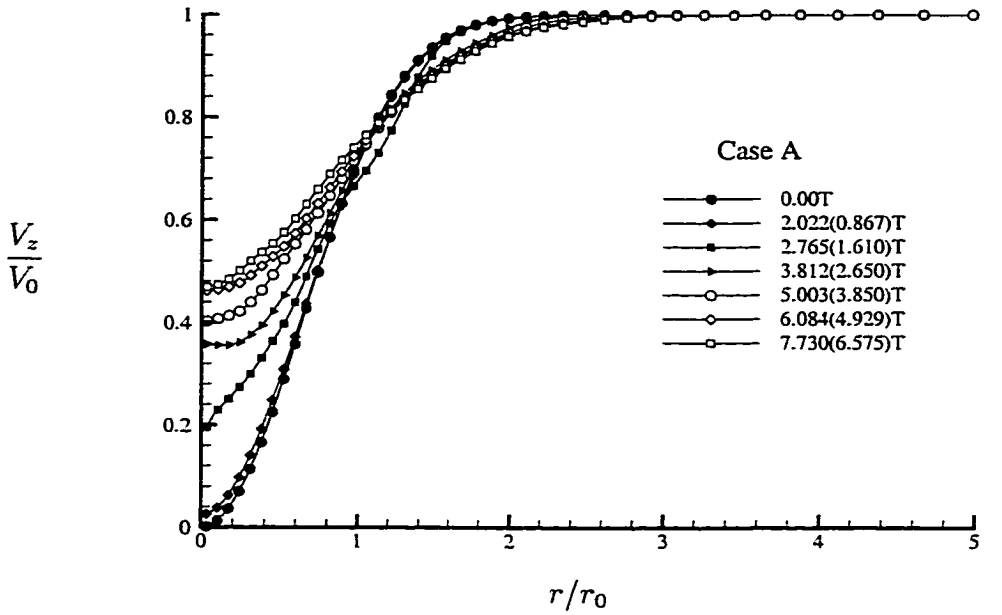

Figure 5.2 The evolution of the mean axial velocity.

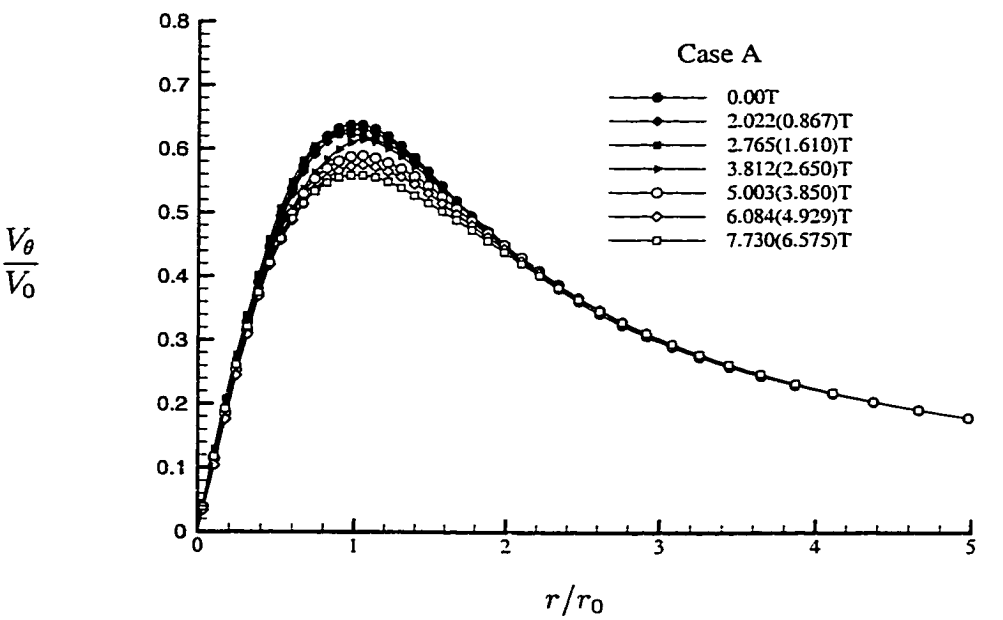

Figure 5.3 The evolution of the mean tangential velocity.

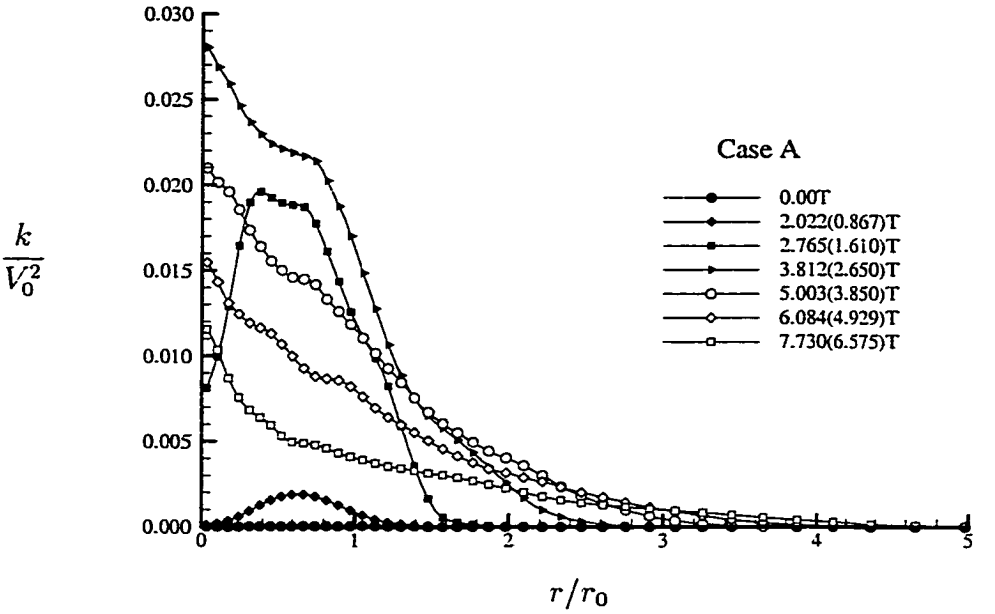

Figure 5.4 The evolution of turbulence kinetic energy.

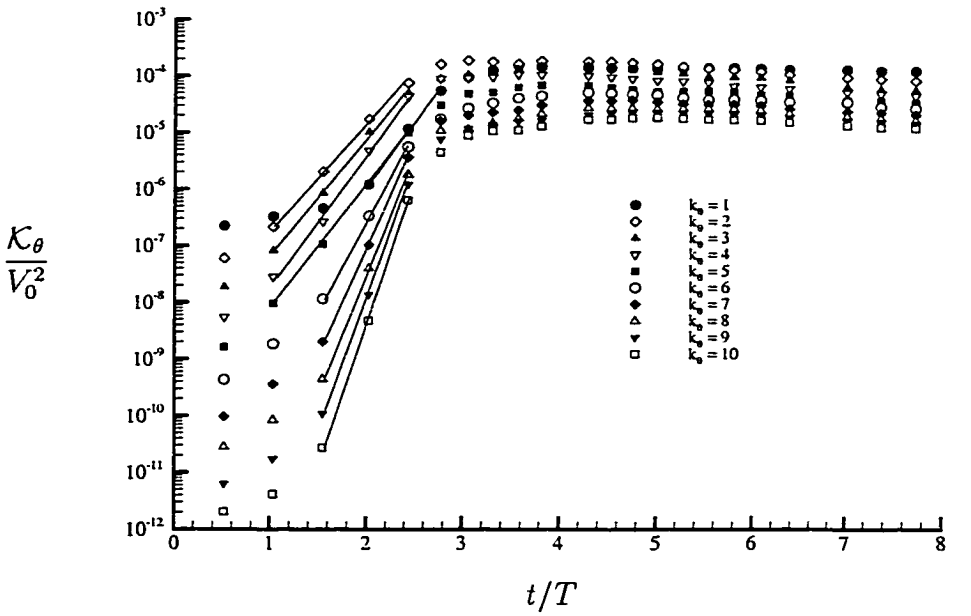

Figure 5.5 The evolution of the $\mathcal{K}_\theta$ in different azimuthal modes.

until $t = 2.0T$. The other high wavenumber modes start to grow exponentially from $t = 1.5T$. The linear instability of most modes, except that of mode $k_\theta = 1$, disappears after $t \approx 2.5T$. Growth rates, $\sigma = (T/\mathcal{K}_\theta)(d\mathcal{K}_\theta/dt)$, evaluated at $t = 2.023T$, are displayed in Figure 5.6. The growth rate is greater for higher k_θ, in agreement with linear theory. For larger wavenumbers, the growth rate is larger than the maximum growth rate predicted by the linear theory (Mayer & Powell 1992). It is not known why this is the case; however, it may be due to the nonlinear transfer of energy into the higher wavenumber modes.

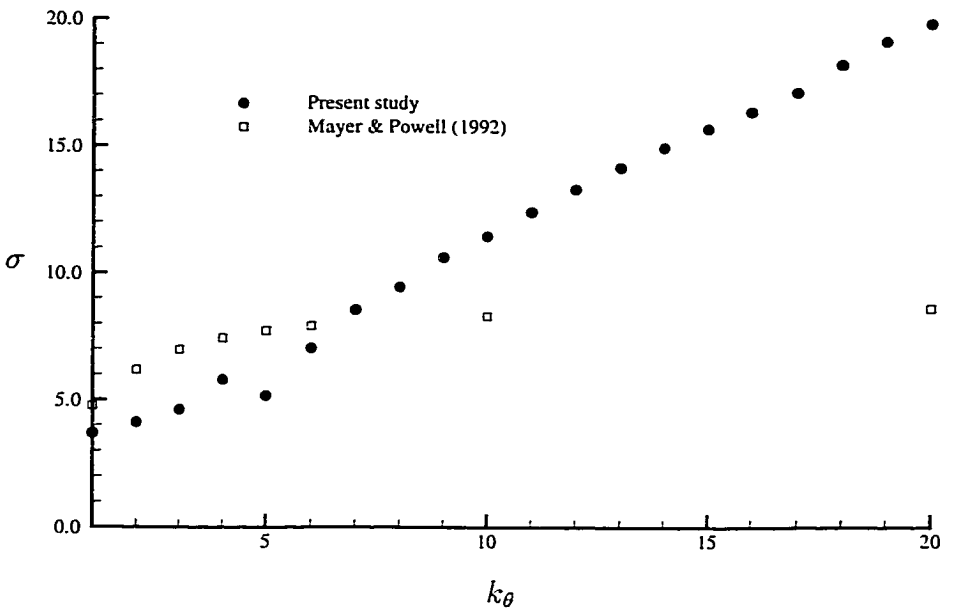

Figure 5.6 The Growth rates for $\mathcal{K}_\theta$ at time t=2.023T.

The relaminarizing process of the isolated vortex is captured by a sequence of snap shots for isovorticity surfaces in Figures 5.7(a) to 5.7(f). Starting from a very weak perturbation shown in Figure 5.7(a), a helical vortex shown in Figure 5.7(b) is formed after a short transition time. Then, the vortex develops higher azimuthal modes as shown in Figure 5.7(c) since the vortex is unstable. With the vortex stabilized, the helical vortex is broken down as shown in Figures 5.7(d) and 5.7(e) and eventually disappears shown in Figure 5.7(f).

(a) $t = 0.75T$

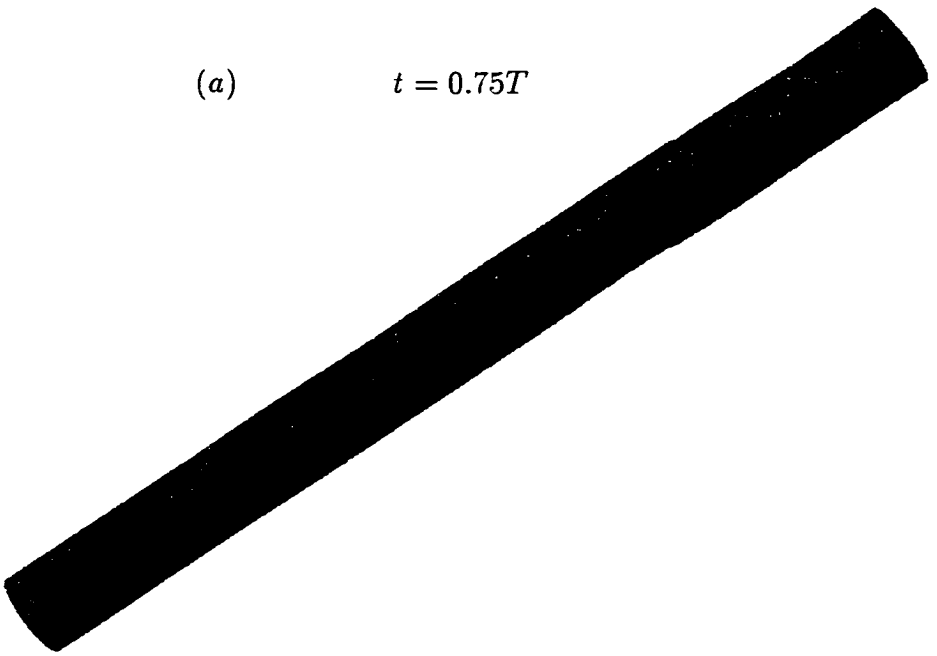

(b) $t = 2.1T$

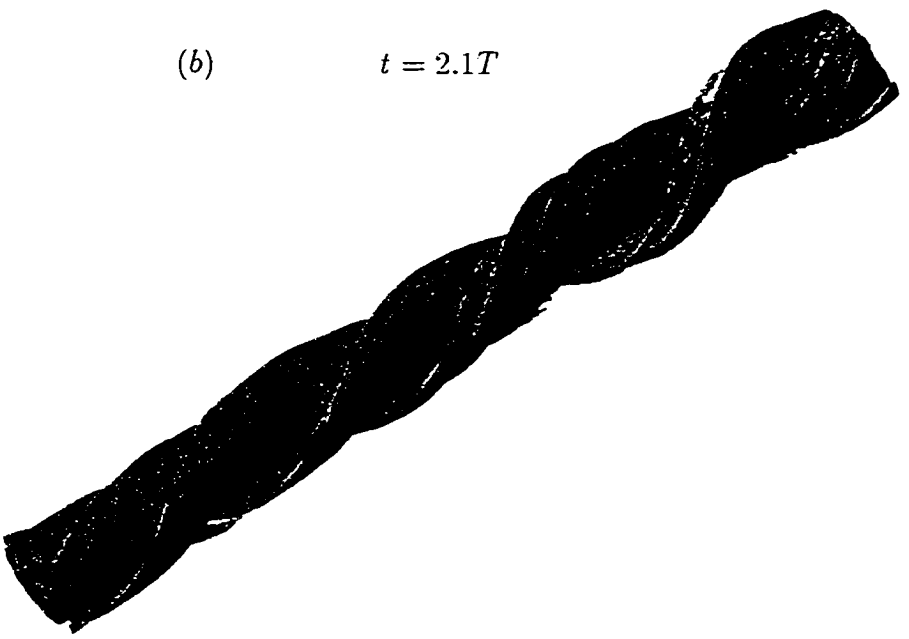

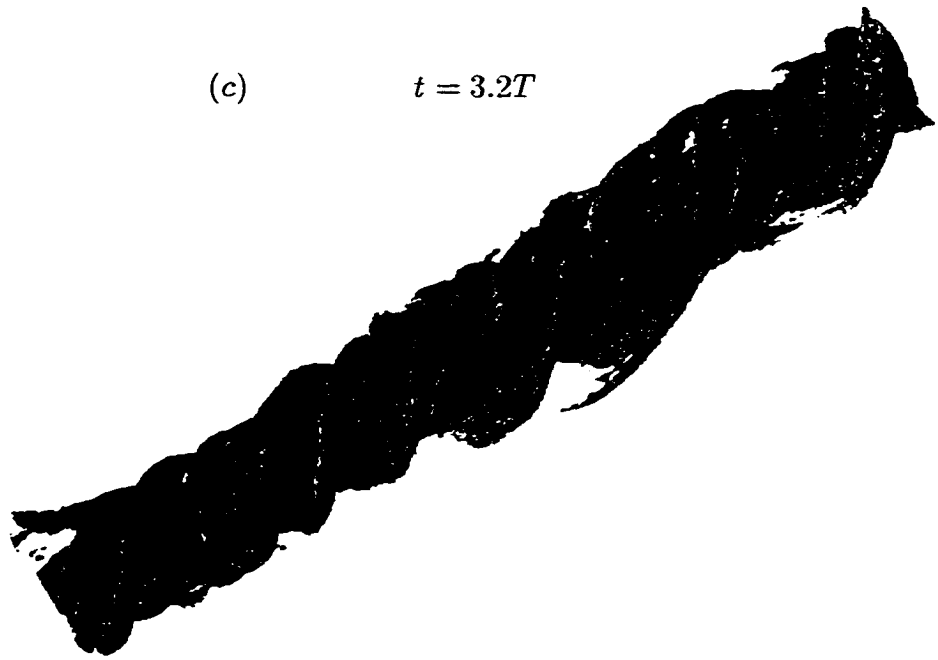

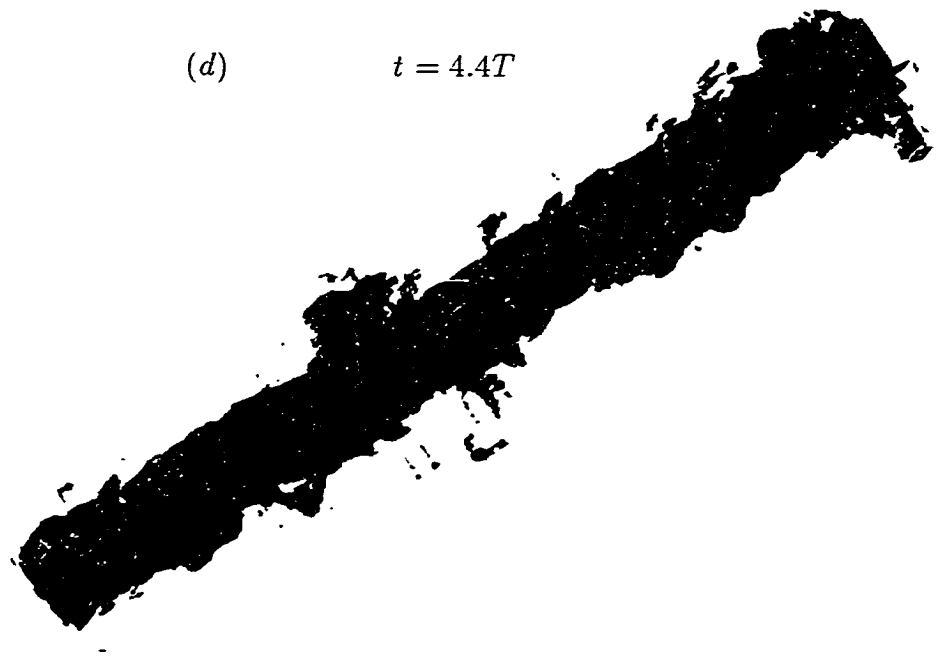

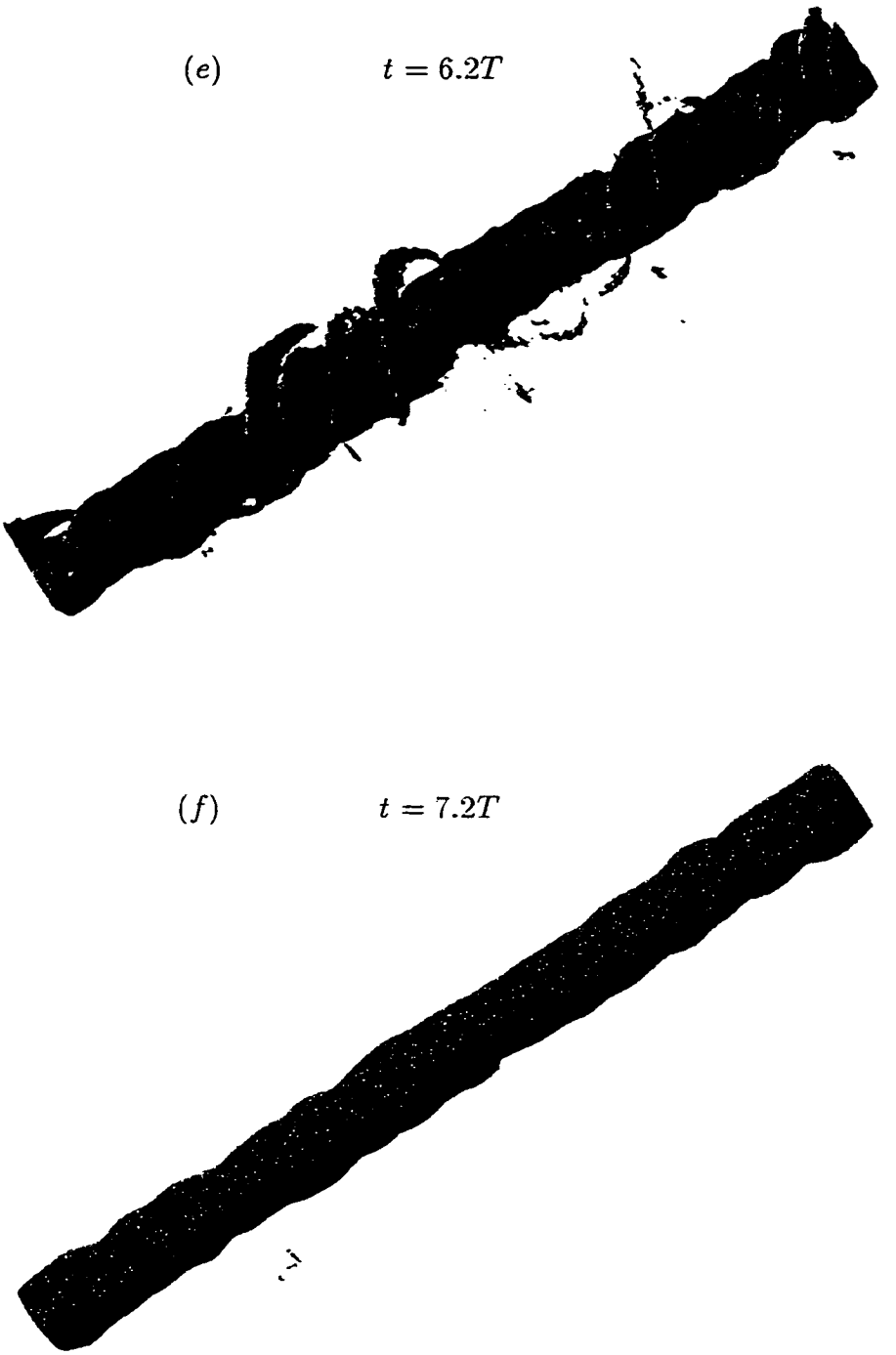

Figure 5.7 A sequence of isosurfaces of vorticity magnitude.

5.3 Simulation of vortex with strain

The numerical simulation of an axial vortex with an external strain is completed using the method described in Chapter 4. Details on the implementation of imposing the external strain field, the choice of parameters for simulations, and statistical results of the simulations are presented in this section.

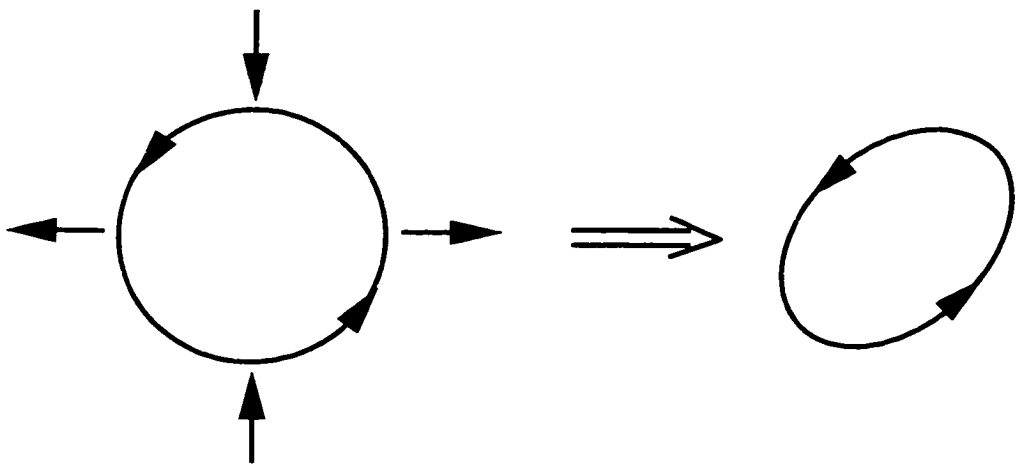

Figure 5.8 A strained vortex.

5.3.1 Imposition of strain

A strained vortex consists of a vortex and an external strain field as shown in Figure 5.8. The imposition of strain can be done by decomposing the full velocity into a strain part and a part that does not include the strain:

$$\mathbf{v} = \mathbf{u_v} + \mathbf{u_s}\,, \tag{5.2}$$

where $\mathbf{u_v}$ represents the velocity that does not include the strain and $\mathbf{u_s}$ represents the velocity that is induced by the external strain. In this work, a steady strain is applied to the vortex for investigating the effect of the strain on the vortex. Hence, with the steady and irrotational properties for the external strain field,

$$\frac{\partial \mathbf{u_s}}{\partial t} = 0 \quad \text{and} \quad \nabla \times \mathbf{u_s} = 0\,,$$

substituting Equation (5.2) into Equation (4.16) yields

$$\left(\xi^{\pm}, \frac{\partial \mathbf{u_v}}{\partial t}\right) = \left(\xi^{\pm}, (\mathbf{u_v} + \mathbf{u_s}) \times \nabla \times \omega\right) + \frac{1}{Re}\left(\xi^{\pm}, \nabla \cdot \nabla \mathbf{u_v}\right) , \qquad (5.3)$$

where $\omega = \nabla \times (\mathbf{u_v} + \mathbf{u_s}) = \nabla \times \mathbf{u_v}$ is the vorticity. Comparing with Equations (4.16) and (5.3), only the nonlinear term needs to be modified. By solving for the velocity $\mathbf{u_v}$ instead of the full velocity $\mathbf{v}$, the external strain can be easily imposed by modifying the nonlinear term alone.

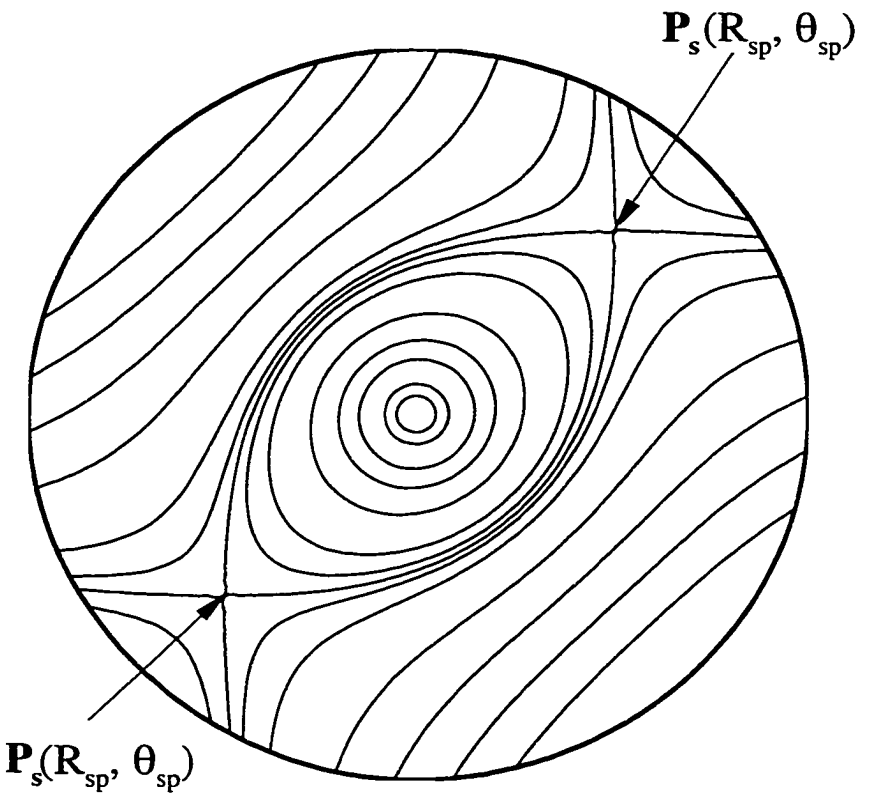

Figure 5.9 Stream lines of a strained vortex on the cross section.

5.3.2 Choice of parameters

For a vortex with a uniform strain field, there are stagnation points in the flow field shown in Figure 5.9. The locations of the stagnation points can be found by solving a potential flow which is a combination of linear strain and a point vortex

$$R_{sp} = \sqrt{\frac{\Gamma_\infty}{2\pi e}}, \quad \text{and} \quad \theta_{sp} = \frac{\pi}{4} \; or \; \frac{3\pi}{4}, \tag{5.4}$$

where R_{sp} is the radius of stagnation points, θ_{sp} is the azimuthal angle, and the strain rate e is defined as

$$\frac{\partial V_r}{\partial r} = e\cos 2\theta \quad \text{and} \quad \frac{1}{r}\frac{\partial V_\theta}{\partial \theta} + \frac{V_r}{r} = -e\sin 2\theta \,. \tag{5.5}$$

In order to avoid the instability of the stagnation point flow, the computation domain has to be small enough so that the domain does not contain any stagnation points. However, since the constant potential flow boundary condition is used in this work, the computational domain has to be large enough to have an irrotational flow at the boundary. To satisfy these two restrictions, a criterion for the strain rate is given as

$$e \le e^* = \frac{\Gamma_\infty}{2\pi R^2} \,. \tag{5.6}$$

where e^* is the critical strain rate.

With viscous effects, the issue of Reynolds number is the key parameter to capture the Widnall instability. For a given strain, if the Reynolds number is too small, the minimum unstable length scale will be larger than the vortex core size so that there will not be any unstable modes within the vortex. The strained vortex is related to a homogeneous turbulent flow that combines uniform strain with solid body rotation. This homogeneous flow has mean flow streamlines that are elliptical and, therefore, it is called the elliptic streamline flow. Landman & Saffman (1987) gave a minimum unstable length scale based on the linear stability analysis of the elliptic streamline flow,

$$l^* = (2\pi)^{\frac{3}{2}}\sqrt{\frac{\nu}{\gamma E_\gamma^*}}, \tag{5.7}$$

where ν is the kinetic viscosity, γ is half the value of the vorticity, and E_γ^* is the critical Ekman number, where E_γ^* depends on $\beta = e/\gamma$ which is the eccentricity parameter.

$$E_\gamma^* = \frac{2\pi\nu k_0^2}{\gamma}\,, \tag{5.8}$$

where k_0 is the wave number of the most amplified perturbation. Shariff, Verzico & Orlandi (1994) showed that the stability of a strained vortex can be found from the stability of the elliptic streamline flow if the *average* vorticity, defined by

$$\zeta = 2\gamma = \frac{\Gamma_\infty}{\pi r_0^2}\,, \tag{5.9}$$

is used to replace the normal definition of vorticity, since the vorticity of the q vortex that is used as a model in this work varies inside the vortex core. Substituting Equation (5.9) into Equation (5.7), the minimum length scale can be rewritten as

$$l^* = \frac{4\pi^2 r_0}{\sqrt{Re_\Gamma E_\gamma^*}}\,, \tag{5.10}$$

where the Reynolds number Re_Γ is defined in Equation (3.9). In order to capture the instability of the strained vortex, the minimum length scale l^* should be less than the size of the vortex core r_0 at least, therefore, the criteria for the Reynolds number Re_Γ can be obtained as

$$Re_\Gamma \geq Re_\Gamma^* = \frac{16\pi^4}{E_\gamma^*}\,, \tag{5.11}$$

where Re_Γ^* is the critical Reynolds number.

Furthermore, Shariff et al. (1994) approximated the the critical value of E_γ^* as

$$E_\gamma^* \approx 3.25\beta^* - c_1\beta^{*2} + O(\beta^{*3})\,, \tag{5.12}$$

where $\beta^* = 4e/\zeta$ and c_1 is a constant. Substituting Equations (5.6) and (5.12) into Equation (5.11) and neglecting the second term for small values of β, the critical Reynolds number Re_Γ^* satisfies the equation

$$Re_\Gamma^* = \frac{8\pi^4}{3.25}\left(\frac{e^*}{e}\right)\left(\frac{R}{r_0}\right)^2\,, \tag{5.13}$$

where R is the computational domain size. For a given computational domain size R, the critical Reynolds number is proportional to the dimensionless strain rate e^*/e.

The selection of the grid size is a very important issue in the capture of the Widnall instability. For a strained vortex with a weak strain rate, there is a very small range of unstable waves with θ around $\pi/3$, where the angle θ is the minimum angle between the wave vector and streamwise axis (Bayly 1986). For the capture of the Widnall instability, the grid size in the radial and streamwise directions has to be aligned with the unstable wave vector. The grid size in the streamwise direction is currently chosen as

$$\triangle z = \frac{(\triangle r)_{avg}}{\cos(\pi/3)}, \tag{5.14}$$

where $(\triangle r)_{avg}$ is the average grid size inside of the vortex core for the stretched grids in the radial direction. For the simulations without strain described in Chapter 3 and Section 5.2, the computational domain is twice as long as the axial wavelength of the most unstable mode. However, because of the need to align the grid with the orientation of the most unstable mode of the elliptic flow instability, a computational domain with two axial wavelengths becomes too expensive to use for these preliminary simulations, given the limited available computer resources. Therefore, in this study, the computational domain only contains one wavelength in the streamwise direction. Of course, the trade-off is to sacrifice the sample size in the streamwise direction.

In this study, a total of four simulations are completed. The first simulation, called STRN1, is a test case. To simulate a strain rate as large as possible, the computational domain size is reduced from $8r_0$ to $6.67r_0$ in the simulation STRN2. The simulations STRN3 and STRN4 are conducted to examine the effect of the external strain field on the Oseen vortex in which the mean axial flow is zero. The effects of Reynolds number also are investigated. Table 5.1 lists the summary of four cases.

5.3.3 Turbulence statistics

The investigation of turbulent statistical quantities for the strained vortex is described in this section. The two-dimensional strain is imposed in the cross section,

Table 5.1 Case parameters for the strained vortex.

Case	r_0/R	e/e^*	β	Re_Γ	l^*/r_0	Axial flow	Domain size
STRN1	0.125	0.8967	0.0281	19268	0.942	wake	$R = 8.0r_0$
STRN2	0.15	0.8967	0.0404	29428	0.635	wake	$R = 6.67r_0$
STRN3	0.15	0.8967	0.0404	29428	0.635	none	$R = 6.67r_0$
STRN4	0.15	0.8967	0.0404	58836	0.449	none	$R = 6.67r_0$

perpendicular to the vortex axis. Thus, in contrast to the isolated vortex, the strained vortex is no longer axisymmetric in the mean. The turbulent quantities presented in this section are obtained by taking the average in the axial direction (see Section 2.3).

5.3.3.1 Global turbulent kinetic energy

One can get a global sense of the stability of the flow by considering the global TKE, that is the volume averaged TKE as defined in Section 3.3.2.

Figure 5.10 shows the evolution of the global TKE for the strained Oseen vortex. For a comparison, the Oseen vortex without strain (Case F in Section 3.3.2) is also plotted. As discussed in Section 3.3.2, without strain, the Oseen vortex shows only decay. In contrast to Case F, both Cases STRN3 and STRN4 show an exponential growth of global TKE after a transition period. However, the global TKE decays shortly thereafter. Due to a larger Reynolds number, Re_Γ, Case STRN4 shows a slightly longer growing period and higher level of global TKE than does Case STRN3. Direct numerical simulations of the elliptic streamline flow (Blaisdell & Shariff 1994, Blaisdell & Shariff 1996) indicate that the vortex should be unstable no matter what the strain rate. The linear analysis of the elliptic streamline flow (Cambon, Teissédre & Jeandel 1985, Bayly 1986, Peierrehumbert 1986, Landman & Saffman 1987, Waleffe 1990) also indicated that the strained vortex is unstable if the Reynolds number for a given strain rate is "large enough". There are two reasons for not completely

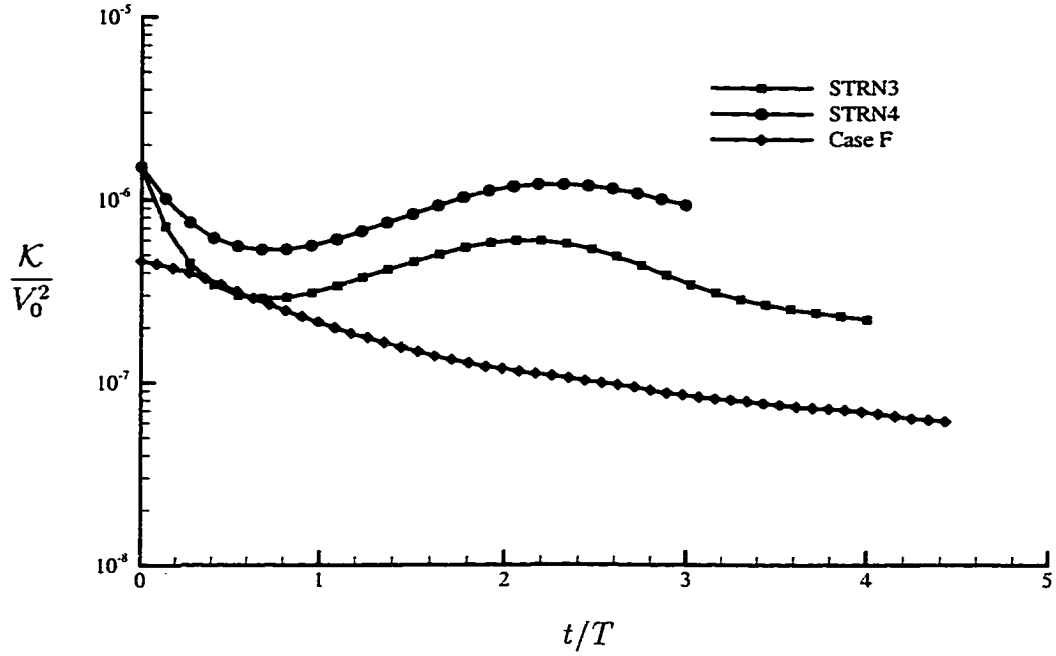

Figure 5.10 The evolution of the Global TKE of the strained Oseen vortex.

capturing the Widnall instability in the present strained Oseen vortex. As mentioned in the previous section, in order to capture the Widnall instability, the grid has to be aligned with the most unstable wave vector because there is a very small range of wave angles θ for such a weak strain rate. In this study, to achieve a reasonable resolution, the grid size is stretched in the radial direction so that it is impossible to align the grid with the most unstable wave vector exactly. The second reason is that most regions inside the vortex core are locally stable. The linear analysis of a strained vortex is based on the vortex with uniform vorticity inside the vortex core. But this is not true in the q vortex.

The minimum unstable length scales, l^*/r_0, in Table 5.1 are calculated based on the *average vorticity* defined by Shariff et al. (1994). If we consider the aspect ratio locally, the vortex should be stable in most regions inside the vortex core since the vorticity of the q vortex decays as the Gaussian profile. Despite the difficulty in completely capturing the Widnall instability for such a weak external strain rate

with a low Reynolds number, the external strain field does cause an instability in the Oseen vortex. Since Cases STRN3 and STRN4 are eventually stable, subsequent discussion will focus mainly on the strained q vortex.

Figure 5.11 shows the development of the global TKE for the strained q vortex. For a comparison, the results of the baseline Case A from the pseudo-spectral method and the B-spline spectral method are also plotted. As mentioned in the previous sections, the global TKE of an isolated vortex grows and then decays when the vortex is stabilized with the decay of the wake. After the transition period, the strained vortex also shows the exponential growth period since the linear instability is mainly caused by the strong initial wake. However, the global TKE of the strained vortex continues to grow for a longer period. For Case STRN1, the strained vortex also displays the periods of saturation and decay since the Reynolds number is too low for such a weak strain rate. With the minimum unstable length scale $l^*/r_0 = 0.944$ as shown in the Table 5.1, there might only be a few unstable modes in the vortex so that the Widnall instability is difficult to catch completely. For Case STRN2, with a higher Reynolds number and strain rate, the global TKE continues to show growth for all time rather than show a saturation and eventual decay at later times because of the presence of the Widnall instability.

Since the strained vortex reaches such a high turbulence level, it is necessary to check the numerical resolution for the simulation. The Kolmogorov length scale is defined by

$$l_K = \left(\frac{\nu^3}{\epsilon}\right)^{(1/4)} , \tag{5.15}$$

where ϵ is the dissipation rate. In this work, based on the assumption of homogeneous turbulence, the Kolmogorov length scale is approximately evaluated by

$$l_K = \left(\frac{\nu}{\sqrt{\overline{\omega_i'\omega_i'}}}\right)^{1/2} , \tag{5.16}$$

where ω_i' is the fluctuating vorticity. Figure 5.12 shows the evolution of the minimum Kolmogorov length scale. It is clear that the simulation did not resolve the small

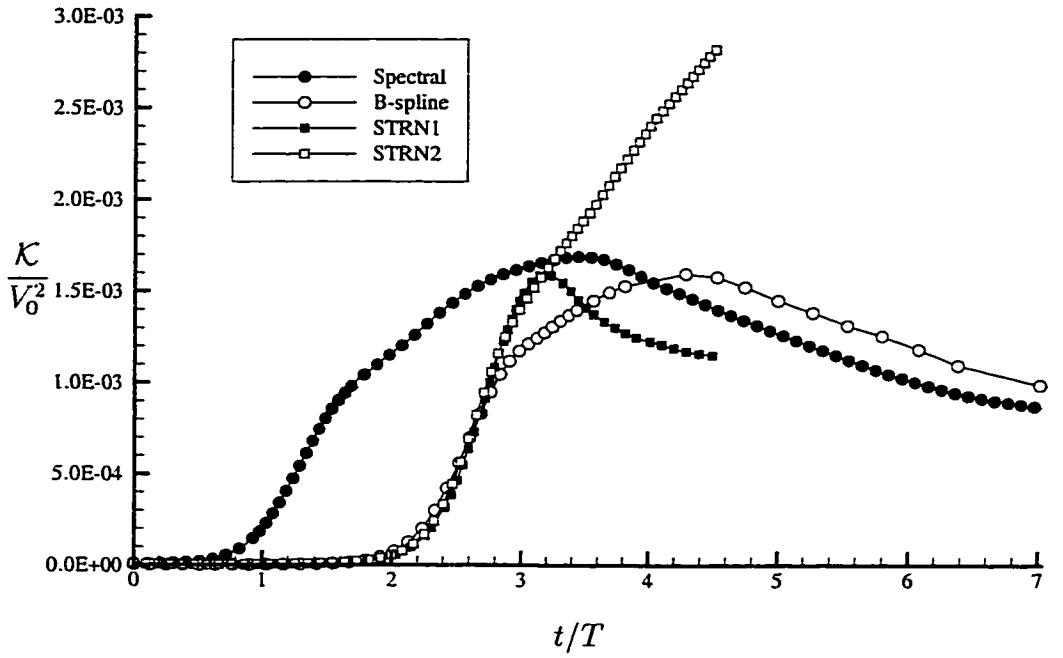

Figure 5.11 The evolution of the Global TKE of the strained vortex.

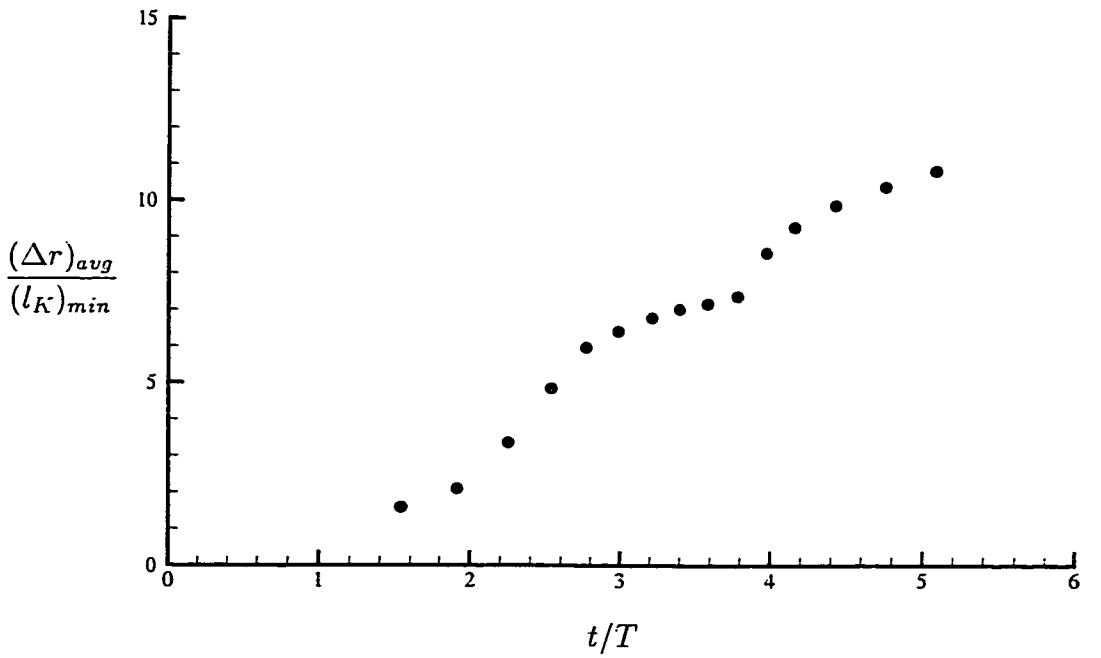

Figure 5.12 The Kolmogorov length scale.

structures well when $t > 4.0T$ since the Kolmogorov length scale reaches one order of magnitude smaller than the grid size.

5.3.3.2 Mean velocity profiles

Contour plots of the mean axial velocity are shown in Figures 5.13 to 5.15 . Since the external strain field is imposed in the cross section, contours are elliptic in shape as expected. The major and minor axes of the elliptic contour lines are the x and y axes , respectively, rotated by $\pi/4$ radians in the counter clockwise direction. However, the feature seems to be distorted at later times when the turbulence reaches a high level. A low statistical sample size and a short computational domain are the two factors that cause the distortion of the velocity profiles. As discussed in the Section 3.3.2, a low statistical sample size is the main reason that causes the results to appear somewhat jagged. However, for the stained vortex, another difficulty in computing the desired statistics is the short one wave length computational domain in the streamwise direction (see Section 5.3.2).

Contours of the mean tangential velocity shown in Figures 5.16 to 5.18 are also elliptic in shape as expected. Unlike the mean axial velocity, the major and minor axes of the elliptic contour lines change from the inside to the outside of the vortex core. It is not surprising since the tangential velocity induced by the vortex is not monotonically increasing along the radial direction, but the velocity induced by the two-dimensional strain is monotonically increasing. The shape of the contour lines is also distorted at a later time because of the low sample size and short computational domain length.

Because there is no axisymmetric property in the strained vortex, profiles of the mean axial velocity along different rays are shown in Figures 5.19 to 5.21 . Like the isolated vortex, the mean axial velocity shows a slow decay at early time because of the weak disturbance. There is some jagged behavior near the center of the vortex at later times because of the low statistical sample size.

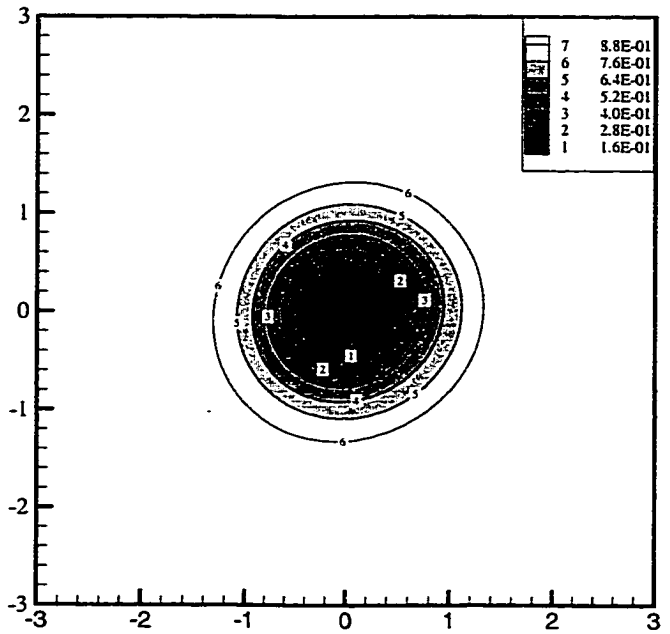

Figure 5.13 Contours of V_z at $t = 2.40T$.

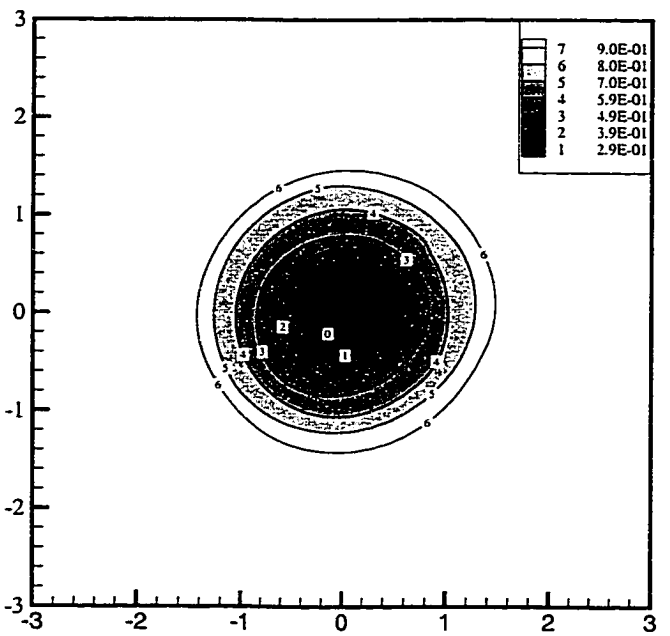

Figure 5.14 Contours of V_z at $t = 2.88T$.

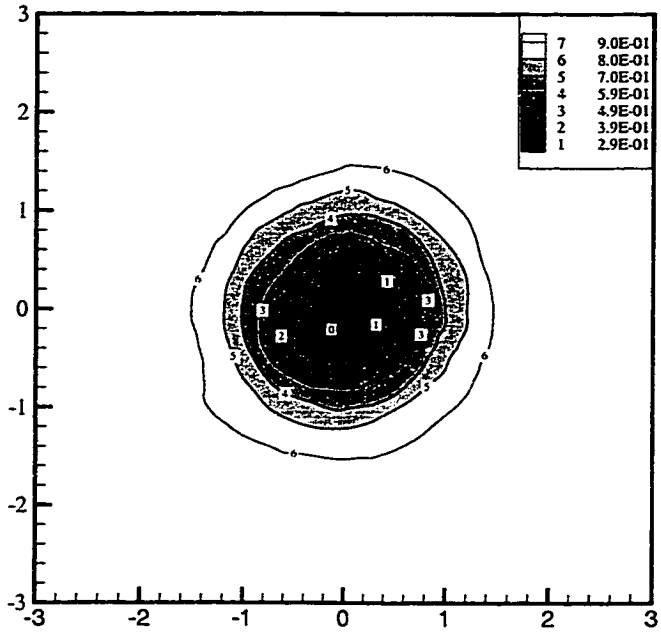

Figure 5.15 Contours of V_z at $t = 3.68T$.

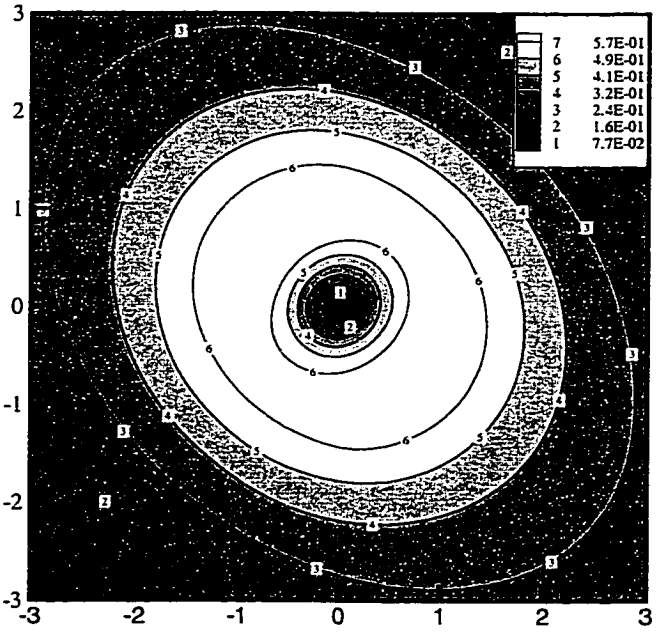

Figure 5.16 Contours of V_θ at $t = 2.40T$.

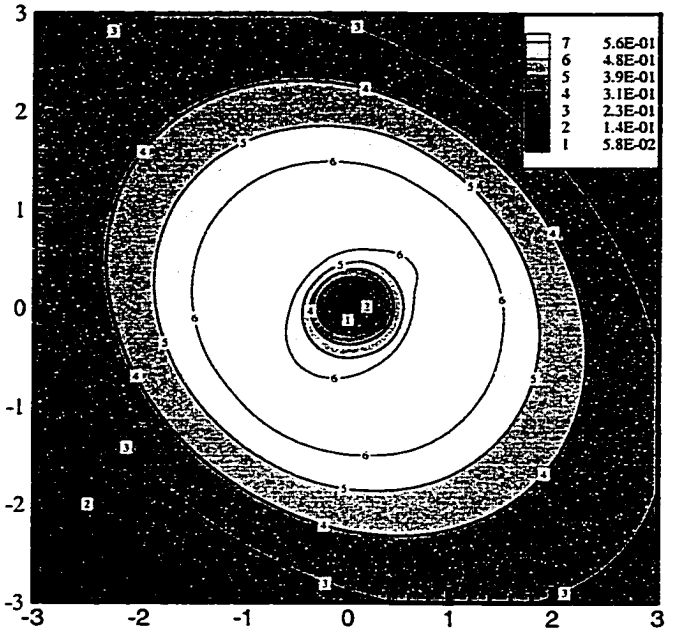

Figure 5.17 Contours of V_θ at $t = 2.88T$.

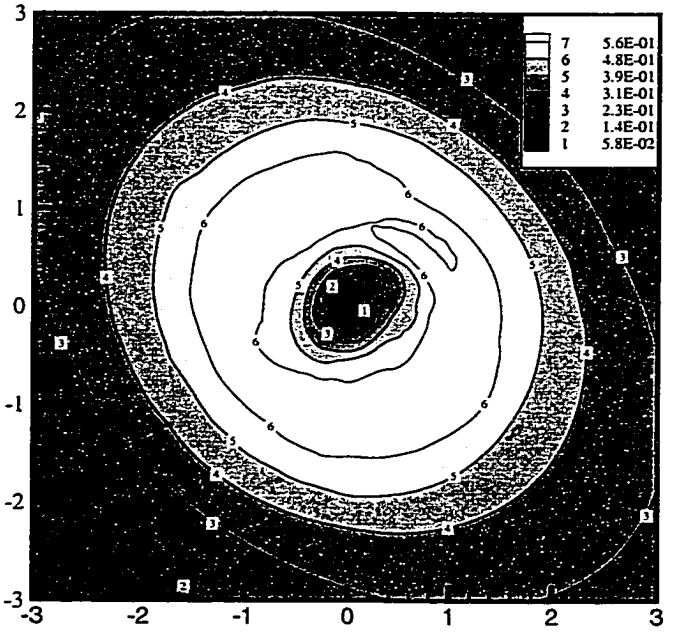

Figure 5.18 Contours of V_θ at $t = 3.68T$.

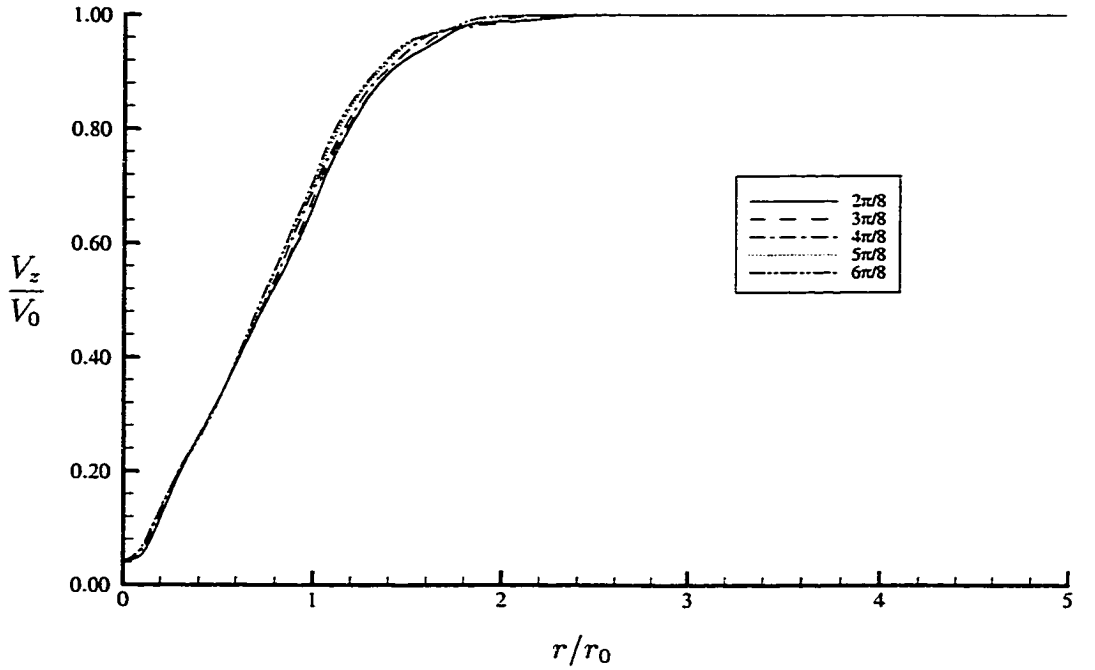

Figure 5.19 Profiles of V_z for the strained vortex shown for various angles (θ) at time $t = 2.40T$.

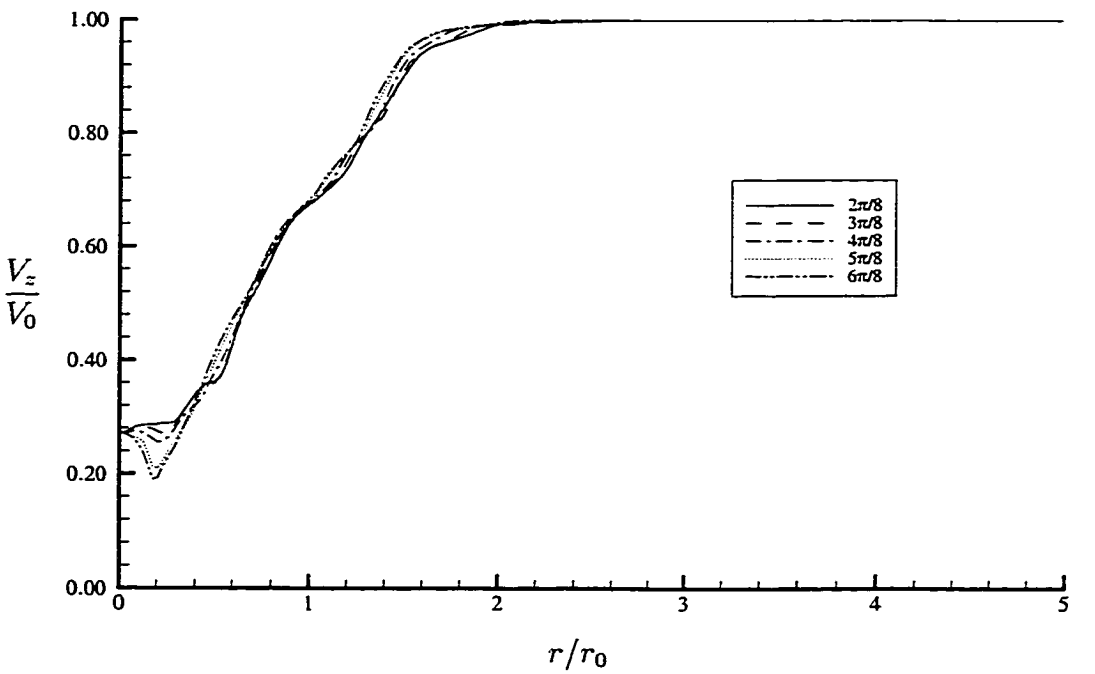

Figure 5.20 Profiles of V_z for the strained vortex shown for various angles (θ) at time $t = 2.88T$.

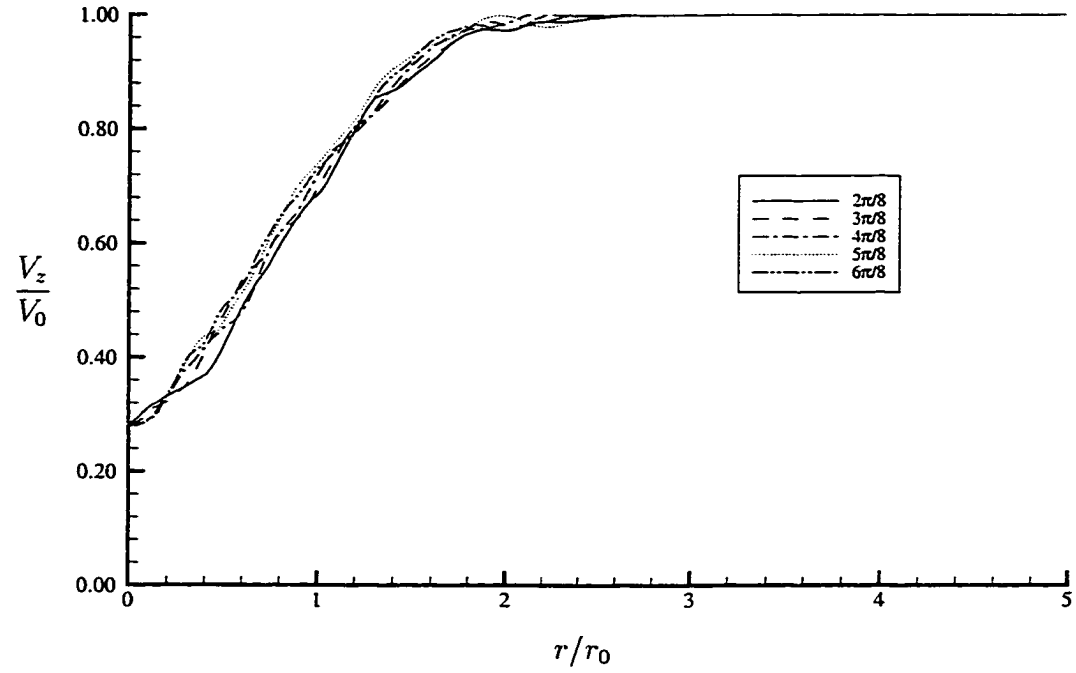

Figure 5.21 Profiles of V_z for the strained vortex shown for various angles (θ) at time $t = 3.68T$.

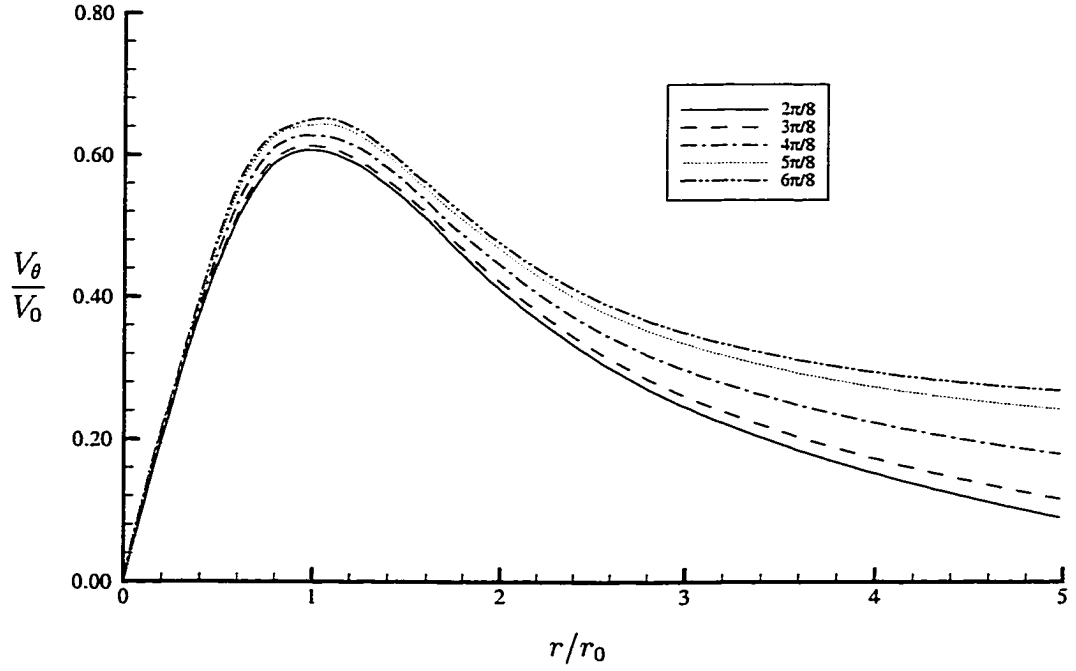

Figure 5.22 Profiles of V_θ for the strained vortex shown for various angles (θ) at time $t = 2.40T$.

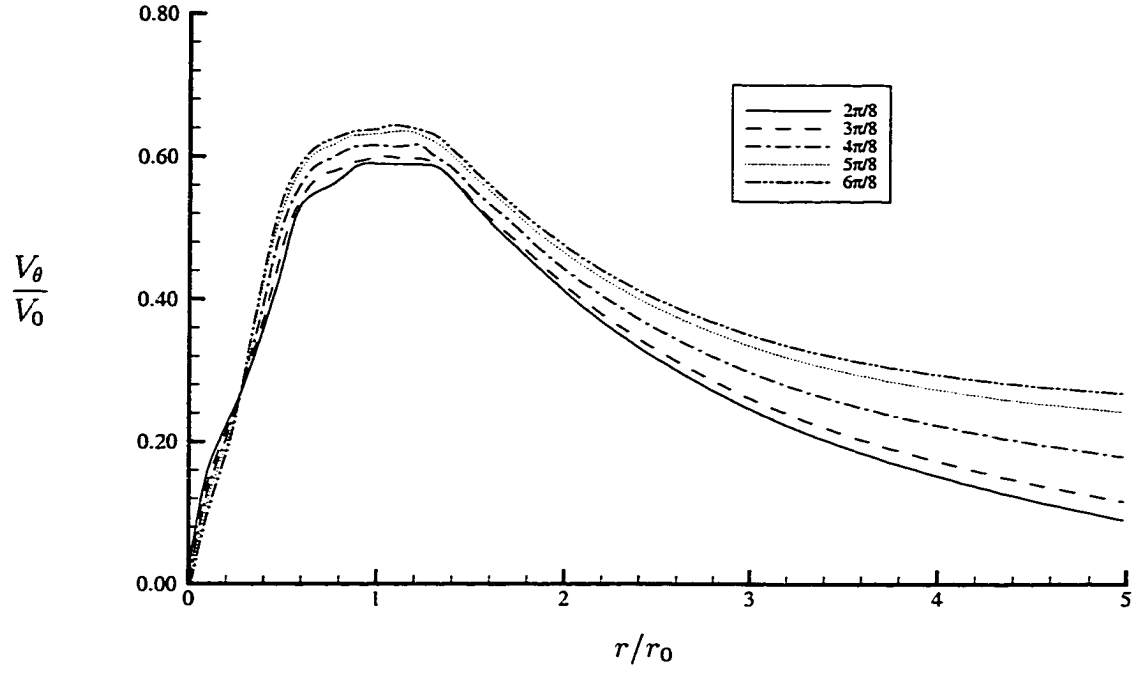

Figure 5.23 Profiles of V_θ for the strained vortex shown for various angles (θ) at time $t = 2.88T$.

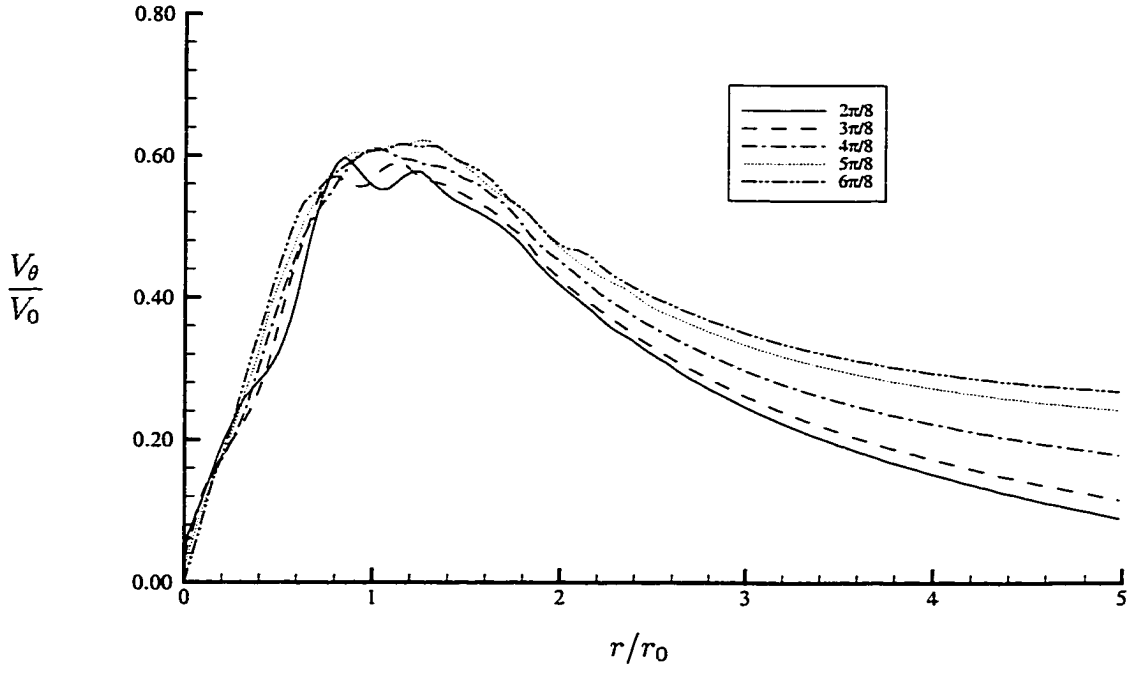

Figure 5.24 Profiles of V_θ for the strained vortex shown for various angles (θ) at time $t = 3.68T$.

Profiles of the mean axial velocity along different rays are shown in Figures 5.22 to 5.24. The peaks of tangential velocity are flattened because of turbulent diffusion. Especially at the time $t = 2.88T$, the tangential velocity appears as a limited constant region near the edge of the vortex core.

5.3.3.3 Turbulent kinetic energy and Reynolds stress

The evolution of the TKE is displayed by a sequence of contour plots shown in Figures 5.25 to 5.29. Once the strained vortex adjusts itself from the unphysical nature of the initial perturbations, the TKE appears as a special structure as shown in Figure 5.25. The peak of the TKE occurs in a strained annular region in which there are three localized peaks along the azimuthal direction because of the effect of the external strain field. However, as shown in Figure 5.26, those three peaks quickly merge once the strained vortex starts the linear growth stage because the lower azimuthal modes ($k_\theta = 1$ and $k_\theta = 2$) dominate, as discussed in Section 5.2.2. At later times during the linearly unstable period, the peak location is pushed towards to the center and the contours form a paired-spiral structure in shape near the origin as shown in Figure 5.27. After the linearly unstable period, as shown in Figure 5.28,

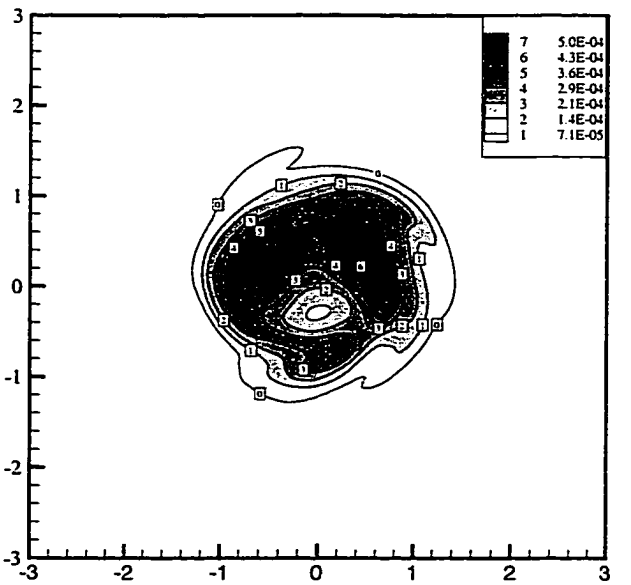

Figure 5.25 Contours of TKE at $t = 1.73T$.

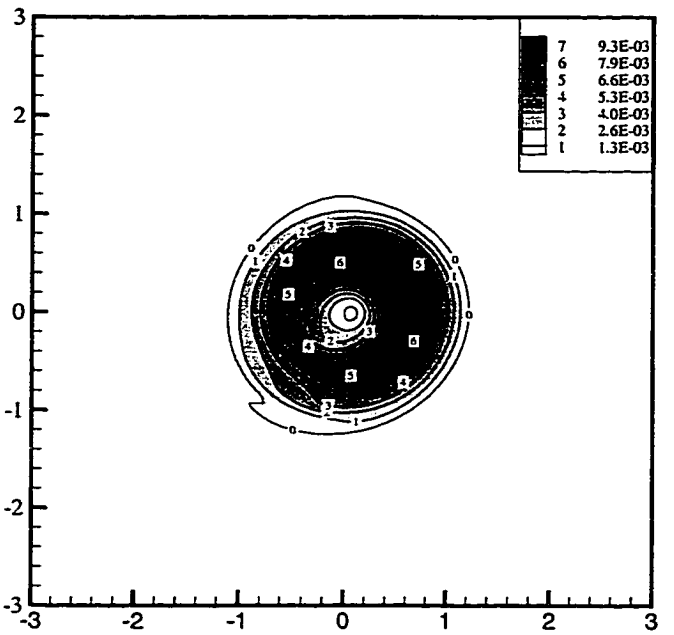

Figure 5.26 Contours of TKE at $t = 2.40T$.

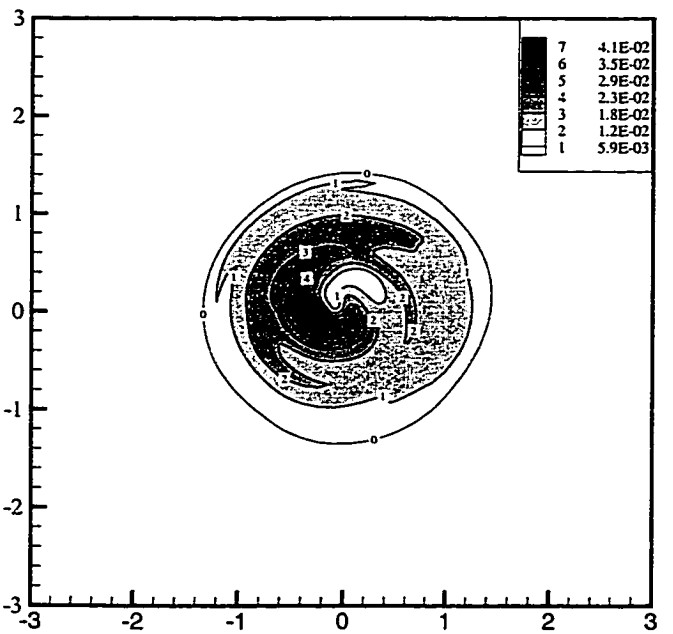

Figure 5.27 Contours of TKE at $t = 2.88T$.

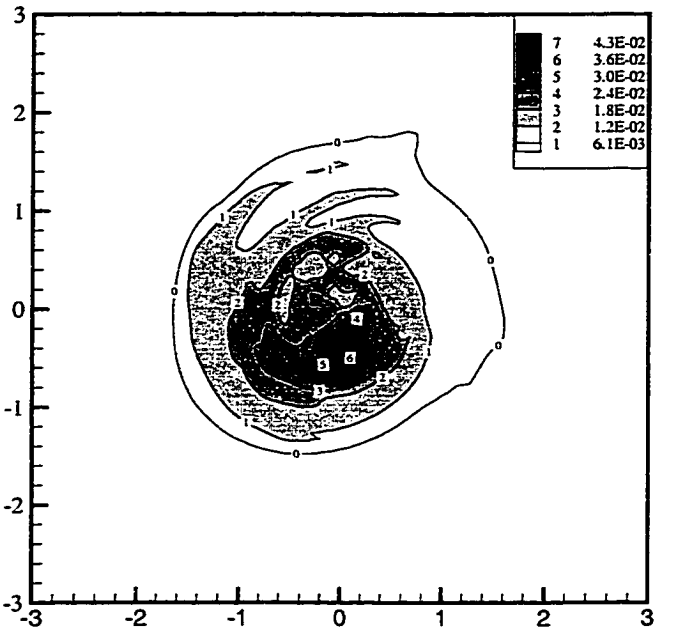

Figure 5.28 Contours of TKE at $t = 3.30T$.

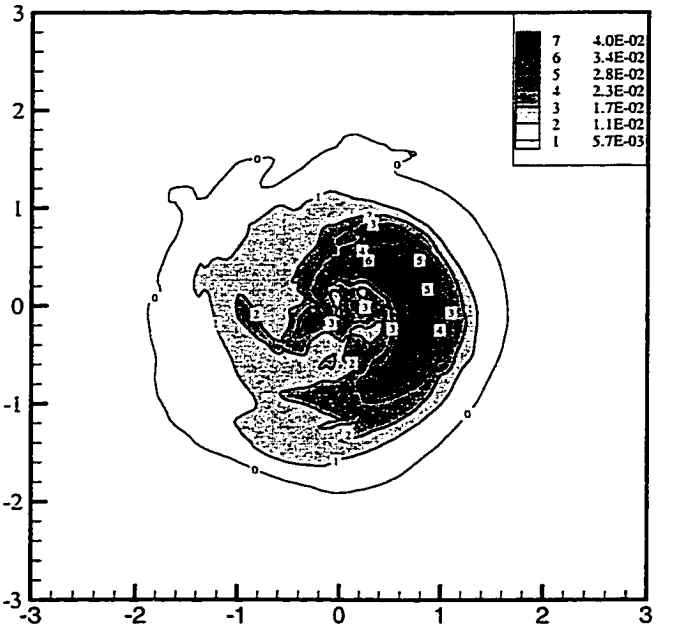

Figure 5.29 Contours of TKE at $t = 3.68T$.

the peak of TKE moves away from the origin by following a spiral trace rather than staying at the origin, as is the case with the isolated vortex. It takes approximately one T for the peak of the TKE to return to the same azimuthal location as shown in Figure 5.29. With the effect of the external strain field, the peak of TKE never reaches the origin of the vortex so that the global TKE continues to grow as shown in the previous section.

The evolution of the Reynolds stress $\overline{v_r' v_z'}$ is displayed by a sequence of contour plots shown in Figures 5.30 to 5.34. At the early times, the contours of stress $\overline{v_r' v_z'}$ have similar structure to that of the TKE except for the opposite sign as shown in Figures 5.30 and 5.31. However, at time $t = 2.88T$ (Figure 5.32), the vortex develops regions of positive stress $\overline{v_r' v_z'}$ because of the effect of the external strain field dominating. At the later time (5.33), not only does the level of positive stress $\overline{v_r' v_z'}$ increase, but the regions also move in the counter clockwise direction which is consistent with the behavior of the TKE. An interesting feature is that the the level of negative stress $\overline{v_r' v_z'}$ does not change from time $t = 2.40T$ to time $t = 3.30T$. Eventually, regions of positive stress $\overline{v_r' v_z'}$ disappear and the level of negative stress $\overline{v_r' v_z'}$ continues to grow.

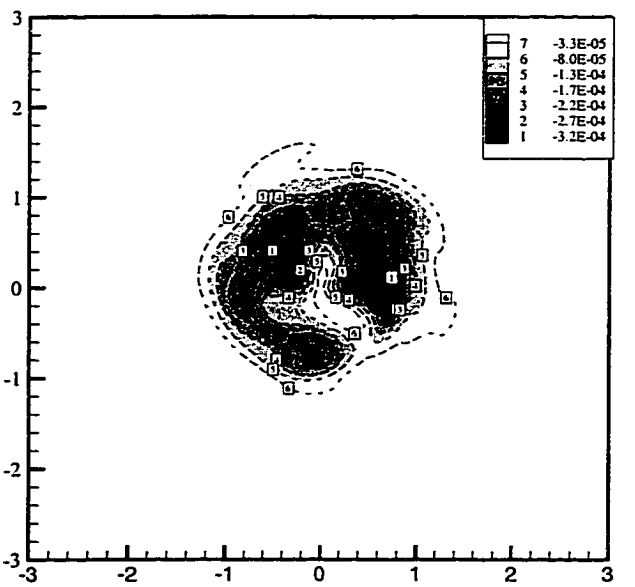

Figure 5.30 Contours of $\overline{v_r' v_z'}$ at $t = 1.73T$.

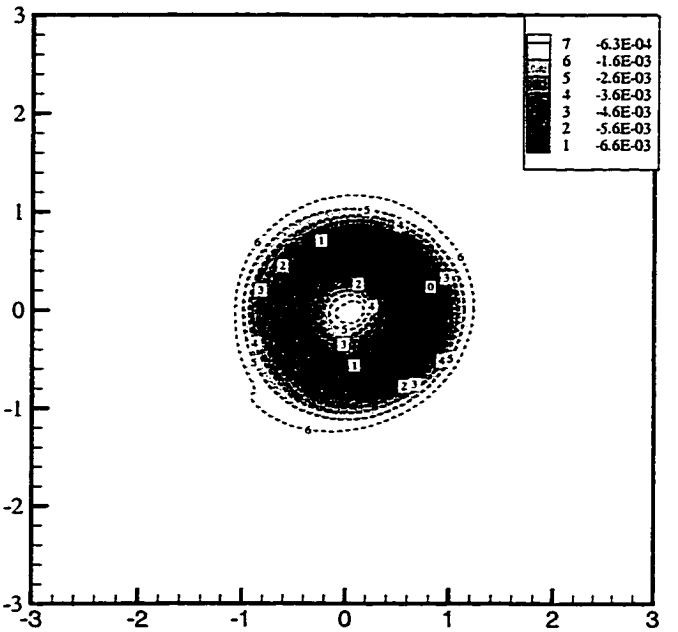

Figure 5.31 Contours of $\overline{v_r' v_z'}$ at $t = 2.40T$.

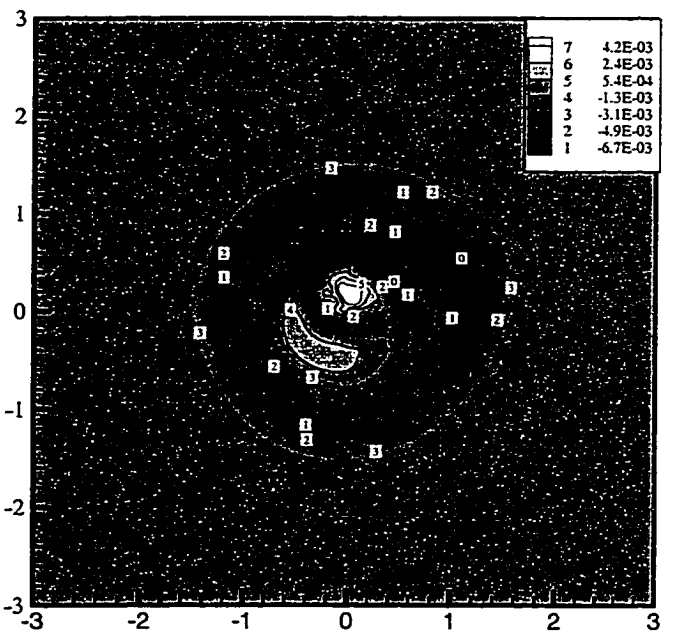

Figure 5.32 Contours of $\overline{v_r' v_z'}$ at $t = 2.88T$.

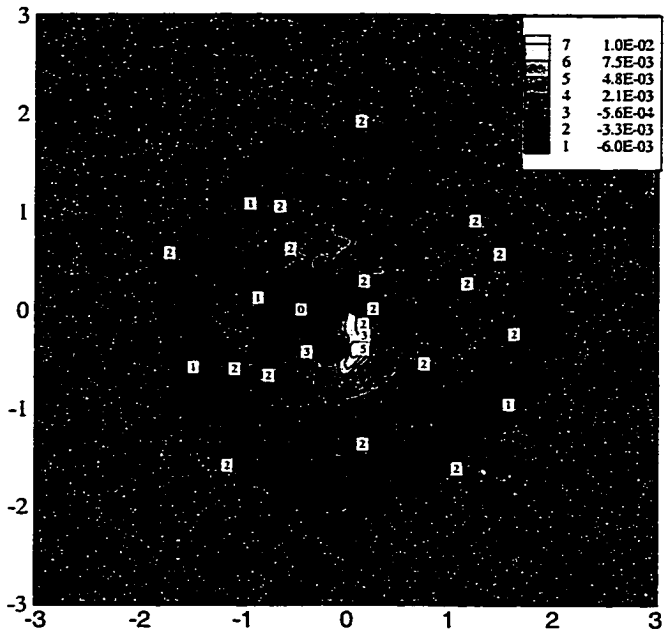

Figure 5.33 Contours of $\overline{v_r' v_z'}$ at $t = 3.30T$.

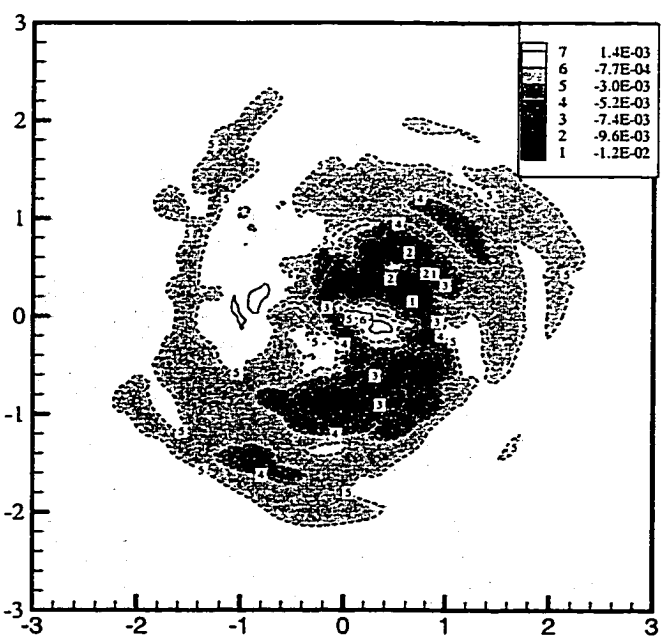

Figure 5.34 Contours of $\overline{v_r' v_z'}$ at $t = 3.68T$.

A time sequence of contours of stress $\overline{v_r' v_\theta'}$ are shown in Figures 5.35 to 5.39. In contrast to the isolated vortex, the strained vortex develops regions of negative stress $\overline{v_r' v_\theta'}$. Once the vortex starts to grow, contours of $\overline{v_r' v_\theta'}$ form a pair of spiral structures shown in Figure 5.36. The negative stress $\overline{v_r' v_\theta'}$ appears around the edge of the vortex core, the positive stress focuses on the inside of the vortex core. However, at time $t = 2.88T$, which is close to the end of the exponential growth stage, regions of negative stress and positive stress switch locations with each other as shown in Figure 5.37 . It seems that the positive stress rotates outwards in the clockwise direction, but the negative stress rotates inwards in the counter clockwise direction. The isolated vortex also shows a region of negative stress near the center at later times. At the later time $t = 3.30T$, as shown in Figure 5.38, the region of negative stress has divided into two subregions. The region of positive stress is quickly enlarged, while both the peaks of negative and positive stress show growth. Figure 5.39 shows a lot of small scale structure because of the limited statistical sample size and because the simulation is not numerically well resolved at this time as mentioned in Section 5.3.3.1.

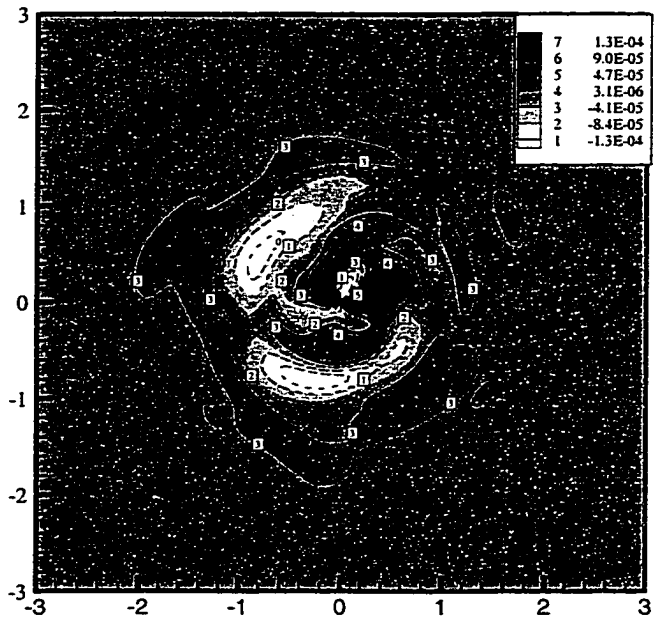

Figure 5.35 Contours of $\overline{v_r' v_\theta'}$ at $t = 1.73T$.

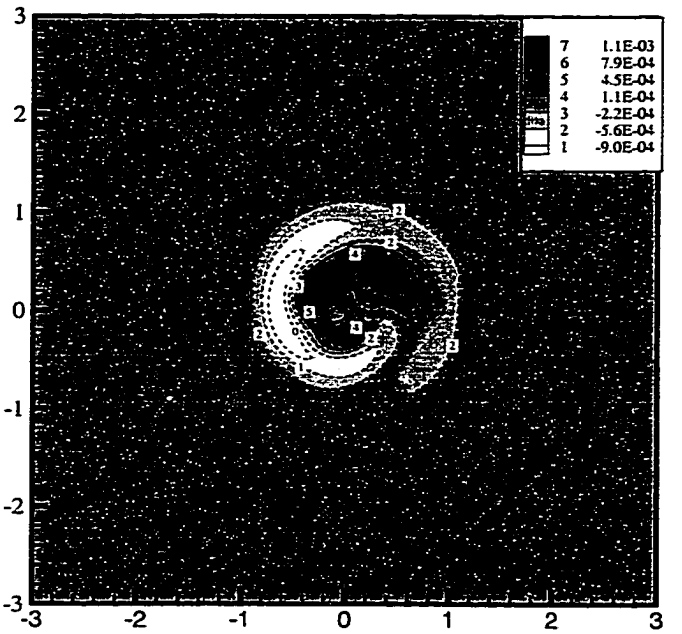

Figure 5.36 Contours of $\overline{v_r' v_\theta'}$ at $t = 2.40T$.

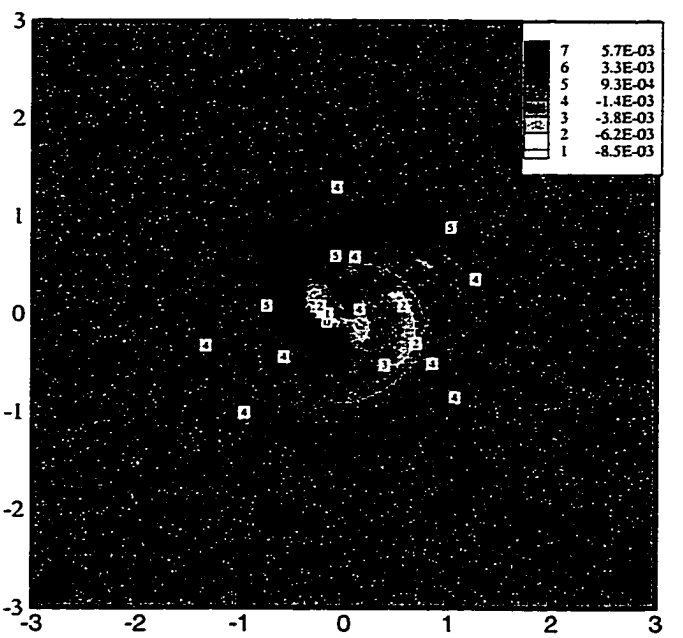

Figure 5.37 Contours of $\overline{v_r' v_\theta'}$ at $t = 2.88T$.

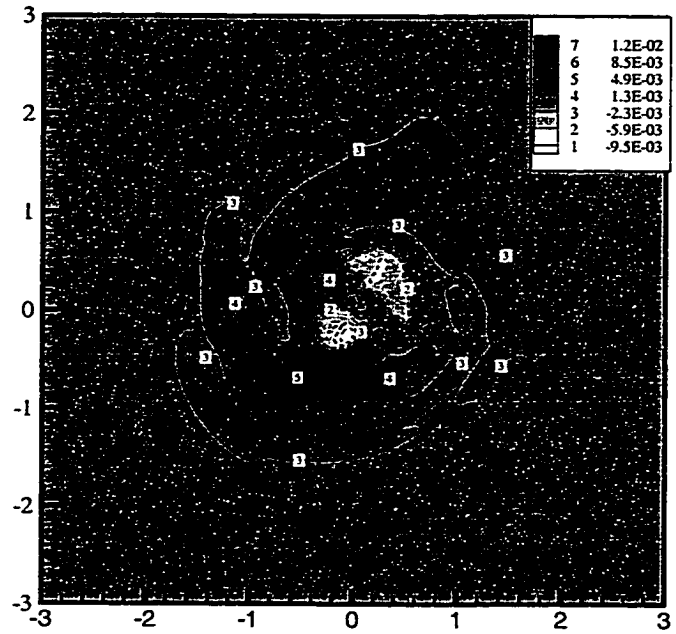

Figure 5.38 Contours of $\overline{v_r' v_\theta'}$ at $t = 3.30T$.

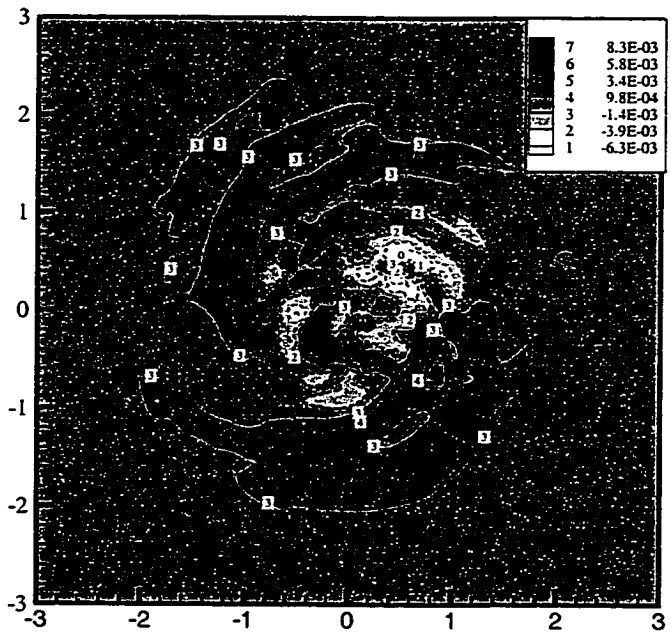

Figure 5.39 Contours of $\overline{v_r' v_\theta'}$ at $t = 3.68T$.

Figures 5.40 to 5.42 show profiles of the TKE along different rays for three different times. At an early time of $t = 2.40T$, the peak of TKE is roughly located at $r \approx 0.6r_0$ which is same as the value of the isolated vortex, and $\theta = \pi/4$. With the decay of the wake, the peak moves to the location of $r \approx 0.3r_0$ which also matches the value of the isolated vortex, and $\theta = \pi$, as shown in Figure 5.41. At a later time of $t = 2.88T$, the peak moves away from the origin to $r \approx 0.6r_0$ which is not the same as for the isolated vortex. It is clear that the effect of external strain field results in the different turbulence structure for the strained vortex.

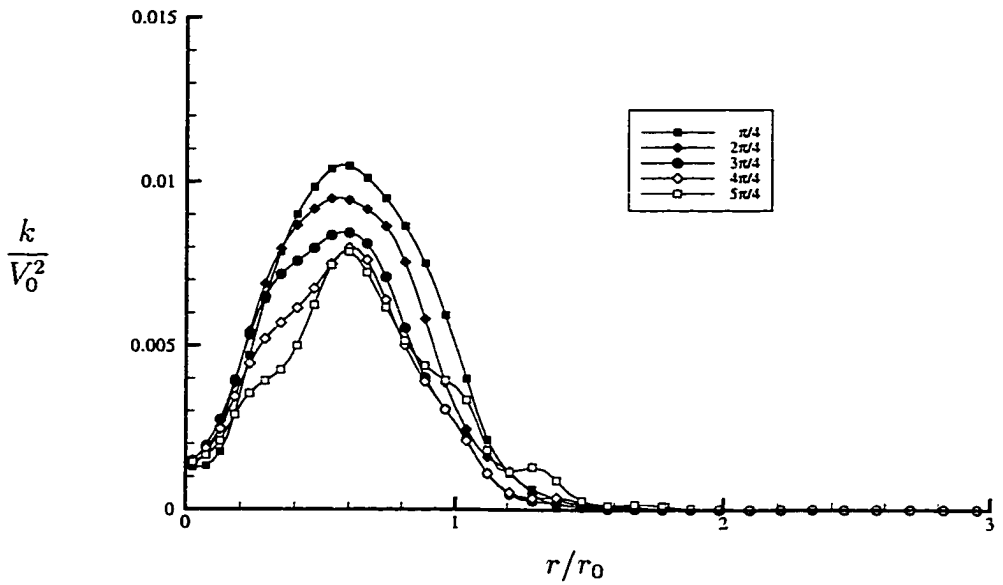

Figure 5.40 Profiles of TKE for the strained vortex shown for various angles (θ) at $t = 2.40T$.

Profiles of the stress $\overline{v_r' v_z'}$ along different rays for the same three times are also shown in Figures 5.43 to 5.45 . At an early time of $t = 2.40T$ (Figure 5.43), since the effect of the wake is dominant, the stress $\overline{v_r' v_z'}$ is seen to be negative as in the isolated vortex. However, the results are not axisymmetric. When the effect of the external strain field becomes dominant over the decay of the wake, a large region of positive stress $\overline{v_r' v_z'}$ develops in the strained vortex at the later times as shown in Figures 5.44 and 5.45.

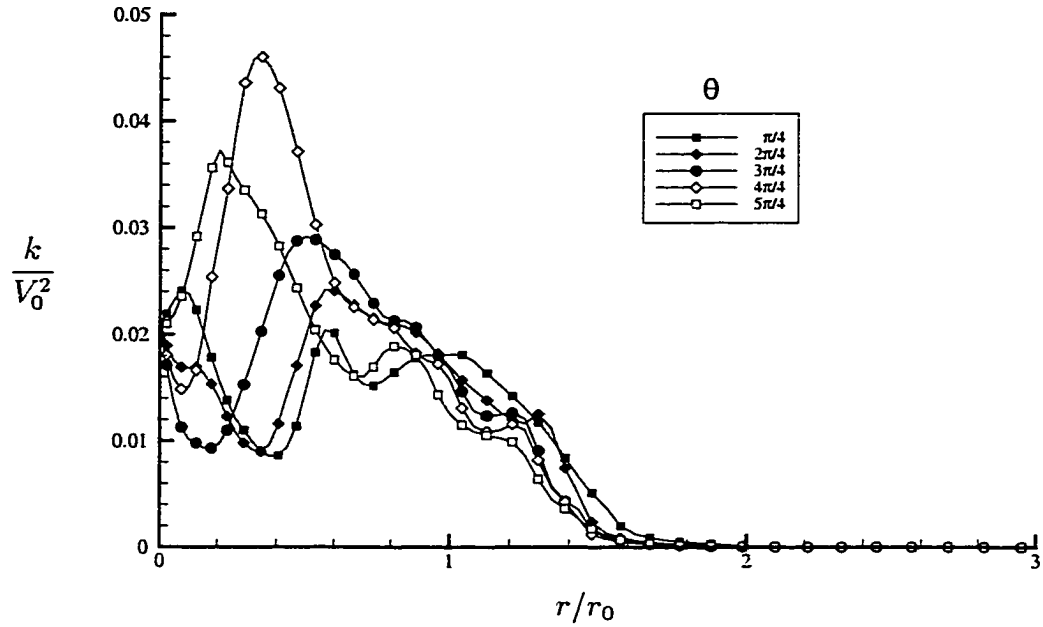

Figure 5.41 Profiles of TKE for the strained vortex shown for various angles (θ) at $t = 2.88T$.

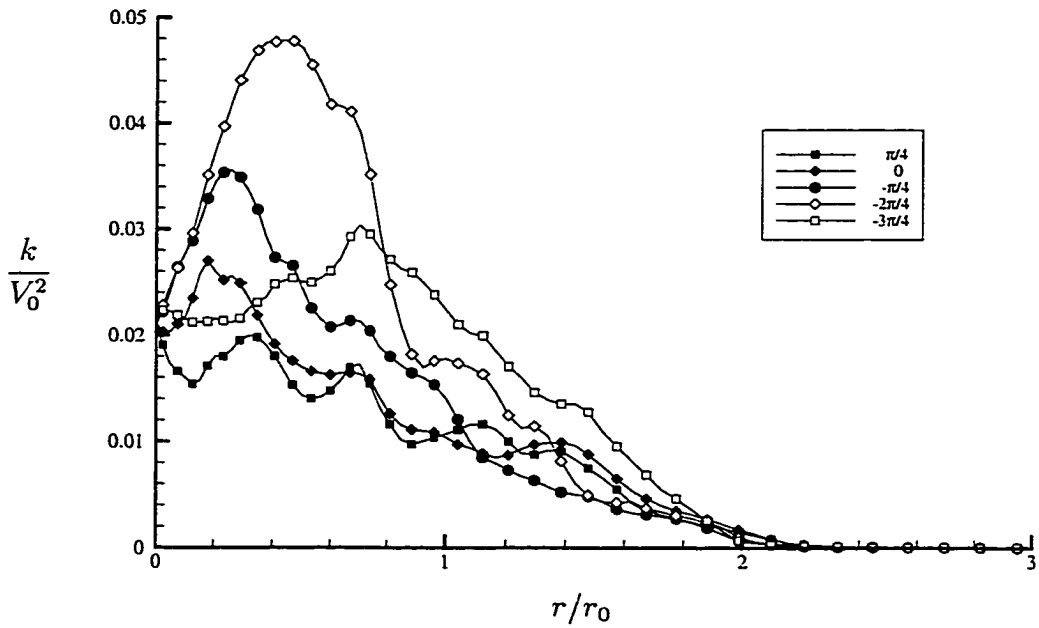

Figure 5.42 Profiles of TKE for the strained vortex shown for various angles (θ) at $t = 3.30T$.

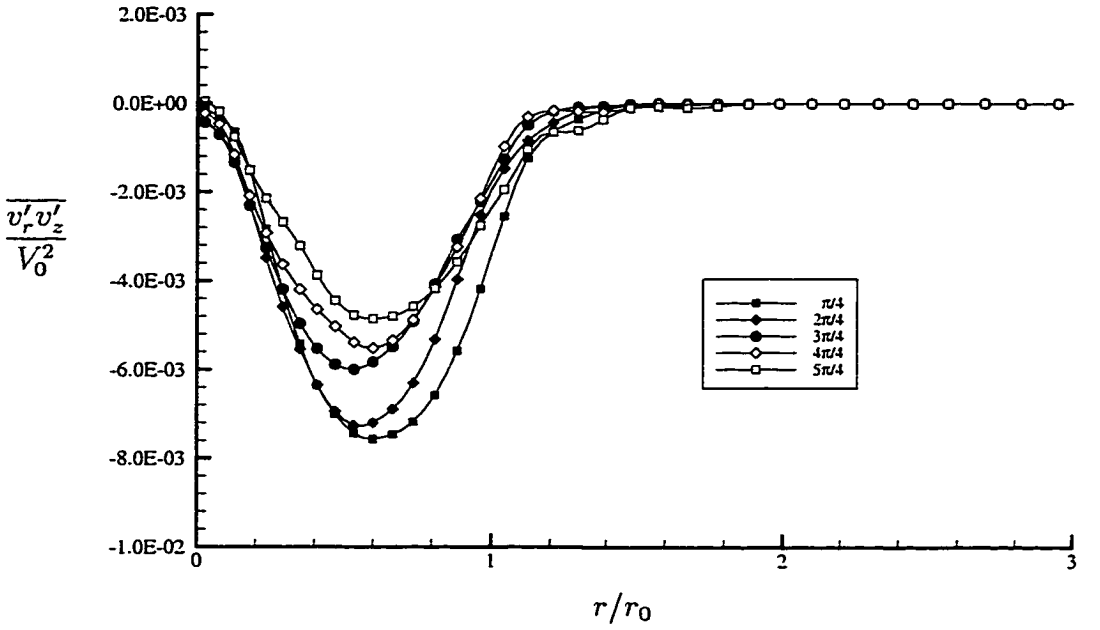

Figure 5.43 Profiles of $\overline{v_r' v_z'}$ for the strained vortex shown for various angles (θ) at $t = 2.40T$.

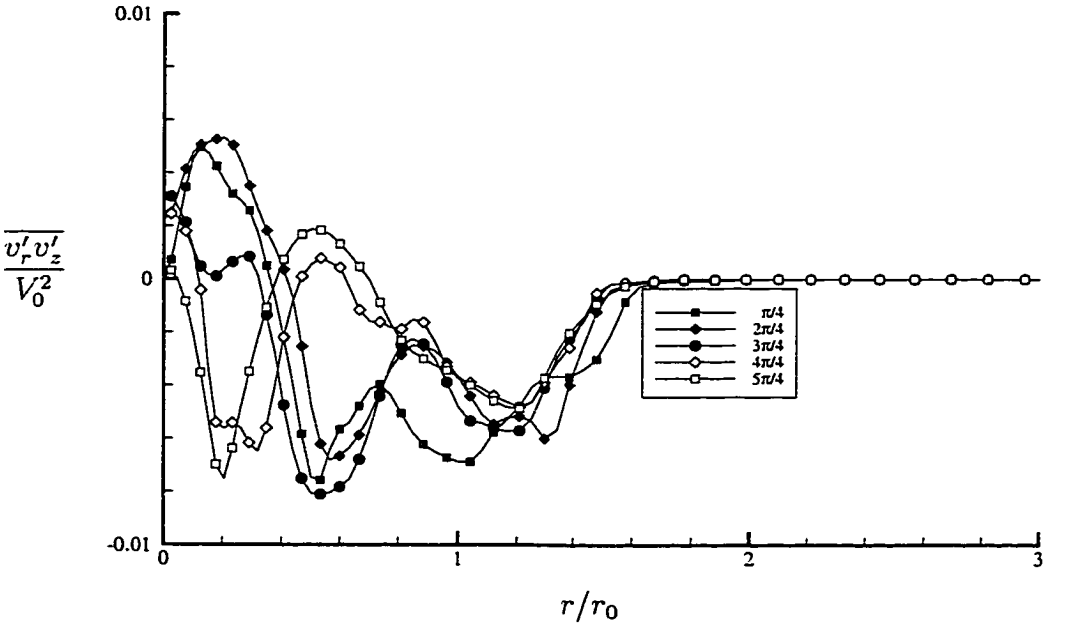

Figure 5.44 Profiles of $\overline{v_r' v_z'}$ for the strained vortex shown for various angles (θ) at $t = 2.88T$.

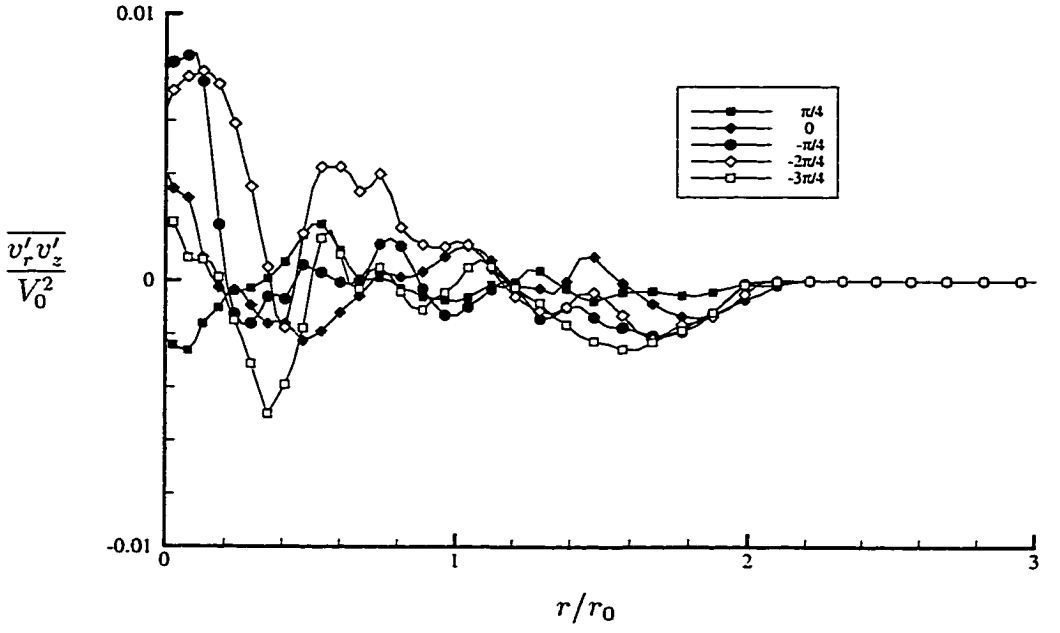

Figure 5.45 Profiles of $\overline{v_r' v_z'}$ for the strained vortex shown for various angles (θ) at $t = 3.30T$.

Figures 5.46 to 5.48 display profiles of the stress $\overline{v_r' v_\theta'}$ along different rays for the same three times. It is clear that a large region of negative stress $\overline{v_r' v_\theta'}$ develops in the vortex because of the effects of the external strain field. Unlike the isolated vortex, the peak of the stress $\overline{v_r' v_\theta'}$ does not move to the location $r \approx 2.0 r_0$ at later times.

5.4 Summary of the Strained Vortex

Direct numerical simulations of the strained vortex have been performed by using the B-spline spectral method. The numerical method and the parallelization of computer code are first validated by the simulation of isolated vortex. Results of the B-spline method qualitatively match well with those from the pseudo-spectral method. For the isolated vortex, all modes start an exponential growth after a short transition period. The relaminarizing process is captured by visualization.

The Widnall instability in the strained Oseen vortex is shown to be difficult to capture because of the localized effects for a low strain rate. An extremely high

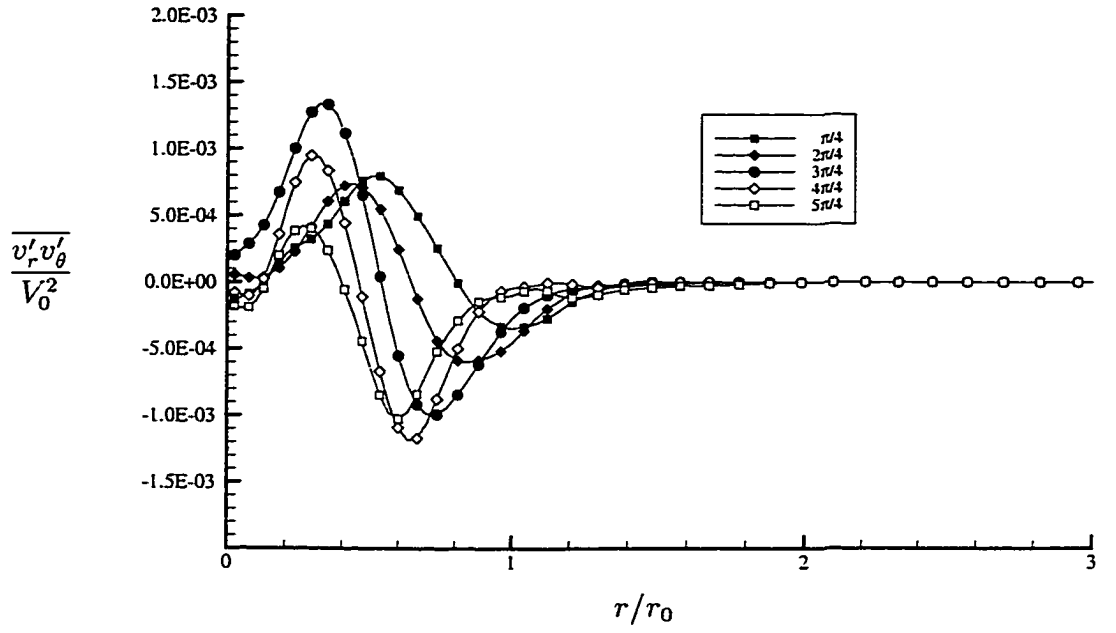

Figure 5.46 Profiles of $\overline{v_r' v_\theta'}$ for the strained vortex shown for various angles (θ) at $t = 2.40T$.

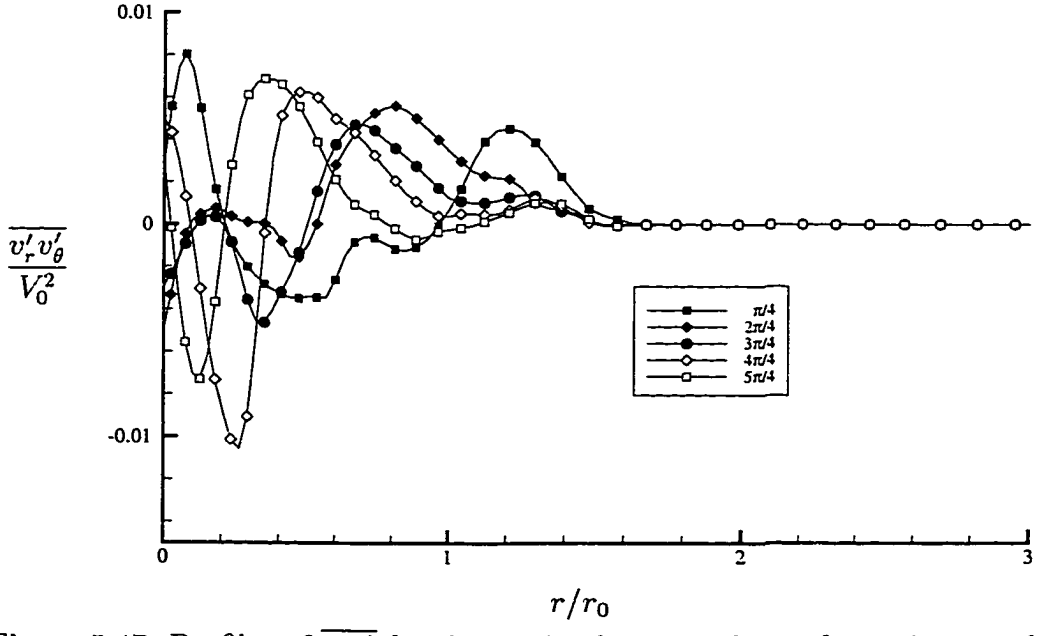

Figure 5.47 Profiles of $\overline{v_r' v_\theta'}$ for the strained vortex shown for various angles (θ) at $t = 2.88T$.

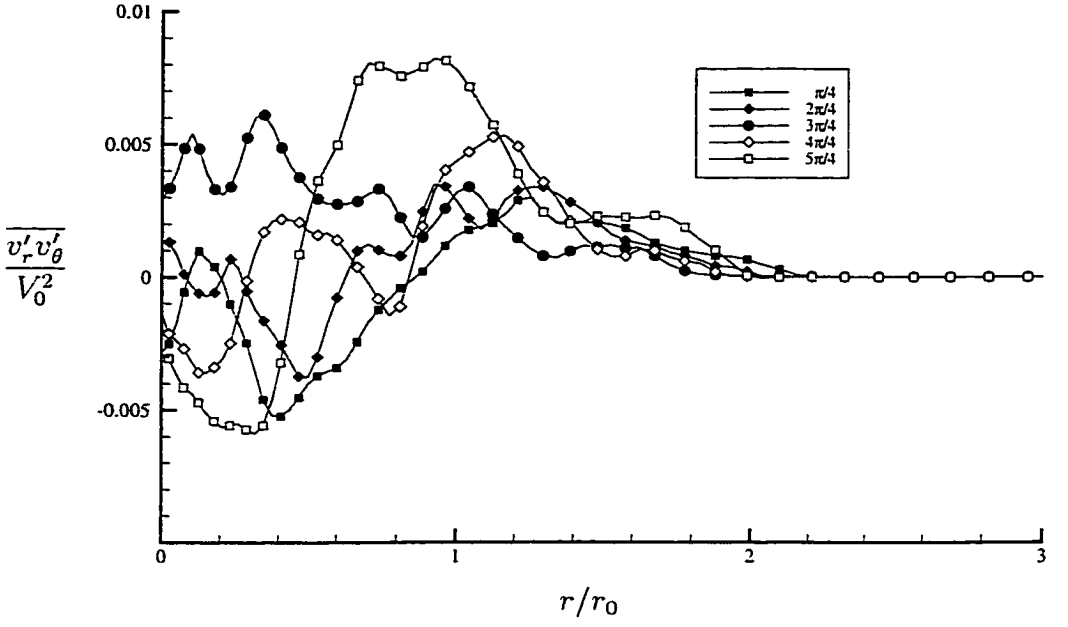

Figure 5.48 Profiles of $\overline{v_r' v_\theta'}$ for the strained vortex shown for various angles (θ) at $t = 3.30T$.

Reynolds number is needed to completely catch the instability in the strained Oseen vortex.

The Widnall instability has been captured in the simulations of the strained vortex with axial flow. Because of the presence of the Widnall instability, the strained vortex is unstable for all time. For a weak strain field, the Reynolds number has to be chosen to be large enough to capture the Widnall instability.

With the effects of the external strain field, the turbulence structure inside the vortex is altered. The peak of the TKE moves towards the center of the vortex core during the linearly unstable period, but moves outwards before it reaches the center. In addition, the location of the peak varies along the azimuthal direction. The Reynolds stresses no longer have a uniform sign inside the vortex core. Since as mentioned in Chapter 3, the negative eddy viscosity in the isolated vortex is associated with an opposite sign of the Reynolds stresses, there may be a negative eddy viscosity in the region with a negative value of $\overline{v_r' v_\theta'}$. This is left for future work to determine.

With the limitation of available computer resources, the results of Case STRN2 are not numerically well resolved at later times ($t > 4.0T$). Simulations with higher Reynolds numbers are needed for further study.

6. CONCLUSIONS AND RECOMMENDATIONS

A study of turbulent axial vortices has been conducted by using direct numerical simulation. Two classes of axial vortices have been considered: an isolated vortex and a strained vortex. A detailed analysis of the Reynolds stress budgets on the isolated vortex has also been completed in order to understand the turbulent transport in the vortex. Based on simulations and analysis, a summary of conclusions is presented below followed by recommendations for future work.

6.1 Summary of Conclusions

6.1.1 Isolated vortex

The simulations of an isolated turbulent axial vortex show that the evolution of the global TKE is independent of the initial profile of the fluctuating velocity. The isolated vortex is stable unless the mean axial wake flow has sufficient magnitude. However, with the decay of the deficit, the centrifugally stabilizing motion of the vortex core takes over the destabilizing effect of the isolated vortex. Eventually, the isolated vortex returns towards a laminar state, but with a weakened wake deficit.

According to the behavior of the global TKE, the development of the isolated vortex can be divided into five periods: transition, linearly unstable, unstable, saturating, and relaminarizing. The mean wake deficit shows a decay during the development of the isolated vortex, but a negative eddy viscosity in the region near the center of the vortex results in the mean tangential velocity profile exhibiting anti-diffusion during the saturating and relaminarizing periods.

The features of the TKE profile are related to the development of the isolated vortex. During the linearly unstable and unstable periods, the peak of the TKE

occurs in an annular region and moves towards the edge of the vortex. During the saturating period, the peak of TKE moves towards the center of vortex. Once the peak of the TKE reaches the center of the vortex, the vortex decays and the peak stays at the center of the vortex. The stress $\overline{v_r' v_\theta'}$ shows a different sign near the center of the vortex during the relaminarizing period. A similar feature is shown in the stress $\overline{v_r' v_z'}$ but with the opposite sign. The presence of the different sign in the Reynolds stresses $\overline{v_r' v_\theta'}$ and $\overline{v_r' v_z'}$ is the key factor of the negative eddy viscosity being created.

By analyzing budgets of the Reynolds stresses, the production term is the dominant term in the Reynolds stress budgets, but it is the pressure strain, pressure transport, and the turbulent transport terms that cause the complicated behavior in the profiles of the Reynolds stresses. It is impossible to model each individual term such as the pressure strain term, pressure transport term, as well as the turbulent transport term, since these terms show complicated oscillating behaviors during the development of the isolated vortex. However, an interesting feature is that the pressure transport term and the turbulen transport term in the TKE equation almost cancel each other. This is a valuable piece of information with which to generate a new turbulence model for the vortex.

The formation of helical vortices is an important phenomenon. The helical vortices sweep the outside fluid with low momentum inward and eject inner fluid with high momentum outward. Therefore, the helical vortex structures are responsible for the generation of the Reynolds stress.

6.1.2 Strained vortex

A preliminary study of the effects of an external strain field on an axial vortex has been completed. The Widnall instability in the strained Oseen vortex is difficult to capture for a weak strain rate. This is because of two reasons: first, the grid could not be perfectly aligned with the most unstable wave vector, because the grid size is

stretched in the radial direction. Second, most regions in the vortex core are locally stable for the current Reynolds number.

The Widnall instability in the strained q vortex has been successfully caught in this work. The strained vortex does not stabilize at later time with the decay of wake. The turbulent structure within the strained vortex is altered by the presence of the external strain. The peak of the TKE never reaches the center of the vortex core, so the vortex remains unstable. This is an important result, because it means that aircraft wake vortices will remain turbulent rather than relaminarizing downstream. In addition, the strained vortex forms a paired-spiral structure in Reynolds stresses $\overline{v_r' v_\theta'}$ and $\overline{v_r' v_z'}$. The Reynolds stresses are no longer of uniform sign inside the vortex core.

6.2 Recommendations for Future Work

There are not only many unanswered issues left after this study, but also a number of interesting issues that have been raised in this study. Some of them deserve future study.

- Based on the completion of the isolated vortex simulations in this study, it would be interesting to simulate the isolated vortex by using existing Reynolds stress models. The comparison for each term based on the budget analysis in this study could be very valuable for modifying existing turbulence models.

- Future simulations for the strained vortex with higher resolution are required to complete the investigation of the effect of strain on the instability of the axial vortex. A larger sample size in the streamwise direction is also expected to improve the quality of the statistical quantities.

- A complete budget analysis of the strained vortex warrants a future study to see which terms drive the peak of the TKE away from the center of the vortex, which is a distinguishing feature in the strained vortex. The visualization of iso-contours of the pressure strain term, the pressure transport term, and turbulent

transport term could be useful to see how the strain affects the development of the vortex.

- A large eddy simulation (LES) of the turbulent axial vortex deserves a future study. The strain rate, in practice, is smaller than in this study. So, to capture the Widnall instability, simulations need to be run at a very large Reynolds number, which is impossible for DNS with the existing limitations on computer resources.

- Currently, constant potential flow is imposed on the whole boundary. Obviously, artificial vorticity is generated by specifying Dirichlet boundary conditions on the outflow boundary, since with elliptic-like streamlines in the cross section, the strained vortex creates inflow and outflow at the boundary. In this study, the artificial vorticity is negligible for a small strain rate, but its effects are uncertain for a large strain rate. If the effects of a large strain rate on the vortex need to be investigated, a conformal mapping which maps the strained physical domain to a circular computational domain should be considered. This eliminates the artificial vorticity on the boundary.

LIST OF REFERENCES

LIST OF REFERENCES

Baker, G. R., Bofah, K. K. & Saffman, P. G. (1974), 'Laser anemometer measurements of trailing vortices in water', *Journal of Fluid Mechanics* **65**, 325–336.

Bandyopadhyay, P. R., Stead, D. J. & Ash, R. L. (1991), 'Organized nature of turbulent trailing vortex', *AIAA Journal* **29**(10), 1627–1633.

Batchelor, G. K. (1964), 'Axial flow in trailing vortices', *Journal of Fluid Mechanics* **20**, 646–658.

Bayly, B. J. (1986), 'Three-dimensional instability of elliptical flow', *Physics Review Letter* **57**, 2160–2163.

Blaisdell, G. A. & Shariff, K. (1994), 'Homogeneous turbulence subjected to mean flow with elliptical streamlines', in *Proceedings of the 1994 center for Turbulence Research Summer Program,* Stanford/NASA Ames pp. 355–371.

Blaisdell, G. A. & Shariff, K. (1996), 'Simulation and modeling of the elliptic streamline flow', in *Proceedings of the 1996 center for Turbulence Research Summer Program,* Stanford/NASA Ames.

Blaisdell, G. A., Mansour, N. N. & Reynolds, W. C. (1991), 'Numerical simulations of compressible homogeneous turbulence', Technical report TF-50, Department of Mechanical Engineering, Stanford University, Stanford, CA 94305.

Blaisdell, G. A., Spyropoulos, E. T. & Qin, J. H. (1996), 'The effect of the formulation of nonlinear terms on aliasing errors in spectral methods', *Applied numerical mathematics* **21**, 207–219.

Bradshaw, P. (1988), 'Physics and prediction of turbulent flows', Lecture Notes.

Cain, A. B., Ferziger, J. H. & Reynolds, W. C. (1984), 'Discrete orthogonal function expansions for non-uniform grids using the fast fourier transform', *Journal of Computational Physics* **56**, 272–286.

Cambon, C., Benoit, J. P., Shao, L. & Jacquin, L. (1994), 'Stability analysis and large-eddy simulation of rotating turbulence with organized eddies', *Journal of Fluid Mechanics.*

Cambon, C., Teissédre, C. & Jeandel, D. (1985), 'Etude d'éffets couplés de déformation et de rotation sur une turbulence homogéne', *J. Méc. Théo. Appl.*

Chigier, N. A. & Corsiglia, V. R. (1972), 'Wind-tunnel studies of wing wake turbulence', *Journal of Aircraft* **9**, 820–825.

Chow, J. S. (1994), 'Turbulence measurement in the near-field of a wingtip vortex', Technical report MD-69, Department of Mechanical Engineering, Stanford University, Stanford, CA 94305.

Chow, J. S. & Zilliac, G. G. (1994), 'Turbulence measurements in the near-field of wingtip vortex', in *Turbulence in Complex Flows,* Vol. 203 of FED, ASME pp. 61–78.

Crow, S. C. (1970), 'Stability theory for a pair of trailing vortices', *AIAA Journal* **8**(12), 2172–2179.

de Boor, C. (1978), *A practical guide to splines*, Vol. 27 of *Applied mathematical science*, Springer-Verlag.

Devenport, W. J., Rife, M. C., Liapis, S. I. & Follin, G. J. (1996), 'The structure and development of a wing-tip vortex', *Journal of Fluid Mechanics* **312**, 67–106.

Donaldson, C. D. (1972), 'Calculation of turbulent shear flows for atmospheric vortex motions', *AIAA Journal* **10**(1), 4–12.

Duck, P. W. & Khorrami, M. R. (1991), 'On the effects of viscosity on the stability of a trailing vortex', *ICASE* 91-6 pp. 524–532.

Govindaraju, S. P. & Saffman, S. P. (1971), 'Flow in turbulent trailing vortex', *Physics of Fluids* **14**(10), 2074–2080.

Hoffmann, E. R. & Joubert, P. N. (1963), 'Turbulent line vortices', *Journal of Fluid Mechanics* **16**, 395–411.

Iversen, J. D. (1976), 'Correlation of turbulent trailing vortex decay data', *Journal of Aircraft,* **13**(5).

Khorrami, M. R. (1991), 'On the viscous modes of instability of a trailing line vortex', *Journal of Fluid Mechanics* **225**, 197–212.

Landman, M. J. & Saffman, P. G. (1987), 'The 3-d instability of strained vortices in a viscous fluid', *Physics of Fluids* **30**, 2339–2342.

Leibovich, S. & Stewartson, K. (1983), 'A sufficient condition for the instability of columnar vortices', *Journal of Fluid Mechanics* **126**, 335–356.

Leonard, A. & Wray, A. (1982), 'A new numerical method for simulation of three-dimensional flow in pipe', Lecture notes in Physics, Springer-Verlag, New York. ed. Krause, E.

Lessen, M. & Paillet, F. (1974), 'The stability of trailing line vortex. part2. viscous theory', *Journal of Fluid Mechanics* **65**, 769–779.

Lessen, M., Singh, P. J. & Paillet, F. (1974), 'The stability of trailing line vortex. part1. inviscid theory', *Journal of Fluid Mechanics* **63**, 753–763.

Loulou, P. (1996), Direct numerical simulation of incompressible pipe flow using a b-spline spectral method, PhD thesis, Department of Aeronautics and Astronautics, Stanford University, Stanford, CA 94305.

Mayer, E. W. & Powell, K. G. (1992), 'Viscous and inviscid instabilities of a trailing vortex', *Journal of Fluid Mechanics* **245**, 91–114.

Moore, D. W. & Saffman, P. G. (1972), 'The motion of a vortex filament with axial flow', *Phil. Trans. Ruyal society* **272**, 403–429.

Moser, R. D., Moin, P. & Leonard, A. (1983), 'A spectral numerical method for the Navier-Stokes equations with applications to Taylor-Couette flow', *Journal of Computational Physics* **52**, 524–544.

Orszag, S. A. (1971), 'On the elimination of aliasing in finite-difference schemes by filtering high wavenumber components', *Journal of Atmospherical Science* **28**, 1074.

Panton, R. L. (1984), *Incompressible Flow*, John Wiley & Son.

Peierrehumbert, R. T. (1986), 'Universal short-wave instability of two-dimensional eddies in an inviscid fluid', *Physics Review Letter* **57**, 2157–2159.

Phillips, W. R. C. (1981), 'The turbulent trailing vortex during roll-up', *Journal of Fluid Mechanics* **105**, 451–467.

Phillips, W. R. C. & Graham, J. A. H. (1984), 'Reynolds-stress measurements in turbulent trailing vortex', *Journal of Fluid Mechanics* **147**, 353–371.

Ragab, S. & Sreedhar, M. (1994), 'Large-scale structures in a trailing vortex', *AIAA Paper* 94-2316.

Ragab, S. & Sreedhar, M. (1995*a*), 'Direct numerical simulation of instability waves in a trailing vortex', *AIAA Paper* 95-0591.

Ragab, S. & Sreedhar, M. (1995*b*), 'Numerical simulation of vortices with axial velocity deficits', *Physics of Fluids* **A 7**(3), 549–558.

Rayleigh, L. (1916), 'On the dynamics of revolving fluids', *Proceedings of the Royal Society of London A* **93**, 148–154.

Reimer, H. (1997), 'A preliminary study of a wake encounter hazard boundary', *AIAA Paper*. 97-0008.

Reynolds, W. C. (1987), 'Turbulence modeling and simulation', Lecture Notes for Von Karman Institute, Department of Mechanical Engineering, Stanford University.

Sampson, G. G. (1977), 'An experimental and theoretical investigation of the structure of a trailing vortex wake', *Aero. Qtrly.* **28**, 39–50.

Sarpkaya, T. & Daly, J. J. (1987), 'Effect of ambient turbulence on trailing vortices', *Journal of Aircraft* **24**(6), 399–404.

Shariff, K., Verzico, R. & Orlandi, P. (1994), 'A numerical study of three-dimentional vortex ring instabilities: viscous corrections and early nonlinear stage', *Journal of Fluid Mechanics* **279**, 351–375.

Singh, A. J. & Uberoi, M. S. (1976), 'Experiments on vortex stability', *Physics of Fluids* **19**, 1858–1863.

Smith, A. J. & Kummer, R. P. (1985), 'The interaction and merger of two turbulent line vortices', *AIAA Paper* 85-0046.

Spalart, P. R. (1996), 'On the motion of aircraft wakes in a stratified fluid', *Journal of Fluid Mechanics* **327**, 139–160.

Spalart, P. R., Moser, R. D. & Rogers, M. M. (1991), 'Spectral methods for navier-stokes equations with one infinite and two periodic directions', *Journal of Computational Physics* **96**, 297–324.

Sreedhar, M. & Ragab, S. (1994), 'Large eddy simulation of longitudinal stationary vortices', *Physics of Fluids* **A 6**(7), 2501–2514.

Takahashi, R. K. & McAlister, K. W. (1987), Preliminary study of a wing-tip vortex using laser velocimetry, Technical Report NASA TM 88343.

Uberoi, M. S. (1979), 'Mechanisms of decay of laminar and turbulent vortices', *Journal of Fluid Mechanics* **90**, 241–255.

Waleffe (1990), 'On the three-dimensional instability of strained vortices', *Physics of Fluids* **A 2**(1), 76–80.

Widnall, S. E., Bliss, D. B. & Tsai, C.-Y. (1974), 'The instability of short waves on a vortex ring', *Journal of Fluid Mechanics* **66**, 35–74.

Widnall, S. E. & Sullivan, J. P. (1973), 'On the stability of vortex rings', *Proceedings of the Royal Society of London A* **332**, 335–353.

Wray, A. A. (1986), 'Very low storage time-advancement schemes', Unpublished technical report, NASA Ames Research Center.

Zang, T. A. (1991), 'On the rotational and skew-symmetric forms for incompressible flow simulations', *Applied numerical mathematics* **7**, 27–40.

Zeman, O. (1995), 'The persistence of trailing vortices: a modeling study', *Physics of Fluids* **A 7**, 135–143.

Zheng, Z. & Ash, R. L. (1993), 'Prediction of turbulent wake vortex motion near the ground', in *Transitional and Turbulent Compressible Flows,* Vol. 203 of FED, ASME pp. 195–207.

APPENDICES

Appendix A: The Transport Equations for Reynolds Stress in Cylindrical Coordinates

In this appendix the transport equations for Reynolds stresses in cylindrical coordinates are presented. The equations in tensor form are given by

$$\frac{\partial}{\partial t}\left(\overline{u_i' u_j'}\right) = C_{ij} + P_{ij} + O_{ij} + \Pi_{ij} + Tt_{ij} + Pt_{ij} + D_{ij} - \epsilon_{ij} \tag{A.1}$$

where C_{ij} is the convection; P_{ij}, the production; O_{ij}, the rotation; Π_{ij}, the pressure strain; Tt_{ij}, the turbulent transport; Pt_{ij}, the pressure transport; D_{ij}, the viscous diffusion; and ϵ_{ij}, the dissipation. Each of these terms has been expanded in cylindrical coordinates and listed in the equations that follow. In these equations, subscripts refer to the component. For example, v_r' is the fluctuation part of the radial velocity and $P_{r\theta}$ is the production term in the equation for $\overline{v_r' v_\theta'}$.

- Convection terms C_{ij}

$$C_{rr} = -V_r\frac{\partial(\overline{v_r'^2})}{\partial r} - \frac{V_\theta}{r}\left(\frac{\partial(\overline{v_r'^2})}{\partial \theta} - 2\overline{v_r' v_\theta'}\right) + V_z\frac{\partial(\overline{v_r'^2})}{\partial z}; \tag{A.2}$$

$$C_{\theta\theta} = -V_r\frac{\partial(\overline{v_\theta'^2})}{\partial r} - \frac{V_\theta}{r}\left(\frac{\partial(\overline{v_\theta'^2})}{\partial \theta} + 2\overline{v_r' v_\theta'}\right) - V_z\frac{\partial(\overline{v_\theta'^2})}{\partial z}; \tag{A.3}$$

$$C_{zz} = -V_r\frac{\partial(\overline{v_z'^2})}{\partial r} - \frac{V_\theta}{r}\frac{\partial(\overline{v_z'^2})}{\partial \theta} - V_z\frac{\partial(\overline{v_z'^2})}{\partial z}; \tag{A.4}$$

$$C_{r\theta} = -V_r\frac{\partial(\overline{v_r' v_\theta'})}{\partial r} - \frac{V_\theta}{r}\left(\frac{\partial(\overline{v_r' v_\theta'})}{\partial \theta} + \overline{v_r'^2} - \overline{v_\theta'^2}\right) - V_z\frac{\partial(\overline{v_r' v_\theta'})}{\partial z}; \tag{A.5}$$

$$C_{rz} = -V_r\frac{\partial(\overline{v_r' v_z'})}{\partial r} - \frac{V_\theta}{r}\left(\frac{\partial(\overline{v_r' v_z'})}{\partial \theta} - \overline{v_\theta' v_z'}\right) - V_z\frac{\partial(\overline{v_r' v_z'})}{\partial z}; \tag{A.6}$$

$$C_{\theta z} = -V_r\frac{\partial(\overline{v_\theta' v_z'})}{\partial r} - \frac{V_\theta}{r}\left(\frac{\partial(\overline{v_\theta' v_z'})}{\partial \theta} + \overline{v_r' v_z'}\right) - V_z\frac{\partial(\overline{v_\theta' v_z'})}{\partial z}; \tag{A.7}$$

- The production terms P_{ij}

$$P_{rr} = -2\left[\frac{\partial V_r}{\partial r}\overline{v_r'^2} + \frac{1}{r}\left(\frac{\partial V_r}{\partial \theta} - V_\theta\right)\overline{v_r' v_\theta'} + \frac{\partial V_r}{\partial z}\overline{v_r' v_z'}\right]; \tag{A.8}$$

$$P_{\theta\theta} = -2\left[\frac{\partial V_\theta}{\partial r}\overline{v_r' v_\theta'} + \frac{1}{r}\left(\frac{\partial V_\theta}{\partial \theta} + V_r\right)\overline{v_\theta'^2} + \frac{\partial V_\theta}{\partial z}\overline{v_\theta' v_z'}\right]; \tag{A.9}$$

$$P_{zz} = -2\left[\frac{\partial V_z}{\partial r}\overline{v_r'v_z'} + \frac{1}{r}\frac{\partial V_z}{\partial \theta}\overline{v_\theta'v_z'} + \frac{\partial V_z}{\partial z}\overline{v_z'^2}\right]; \quad \text{(A.10)}$$

$$P_{r\theta} = -\frac{1}{2}\left(\frac{\partial V_\theta}{\partial r} + \frac{1}{r}\frac{\partial V_r}{\partial \theta} - \frac{V_\theta}{r}\right)\left(\overline{v_r'^2} + \overline{v_\theta'^2}\right) - \left(\frac{\partial V_r}{\partial r} + \frac{1}{r}\frac{\partial V_\theta}{\partial \theta} - \frac{V_r}{r}\right)\overline{v_r'v_\theta'}$$
$$-\frac{1}{2}\left(\frac{1}{r}\frac{\partial V_z}{\partial \theta} + \frac{\partial V_\theta}{\partial z}\right)\overline{v_r'v_z'} - \frac{1}{2}\left(\frac{\partial V_r}{\partial z} + \frac{\partial V_z}{\partial r}\right)\overline{v_\theta'v_z'}; \quad \text{(A.11)}$$

$$P_{rz} = -\frac{1}{2}\left(\frac{\partial V_\theta}{\partial r} + \frac{1}{r}\frac{\partial V_r}{\partial \theta} - \frac{V_\theta}{r}\right)\overline{v_\theta'v_z'} - \left(\frac{\partial V_r}{\partial r} + \frac{\partial V_z}{\partial z}\right)\overline{v_r'v_z'}$$
$$-\frac{1}{2}\left(\frac{1}{r}\frac{\partial V_z}{\partial \theta} + \frac{\partial V_\theta}{\partial z}\right)\overline{v_r'v_\theta'} - \frac{1}{2}\left(\frac{\partial V_r}{\partial z} + \frac{\partial V_z}{\partial r}\right)\left(\overline{v_r'^2} + \overline{v_z'^2}\right); \quad \text{(A.12)}$$

$$P_{\theta z} = -\frac{1}{2}\left(\frac{\partial V_\theta}{\partial z} + \frac{1}{r}\frac{\partial V_z}{\partial \theta} - \frac{V_\theta}{r}\right)\left(\overline{v_\theta'^2} + \overline{v_z'^2}\right) - \left(\frac{1}{r}\frac{\partial V_\theta}{\partial \theta} + \frac{\partial V_z}{\partial z} + \frac{V_r}{r}\right)\overline{v_\theta'v_z'}$$
$$-\frac{1}{2}\left(\frac{1}{r}\frac{\partial V_z}{\partial \theta} + \frac{\partial V_\theta}{\partial z}\right)\overline{v_r'v_\theta'} - \frac{1}{2}\left(\frac{\partial V_r}{\partial z} + \frac{\partial V_z}{\partial r}\right)\overline{v_r'v_\theta'}. \quad \text{(A.13)}$$

- The rotation terms O_{ij}

$$O_{rr} = 0; \quad \text{(A.14)}$$

$$O_{\theta\theta} = 0; \quad \text{(A.15)}$$

$$O_{zz} = 0; \quad \text{(A.16)}$$

$$O_{r\theta} = -\frac{1}{2}\left(\frac{1}{r}\frac{\partial V_r}{\partial \theta} - \frac{V_\theta}{r} - \frac{\partial V_\theta}{\partial r}\right)\overline{v_r'^2} - \frac{1}{2}\left(\frac{\partial V_\theta}{\partial r} + \frac{V_\theta}{r} - \frac{1}{r}\frac{\partial V_r}{\partial \theta}\right)\overline{v_\theta'^2}$$
$$-\frac{1}{2}\left(\frac{1}{r}\frac{\partial V_z}{\partial \theta} - \frac{\partial V_\theta}{\partial z}\right)\overline{v_r'v_z'} - \frac{1}{2}\left(\frac{\partial V_z}{\partial r} - \frac{\partial V_r}{\partial z}\right)\overline{v_\theta'v_z'}; \quad \text{(A.17)}$$

$$O_{rz} = -\frac{1}{2}\left(\frac{\partial V_r}{\partial z} - \frac{\partial V_z}{\partial r}\right)\overline{v_r'^2} - \frac{1}{2}\left(\frac{\partial V_\theta}{\partial z} - \frac{1}{r}\frac{\partial V_z}{\partial \theta}\right)\overline{v_r'v_\theta'}$$
$$-\frac{1}{2}\left(\frac{\partial V_\theta}{\partial r} + \frac{V_\theta}{r} - \frac{1}{r}\frac{\partial V_r}{\partial \theta}\right)\overline{v_\theta'v_z'} - \frac{1}{2}\left(\frac{\partial V_z}{\partial r} - \frac{\partial V_r}{\partial z}\right)\overline{v_z'^2}; \quad \text{(A.18)}$$

$$O_{\theta z} = -\frac{1}{2}\left(\frac{\partial V_r}{\partial z} - \frac{\partial V_z}{\partial r}\right)\overline{v_r'v_\theta'} - \frac{1}{2}\left(\frac{\partial V_\theta}{\partial z} - \frac{1}{r}\frac{\partial V_z}{\partial \theta}\right)\overline{v_\theta'^2}$$
$$-\frac{1}{2}\left(\frac{1}{r}\frac{\partial V_r}{\partial \theta} - \frac{V_\theta}{r} - \frac{\partial V_\theta}{\partial r}\right)\overline{v_r'v_z'} - \frac{1}{2}\left(\frac{1}{r}\frac{\partial V_z}{\partial \theta} - \frac{\partial V_\theta}{\partial z}\right)\overline{v_z'^2} \quad \text{(A.19)}$$

- The turbulent transport terms Tt_{ij}

$$Tt_{rr} = -\frac{1}{r}\frac{\partial}{\partial r}(r\overline{v_r'v_r'v_r'}) - \frac{1}{r}\left(\frac{\partial}{\partial \theta}(\overline{v_r'v_r'v_\theta'}) - 2\overline{v_r'v_\theta'v_\theta'}\right) - \frac{\partial}{\partial z}(\overline{v_r'v_r'v_z'}); \quad \text{(A.20)}$$

$$Tt_{\theta\theta} = -\frac{1}{r}\frac{\partial}{\partial r}(r\overline{v_r' v_\theta' v_\theta'}) - \frac{1}{r}\left(\frac{\partial}{\partial \theta}(\overline{v_\theta' v_\theta' v_\theta'}) + 2\overline{v_r' v_\theta' v_\theta'}\right) - \frac{\partial}{\partial z}(\overline{v_\theta' v_\theta' v_z'}); \quad \text{(A.21)}$$

$$Tt_{zz} = -\frac{1}{r}\frac{\partial}{\partial r}(r\overline{v_r' v_z' v_z'}) - \frac{1}{r}\frac{\partial}{\partial \theta}(\overline{v_\theta' v_z' v_z'}) - \frac{\partial}{\partial z}(\overline{v_z' v_z' v_z'}); \quad \text{(A.22)}$$

$$Tt_{r\theta} = -\frac{1}{r}\frac{\partial}{\partial r}(r\overline{v_r' v_r' v_\theta'}) - \frac{1}{r}\left(\frac{\partial}{\partial \theta}(\overline{v_r' v_\theta' v_\theta'}) + \overline{v_r' v_r' v_\theta'} - \overline{v_\theta' v_\theta' v_\theta'}\right) - \frac{\partial}{\partial z}(\overline{v_r' v_\theta' v_z'}); \quad \text{(A.23)}$$

$$Tt_{rz} = -\frac{1}{r}\frac{\partial}{\partial r}(r\overline{v_r' v_r' v_z'}) - \frac{1}{r}\left(\frac{\partial}{\partial \theta}(\overline{v_r' v_\theta' v_z'}) - \overline{v_\theta' v_\theta' v_z'}\right) - \frac{\partial}{\partial z}(\overline{v_r' v_z' v_z'}); \quad \text{(A.24)}$$

$$Tt_{\theta z} = -\frac{1}{r}\frac{\partial}{\partial r}(r\overline{v_r' v_\theta' v_z'}) - \frac{1}{r}\left(\frac{\partial}{\partial \theta}(\overline{v_\theta' v_\theta' v_z'}) + \overline{v_r' v_\theta' v_z'}\right) - \frac{\partial}{\partial z}(\overline{v_\theta' v_z' v_z'}); \quad \text{(A.25)}$$

- The pressure transport terms Pt_{ij}

$$Pt_{rr} = -\frac{2}{\rho}\left(\frac{\partial}{\partial r}(\overline{v_r' p'}) - \overline{v_r' p'}\right); \quad \text{(A.26)}$$

$$Pt_{\theta\theta} = -\frac{2}{r\rho}\left(\frac{\partial}{\partial \theta}(\overline{v_\theta' p'}) + \overline{v_r' p'}\right); \quad \text{(A.27)}$$

$$Pt_{zz} = -\frac{2}{\rho}\frac{\partial}{\partial z}(\overline{v_z' p'}); \quad \text{(A.28)}$$

$$Pt_{r\theta} = -\frac{1}{\rho}\left[\frac{\partial}{\partial r}(\overline{v_\theta' p'}) + \frac{\partial}{r\partial \theta}(\overline{v_r' p'}) - \frac{1}{r}\overline{v_\theta' p'}\right]; \quad \text{(A.29)}$$

$$Pt_{rz} = -\frac{1}{\rho}\left[\frac{\partial}{\partial r}(\overline{v_z' p'}) + \frac{\partial}{\partial z}(\overline{v_r' p'})\right]; \quad \text{(A.30)}$$

$$Pt_{\theta z} = -\frac{1}{\rho}\left[\frac{\partial}{r\partial \theta}(\overline{v_z' p'}) + \frac{\partial}{\partial z}(\overline{v_\theta' p'})\right]; \quad \text{(A.31)}$$

(A.32)

- The pressure strain terms Π_{ij}

$$\Pi_{rr} = 2\overline{\frac{p'}{\rho}\frac{\partial v_r'}{\partial r}}; \quad \text{(A.33)}$$

$$\Pi_{\theta\theta} = \frac{2}{r}\overline{\frac{p'}{\rho}\left(\frac{\partial v_\theta'}{\partial \theta} + v_r'\right)}; \quad \text{(A.34)}$$

$$\Pi_{zz} = 2\overline{\frac{p'}{\rho}\frac{\partial v_z'}{\partial z}}; \quad \text{(A.35)}$$

$$\Pi_{r\theta} = \overline{\frac{p'}{\rho}\left[\frac{1}{r}\left(\frac{\partial v_r'}{\partial \theta} - v_\theta'\right) + \frac{\partial v_\theta'}{\partial r}\right]}; \quad \text{(A.36)}$$

$$\Pi_{rz} = \overline{\frac{p'}{\rho}\left(\frac{\partial v_r'}{\partial z}+\frac{\partial v_z'}{\partial r}\right)}; \tag{A.37}$$

$$\Pi_{\theta z} = \overline{\frac{p'}{\rho}\left(\frac{1}{r}\frac{\partial v_z'}{\partial \theta}+\frac{\partial v_\theta'}{\partial z}\right)} \tag{A.38}$$

- The dissipation terms ϵ_{ij}

$$\epsilon_{rr} = -\nu\left[\overline{\left(\frac{\partial v_r'}{\partial r}\right)^2}+\overline{\frac{1}{r^2}\left(\frac{\partial v_r'}{\partial \theta}-v_\theta'\right)^2}+\overline{\left(\frac{\partial v_r'}{\partial z}\right)^2}\right]; \tag{A.39}$$

$$\epsilon_{\theta\theta} = -\nu\left[\overline{\left(\frac{\partial v_\theta'}{\partial r}\right)^2}+\overline{\frac{1}{r^2}\left(\frac{\partial v_\theta'}{\partial \theta}+v_r'\right)^2}+\overline{\left(\frac{\partial \overline{v_\theta'^2}}{\partial z}\right)^2}\right]; \tag{A.40}$$

$$\epsilon_{zz} = -\nu\left[\overline{\left(\frac{\partial v_z'}{\partial r}\right)^2}+\overline{\frac{1}{r^2}\left(\frac{\partial v_z'}{\partial \theta}-v_\theta'\right)^2}+\overline{\left(\frac{\partial v_z'}{\partial z}\right)^2}\right]; \tag{A.41}$$

$$\epsilon_{r\theta} = -\nu\left[\overline{\frac{\partial v_r'}{\partial r}\frac{\partial v_\theta'}{\partial r}}+\overline{\frac{1}{r^2}\left(\frac{\partial v_r'}{\partial \theta}-v_\theta'\right)\left(\frac{\partial v_\theta'}{\partial \theta}+v_r'\right)}+\overline{\frac{\partial v_r'}{\partial z}\frac{\partial v_\theta'}{\partial z}}\right]; \tag{A.42}$$

$$\epsilon_{rz} = -\nu\left[\overline{\frac{\partial v_r'}{\partial r}\frac{\partial v_z'}{\partial r}}+\overline{\frac{1}{r^2}\left(\frac{\partial v_r'}{\partial \theta}-v_\theta'\right)\left(\frac{\partial v_z'}{\partial \theta}+v_r'\right)}+\overline{\frac{\partial v_r'}{\partial z}\frac{\partial v_\theta'}{\partial z}}\right]; \tag{A.43}$$

$$\epsilon_{\theta z} = -\nu\left[\overline{\frac{\partial v_\theta'}{\partial r}\frac{\partial v_z'}{\partial r}}+\overline{\frac{1}{r^2}\left(\frac{\partial v_\theta'}{\partial \theta}+v_r'\right)\frac{\partial v_z'}{\partial \theta}}+\overline{\frac{\partial v_\theta'}{\partial z}\frac{\partial v_z'}{\partial z}}\right]; \tag{A.44}$$

(A.45)

- The diffusion term D_{ij}

$$D_{rr} = \nu\left[\frac{1}{r}\frac{\partial}{\partial r}\left(r\frac{\partial \overline{v_r'^2}}{\partial r}\right)+\frac{1}{r^2}\left(\frac{\partial^2\overline{v_r'^2}}{\partial\theta^2}-4\frac{\partial(\overline{v_r'v_\theta'})}{\partial\theta}+2(\overline{v_\theta'^2}-\overline{v_r'^2})\right)+\frac{\partial^2\overline{v_r'^2}}{\partial z^2}\right]; \tag{A.46}$$

$$D_{rr} = \nu\left[\frac{1}{r}\frac{\partial}{\partial r}\left(r\frac{\partial \overline{v_\theta'^2}}{\partial r}\right)+\frac{1}{r^2}\left(\frac{\partial^2\overline{v_\theta'^2}}{\partial\theta^2}+4\frac{\partial(\overline{v_r'v_\theta'})}{\partial\theta}-2(\overline{v_\theta'^2}-\overline{v_r'^2})\right)+\frac{\partial^2\overline{v_\theta'^2}}{\partial z^2}\right]; \tag{A.47}$$

$$D_{zz} = \nu\left[\frac{1}{r}\frac{\partial}{\partial r}\left(r\frac{\partial \overline{v_z'^2}}{\partial r}\right)+\frac{1}{r^2}\frac{\partial^2\overline{v_r'^2}}{\partial\theta^2}+\frac{\partial^2\overline{v_r'^2}}{\partial z^2}\right]; \tag{A.48}$$

$$D_{r\theta} = \nu\left[\frac{1}{r}\frac{\partial}{\partial r}\left(r\frac{\partial\overline{v_r'v_\theta'}}{\partial r}\right)+ \frac{1}{r^2}\left(\frac{\partial^2(\overline{v_\theta'^2})}{\partial\theta^2}+2\frac{\partial(\overline{v_r'^2})}{\partial\theta}-2\frac{\partial\overline{v_\theta'^2}}{\partial\theta}-4\overline{v_r'v_\theta'}\right)+\frac{\partial^2\overline{v_r'v_\theta'}}{\partial z^2}\right]; \quad \text{(A.49)}$$

$$D_{rz} = \nu\left[\frac{1}{r}\frac{\partial}{\partial r}\left(r\frac{\partial(\overline{v_r'v_z'})}{\partial r}\right)+ \frac{1}{r^2}\left(\frac{\partial^2(\overline{v_r'v_z'})}{\partial\theta^2}-2\frac{\partial(\overline{v_\theta'v_z'})}{\partial\theta}-\overline{v_r'v_z'}\right)+\frac{\partial^2\overline{v_r'v_z'}}{\partial z^2}\right]; \quad \text{(A.50)}$$

$$D_{\theta z} = \nu\left[\frac{1}{r}\frac{\partial}{\partial r}\left(r\frac{\partial(\overline{v_\theta'v_z'})}{\partial r}\right)+ \frac{1}{r^2}\left(\frac{\partial^2(\overline{v_\theta'v_z'})}{\partial\theta^2}+2\frac{\partial(\overline{v_r'v_z'})}{\partial\theta}-\overline{v_\theta'v_z'}\right)+\frac{\partial^2\overline{v_\theta'v_z'}}{\partial z^2}\right]. \quad \text{(A.51)}$$

Appendix B: Introduction to B-splines

This appendix gives some of the basic properties of B-spline functions and the Galerkin method based on B-splines. The class of B-spline based numerical method discussed here is most easily understood in one spatial dimension.

B.1 Construction of B-splines

B-splines, or Basis splines, are defined as basis functions for the space of piecewise polynomials. Traditionally, B-splines are constructed by solving a linear set of equations. However, from the method developed by de Boor (1978), given a set of $N+1$ grid points: $[\xi_0, \xi_1, \xi_2, \ldots, \xi_N]$, one can construct $N+k$ splines of order k using a simple recurrence relation:

$$g_l^k(r) = \frac{(r - \xi_{l-k-1})}{(\xi_{l-1} - \xi_{l-k-1})} g_{l-1}^{k-1}(r) + \frac{(\xi_l - r)}{(\xi_l - \xi_{l-k})} g_l^{k-1}(r) \,, \tag{B.1}$$

where $l = 1, 2, \ldots, N+k$, $g_l^k(r)$ is the l^{th} B-spline of order k, and the B-spline of order zero is defined as

$$g_l^0(r) = \begin{cases} 1, & \text{if} \xi_{l-1} \le \xi \le \xi_l \,, \\ 0, & \text{otherwise.} \end{cases} \qquad \text{for } j = 1, 2, \ldots, N+k \tag{B.2}$$

Following de Boor (1978), the near-boundary B-splines can be constructed by considering each of the boundary knots to have a multiplicity of $k+1$, where k is the order of the B-splines. For example the B-spline of k^{th} order, $g_1^k(r)$, needs points ξ_{-1},ξ_{-2}, ..., and ξ_{-k} which are not defined. The multiple virtual points at the boundaries for a B-spline of order k are shown in Figure B.1. de Boor (1978) also developed the

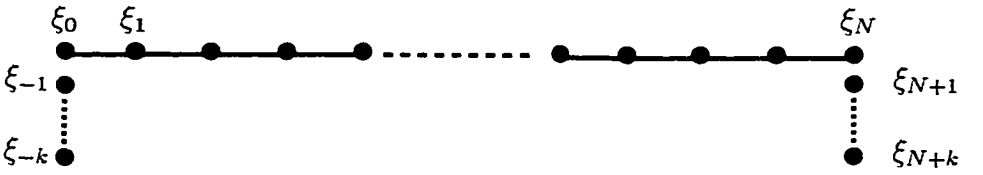

Figure B.1 Uniform knots with virtual points at boundaries.

following recursive relationship for evaluating the first derivative of a B-spline

$$\frac{d}{dr}g_l^k = \frac{kg_{l-1}^{k-1}}{(\xi_{l-1} - \xi_{l-k-1})} - \frac{kg_{l-1}^k}{(\xi_l - \xi_{l-k})} . \tag{B.3}$$

The higher derivatives can be evaluated by repeated application of equation (B.3).

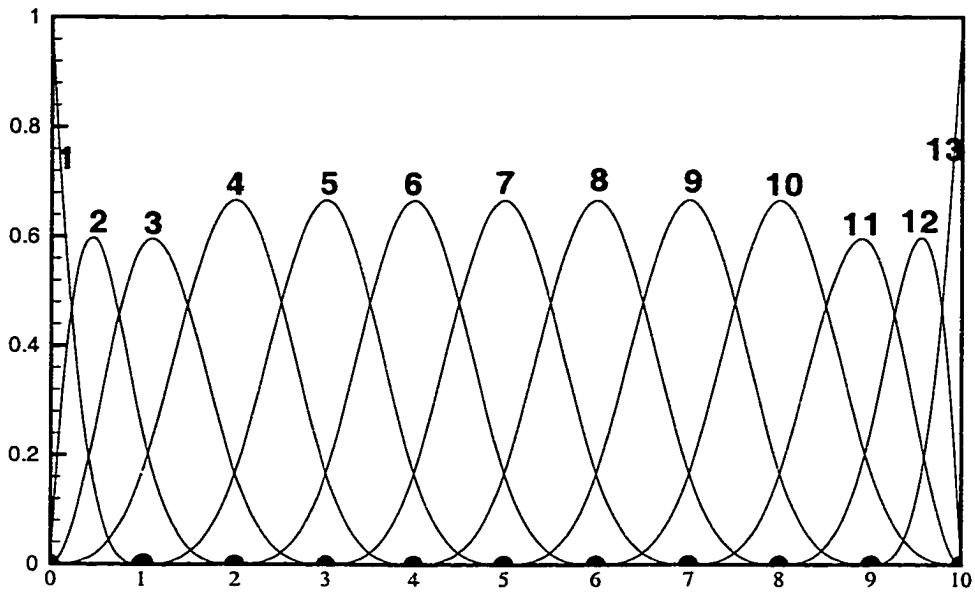

Figure B.2 Cubic B-splines on an 11-knot uniform grid.

B.2 The B-spline Properties

Most of the B-spline properties are given by de Boor (1978). Here, some important properties that are helpful for understanding the B-spline spectral method are listed below:

1. B-splines have local support and are positive on their support,

$$g_l^k(r) > 0 , \quad \text{for} \quad \xi_{l-k-1} < r < \xi_l ,$$
$$g_l^k(r) = 0 , \quad \text{for} \quad r < \xi_{l-k-1} \text{ or } r > \xi_l .$$

Each B-spline of order k has support on $k+1$ intervals, which is delimited by knots. Figure B.2 shows an example of cubic B-splines. The local support of B-splines leads to banded matrices that can be stored and solved.

2. The B-spline basis built by equation (B.1) satisfies

$$\sum_{l=1}^{N+k} g_l^k(r) = 1$$

3. Only $l+1$ of the B-splines has a non-zero l^{th} derivative at the boundary for $l = 0$ to k. This allows boundary conditions to be imposed conveniently.

4. Combining properties 2 and 3, two important properties can be derived

$$\begin{aligned} g_1^k(r)\big|_{r=0} &= g_N^k(r)\big|_{r=1} = 1\,, \\ \frac{d}{dr}\left[g_1^k(r)\right]\big|_{r=0} &= -\frac{d}{dr}\left[g_2^k(r)\right]\big|_{r=0}\,, \\ \frac{d}{dr}\left[g_N^k(r)\right]\big|_{r=1} &= -\frac{d}{dr}\left[g_{N-1}^k(r)\right]\big|_{r=1}\,. \end{aligned}$$

B.3 Galerkin method

To illustrate the numerical techniques based on B-splines and the Galerkin method, we consider the following model equation,

$$\frac{d^n}{dr^n}\phi(r) = f(r) \tag{B.4}$$

which is solved on the domain $r \in [t_0, t_n]$. If $n = 0$, Equation (B.4) is a representation problem. We first approximate ϕ in term of B-splines for order k and the knot set that we have selected:

$$\phi(r) = \tilde{\phi}(r) = \sum_l \alpha_l g_l(r) \tag{B.5}$$

The expansion coefficients in equation (B.5) can be obtained by substituting the expansion Equation (B.5) into equation (B.4) and applying the well-know Galerkin projection. For the Galerkin method, we have

$$\int_{t_0}^{t_n} g_k(r) \sum_{l=1}^{N+k} \frac{d^n}{dr^n}\left[g_l(r)\right] \alpha_l r dr = \int_{t_0}^{t_n} g_k(r) f(r) r dr. \tag{B.6}$$

Evaluating the integrals in equation (B.6), we obtain system of linear equations for α:

$$A\alpha = b \tag{B.7}$$

where

$$A = \{a_{kl}\} = \int_{t_0}^{t_n} g_k(r)\frac{d^n}{dr^n}g_l(r)rdr\ , \tag{B.8}$$

and

$$b = \{b_k\} = \int_{t_0}^{t_n} f(r)g_k(r)rdr \tag{B.9}$$

The matrix A a multidialognal matrix. The bandwidth of matrix A in the Galerkin method is equal to $2k + 1$.

Appendix C: Formulation for B-spline Spectral Method

This appendix gives the details of formulations for the B-spline spectral method including the full definition of the mass and viscous matrices and the details on how the nonlinear term is computed.

C.1 Mass and Viscous Matrices

The mass and viscous matrices defined in Equations (4.37) to (4.40) are assembled from the following fourteen elemental matrices $\mathbf{m}_1$ to $\mathbf{m}_{14}$. All elemental matrices are calculated once at the beginning of the code using Gaussian quadratures; However, with the limitation of the computer memory, the mass and viscous matrices need to be reassembled at every time step. Substituting the basis expansion vectors and weight vectors given in Table 4.3.1 into Equations (4.37) to (4.40), we can obtain the definitions of all elemental matrices as:

$$
\begin{aligned}
\mathbf{m}_1 &= \int_0^R \frac{1}{r} g_k(r) g_l(r) dr \,, \\
\mathbf{m}_2 &= \int_0^R g_k'(r) g_l'(r) r \, dr \,, \\
\mathbf{m}_3 &= \int_0^R g_k(r) g_l(r) r \, dr \,, \\
\mathbf{m}_4 &= \int_0^R g_k'(r) g_l'(r) r^3 \, dr + R^2 g_l(R) g_k(R) \,, \\
\mathbf{m}_5 &= \int_0^R g_k(r) g_l'(r) r^2 \, dr \,, \\
\mathbf{m}_6 &= \int_0^R g_k'(r) g_l(r) r^2 \, dr \,, \\
\mathbf{m}_7 &= \int_0^R \frac{1}{r^3} g_k(r) g_l(r) dr \; - g_k'(0) g_l'(0) \,, \\
\mathbf{m}_8 &= \int_0^R \frac{1}{r} g_k'(r) g_l'(r) \, dr \,, \\
\mathbf{m}_9 &= \int_0^R g_k''(r) g_l''(r) r \, dr - R g_k'(R) g_l''(R) \,, \\
\mathbf{m}_{10} &= \int_0^R g_k''(r) g_l''(r) r^3 \, dr - R^3 g_k'(R) g_l''(R) - R^3 g_k(R) g_l''(R) \,, \\
\mathbf{m}_{11} &= \int_0^R g_k(r) g_l'(r) \, dr \,,
\end{aligned}
$$

$$\begin{aligned}
\mathbf{m}_{12} &= \int_0^R g_k'(r) g_l(r)\, dr\,, \\
\mathbf{m}_{13} &= \int_0^R g_k'(r) g_l''(r) r^2\, dr - R^2 g_k(R) g_l''(R)\,, \\
\mathbf{m}_{14} &= \int_0^R g_k''(r) g_l''(r) r^2\, dr - R^2 g_k'(R) g_l''(R)\,.
\end{aligned}$$

The boundary terms used below are defined as

$$\mathbf{bt}_1 = g_k(R) g_l(R)\,, \quad \mathbf{bt}_2 = R g_k(R) g_l'(R)\,, \quad \mathbf{bt}_3 = \frac{g_k(R) g_l(R)}{R^2}\,,$$
$$\mathbf{bt}_4 = \frac{g_k(R) g_l'(R)}{R} + g_k(R) g_l''(R)\,, \quad \mathbf{bt}_5 = \frac{g_k(R) g_l'(R)}{R} + \frac{g_k(R) g_l(R)}{R^2}\,.$$

C.1.1 Mass matrices

The definition of the mass matrix for each Fourier mode is presented as followings:

- $k_z = 0$ and $k_\theta = 0$

  $\mathbf{A}^{++} = \mathbf{m}_3\,,$

  $\mathbf{A}^{--} = \mathbf{m}_1\,,$

  $\mathbf{A}^{+-} = 0\,,$

  $\mathbf{A}^{-+} = 0\,.$

- $k_z \neq$ and $k_\theta = 0$

  $\mathbf{A}^{++} = {k_z}^2 \mathbf{m}_3\,,$

  $\mathbf{A}^{--} = 2{k_z}^2 \mathbf{m}_3 + \mathbf{m}_1 + \mathbf{m}_2 + \mathbf{bt}_1\,,$

  $\mathbf{A}^{+-} = {k_z}^2 \mathbf{m}_3\,,$

  $\mathbf{A}^{-+} = {k_z}^2 \mathbf{m}_3\,.$

- $k_z = 0$ and $k_\theta \neq 0$

  $\mathbf{A}^{++} = ({k_\theta}^2 - 1)\mathbf{m}_3 + \mathbf{m}_4\,,$

  $\mathbf{A}^{--} = ({k_z}^2 - 1)\mathbf{m}_1 + \mathbf{m}_2 + \mathbf{m}_2 + (1 - k_\theta)\mathbf{bt}_1\,,$

  $\mathbf{A}^{+-} = 0\,,$

  $\mathbf{A}^{-+} = 0$

- $k_z \neq$ and $k_\theta \neq 0$

$$\mathbf{A}^{++} = {k_z}^2 \left[(k_\theta{}^2 - 1)\mathbf{m}_3 + \mathbf{m}_4\right] ,$$
$$\mathbf{A}^{--} = 2{k_z}^2\mathbf{m}_3 + (k_\theta - 1)\mathbf{m}_1 + \mathbf{m}_2 + (1 - k_\theta)\mathbf{bt}_1 ,$$
$$\mathbf{A}^{+-} = {k_z}^2 \left[(k_\theta + 1)\mathbf{m}_3 + \mathbf{n}_5\right] ,$$
$$\mathbf{A}^{-+} = {k_z}^2 \left[(k_\theta + 1)\mathbf{m}_3 + \mathbf{m}_6\right] .$$

C.1.2 Viscous matrices

The definition of the viscous matrix for each Fourier mode is presented as followings:

- $k_z = 0$ and $k_\theta = 0$

$$\begin{aligned}
\mathbf{B}^{++} &= -\frac{1}{Re}(\mathbf{m}_1 + \mathbf{m}_2 - \mathbf{bt}_2) , \\
\mathbf{B}^{--} &= -\frac{1}{Re}(\mathbf{m}_8 - \mathbf{m}_7 - \mathbf{bt}_5 - \mathbf{bt}_3) , \\
\mathbf{B}^{+-} &= 0 , \\
\mathbf{B}^{-+} &= 0 .
\end{aligned}$$

- $k_z \neq 0$ and $k_\theta = 0$

$$\begin{aligned}
\mathbf{B}^{++} &= -\frac{k_z^2}{Re}\left[k_z^2\mathbf{m}_3 + \mathbf{m}_1 + \mathbf{m}_2 - \mathbf{bt}_2\right] , \\
\mathbf{B}^{--} &= -\frac{1}{Re}\left[2k_z^4\mathbf{m}_3 - 3(\mathbf{m}_7 - \mathbf{m}_8) + 3k_z^2(\mathbf{m}_1 + \mathbf{m}_2) + \mathbf{m}_9 + \right. \\
&\qquad \left. k_z^2(\mathbf{bt}_1 - \mathbf{bt}_2) - 2\mathbf{bt}_3 - \mathbf{bt}_4 - \mathbf{bt}_5\right] , \\
\mathbf{B}^{+-} &= -\frac{k_z^2}{Re}\left[k_z^2\mathbf{m}_3 + \mathbf{m}_1 + \mathbf{m}_2 - \mathbf{bt}_2\right] , \\
\mathbf{B}^{-+} &= -\frac{k_z^2}{Re}\left[k_z^2\mathbf{m}_3 + \mathbf{m}_1 + \mathbf{m}_2 - \mathbf{bt}_2\right] .
\end{aligned}$$

- $k_z = 0$ and $k_\theta \neq 0$

$$\begin{aligned}
\mathbf{B}^{++} &= -\frac{1}{Re}\Big[(k_z^2-1)^2\mathbf{m}_1 + (2k_\theta^2+1)\mathbf{m}_2 + \\
&\qquad \mathbf{m}_{10} - (1-k_\theta^2)\mathbf{bt}_1 - (2+k_\theta^2)\mathbf{bt}_2\Big] , \\
\mathbf{B}^{--} &= -\frac{1}{Re}\Big[(-3+4k_\theta+2k_\theta^-4k_\theta^3)\mathbf{m}_7 + (3-4k_\theta+2k_\theta^2)\mathbf{m}_8 + \mathbf{m}_9 + \\
&\qquad (-2+3k_\theta-k_\theta^3)\mathbf{bt}_3 + (k_\theta+1)(\mathbf{bt}_4 - (k_\theta-1)\mathbf{bt}_5)\Big] , \\
\mathbf{B}^{+-} &= 0 , \\
\mathbf{B}^{-+} &= 0 .
\end{aligned}$$

- $k_z \neq 0$ and $k_\theta \neq 0$

$$\begin{aligned}
\mathbf{B}^{++} &= -\frac{k_z^2}{Re}\Big[k_z^2((k_\theta^2-1)\mathbf{m}_3 + \mathbf{m}_4) + (k_\theta^2-1)\mathbf{m}_1 + (2k_\theta^2+1)\mathbf{m}_2 + \mathbf{m}_{10} + \\
&\qquad (1-k_\theta^2)\mathbf{bt}_1 - (2+k_\theta^2)\mathbf{bt}_2\Big] , \\
\mathbf{B}^{--} &= -\frac{1}{Re}\Big[2k_z^4\mathbf{m}_3 - (-3+4k_\theta+2k_\theta^2-4k_\theta^3+k_\theta^4)\mathbf{m}_7 + \\
&\qquad 3k_z^2((k_\theta-1)^2 bfm_1 + \mathbf{m}_2) + (3-4k_\theta+2k_\theta^2)\mathbf{m}_8 + \mathbf{m}_9 + \\
&\qquad k_z^2((1-k_\theta)\mathbf{bt}_1 - 2\mathbf{bt}_2) + (-2+3k_\theta-k_\theta^3)\mathbf{bt}_3 + \\
&\qquad (k_\theta-1)(\mathbf{bt}_4 - (k_\theta-1)\mathbf{bt}_5)\Big] , \\
\mathbf{B}^{+-} &= -\frac{k_z^2}{Re}\Big[k_z^2((k_\theta+1)\mathbf{m}_3 + \mathbf{m}_5) + (k_\theta-1)^2((k_\theta+1)\mathbf{m}_1 + \mathbf{m}_{11}) + \\
&\qquad (k_\theta+2)\mathbf{m}_2 + \mathbf{m}_{13} - (2k_\theta)\mathbf{bt}_2\Big] , \\
\mathbf{B}^{-+} &= -\frac{k_z^2}{Re}\Big[k_z^2((k_\theta+1)\mathbf{m}_3 + \mathbf{m}_6) + (k_\theta-1)^2((k_\theta+1)\mathbf{m}_1 + \mathbf{m}_{12}) + \\
&\qquad (k_\theta+2)\mathbf{m}_2 + \mathbf{m}_{14} - (1+k_\theta)\mathbf{bt}_2\Big] .
\end{aligned}$$

The mass and viscous matrices are stored in a special banded form for minimizing storage. The structure of the mass matrix is shown in Figure C.1. By imposing the regularity conditions (Loulou 1996), the bandwidth of the matrix in the first $2k$ rows is locally widened. The elements denoted by $*$ in Figure C.1 are the extra terms introduced by the regularity conditions. In order to form such special banded mass and viscous matrices, the expansion coefficients α and the nonlinear term vector $\mathbf{F}^{\pm}$ have to be ordered with the $+$ and $-$ modes alternating, i.e. $\alpha = \{\alpha_1^+, \alpha_1^-, \alpha_2^+, \alpha_2^-, \ldots\}$.

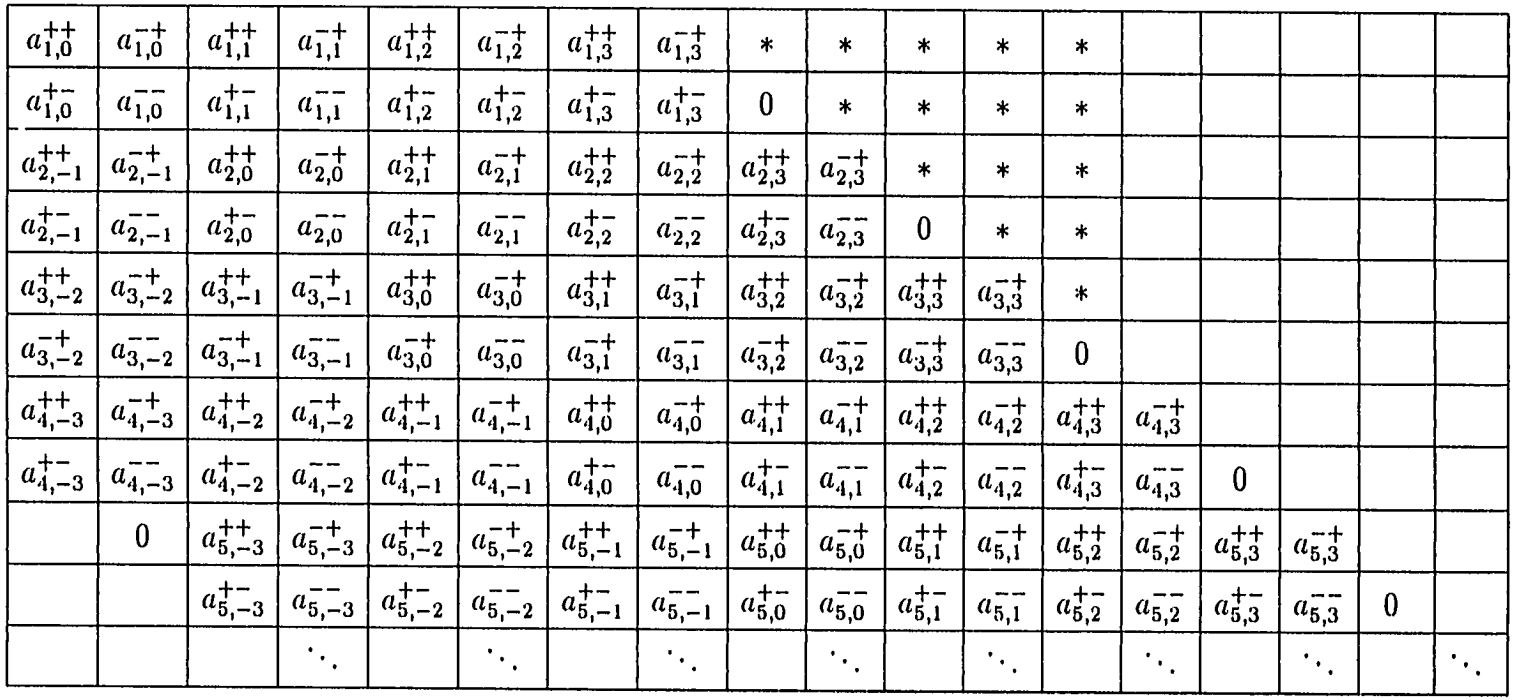

Figure C.1 The Mass matrix with cubic B-splines

C.2 Nonlinear Term

The computation of the nonlinear term is the most expensive operation of the code, since the radial direction in which the B-splines are applied needs $O(N^2)$ operations. The details on how to evaluate the nonlinear term are presented in this section.

Substituting the expansion and weight basis vectors in Table 4.3.1 into Eq. (4.41), we can obtain the nonlinear terms

$$\begin{aligned}\mathbf{F}_k^+ &= \frac{1}{2\pi L_z}\int_0^{L_z}\int_0^{2\pi}\int_0^{R}\mathbf{w}_k^+\cdot(\mathbf{v}\times\omega)e^{-i(k_\theta\theta+k_z z)}\,rdrd\theta dz \\ &= \mathcal{I}^+(ik_\theta\gamma_k^+ - \Upsilon_k^-) - \mathcal{J}^+\tilde{\Upsilon}_k\,, \end{aligned} \tag{C.1}$$

$$\begin{aligned}\mathbf{F}_k^- &= \frac{1}{2\pi L_z}\int_0^{L_z}\int_0^{2\pi}\int_0^{R}\mathbf{w}_k^-\cdot(\mathbf{v}\times\omega)e^{-i(k_\theta\theta+k_z z)}\,rdrd\theta dz \\ &= \mathcal{I}^-(i\gamma_k^+ - \Upsilon_k^-) + \mathcal{F}^-\beta_k^- - \mathcal{G}^-\tilde{\delta}_k\,, \end{aligned} \tag{C.2}$$

where

$$\mathcal{I}^+ = \begin{cases} k_z, & k_z \neq 0 \\ 1, & k_z = 0 \end{cases}, \quad \mathcal{J}^+ = \begin{cases} k_z, & k_z \neq 0 \text{ and } k_\theta \neq 0 \\ 1, & k_z = 0 \text{ and } k_\theta \neq 0 \\ 0, & k_\theta = 0 \end{cases}, \tag{C.3}$$

$$\mathcal{I}^- = k_z, \quad \mathcal{F}^- = k_\theta - 1, \quad \mathcal{G}^- = \begin{cases} 1, & k_\theta \neq 0 \text{ or } k_\theta \neq 0 \\ 0, & \text{otherwise} \end{cases} \tag{C.4}$$

Terms γ_k^+, β_k^-, Υ_k^-, $\tilde{\Upsilon}_k$, and $\tilde{\delta}_k$ can be assembled from 11 nonlinear three-dimensional matrices $\mathbf{f}_1$ to $\mathbf{f}_{11}$ and expansion coefficients, A_l to K_l, defined in Section 4.3.3. The definition of terms γ_k^+, β_k^-, Υ_k^-, $\tilde{\Upsilon}_k$, and $\tilde{\delta}_k$ is given as

$$\begin{aligned}\gamma_k^+ &= \sum_{m=1}^{N_r}\sum_{l=1}^{N_r}(E_mF_l + H_mI_l)\mathbf{f}_1 + (E_mG_l + H_mJ_l)r\mathbf{f}_2 + \\ &\quad (I_m + 2J_m)(I_lr\mathbf{f}_5 + J_lr^2\mathbf{f}_6) + F_m\left[F_l\left(\frac{\mathbf{f}_5}{r} - \frac{\mathbf{f}_1}{r^2}\right) + G_l\left(\mathbf{f}_6 - \frac{\mathbf{f}_2}{r}\right)\right] + \\ &\quad G_m(F_l\mathbf{f}_9 + G_lr\mathbf{f}_{10}) + J_m(I_lr^2\mathbf{f}_9 + J_lr^3\mathbf{f}_{10}) \\ \beta_k^- &= \sum_{m=1}^{N_r}\sum_{l=1}^{N_r}(A_mI_l - E_mK_l)\mathbf{f}_1 + (C_mI_l + F_mK_l)\frac{\mathbf{f}_1}{r^2} + J_l\left(rA_m\mathbf{f}_2C_m\frac{\mathbf{f}_2}{r}\right) +\end{aligned}$$

$$D_m J_l \mathbf{f}_6 - G_m K_l \mathbf{f}_9 + B_m(I_l r \mathbf{f}_5 + J_l r^2 \mathbf{f}_6) + (D_m I_l - F_m K_l)\frac{\mathbf{f}_5}{r}$$

$$\Upsilon_k^- = \sum_{m=1}^{N_r}\sum_{l=1}^{N_r} (A_m F_l + H_m K_l)\mathbf{f}_1 + A_m G_l r \mathbf{f}_2 + C_m\left(F_l\frac{\mathbf{f}_1}{r^2} + G_l\frac{\mathbf{f}_2}{r}\right) + B_M G_l r^2 \mathbf{f}_2 +$$
$$(B_m F_l + I_m K_l + 2J_m K_l) r \mathbf{f}_5 + D_m\left(K_l\frac{\mathbf{f}_5}{r} + G_l \mathbf{f}_6\right) + J_m K_l r^2 \mathbf{f}_9$$

$$\tilde{\Upsilon}_k = \sum_{m=1}^{N_r}\sum_{l=1}^{N_r} (A_m F_l + H_m K_l) r \mathbf{f}_3 + A_m G_l r^2 \mathbf{f}_4 + C_m\left(F_l\frac{\mathbf{f}_3}{r} + G_l \mathbf{f}_4\right) + B_M G_l r^3 \mathbf{f}_8 +$$
$$(B_m F_l + I_m K_l + 2J_m K_l) r^2 \mathbf{f}_7 + D_m(K_l \mathbf{f}_7 + G_l r \mathbf{f}_8) + J_m K_l r^3 \mathbf{f}_{11}$$

$$\tilde{\delta}_k = \sum_{m=1}^{N_r}\sum_{l=1}^{N_r} (A_m I_l - E_m K_l) r \mathbf{f}_3 + (C_m I_l + F_m K_l)\frac{\mathbf{f}_3}{r} + J_l \mathbf{f}_4(C_m + r^2 A_m) +$$
$$(D_m I_l - F_m K_l)\mathbf{f}_7 + B_m(I_l r^2 \mathbf{f}_7 + J_l r^3 \mathbf{f}_8) + D_m J_l r \mathbf{f}_8 - G_m K_l r \mathbf{f}_{11} .$$

where

$$\mathbf{f}_1 = \int_0^R g_k(r) g_l(r) g_m(r) dr , \qquad \mathbf{f}_2 = \int_0^R g_k(r) g_l'(r) g_m(r) dr$$
$$\mathbf{f}_3 = \int_0^R g_k'(r) g_l(r) g_m(r) dr , \qquad \mathbf{f}_4 = \int_0^R g_k'(r) g_l'(r) g_m(r) dr$$
$$\mathbf{f}_5 = \int_0^R g_k(r) g_l(r) g_m'(r) dr , \qquad \mathbf{f}_6 = \int_0^R g_k(r) g_l'(r) g_m'(r) dr$$
$$\mathbf{f}_7 = \int_0^R g_k'(r) g_l(r) g_m'(r) dr , \qquad \mathbf{f}_8 = \int_0^R g_k'(r) g_l'(r) g_m'(r) dr$$
$$\mathbf{f}_9 = \int_0^R g_k(r) g_l(r) g_m''(r) dr , \qquad \mathbf{f}_{10} = \int_0^R g_k(r) g_l'(r) g_m''(r) dr$$
$$\mathbf{f}_{11} = \int_0^R g_k'(r) g_l(r) g_m''(r) dr .$$

As mentioned in Section 4.3.5, the nonlinear terms are evaluated in physical space. The first step is to compute the expansion coefficients A_l to K_l in Fourier wave space. Then they are transformed to physical space. The second step is to evaluate terms γ_k^+, β_k^-, Υ_k^-, $\tilde{\Upsilon}_k$, and $\tilde{\delta}_k$ in physical space and transform them back to Fourier wave space. Finally, the nonlinear terms can be evaluated from Equations (C.1) and (C.2).

VITA

VITA

Jim Hongxin Qin was born in Zhejing province, P. R. of China in 1964. He received his Bachelor of Science and Master of Science degrees from the Department of Power Engineering of the Shanghai Institute of Mechanical Engineering (SIME) in 1984 and 1989, respectively. From 1984 to 1986, he worked for Hangzhou Institute of Air Separation Plant as a Project Engineer. After receiving his Master's degree, he joined SIME as an Assistant Professor.

Before enrolling in the doctoral program of the School of Aeronautics and Astronautics at Purdue University in 1994, Mr. Qin worked for one year as a Senior Sales Executive at the Shanghai office of Kawasaki Kisen Kaisha Ltd. His Ph.D. dissertation is entitled "Numerical Simulations of a Turbulent Axial Vortex". During his stay at Purdue University, he also enrolled in the Master's program of the School of Computer Science.

In 1995, Mr. Qin married Sunny Haoyin Zhang.